Metasurfaces: beyond diffractive and refractive optics

Thesis by
Ehsan Arbabi

In Partial Fulfillment of the Requirements for the
Degree of
Doctor of Philosophy

CALIFORNIA INSTITUTE OF TECHNOLOGY
Pasadena, California

2019
Defended April 11, 2019

Ehsan Arbabi
ORCID: 0000-0002-5328-3863

To Mahsa, my parents, and Amir.

ACKNOWLEDGEMENTS

Caltech has been a special place for me, as it has provided me with everything that I would have asked for to have a great graduate experience. While many at the institute have played significant roles in giving me this opportunity, I owe a great deal to Prof. Andrei Faraon, who was both a great advisor and a nice friend. He gave me the freedom to explore what I liked, was open, friendly, and helped me develop self confidence, allowing me to freely express my opinions. His calm and positive attitude was of great assistance for pushing forward when facing hardships and failures, and his passion and determination for doing *good and useful science* has been a great inspiration. I have learnt a lot from him, both scientifically and personally, and for this I express my tremendous gratitude.

Several Caltech faculty have helped me during these years, especially my candidacy and thesis committee members, Professors Ali Hajimiri, Yu-Chong Tai, Kerry Vahala, and Amnon Yariv. I sincerely appreciate their time and helpful pieces of advice. I also acknowledge the great help and support I have received from my collaborators both inside and outside of Caltech, including Professors Daniel Wagenaar, Viviana Gradinaru, William E. Moerner, Alan Willner, and Pol Van Dorpe. In addition, Caltech staff have been super helpful and friendly, speeding everything up and assisting in every aspect they could. I am therefore grateful to all of them, especially Cecilia Gamboa, Christine Jenstad, Tanya Owen, Carol Sosnowski, Jonathan Gross, Connie Rodriguez, Jennifer Blankenship, Tess Legaspi, and Daniel Yoder. In addition, almost nothing I have done during my doctoral studies would have been possible without the support I have received from the Kavli Nanoscience Institute at Caltech, for which I am greatly thankful to the institute and its past and current staff, especially Dr. Guy DeRose, Melissa Melendes, Dr. Matthew Sullivan Hunt, Steven Martinez, Bert Mendoza, Alex Wertheim, Nathan Lee, Tiffany Kimoto, Jennifer Palmer, and Mary Sikora. I would also like to thank our collaborators from Samsung Electronics, especially Dr. Seunghoon Han and Dr. Duhyun Lee, for discussions and collaborations on various ideas.

I have been extremely fortunate to be part of the Faraon group, who have always been very open, helpful, and collaborative. I am thankful to all the members for generating this great atmosphere of friendship, and for always being there when I needed them. Especially I would like to thank Yu Horie for teaching me a lot in the cleanroom and the lab, and for a lot of great discussions and collaborations. I am thankful to

Sadegh Faraji-Dana, Hyounghan Kwon, Jiaqi Li, Leon Ding, and Romanus Hutchins because of our friendship and close collaborations on many projects. I have learnt a great deal in my discussions with Philip Camayd-Munoz, Conner Ballew, Greg Roberts, and Tianzhe Zheng, for which I express my gratitude. I would also like to thank Evan Miyazono, Max Jones, John Bartholomew, Jonathan Kindem, Tian Zhong, Chuting Wang, Ioana Craiciu, Jake Rochman, Andrei Ruskuc, Daniel Riedel, Mi Lei, and Tian Xie for everything, and above all, for being great friends.

The number of teachers who have prepared me for this day is indeed very large, and I am tremendously in debt to all of them for what they have taught me. While it is not possible to name all of them here, I would like to specifically thank my masters and bachelors advisor, Prof. Mahmoud Shahabadi, to whom I owe most of what I know about electromagnetics. In addition I would like to thank Professors Lynford Goddard, Parviz Jabehdar Maralani, Reza Faraji-Dana, Mehdi Ahmadi-Boroujeni, Karim Mohammadpour-Aghdam, and Jalil Rashed-Mohassel, all of whom I have learned a lot from. In addition, I am forever thankful to my high school teachers Mr. Zare' and Mr. Yaqoubi for their role in my scientific upbringing.

My family and friends have provided me with crucial support during all these years. My parents have always supported me in the pursuit of my interests, often sacrificing their own happiness for mine. I especially appreciate that they patiently bore through about six years during which I wasn't able to visit them. My father- and mother-in-law have also been extremely supportive of me and Mahsa. Their help and patience have definitely helped us a lot in pulling through these years. Our several kind friends in the Los Angeles area were always a source of joy and energy for us, giving us a sense of community and belonging. It is hard for me to imagine how we could have tolerated being far from home and family without them. I would specifically like to thank Hassan, Mohammad, Alireza, Mostafa, Jalil, Pouya, Ali, Hossein, Reza, Massoud, Zahra, Marzieh, Hanieh, Fahimeh, Sahar, Fatemeh, Mona, and Nasrin.

Amir has always played an irreplaceable role in my life. I have learnt from him more than I have learnt from anyone else, and he has always served as a great mentor and role model for me. He introduced me to the world of physics and mathematics when I was in high school, and has continued to fascinate me with his insight and knowledge up to this date. Like always, during my PhD, he was a supportive older brother and a great mentor. He has been instrumental in all of the work I have done in my doctoral studies, and this thesis would have not been possible without his guidance and collaboration.

It is hard for me to imagine a better collaborator, partner, and wife than Mahsa. It is not often that spouses become coworkers as well, and for me, despite the warnings I got from some, this was a great experience. Some of our best ideas were developed in discussions outside of the work places and hours, and several of our problems and issues were resolved during those same discussions. She was always understanding and supportive of me and my work, as we were almost always in the same boat. She has played a key role in all I have achieved so far, and there is no way I can thank her enough in such a short passage.

Throughout my life, I have always been blessed to have the means and opportunities to follow my passion. For these, I am in deep gratitude to all who have made this possible, and above all, to God for his unending blessings. I hope that as a result of these, I am not only better educated now, but generally a better and more useful person for the world.

Ehsan Arbabi
Pasadena, California
April 11, 2019

ABSTRACT

Optical metasurfaces are a category of thin diffractive optical elements, fabricated using the standard micro- and nano-fabrication techniques. They provide new ways of controlling the flow of light based on various properties such as polarization, wavelength, and propagation direction. In addition, their compatibility with standard micro-fabrication techniques and compact form factor allows for the development of several novel platforms for the design and implementation of various complicated optical elements and systems. In this thesis, I first give a short overview and a brief history of the works on optical metasurfaces. Then I discuss the capabilities of metasurfaces in controlling the polarization and phase of light, and showcase their potential applications through the cases of polarimetric imaging and vectorial holography. Then, a discussion of the chromatic dispersion in optical metasurfaces is given, followed by three methods that can be utilized to design metasurfaces working at multiple discrete wavelengths. As a potential application of such metasurfaces, I present results of using them as objective lenses in two-photon microscopy. In addition, I discuss how metasurfaces enable the at-will control of chromatic dispersion in diffractive optical elements, demonstrate metasurfaces with controlled dispersion, and provide a discussion of their limitations. Integration of multiple metasurfaces into *metasystems* allows for implementation of complicated optical functions such as imaging and spectrometry. In this regard, I present several examples of how such metasystems can be designed, fabricated, and utilized to provide wide field of view imaging and projection, microelectromechanically tunable lenses, optical spectrometers, and retroreflectors. I conclude with an outlook on where metasurfaces can be most useful, and what limitations should be overcome before they can find wide-spread application.

Thesis supervisor:

- Andrei Faraon
  Professor of Applied Physics and Electrical Engineering

Thesis committee:

- Andrei Faraon
  Professor of Applied Physics and Electrical Engineering
- Ali Hajimiri (Chair)
  Bren Professor of Electrical Engineering and Medical Engineering
- Yu-Chong Tai
  Anna L. Rosen Professor of Electrical Engineering and Medical Engineering
- Kerry J. Vahala
  Ted and Ginger Jenkins Professor of Information Science and Technology and Applied Physics
- Amnon Yariv
  Martin and Eileen Summerfield Professor of Applied Physics and Electrical Engineering

PUBLISHED CONTENT AND CONTRIBUTIONS

[1] S. M. Kamali*, E. Arbabi*, A. Arbabi, and A. Faraon, "A review of dielectric optical metasurfaces for wavefront control", Nanophotonics **7**, 1041–1068 (2018) DOI: 10.1515/nanoph-2017-0129,

E.A. and S.M.K. have participated equally in the collection and analysis of the data and writing of this review paper.

[2] E. Arbabi, S. M. Kamali, A. Arbabi, and A. Faraon, "Full-stokes imaging polarimetry using dielectric metasurfaces", ACS Photonics **5**, 3132–3140 (2018) DOI: 10.1021/acsphotonics.8b00362,

E.A. has participated in the conception of the experiments, design, fabrication, and measurement of the samples, analysis of the data, and writing the manuscript.

[3] E. Arbabi, S. M. Kamali, A. Arbabi, and A. Faraon, "Vectorial holograms with a dielectric metasurface: ultimate polarization pattern generation", Submitted,

E.A. has participated in the conception of the experiments, design, fabrication, and measurement of the samples, analysis of the data, and writing the manuscript.

[4] E. Arbabi, A. Arbabi, S. M. Kamali, Y. Horie, and A. Faraon, "Multiwavelength polarization-insensitive lenses based on dielectric metasurfaces with meta-molecules", Optica **3**, 628–633 (2016) DOI: 10.1364/OPTICA.3.000628,

E.A. has participated in the conception of the experiments, design, fabrication, and measurement of the samples, analysis of the data, and writing the manuscript.

[5] E. Arbabi, A. Arbabi, S. M. Kamali, Y. Horie, and A. Faraon, "Multiwavelength metasurfaces through spatial multiplexing", Sci. Rep. **6**, 32803 (2016) DOI: 10.1038/srep32803,

E.A. has participated in the conception of the experiments, design, fabrication, and measurement of the samples, analysis of the data, and writing the manuscript.

[6] E. Arbabi, A. Arbabi, S. M. Kamali, Y. Horie, and A. Faraon, "High efficiency double-wavelength dielectric metasurface lenses with dichroic birefringent meta-atoms", Opt. Express **24**, 18468–18477 (2016) DOI: 10.1364/OE.24.018468,

E.A. has participated in the conception of the experiments, design, fabrication, and measurement of the samples, analysis of the data, and writing the manuscript.

[7] E. Arbabi, J. Li, R. J. Hutchins, S. M. Kamali, A. Arbabi, Y. Horie, P. Van Dorpe, V. Gradinaru, D. A. Wagenaar, and A. Faraon, "Two-photon microscopy with a double-wavelength metasurface objective lens", Nano Lett. **18**, 4943–4948 (2018) DOI: 10.1021/acs.nanolett.8b01737,

E.A. has participated in the conception of the experiments, design, fabrication, and measurement of the samples, analysis of the data, and writing the manuscript.

[8] E. Arbabi, A. Arbabi, S. M. Kamali, Y. Horie, and A. Faraon, "Controlling the sign of chromatic dispersion in diffractive optics with dielectric metasurfaces", Optica **4**, 625–632 (2017) DOI: 10.1364/OPTICA.4.000625,

E.A. has participated in the conception of the experiments, design, fabrication, and measurement of the samples, analysis of the data, and writing the manuscript.

[9] A. Arbabi, E. Arbabi, S. M. Kamali, Y. Horie, S. Han, and A. Faraon, "Miniature optical planar camera based on a wide-angle metasurface doublet corrected for monochromatic aberrations", Nat. Commun. **7**, 13682 (2016) DOI: 10.1038/ncomms13682,

E.A. has participated in the fabrication and measurement of the samples, analysis of the data, and writing the manuscript.

[10] S. M. Kamali*, E. Arbabi*, and A. Faraon, "Metasurface-based compact light engine for ar headsets", in Spie photon. west (2019), p. 11040, DOI: 10.1117/12.2523720,

E.A. and S.M.K. have participated equally in the conception of the ideas, design of the devices, performing the simulations, analysis of the data, and writing the manuscript.

[11] E. Arbabi, A. Arbabi, S. M. Kamali, Y. Horie, M. Faraji-Dana, and A. Faraon, "Mems-tunable dielectric metasurface lens", Nat. Commun. **9**, 812 (2018) DOI: 10.1038/s41467-018-03155-6,

E.A. has participated in the conception of the experiments, design, fabrication, and measurement of the samples, analysis of the data, and writing the manuscript.

[12] M. Faraji-Dana*, E. Arbabi*, A. Arbabi, S. M. Kamali, H. Kwon, and A. Faraon, "Compact folded metasurface spectrometer", Nat. Commun. **9**, 4196 (2018) DOI: 10.1038/s41467-018-06495-5,

E.A. and M.F. have participated equally in the conception of the experiments, design, fabrication, and measurement of the samples, analysis of the data, and writing the manuscript.

[13] A. Arbabi, E. Arbabi, Y. Horie, S. M. Kamali, and A. Faraon, "Planar metasurface retroreflector", Nat. Photon. **11**, 415–420 (2017) DOI: 10.1038/nphoton.2017.96,

E.A. has participated in the fabrication and measurement of the samples, analysis of the data, and writing the manuscript.

OTHER PUBLICATIONS

[1] S. M. Kamali, A. Arbabi, E. Arbabi, Y. Horie, and A. Faraon, "Decoupling optical function and geometrical form using conformal flexible dielectric metasurfaces", Nat. Commun. **7**, 11618 (2016) DOI: doi.org/10.1038/ncomms11618.

[2] S. M. Kamali, E. Arbabi, A. Arbabi, Y. Horie, and A. Faraon, "Highly tunable elastic dielectric metasurface lenses", Laser Photon. Rev. **10**, 1062–1062 (2016) DOI: 10.1002/lpor.201600144.

[3] M. P. Backlund, A. Arbabi, P. N. Petrov, E. Arbabi, S. Saurabh, A. Faraon, and W. E. Moerner, "Removing orientation-induced localization biases in single-molecule microscopy using a broadband metasurface mask", Nat. Photon. **10**, 459–462 (2016) DOI: 10.1038/nphoton.2016.93.

[4] Y. Horie, A. Arbabi, E. Arbabi, S. M. Kamali, and A. Faraon, "Wide bandwidth and high resolution planar filter array based on DBR-metasurface-DBR structures", Opt. Express **24**, 11677–11682 (2016) DOI: 10.1364/OE.24.011677.

[5] Y. Ren, L. Li, Z. Wang, S. M. Kamali, E. Arbabi, A. Arbabi, Z. Zhao, G. Xie, Y. Cao, N. Ahmed, Y. Yan, C. Liu, A. J. Willner, S. Ashrafi, M. Tur, A. Faraon, and A. E. Willner, "Orbital angular momentum-based space division multiplexing for high-capacity underwater optical communications", Sci. Rep. **6**, 33306 (2016) DOI: doi.org/10.1038/srep33306.

[6] S. M. Kamali, E. Arbabi, A. Arbabi, Y. Horie, M. Faraji-Dana, and A. Faraon, "Angle-multiplexed metasurfaces: encoding independent wavefronts in a single metasurface under different illumination angles", Phys. Rev. X **7**, 041056 (2017) DOI: 10.1103/PhysRevX.7.041056.

[7] Y. Horie, A. Arbabi, E. Arbabi, S. M. Kamali, and A. Faraon, "High-speed, phase-dominant spatial light modulation with silicon-based active resonant antennas", ACS Photonics **5**, 1711–1717 (2018) DOI: 10.1021/acsphotonics.7b01073.

[8] Y. Horie, S. Han, J.-Y. Lee, J. Kim, Y. Kim, A. Arbabi, C. Shin, L. Shi, E. Arbabi, S. M. Kamali, H.-S. Lee, S. Hwang, and A. Faraon, "Visible wavelength color filters using dielectric subwavelength gratings for backside-illuminated CMOS image sensor technologies", Nano Lett. **17**, 3159–3164 (2017) DOI: 10.1021/acs.nanolett.7b00636.

[9] Z. Wang, Y. Yan, A. Arbabi, G. Xie, C. Liu, Z. Zhao, Y. Ren, L. Li, N. Ahmed, A. J. Willner, E. Arbabi, A. Faraon, R. Bock, M. Ashrafi, Solyman Tur, and A. E. Willner, "Orbital angular momentum beams generated by passive dielectric phase masks and their performance in a communication link", Opt. Lett. **42**, 2746–2749 (2017) DOI: 10.1364/OL.42.002746.

[10] H. Kwon, E. Arbabi, S. M. Kamali, M. Faraji-Dana, and A. Faraon, "Computational complex optical field imaging using a designed metasurface diffuser", Optica **5**, 924–931 (2018) DOI: 10.1364/OPTICA.5.000924.

[11] H. Kwon, E. Arbabi, S. M. Kamali, M. Faraji-Dana, and A. Faraon, "Quantitative phase gradient microscopy using a system of multifunctional metasurfaces", Submitted.

[12] M. Faraji-Dana, E. Arbabi, H. Kwon, S. M. Kamali, A. Arbabi, J. G. Bartholomew, and A. Faraon, "Miniaturized metasurface hyperspectral-imager", Submitted.

TABLE OF CONTENTS

LIST OF FIGURES

ABBREVIATIONS

DOE	diffractive optical element.
NA	numerical aperture.
HCA	high-contrast transmit/reflect array.
EMT	effective medium theory.
TiO_2	titanium dioxide.
α-Si	amorphous silicon.
NIR	near infrared.
FOV	field of view.
TPM	tow-photon microscopy.
HCRA	high-contrast reflectarray.
HCTA	high-contrast transmitarray.
AR	augmented reality.
MEMS	microelectromechanical systems.
DoFP-PC	division of focal plane polarization camera.
LED	light emitting diode.
HWP	half waveplate.
QWP	quarter waveplate.
H/V	horizontal/vertical.
RHCP	right-hand circular polarization.
LHCP	left-hand circular polarization.
PBS	polarizing beamsplitter.
LP	linear polarizer.
DoFP	division of focal plane.
FWHM	full width at half maximum.
GS	Gerchberg-Saxton.
RGB	red-green-blue.
Al_2O_3	aluminum oxide.
RCWA	rigorous coupled-wave analysis.
EBL	electron beam lithography.
CCD	charge-coupled device.
DUV	deep ultraviolet.
DW-ML	double wavelength metasurface lens.
FDTD	finite difference time domain.
PECVD	plasma-enhanced chemical vapor deposition.

SEM	scanning electron microscope.
p-Si	polycrystalline silicon.
PWE	plane wave expansion.
SiO_2	silicon dioxide.
MTF	modulation transfer functions.
CMOS	complementary metal oxide transistor.
SiN_x	silicon nitride.
RMS	root mean square.
c-Si	crystalline silicon.
SLM	spatial light modulator.
MOEMS	micro-opto-electromechanical systems.
EFL	effective focal length.
UV	ultraviolet.
DC	direct current.
PSF	point spread function.
OSA	optical spectrum analyzer.
MS	metasurface spectrometer.
DBR	distributed Bragg reflector.

Chapter 1

INTRODUCTION

The material in this chapter was in part presented in [1].

During the past few years, optical metasurfaces have gained a great deal of attention for *introducing a new category of thin optical elements operating based on new underlying principles*. In this chapter, we give a brief historic perspective in an effort to put metasurfaces in the right context. Then, we briefly discuss the recently demonstrated metasurface optical elements and systems that have capabilities surpassing those of conventional diffractive and refractive optics. We continue with an explanation of the operation principles of high-contrast dielectric optical metasurfaces that form the basis for all works presented in this thesis. A short outline of the thesis contents concludes the chapter.

1.1 Metasurfaces, a historical perspective

Optical metasurfaces are two-dimensional arrays of subwavelength scatterers that are designed to modify different characteristics of light such as its wavefront, polarization distribution, intensity distribution, or spectrum [2–13]. The subwavelength scatterers (referred to as meta-atoms in this context), capture and reradiate (or scatter) the incident light. Depending on the meta-atom design, the scattered light might have different characteristics compared to the incident light. For instance, it might have a different phase, polarization ellipse, angular distribution, intensity, and/or spectral content. For most metasurfaces, the output is either the scattered light or the interference between the scattered and the incident light. By proper selection of the meta-atoms and their locations in the array, the characteristics of light interacting with the metasurface can be engineered. As a result, different conventional optical components such as gratings, lenses, mirrors, holograms, waveplates, polarizers, and spectral filters may be realized. Furthermore, a single metasurface might provide a functionality that may only be achieved by a combination of conventional optical components [14] or an entirely novel functionality [15]. Typically metasurface optical components are subwavelength thick, have a planar form factor, and can be batch-fabricated at potentially low costs using the standard micro and nano-fabrication processes. In the past few years, the efficiency of the optical metasurfaces has

improved significantly by switching from metallic (or plasmonic) meta-atoms to high refractive index dielectric ones. The combination of the relatively high efficiency, potentially low cost, and the planar and thin form factor has generated significant interest in metasurface optical components, and has attracted a large number of researchers from different disciplines. The result has been the rapid expansion of the field. Here we discuss the recent progress in the development of optical metasurfaces, focusing on dielectric metasurfaces that modify the wavefront and/or polarization distribution of light.

Optical metasurfaces are conceptually similar and are technically closely related to the reflectarrays and transmitarrays which have been studied for decades in the microwave community [16]. For example, the idea of using elements (or meta-atoms) with different sizes and shapes has been used as early as 1993 in that community for creating spatially varying phase profiles [17]. Early demonstrations of optical metasurfaces which used metallic meta-atoms are similar to their microwave counterparts [18]. Another example is the use of the geometric (or Pancharatnam-Berry) phase for controlling the wavefront of circularly polarized waves that also has been used before in the microwave community [19, 20]. In addition, many of the properties, design techniques, and models for metasurface components are similar to those used in the context of diffractive optical elements (DOEs). The recognition of these similarities can be beneficial in the design and development of metasurfaces. An example of results that are similarly applicable to metasurfaces and DOEs is the ray optics treatment of the refraction, reflection, and transmission of rays upon interaction with surfaces that impart a spatially varying phase. This topic has been well studied in diffractive optics and the resulting relation is known as the grating equation. A general treatment of this problem when the phase imparting surface has an arbitrary curved shape can be found in [21]. Depending on how they are realized, DOEs have different categories including kinoforms [22], holographic optical elements, computer-generated holograms [23], and effective medium structures [24, 25], and are realized using structures that are different from metasurfaces. However, similar to metasurfaces, they impart spatially varying phase excursion and are modeled as spatially varying phase masks. As a result, many of the techniques, theories, and designs developed for and using DOEs are directly applicable and transformable to metasurfaces. Some of the examples include the algorithms for the design of phase profiles that project desired intensity patterns [23], estimations of diffraction efficiency for quantized phase levels [26], elimination of the spherical aberrations by proper selection of the phase profile [27], elimination of coma aberration of a

phase profile by applying it on a curved spherical surface [28], and removal of other monochromatic aberrations by using a stop [29] or multiple cascaded elements [30].

One of the advantages of recognizing the relation of the metasurfaces to other DOEs is the identification of the potential advantages of the metasurfaces over conventional DOEs. For instance, low-cost, efficient, and relatively wideband diffractive lenses can be realized using conventional DOEs [31], but their performance degrades significantly with increasing their numerical apertures (NAs). As we discuss in section 1.3, properly designed metasurfaces can outperform conventional DOEs.

1.2 Recent developments

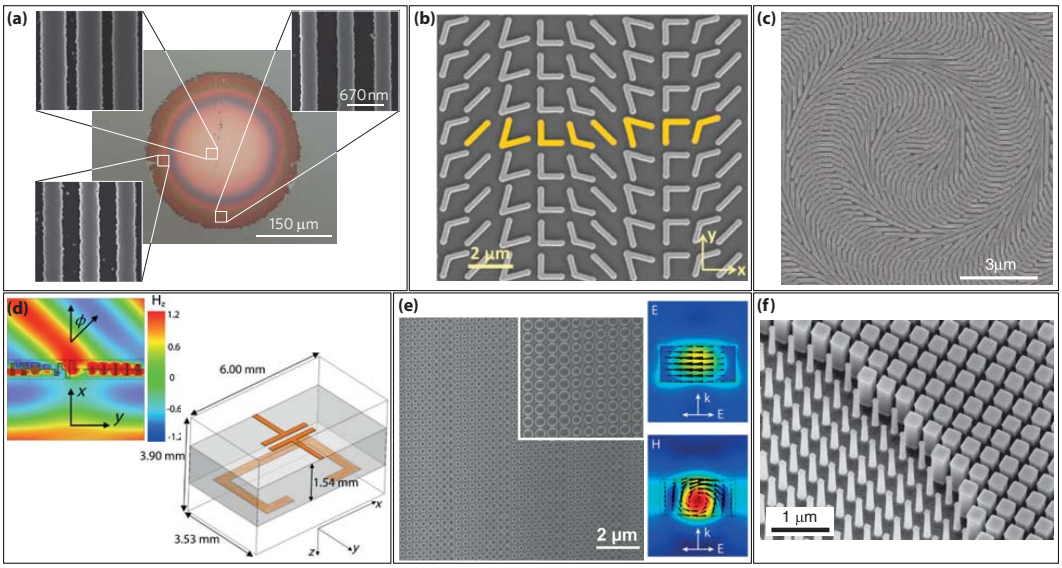

Figure 1.1: **Recent advances in metasurfaces. (a)** Optical and scanning electron micrographs of a high-contrast grating mirror with focusing ability, adapted from [32]. **(b)** Scanning electron micrograph of a plasmonic metasurface beam deflector, adapted from [18]. **(c)** A geometric phase axicon with dielectric micro-bars, adapted from [33]. **(d)** Microwave beam deflection with a metallic Huygens' metasurface along with unit cell of the beam deflector, adapted from [34]. **(e)** Scanning electron micrograph of a dielectric Huygens' beam deflector. Simulated field intensities are plotted on the right, adapted from [35]. **(f)** Scanning electron micrograph of a portion of a high-contrast transmitarray lens, adapted from [36].

In the past few years, the advances and the wider accessibility of micro and nano-fabrication technologies, along with an increased interest in dielectric high-contrast [32, 37, 38] and plasmonic structures [18, 39–42] for manipulation of optical wavefronts, have caused a surge in the research field of metasurfaces. Two of the early

works using high contrast mirrors and plasmonic scatterers are shown in Figs. **1.1**a and **1.1**b, respectively. The ultra-thin form factor of plasmonic structures, and the great interest in the field of plasmonics itself, resulted using a single metallic layer to manipulate light using resonance phase, geometric phase, or their combination in most of the earlier works [3, 41, 43–48]. However, material losses and fundamental limitations of single layer thin plasmonic metasurfaces (especially in the transmission mode) [49–51] significantly limit their performance. Dielectric geometric phase elements based on nano-beam half waveplates (similar to the example shown in Fig. **1.1**c) have also been investigated [33, 52] for wavefront shaping. These elements are designed to work with one polarization, and achieving simultaneously both high efficiency and large deflection angles is challenging because of significant coupling between the elements.

To overcome the fundamental limitations of ultra-thin metasurfaces, Huygens' metasurfaces were introduced [34] that allow for simultaneous excitation of modes with equal electric and magnetic dipole moments. These structures do not have deep subwavelength thicknesses, as shown in Fig. **1.1**d, where the wavelength is 30 mm. Despite their success in lower frequencies [53–58], in the optical domain metallic Huygens' metasurfaces are still limited by material losses and often require complicated fabrication. As a result, dielectric Huygens' metasurfaces were explored [35, 59–64] that allowed for two longitudinal resonance modes with dominant electric and magnetic dipole moments with the same frequency to circumvent material losses [Fig. **1.1**e]. There are, however, some challenges that limit the practicality of dielectric Huygens' metasurfaces. First, full 2π phase coverage at a single wavelength, which is what matters for wavefront manipulation, while keeping a high transmission requires changing all sizes of the resonators (including their heights) which is challenging to achieve with the conventional planar micro-fabrication technology. Second, the coupling between adjacent meta-atoms is considerable in Huygens' metasurfaces and this significantly degrades the performance of devices with large deflection angles as they require fast varying structures [35]. As a result, more groups started investigating the high-contrast transmit/reflect arrays (HCAs) structures (similar to the one shown in Fig. **1.1**f) that use thicker (about 0.5λ to λ) high-index layers to pattern the metasurface [14, 38, 65–74]. These structures are very similar to the blazed binary optical elements that are at least two decades old [75–78], nevertheless, they outperform other classes of metasurfaces in many wavefront manipulation applications. In the following, we will briefly discuss and explain their operation principle, and review the areas

where metasurfaces have demonstrated wavefront control capabilities beyond those of conventional diffractive optical elements.

We should note here that the applications of optical metasurfaces in the general sense of the word (i.e., patterned thin layers on a substrate) go beyond spatial wavefront manipulation. Thin light absorbers [79–93], optical filters [94–106], nonlinear [107–114], and anapole metasurfaces [115, 116] are a few examples of such elements. However, since our work has been focused on applications of metasurfaces in wavefront manipulation, we don't cover these other types of metasurfaces in this brief background.

1.3 High-contrast reflect/transmit arrays

Since HCAs are central to all the works presented in this thesis, we first briefly discuss their operation. We are primarily interested in the two-dimensional HCAs, and therefore we consider their case here, although much of the discussions are also valid for the one-dimensional case. In general, these devices are based on high-refractive-index dielectric nano-scatterers surrounded by low-index media [14, 38, 65, 67, 70–72, 76, 78]. The structure can be symmetric (i.e., with the substrate and capping layers having the same refractive indexes) [36] or asymmetric [66, 67, 76, 78]. Depending on the materials and the required phase coverage, the thickness of the high-index layer is usually between $0.5\lambda_0$ and λ_0, where λ_0 is the free space wavelength. Typically, these structures are designed to be compatible with conventional micro-fabrication techniques; therefore, they are composed of nano-scatterers made from the same material structure and with the same thickness over the device area. Various scatterers can have different cross-sections in the metasurface plane, but the cross-section of any single scatterer is usually kept the same along the layer thickness to facilitate its fabrication using binary lithography techniques. For wavefront shaping, the nano-scatterers should be on the vertices of a subwavelength lattice that satisfies the Nyquist sampling criterion [36] in order to avoid excitation of unwanted diffraction orders. For simplicity, the lattices are usually selected to be periodic. Figure **1.2**a shows two typically used structures with triangular and square lattices [38, 78]. For polarization-independent operation (in the case of normal incidence with small deflection angle) the nano-scatterers should have symmetric cross-sections such as circles, squares, regular hexagons, etc. (Fig. **1.2**a). Similar to high-contrast gratings [32, 37, 117], these structures can also be used in reflection mode by backing them with a metallic or dielectric reflector [118–120]

[Fig. 1.2a, bottom], or by properly selecting their thicknesses [121, 122].

The first HCA diffractive devices demonstrated by Lalanne et al. (referred to as blazed binary diffractive devices at the time) were designed to operate in an effective medium theory (EMT) regime where only one transverse mode could be excited in the HCA layer [76, 78]. In 2011, it was suggested by Fattal et al. [38] and later demonstrated [65–67] that using higher index materials (silicon or amorphous silicon (α-Si) instead of titanium dioxide (TiO_2)) can result in devices with higher efficiency for large deflection angles, despite a departure from the HCA regime (where the lattice constant is larger than the structural cut-off [78], yet it is small enough to avoid unwanted diffraction [65, 66]). It is worth noting that even for the lower index materials like TiO_2, the optimal operation regime seems to be where the lattice is designed just below the structural cut-off [77]. It is worth noting that depending on the design parameters, higher index devices (such as silicon ones) can operate in the EMT regime [123]. One example of such devices is shown in Fig. 1.2b, where a graded index lens was etched into a silicon wafer to focus light inside the wafer [123]. The ability of the EMT blazed binary structures to significantly outperform the conventional échelette gratings is dominantly attributed to the waveguiding effect of the nano-posts that results in a sampling of the incoming and outgoing waves with small coupling between adjacent nano-posts [77]. In devices using higher refractive index materials like silicon, the coupling between adjacent nano-posts remains small even above the structural cut-off. In Fig. 1.2c, the simulated magnetic energy density is plotted for α-Si nano-posts, showing that the field is highly confined inside the nano-posts, which reduces the coupling between nanoposts. In this case, there are multiple propagating transverse modes inside the layer [67]. In addition, due to the larger number of resonances, the transmission phase for the nano-posts with the higher refractive index is a steeper function of the nano-post's size (compared to the EMT structures) as shown in Fig. 1.2d [66, 124]. This relieves the requirements of the nano-posts aspect ratio and makes their fabrication more feasible [66].

A second effect of the high field confinement is that the behavior of the structure becomes more insensitive to the lattice parameters, as shown in Fig. 1.2e [67]. More importantly, this means that the transmission phase of a nano-post is largely insensitive to its neighboring posts; therefore, adjacent nano-posts can have significantly different sizes without much degradation of their performance. This is in contrast to the dielectric Huygens metasurfaces [35, 59, 61, 118, 126, 127] where the coupling between neighboring scatterers results in significant performance degradation if

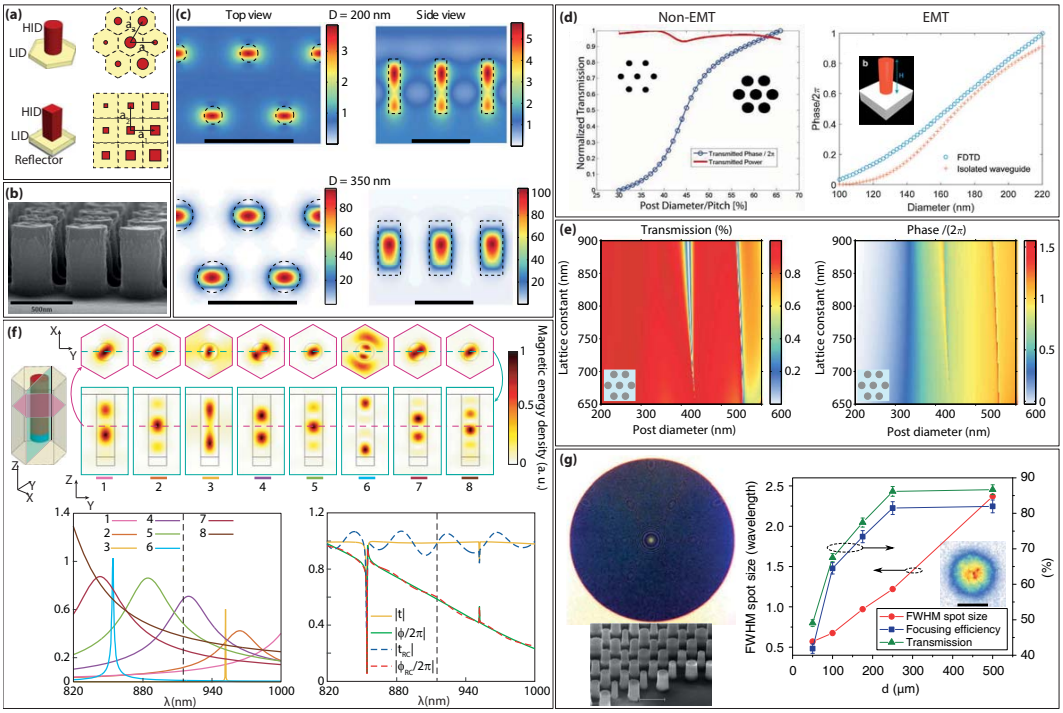

Figure 1.2: **Operation principles of HCAs**. **(a)** Schematic illustration of some possible HCA configurations with different nano-post shapes and lattice structures. HID: high-index dielectric, LID: low -index dielectric. **(b)** Scanning electron micrograph of a graded index lens, etched directly into a silicon wafer [123].**(c)** Simulated magnetic energy density in a periodic array of α-Si nano-posts plotted in cross sections perpendicular to (left), and passing through (right) the nano-posts' axes. For larger nano-posts, the field is highly confined inside the nano-posts. The scale bars are 1 μm [67]. **(d)** Simulated transmission phase for α-Si nano-posts operating beyond the EMT regime (left, [66]), and TiO_2 nano-posts operating within the EMT regime (right, [124]). **(e)** Simulated transmission amplitude and phase of a periodic array of circular α-Si nano-posts versus posts diameter and lattice constant [67]. **(f)** Top: Magnetic energy distribution of optical resonances inside an α-Si nano-post that contribute to the transmission amplitude and phase of the structure around 900 nm [125]. Bottom: Reconstruction of the nano-post transmission and phase using the frequency responses of the resonance modes. The left figure shows relative contributions of the different modes. **(g)** near infrared (NIR) lenses fabricated with amorphous silicon (α-Si) HCAs, and their performance as high-NA lenses with high efficiency [67]. The lenses are designed to focus light emitted by a single-mode optical fiber to a diffraction-limited spot. The lenses have NAs from ~0.5 to ~0.97, and measured focusing efficiencies of 82% to 42%. Scale bar: 1μm.

the size of the neighboring scatterers changes too abruptly. In addition, unlike the Huygens metasurfaces, the high transmission amplitude and full 2π-phase-coverage of the HCAs result from the contributions of multiple resonances. Such resonances are shown for a typical α-Si nano-post in Fig. **1.2**f [125]. An expansion of the optical scattering of the nano-posts to electric and magnetic multipoles is also possible [70]. However, capturing the full physics requires the use of higher order multipoles, and the expansion does not give much direct information about the contribution of each resonance to each of the multipole terms, or how they can be tailored for a specific application.

In recent years, multiple groups have demonstrated high-efficiency high-NA lenses using the HCA platform [66, 67, 69, 72, 124, 128]. Figure **1.2**g, shows one of the early demonstrations where lenses with NAs ranging from ~0.5 to above 0.95 were demonstrated, with measured absolute focusing efficiencies from 82% to 42% depending on the NA, while keeping a close to diffraction-limited spot.

In both EMT and non-EMT regimes, the standard design method for optical phase masks (lenses in particular) has been to extract the transmission (reflection) coefficient for a periodic array of nano-posts and use them directly to design aperiodic devices that manipulate the phase profile [38, 65–67, 78]. This design process is based on the assumptions that the sampling is local, there is not much coupling between the nano-posts, and the transmission phase and amplitude remain the same for different scattering angles. The validity of these assumptions starts to break at large deflection angles and contributes to the lower efficiency of the devices at such angles. More recently, a few methods have been proposed and demonstrated potential for increasing the efficiency of these devices [129–131]. While periodic devices (i.e., blazed gratings) with measured efficiencies as high as 75% at 75-degree deflection angles have been demonstrated, the case for non-periodic devices is more challenging, and to the best of our knowledge, the absolute measured focusing efficiencies for lenses with NAs about 0.8 have been limited to slightly above 75% [130]. Proper measurement and reporting of the efficiency is a very important parameter in phase control devices with high-gradients. A proper definition of efficiency for lenses is the power of light focused to a small area around the focal point (for instance a disk with a diameter that is two to three times the diffraction-limited Airy diameter). With this definition, it is essential in experiments that a pinhole be used around the focal spot to block the light outside this area; otherwise, the measured value would be the transmission efficiency. It is also important to identify the illuminating beam size

when measuring efficiencies. Using a beam smaller than the clear aperture of the lens will effectively reduce the NA of the lens and leads to an overestimation of the device efficiency. The type of power detector used may also significantly bias the efficiency measurements. The light focused by a high-NA device has a wide angular spectrum and many detectors are sensitive to the incident angle of light. Ideally, a detector with a wide acceptance angle such as an integrating sphere should be used in the efficiency measurements.

The discussed ability of HCAs to deflect light to large angles with high efficiencies has been a main motivation for their unprecedented investigation and growth in the past few years. However, a more important property of metasurfaces is their capability to control light independently based on its various degrees of freedom like polarization [14, 132–134], wavelength [119, 135–137], and angle [15, 138]. Furthermore, their compact and two-dimensional form factor in addition to their compatibility with the standard micro-fabrication techniques enables new platforms for optical elements and systems. Among these, we have developed conformal and tunable optical elements based on metasurfaces embedded in flexible substrates [36, 125], wide field of view (FOV) cameras and retroreflectors using vertically cascaded metasurfaces [120, 139], micro-electro-mechanically tunable lenses [140], and compact folded optical systems like spectrometers and hyper-spectral imagers [141, 142]. These properties are what truly set metasurfaces in general, and HCAs in particular, apart from conventional diffractive and refractive optics. As such, my doctoral work has been focused on the development of HCAs with these capabilities.

1.4 Thesis outline

Chapters 2, 3, and 4 of this dissertation are focused on conceptually new metasurface elements that enable the control of light based on its polarization and wavelength degrees of freedom, and Chapter 5 includes several works on the development of integrated optical metasurface systems.

More specifically, Chapter 2 explains how the birefringent HCA platform enables complete and simultaneous control of polarization and phase, and how this allows for the imaging and generation of polarization state distributions with arbitrary complexity. Chapter 3 introduces three different methods for designing and making multi-wavelength metasurface elements that allow for independent control of phase based on the incident light wavelength at a few distinct wavelengths. The methods are based on metasurfaces with multi-element unit-cells or meta-molecules, spatial

multiplexing of different metasurfaces, or the use of birefringent meta-atoms. At the end of Chapter 3 we will discuss how such multi-wavelength platforms allow for the use of metasurface elements in tow-photon microscopy (TPM). In Chapter 4, we introduce the concept of chromatic dispersion control in diffractive optical elements, derive the physical requirements and intuition for what it means, and report the development of an HCRA platforms that allows for partial control of chromatic dispersion.

Chapter 5 discusses five different optical systems based on integrated optical elements. There, we demonstrate how vertical integration of several HCTAs enables the design and implementation of wide-FOV lenses for cameras and projection optics in compact augmented reality (AR) headsets. Then, we demonstrate highly tunable and compact lens doublets based on the integration of metasurface lenses into a microelectromechanical systems (MEMS). Chapter 5 ends with the demonstration of a flat retroreflector formed from vertical integration of an HCRA and an HCTA. We conclude the dissertation with a discussion of potentials and challenges facing metasurface optical elements, and an outlook towards a possible future for the field in Chapter 6.

Chapter 2

POLARIZATION AND PHASE CONTROL

The material in this chapter was in part presented in [133, 134].

A unique property of HCTAs is their unprecedented capability to control polarization and phase simultaneously. In this chapter we explain why this capability to control polarization and phase is important and how it can be achieved using the HCA platform. We discuss the two different manifestation of this control, and present an example application for each manifestation. The first application, which makes use of the independent phase control for orthogonal polarizations is that of division of focal plane polarization cameras (DoFP-PCs). The second application is that of vectorial holograms that generate arbitrary polarization distributions by utilizing the simultaneous polarization and phase control capability.

2.1 Polarization and polarimetric imaging

Polarization is a degree of freedom of light carrying important information that is usually absent in the intensity and spectral content. Polarimetric imaging is the measurement of the polarization state of light over a scene of interest. While spectral and hyperspectral imaging techniques provide information about the molecular and material composition of a scene [143, 144], polarimetric imaging contains information about the shape and texture of reflecting surfaces, the orientation of light emitters, or the optical activity of various materials [145, 146]. This additional information has led to many applications for imaging polarimetry ranging from astronomy and remote sensing to marine biology and medicine [145, 147–153]. Therefore, several methods have been developed over the past five decades to enable mapping of the polarization state over an extended scene [153–160].

Generally, polarimetric imaging techniques can be categorized into three groups: division of amplitude, division of aperture, and division of focal plane [145]. All of these techniques are based on measuring the intensity in different polarization bases and using them to estimate the full Stokes vector or a part of it. DoFP-PCs are less expensive, more compact, and require less complicated optics compared to the two other categories of polarimetric imaging systems [145, 158–160]. In

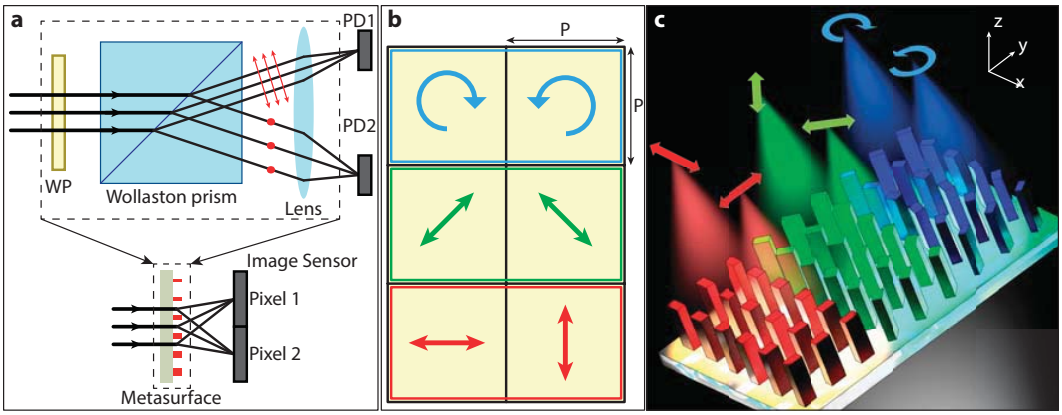

Figure 2.1: **Concept of a metasurface polarization camera. (a)** Top: Schematics of a conventional setup used for polarimetry: a waveplate (quarter or half) followed by a Wollaston prism and a lens that focuses light on detectors. Bottom: A compact metasurface implements the functionality of all three components combined, and can be directly integrated on an image sensor. WP: waveplate; PD: photodetector. **(b)** A possible arrangement for a superpixel of the polarization camera, comprising six image sensor pixels. Three independent polarization basis (H/V, ±45°, and RHCP/LHCP) are chosen to measure the Stokes parameters at each superpixel. **(c)** Three-dimensional illustration of a superpixel focusing different polarizations to different spots. The colors are used only for clarity of the image and bear no wavelength information.

addition, they require much less effort for registering images of different polarizations as the registration is automatically achieved in the fabrication of the polarization sensitive image sensors. The advances in micro/nano-fabrication have increased the quality of DoFP-PCs and reduced their fabrication costs, making them commercially available. DoFP-PCs either use a birefringent crystal to split polarizations [161, 162], or thin-film [159, 163] or wire-grid [153, 158, 164] polarization filters. To enable the measurement of degree of circular polarization, form-birefringent quarter waveplates were integrated with linear polarizers in the mid-IR [165]. Recently, liquid crystal retarders have been integrated with linear polarization filters to enable full Stokes polarimetric imaging by implementing circular [166] and elliptical polarization filters [167, 168]. An issue with the previously demonstrated DoFP-PCs is that they all have a theoretical efficiency limit of 50% due to using polarization filters [145], or spatially blocking half of the aperture [162].

Optical metasurfaces have enabled high-efficiency phase and polarization control with large gradients [14, 67, 71, 72, 75, 76]. In addition, their compatibility with conventional micro-fabrication techniques allows for their integration into optical

metasystems [120, 139, 140, 169] or with optoelectronic components. They have also been used for polarimetry [98, 170–177], but not polarimetric imaging. An important capability of high contrast dielectric metasurfaces is the simultaneous control of polarization and phase [14]. Here, we show how this capability can be utilized to demonstrate a dielectric metasurface mask for DoFP-PCs with the ability to fully measure the Stokes parameters, including the degree of circular polarization and helicity. In addition, since the mask operates based on polarization splitting and focusing instead of polarization filtering, it overcomes both the 50% theoretical efficiency limit, and the one-pixel registration error (resulting from distinct physical areas of the polarization filters) of the previously demonstrated DoFP-PCs [145]. In addition, unlike the previously demonstrated full Stokes DoFP-PCs, the metasurface is fabricated in a single dielectric layer and does not require integration of multiple layers operating as retarders and polarization filters. For the experimentally demonstrated metasurface mask designed for an 850-nm center wavelength, the polarization cross-talk ranges from 10% to 15% for pixel sizes from 7.2 μm to 2.4 μm when using an 850-nm light emitting diode (LED) as the light source. In addition, we use a polarization mask to demonstrate that the metasurface DoFP-PC can be used to form polarization images over extended scenes.

There are several representations for the polarization of light [178]. Among them, the Stokes vector formalism has some conceptual and experimental advantages since it can be used to represent light with various degrees of polarization, and can be directly determined by measuring the power in certain polarization bases [178]. Therefore, most imaging polarimetry systems determine the Stokes vector $\mathbf{S} = [S_0, S_1, S_2, S_3]$ [145], where the components are defined as $S_0 = I$, $S_1 = I_x - I_y$, $S_2 = I_{45} - I_{-45}$, and $S_3 = I_R - I_L$. Here I is the total intensity, I_x, I_y, I_{45}, and I_{-45} are the intensity of light in linear polarization bases along the x, y, +45-degree, and -45-degree directions, respectively. I_R and I_L denote the intensities of the right-hand and left-hand circularly polarized light. Usually, S_1, S_2, and S_3 are normalized to S_0 such that their value changes between -1 and +1. To fully characterize the state of polarization, all these intensities should be determined. A conventional setup used to measure the full Stokes vector is shown in Fig. **2.1a**: a waveplate (half or quarter), followed by a Wollaston prism and a lens that focuses the beams on photodetectors. One can determine the four Stokes parameters [178] from the detector signals acquired under three different conditions: without a waveplate, with a half waveplate (HWP) inserted, and with a quarter waveplate (QWP) inserted in the setup. An optical metasurface with the ability to fully control phase and polarization

of light [14] can perform the same task over a much smaller volume and without changing any optical components. The metasurface can split any two orthogonal states of polarization and simultaneously focus them to different points with high efficiency and on a micron-scale. This is schematically shown in Fig. **2.1a**. Such a metasurface can be directly integrated on an image sensor for making a polarization camera. To fully measure the Stokes parameters, the projection of the input light on three different polarization basis sets should be measured. A typical choice of basis is horizontal/vertical (H/V), ±45° linear, and right-hand-circular/left-hand-circular (RHCP/LHCP) that can be used to directly measure the Stokes parameters. Figure **2.1b** shows a possible configuration where the three metasurface polarizing beamsplitters (PBSs) are multiplexed to make a superpixel, comprising of six image sensor pixels. Each image sensor pixel can then be used to measure the power in a single polarization state. A schematic illustration of a superpixel is shown in Fig. **2.1c**. The colors are only used to distinguish different parts of the super pixel more easily, and do not correspond to actual wavelengths. The blue nano-posts, separate and focus RHCP/LHCP, the green ones and the red ones do the same for ±45° and H/V, respectively.

2.2 Simultaneous polarization and phase control

As seen in Fig. **2.2a**, the metasurface is composed of α-Si nano-posts with rectangular cross-sections on a low-index fused silica substrate. With a proper choice of the α-Si layer thickness and lattice constant (650 nm and 480 nm respectively for an operating wavelength of 850 nm), the nano-posts can provide full and independent 2π phase control over x- and y-polarized light, where x- and y are aligned with the nano-post axes (see Fig. **2.A1**) [14]. Using the phase versus dimension graphs, one could calculate the nano-post dimensions required to provide a specific pair of phase values, ϕ_x and ϕ_y, as shown in Fig. **2.2b**. This allows for designing a metasurface that controls x and y-polarized light independently. With a simple generalization, the same can be applied to any two orthogonal linear polarizations using nano-posts that are rotated around their optical axis with the correct angle to match the new linear polarizations (e.g., the $x' - y'$ axis in Fig. **2.2c**). An important and interesting point demonstrated in [14] is that this can be done on a point-by-point manner, where the polarization basis is different for each nano-post. This property allows us to easily design the metasurface PBS for the two linear bases of interest. Moreover, as demonstrated in [14], an even more interesting property of this seemingly simple structure is that

the independent control of orthogonal polarizations can be generalized to elliptical and circular polarizations as well (with a small drawback that the output and input polarizations will have the opposite handedness). To see this, here we reiterate the results presented in the supplementary material of [14], as it is important to make the design process clear.

The operation of a nano-post can be modeled by a Jones [179] matrix relating the input and output electric fields (i.e., $\mathbf{E}^{\text{out}} = \mathbf{T}\mathbf{E}^{\text{in}}$). For the rotated nano-post shown in Fig. **2.2c**, the Jones matrix can be written as:

$$\mathbf{T} = \begin{bmatrix} T_{xx} & T_{xy} \\ T_{yx} & T_{yy} \end{bmatrix} = \mathbf{R}(\theta) \begin{bmatrix} e^{i\phi_{x'}} & 0 \\ 0 & e^{i\phi_{y'}} \end{bmatrix} \mathbf{R}(-\theta), \tag{2.1}$$

where $\mathbf{R}(\theta)$ denotes the rotation matrix by an angle θ in the counter-clockwise direction. Here we have assumed a unity transmission since the nano-posts are highly transmissive. We note here that the right hand side of Equation 2.1 is a unitary and symmetric matrix. Using only these two conditions (i.e., unitarity and symmetry), we find $T_{xy} = T_{yx}$, $|T_{yx}| = \sqrt{1 - |T_{xx}|^2}$, and $T_{yy} = -\exp(\mathrm{i}2\angle T_{yx})T_{xx}$. As one could expect, these reduce the available number of controllable parameters to three ($|T_{xx}|$, $\angle T_{xx}$, and $\angle T_{yx}$), corresponding to the three available physical parameters ($\phi_{x'}$, $\phi_{y'}$, and θ). Using these relations to simplify $\mathbf{E}^{\text{out}} = \mathbf{T}\mathbf{E}^{\text{in}}$, we can rewrite it to find the Jones matrix elements in terms of the input and output fields:

$$\begin{bmatrix} E_x^{\text{out}*} & E_y^{\text{out}*} \\ E_x^{\text{in}} & E_y^{\text{in}} \end{bmatrix} \begin{bmatrix} T_{xx} \\ T_{yx} \end{bmatrix} = \begin{bmatrix} E_x^{\text{in}*} \\ E_x^{\text{out}} \end{bmatrix}, \tag{2.2}$$

where $*$ denotes complex conjugation. Equation 2.2 is important as it shows how one can find the Jones matrix required to transform any input field with a given phase and polarization, to any desired output field with a different phase and polarization. This is the first application of the birefringent meta-atoms, i.e., *complete and independent polarization and phase control*. This capability is what allows us to design and implement the vectorial holograms discussed in the following sections.

The Jones matrix is uniquely determined by Eq. 2.2, unless the determinant of the coefficients matrix on the left hand side is zero. In this case, the matrix rows (i.e., $\mathbf{E}^{\text{out}*}$ and $\mathbf{E}^{\text{in}}$) will be proportional. Since the Jones matrix is unitary (i.e., the input and output powers are equal), the proportionality coefficient must have a unit amplitude: $\mathbf{E}^{\text{out}*} = \exp(\mathrm{i}\phi)\mathbf{E}^{\text{in}}$. This equation means that $\mathbf{E}^{\text{out}}$ and $\mathbf{E}^{\text{in}}$ have the same polarization ellipse, but an opposite handedness. Now, this input/output field set imposes only one equation on the Jones matrix elements. To uniquely determine

the Jones matrix, a second equation is required. To get this second equation, we use a second set of input/output fields that satisfy the same condition as the first set: $\mathbf{E}_2^{\text{out}*} = \exp(\mathrm{i}\phi_2)\mathbf{E}_2^{\text{in}}$. Here we are using the numeral subscripts to distinguish between the two input/output field sets. This way, the equation for the first set becomes $\mathbf{E}_1^{\text{out}*} = \exp(\mathrm{i}\phi_1)\mathbf{E}_1^{\text{in}}$. If ϕ_1 and ϕ_2 can be independently controlled, one can see using a conservation of energy argument that $\mathbf{E}_1^{\text{in}}$ and $\mathbf{E}_2^{\text{in}}$ (as well as $\mathbf{E}_1^{\text{out}}$ and $\mathbf{E}_2^{\text{out}}$) should be orthogonal to each other. Thus, we can write the final equation as:

$$\begin{bmatrix} E_{1,x}^{\text{in}} & E_{1,y}^{\text{in}} \\ E_{2,x}^{\text{in}} & E_{2,y}^{\text{in}} \end{bmatrix} \begin{bmatrix} T_{xx} \\ T_{yx} \end{bmatrix} = \begin{bmatrix} E_{1,x}^{\text{out}} \\ E_{2,x}^{\text{out}} \end{bmatrix} = \begin{bmatrix} \exp(\mathrm{i}\phi_1)E_{1,x}^{\text{in}*} \\ \exp(\mathrm{i}\phi_2)E_{2,x}^{\text{in}*} \end{bmatrix}. \tag{2.3}$$

This is the second important application of the method, *polarization controlled phase manipulation*: given *any* two orthogonal input polarizations (denoted by $\mathbf{E}_1^{\text{in}}$ and $\mathbf{E}_2^{\text{in}}$), their phase can be independently controlled using the Jones matrix given by Equation 2.3. For instance, Arbabi et. al. [14], demonstrated a metasurface that focuses RHCP input light to a tight spot, and LHCP input light to a doughnut shape. The cost is that the output orthogonal polarizations have the opposite handedness compared to the input ones. This second capability allows for the design and implementation of the metasurface polarization camera. Once the Jones matrix is calculated from Eq. 2.3 (or 2.2, depending on the function), the two phases, $\phi_{x'}$ and $\phi_{y'}$, and the rotation angle θ can be calculated from Eq. 2.1. Let us emphasize here that since this is a point-by-point design, all the steps can be repeated independently for each nano-post, meaning that the polarization basis can be changed from one nano-post to the next.

2.3 Metasurface mask for polarization camera

Based on the concept and technique just described, the first design step is identifying the input polarizations at each point. For the DoFP-PC, three different sets of H/V, ±45°, and RHCP/LHCP are chosen, corresponding to the three distinct areas in the superpixel shown in Fig. **2.1b**. Then, the required phase profiles are determined to split each two orthogonal polarizations and focus them to the centers of adjacent pixels on the image sensor as shown schematically in Fig. **2.1c**. For a pixel size of 4.8 μm, the calculated phase profiles are shown in Fig. **2.2d**, where the focal distance is assumed to be 9.6 μm. Since each polarization basis covers two image sensor pixels, the phases are defined over the area of two pixels. In addition, the calculated phases are the same for the three different polarization bases, and therefore only one basis is shown in Fig. **2.2d**. Using these phases and knowing the desired polarization

basis at each point, we calculated the rotation angles and nano-post dimensions from Eqs. 2.3 and 2.1 along with the data shown in Fig. **2.2b**.

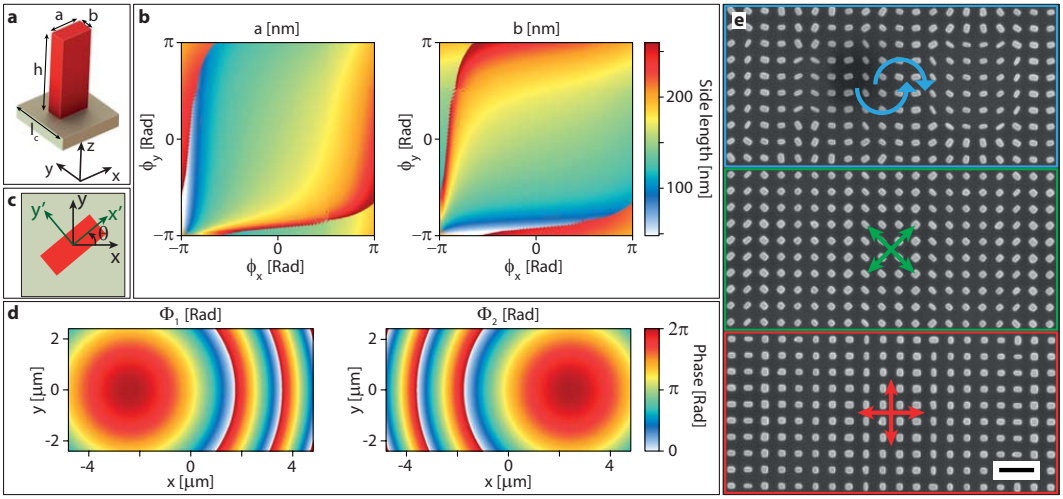

Figure 2.2: **Meta-atom and pixel design.** **(a)** An α-Si nano-post with a rectangular cross section resting on a glass substrate provides full polarization and phase control. **(b)** Design graphs used for finding the in-plane dimensions of a nano-post. Given a pair of transmission phases ϕ_x and ϕ_y, one can find the corresponding nano-post dimensions a and b from the two graphs. The nano-posts are 650 nm tall, and the lattice constant is 480 nm. **(c)** Schematic illustration of a rotated nano-post, showing the rotation angle and the old and the new optical axis sets. **(d)** Required phase profiles for a metasurface that does both polarization beam splitting and focusing at two orthogonal polarizations. These can be any set of orthogonal polarizations, linear or elliptical. The focal distance for these phase profiles is 9.6 µm, equal to the width of the superpixel in the x direction. The lateral positions of the focal spots are x= ±2.4 µm and y=0. **(e)** Scanning electron micrograph of a fabricated superpixel. The polarization basis for each part is shown with the colored arrows. Scale bar: 1 µm.

The metasurface mask was then fabricated in a process explained in more detail in Appendix 2.1. A 650-nm-thick layer of α-Si was deposited on a fused silica wafer. The metasurface pattern was defined using electron-beam lithography, and transferred to the α-Si layer through a lift-off process used to form a hard etch-mask, followed by dry etching. Fig. **2.2e** shows a scanning electron micrograph of a fabricated superpixel, with the polarization bases denoted by arrows for each section. In addition to the metasurface mask corresponding to a pixel size of 4.8 µm that is mentioned above and shown in Fig. **2.2e**, two other masks with pixel sizes of 7.2 µm and 2.4 µm were also fabricated with focal distances of 14.4 µm and 4.8 µm, respectively. We used these to study the effect of pixel size on performance.

To characterize the metasurface mask we illuminated it with light from an 850-nm LED filtered by a 10-nm bandpass filter with different states of polarization. We then imaged the plane corresponding to the image sensor location using a custom-built microscope (see Fig. **2.A2** for measurement details and the setup). Figure **2.3** summarizes the superpixel characterization results for the 4.8-μm pixel design. The measured Stokes parameters are plotted in Fig. **2.3a** for different input polarizations, showing a $< 10\%$ cross-talk between polarizations and high similarity between different superpixels. The measurements were averaged over the field of view of the microscope that corresponds to about 120 superpixels. The standard deviations are shown in the graph as error bars. In addition, the intensity distribution over a sample superpixel area is shown in Fig. **2.3b**. The graphs show the clear ability of the metasurface mask to route light as desired for various input polarizations. Similar characterization results without a bandpass filter, corresponding to a bandwidth of about 5%, are presented in Fig. **2.A3**. Slight performance degradation is observed with a maximum cross-talk of $\sim 13\%$ since the metasurface efficiency decreases with changing the wavelength. In addition, similar measurement results for metasurface masks with pixel sizes of 7.2 μm and 2.4 μm are presented in Figs. **2.A4** and **2.A5**, respectively. The results show a degradation of performance with reducing the pixel size as the cross-talk is smaller than 7.5% and 13% for 7.2-μm and 2.4-μm pixels, respectively. To show the ability of the metasurface mask to characterize the polarization state of unpolarized light, we repeated the same measurements with the polarization filter removed from the setup. Figure **2.3c** summarizes the results of this measurement that determines the polarization state of light emitted by the LED. The data given in Fig. **2.7a** is used to estimate the calibration matrix. As expected, the emitted light has a low degree of polarization (<0.08). We also characterized the polarization state of the emitted LED light using a QWP and a linear polarizer (LP), and found the degree of polarization to be equal to zero up to the measurement error.

In addition, we measured the transmission efficiency of the metasurface mask and found it to be in the range of 60% to 65% for all pixel size designs and input polarizations. The lower than expected transmission is mainly due to a few factors. First, the metasurface has a maximum deflection angle larger than 50°, which results in lower transmission efficiency [67, 130]. Second, the relatively large metasurface lattice constant of 480 nm does not satisfy the Nyquist sampling theorem for the large-deflection-angle transmission masks inside the fused silica substrate [36]. This results in spurious diffraction of light inside the substrate. Finally, the mask is periodic with a larger-than-wavelength period equal to the superpixel dimensions.

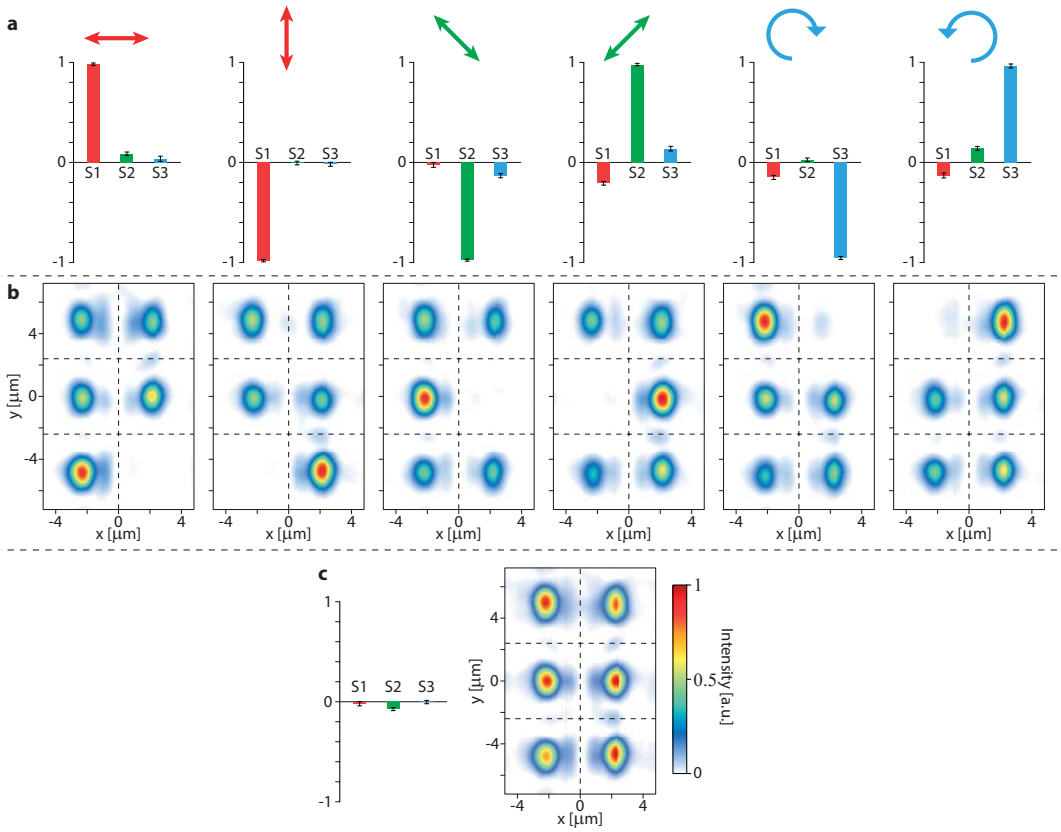

Figure 2.3: **Characterization results of the superpixels of the DoFP metasurface mask. (a)** Measured average Stokes parameters for different input polarizations (shown with colored arrows), and **(b)** the corresponding intensity distributions for a sample superpixel. The Stokes parameters are averaged over about 120 superpixels (limited by the microscope field of view), and the error bars represent the statistical standard deviations. **(c)** Measured average Stokes parameters and the corresponding intensity distribution for the LED light source without any polarization filters in the setup. All the measurements are performed with an 850-nm LED filtered by a bandpass filter (center: 850 nm, full width at half maximum (FWHM): 10 nm) as the light source.

This results in excitation of higher diffraction orders especially inside the substrate that has a higher refractive index. It is worth noting that the achieved ~ 65% efficiency is still higher than the 50% theoretical limit of a polarimetric camera that is based on polarization filtering.

Polarimetric imaging results and discussion

Finally, we show polarimetric imaging using the DoFP metasurface mask. We designed and used a custom dielectric metasurface polarization target for imaging as well. We utilized the polarization-phase control method described above, and a fabrication process similar to the DoFP metasurface mask for the imaging target as well. The mask converts x-polarized input light to an output polarization state characterized by the polarization ellipses and the Stokes parameters shown in Figs. **2.4a** and **2.4b**, respectively. Each Stokes parameter is +1 or -1 in an area of the image corresponding to the specific polarization. For instance, S_3 is +1 in the right half circle, -1 in the left half circle, and 0 elsewhere. Using a second custom-built microscope, the image of the polarization mask was projected onto the DoFP metasurface mask (see Fig. **2.A2** for the measurement setup and the details). First, we removed the metasurface mask and performed a conventional polarimetric imaging of the projected image using a LP and a QWP. To this end, six different images were captured with different rotations of the LP and the QWP to determine the Stokes parameters. The results are shown in Fig. **2.4c**. Second, we removed the LP and the QWP and inserted the DoFP metasurface mask. The Stokes parameters were extracted from a single image captured at the focal plane of the DoFP metasurface mask. The results are shown in Fig. **2.4d**, and are in good agreement with the results of regular polarimetric imaging. The lower quality of the metasurface polarimetric camera image is mainly due to the limited number of superpixels that fit inside a single field of view of the microscope. The field of view is limited by the microscope magnification and image sensor size which are ×22 and ~15 mm, respectively. This results in a low resolution of 70-by-46 points for the metasurface polarimetric image versus a ~2000-by-2000 point resolution for the regular polarimetric image. In addition, to form the final image, we need to know the coordinates of each superpixel a priori. The existing errors in estimating these coordinates that result from small tilts in the setup, aberrations of the custom-built microscope, and etc. cause a degraded performance over some superpixels. In a polarization camera made using the DoFP metasurface mask, both of these issues will be resolved as the resolution can be much higher, and the mask and image sensor are lithographically aligned.

To extract the polarization information of the image we integrated the intensity inside the area of two adjacent DoFP mask pixels. Then, we calculated the corresponding Stokes parameters simply by dividing the difference between the two measured intensities by their sum. While straightforward, this is not the optimal method to perform this task as there is non-negligible cross-talk between different polarization intensities measured by the pixels (Fig. **2.3**). The issue becomes more pronounced moving toward smaller pixel sizes as seen for the 2.4-μm case (Fig. **2.A5**). To address this issue, a better polarization extraction method is to form a calibration matrix that relates the actual intensities to the corresponding measured values for a specific DoFP metasurface mask design (for instance using the data in Fig. **2.3**). This allows one to reduce the effect of the cross-talk and measure the polarization state more precisely.

The designed small focal distances (e.g., 9.6 μm for the 4.8-μm pixel) result in an upper limit of 40% for the operation bandwidth of the device due to diffractive chromatic dispersion. To get this upper limit we assumed a constant phase profile that doesn't change with wavelength and used the criterion given in [139]. Therefore, the actual bandwidth of the device is limited by the focusing and polarization control efficiencies that drop with detuning from the design wavelength. In addition, it is expected that the same level of performance achieved from the 2.4-μm pixel in this work, can be achieved from a ~1.7-μm pixel if the material between the mask and the image sensor has a refractive index of 1.5, which is the case when the DoFP mask is separated from the image sensor by an oxide or polymer layer as in a realistic device. To achieve smaller pixel sizes, better performance, and larger operation bandwidths one could use more advanced optimization [131] or chromatic-dispersion control techniques [119], especially since the size of a single superpixel is small and allows for a fast simulation of the forward problem. In addition, a spatial multiplexing scheme [136, 180–182] can be used to interleave multiple superpixels corresponding to different optical bands, and therefore make a color-polarization camera.

Using the polarization-phase control method and the platform introduced in [14], we demonstrated a metasurface mask for DoFP-PCs. The mask is designed to split and focus light to six different pixels on an image sensor for three different polarization bases. This allows for complete characterization of polarization by measuring the four Stokes parameters over the area of each superpixel which corresponds to the area of six pixels on an image sensor. We experimentally demonstrated the ability of the metasurface masks to correctly measure the polarization state for different input

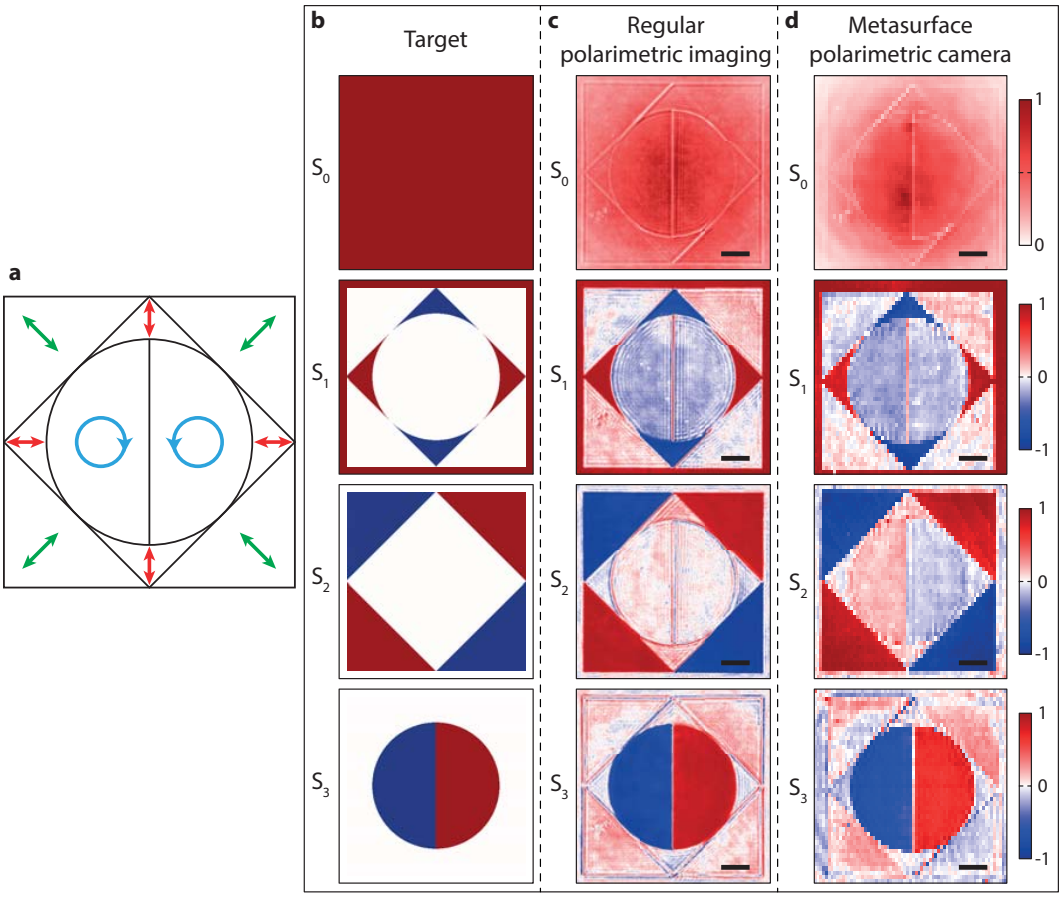

Figure 2.4: **Polarimetric imaging. (a)** Schematic illustration of target polarization ellipse in different parts of the polarization sample. Stokes parameters of the polarization sample: **(b)** the targeted polarization mask, **(c)** the fabricated mask imaged using conventional polarimetry, and **(d)** the same mask imaged using the metasurface polarimetric camera. The scale bars denote 100 μm in the metasurface polarization camera mask plane.

polarizations. In addition, we used the DoFP metasurface mask to form an image of a complicated polarization object, showing the ability to make a polarization camera. Many of the limitations faced here can be overcome using more advanced optimization techniques or better data extraction methods. We anticipate that polarization cameras based on metasurface masks will be able to replace the conventional polarization cameras for many applications as they enable measurement of the full polarization state including the degree of circular polarization and handedness.

2.4 Vectorial holograms

Polarization is an important property of light, with the ability to store and transfer information. Its control has been of great interest for various applications in display systems [183, 184], particle trapping [185, 186], laser materials processing [187, 188], and polarized Raman spectroscopy [189, 190]. Polarization has conventionally been manipulated using naturally birefringent materials. Polarization holograms are in general two- or three-dimensional holograms with a spatially varying degree or direction of birefringence [191–194], encoding phase, polarization, and/or amplitude data. Computer generated polarization holograms have mostly been utilized to store phase information using the geometric phase and perform as polarization dependent gratings, lenses, and holograms [192, 195–197]. While polarization holograms can in principle be used to control the phase and amplitude [198], or phase and polarization simultaneously [199], limited phase control levels, complex fabrication, and large pixel sizes significantly limit their applicability for these purposes.

Computer generated polarization holograms implemented using structural birefringence and fabricated using conventional micro-fabrication techniques [33, 200–204] overcome some of the limitations of conventional polarization holograms, but the level of control over polarization and phase is limited in these structures. Metasurface HCTAs [1, 7, 11, 125, 205–207], on the other hand, enable full and simultaneous control of polarization and phase on a subwavelength lattice and with high efficiency [14]. While most demonstrations so far have either focused on solely controlling the polarization [70, 132, 208] or independent control of phase for two orthogonal polarizations [133, 209–212], another important application of the concept and platform demonstrated in [14] and discussed in the previous sections is the simultaneous control of polarization and phase. Although this ability has been partially utilized to demonstrate metasurfaces that shape the beam and work as half-wave plates simultaneously [118, 213], its full potential has not been explored yet.

In these sections, we use the simultaneous polarization and phase control capability to demonstrate a new category of vectorial (polarization) holograms, where the electric field vector is controlled independently on each point of the mask. The holograms project vectorial images in which the data is stored in the state of polarization. We propose and employ a modified Gerchberg-Saxton (GS) algorithm that enables the design of these vectorial holograms. Given the existence of three independent degrees of freedom in the polarization of light for fully polarized beams, we experimentally

show that these vectorial holograms can store and project the data in complicated red-green-blue (RGB) full-color images. It is worth noting that diatomic plasmonic as well as high-contrast dielectric metasurfaces were recently used to demonstrate vectorial holograms [214, 215]. However, the vectorial holograms demonstrated in [214, 215] are basically spatial superpositions of multiple holograms that have specific output polarizations (e.g., the metasurface consists of a few spatially multiplexed holograms projecting images with different polarization states). In contrast, the metasurface holograms demonstrated in the following sections act as a whole to create polarization patterns of arbitrary complexity as evidenced by the encoded RGB images.

Concept and design

Figure **2.5** shows a schematic of the metasurface, and the color-encoded polarization hologram generated. The metasurface is illuminated by a beam with known wavelength and polarization state. The dielectric metasurface, made up of high index nano-posts, enables simultaneous and independent control of the output phase and polarization [14]. Since each nano-post operates almost independently, this full control can be implemented on a subwavelength lattice. This allows for an unprecedented control of the vectorial electric field on the output side of the metasurface. As we show in the following, this control can be utilized to encode the data of a color image into the polarization state of light which the metasurface can generate and project.

As discussed above, polarization of light can be fully characterized using the Stokes parameters S_0, S_1, S_2, and S_3, usually defined as $S_0 = I$, $S_1 = I_x - I_y$, $S_2 = I_{45} - I_{-45}$, and $S_2 = I_R - I_L$. Here, I denotes the total light intensity, I_x and I_y are the partial intensities of light linearly polarized along the x and y axes, I_{45} and I_{-45} are the intensity in the linear bases along +45 and -45 degree axes, and I_R and I_L denote the right hand and left hand circular intensities, respectively. For fully polarized light, the four parameters are related through the relation $S_0 = \sqrt{{S_1}^2 + {S_2}^2 + {S_3}^2}$. This reduces the number of independent parameters to three, which in a different representation correspond to the amplitude of the electric field along the x and y axes and their phase difference.

As shown in Figs. **2.6a** and **2.6b**, the red, green, and blue components of a color image can be mapped to the Stokes parameters S_1, S_2, and S_3 through a simple linear transformation that maps the color ranges to the [-1,1] interval. Figure **2.6c** shows

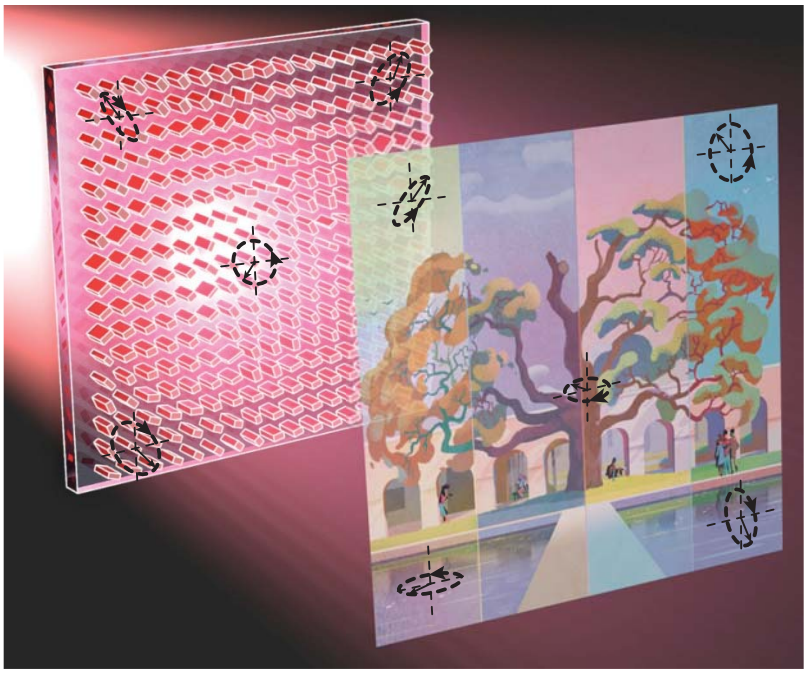

Figure 2.5: **Schematic illustration of a metasurface polarization hologram, projecting a polarization pattern encoding an RGB image.** The metasurface is illuminated with a beam of known wavelength and polarization. Each dielectric nano-post is designed to control the polarization and phase of the output light at the corresponding lattice site.

the distribution of the pixels of the image shown in Fig. 2.6**a** on the Poincare sphere. This shows that the points cover a very large portion of possible polarization states, denoting the capability of the method to generate images with arbitrarily complex polarization distributions. Finally, for the actual hologram design process it is more helpful to use the electric field representation of polarization, which is possible as the light is fully polarized. Figure 2.6**d** shows the amplitudes of the electric field along the x and y axes, $|E_x|$ and $|E_y|$, and their phase difference, $\phi = \angle E_y - \angle E_y$, which are calculated form the Stokes parameters plotted in Fig. 2.6**b**.

To design the metasurface, we developed and used a modified GS algorithm. As shown in Fig. 2.7, the field right before the metasurface has an amplitude of one and is polarized along the x axis. The field right after the metasurface can have any arbitrary polarization and phase distributions, however, it has a unity amplitude, i.e., $\sqrt{|{E_x}^m|^2 + |{E_y}^m|^2} = 1$. On the hologram plane (infinity), polarization and amplitude distributions, $|{E_x}^h|$, $|{E_y}^h|$, and ϕ are set, while the relative phases between different points, $\angle {E_x}^h$, are available degrees of freedom. We start the process by assigning a uniform phase to the field in the hologram plane, and setting the initial hologram

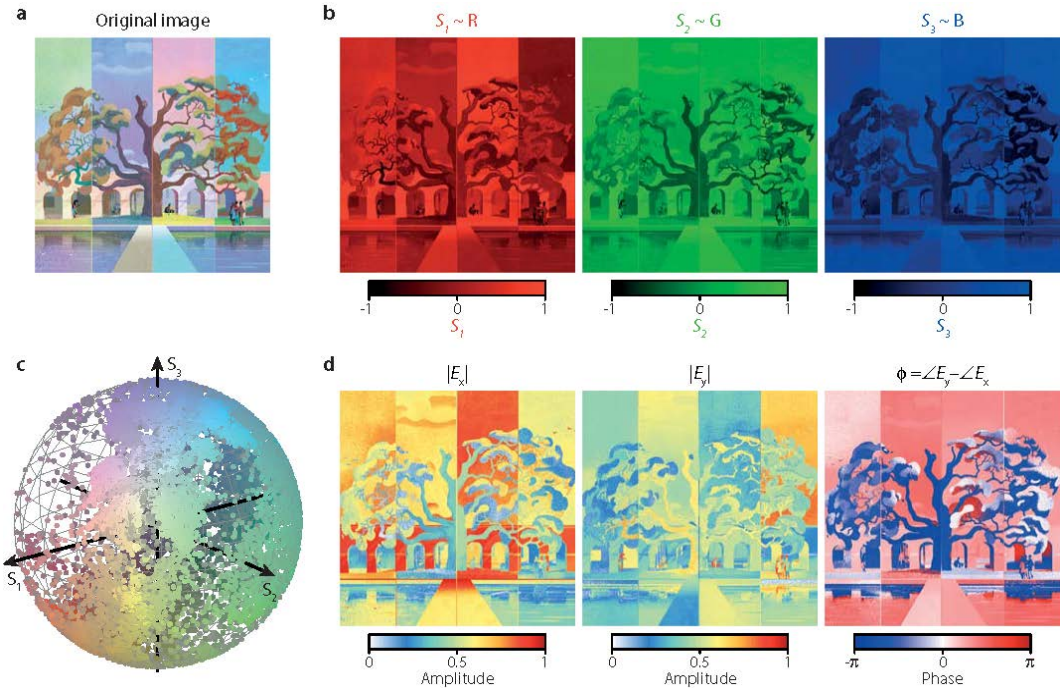

Figure 2.6: **Mapping an RGB image data to polarization.** **(a)** The original RGB image. **(b)** The red, green, and blue components of the image in **a**, corresponding to the Stokes parameters characterizing the polarization pattern. **(c)** A Poincare sphere representation of the polarization pattern corresponding to the image in **a**. The position of each point and its color demonstrate the polarization and intensity of light at one point in the image. For the data to be more clear, only about two percent of the original image pixels are used. **(d)** The electric field amplitudes along the *x* and *y* axes and their phase difference, calculated from the Stokes parameters in **b**. This data is directly used in the metasurface hologram design algorithm through a modified GS algorithm.

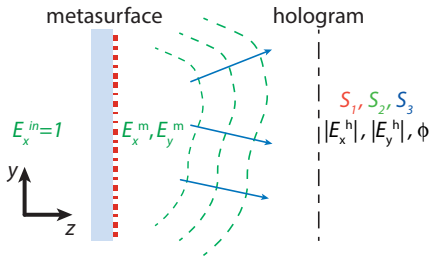

Figure 2.7: **Vectorial hologram design schematic.** Schematic of the metasurface generating the desired polarization pattern. The required electric field vector on the metasurface, $E_x{}^m$ and $E_y{}^m$, is calculated directly from the modified GS algorithm.

fields as follows:

$$\begin{aligned} {E_x}^h(1) &= |{E_x}^h| \\ {E_y}^h(1) &= |{E_y}^h|\mathrm{e}^{j\phi} \end{aligned}. \tag{2.4}$$

At each subsequent step, the metasurface field is calculated through the following Fourier transform relations:

$$\begin{aligned} {E_x}^m(i) &= \frac{\mathcal{F}[{E_x}^h(i)]}{I(i)} \\ {E_y}^m(i) &= \frac{\mathcal{F}[{E_y}^h(i)]}{I(i)} \\ I(i) &= \sqrt{\mathcal{F}[{E_x}^h(i)]^2 + \mathcal{F}[{E_y}^h(i)]^2} \end{aligned}, \tag{2.5}$$

where i is the iteration step, $\mathcal{F}[\cdot]$ represents the Fourier transform operator, and $I(i)$ is the total intensity used to normalize the field as it should have an almost unity amplitude. The hologram fields in the next iterations should satisfy $\phi = \angle E_y - \angle E_x$. Therefore, in each step we can only set the phase of one polarization from the GS algorithm, and the phase of the other polarization should be calculated using the known phase difference, ϕ. To make the process symmetric for the two polarizations, we alternate between them in each pair of iterations, i.e.,

$$\begin{aligned} i \text{ is even}: &\begin{cases} {E_x}^h(i) = |{E_x}^h|\exp(j\angle\mathcal{F}^{-1}[{E_x}^m(i-1)]) \\ {E_y}^h(i) = |{E_y}^h|\exp(j\angle\mathcal{F}^{-1}[{E_x}^m(i-1)]+j\phi) \end{cases} \\ i \text{ is odd}: &\begin{cases} {E_x}^h(i) = |{E_x}^h|\exp(j\angle\mathcal{F}^{-1}[{E_y}^m(i-1)]-j\phi) \\ {E_y}^h(i) = |{E_y}^h|\exp(j\angle\mathcal{F}^{-1}[{E_y}^m(i-1)]) \end{cases} \end{aligned}. \tag{2.6}$$

In the examples used in this work, the modified algorithm converged to the final designs in less than twenty iterations.

After determining the required field distributions on the metasurface, we need to design a metasurface structure that can generate these field distributions with high efficiency. As shown in Figs. **2.8a**, **2.8b**, and **2.8d**, the metasurface is based on high-index cuboid nanoposts with different dimensions along the x and y axes, a and b, respectively. For proper choices of the nanoposts height and distance, the transmission phases can be controlled independently from 0 to 2π, while keeping the transmission amplitude close to 1. For the operation wavelength of 850 nm, here we have used α-Si nanoposts that are 682 nm tall and located on a square lattice with a 420-nm long lattice constant. Figure **2.8c** shows the nanopost side lengths, a and b, versus the transmission phases for x- and y-polarized light.

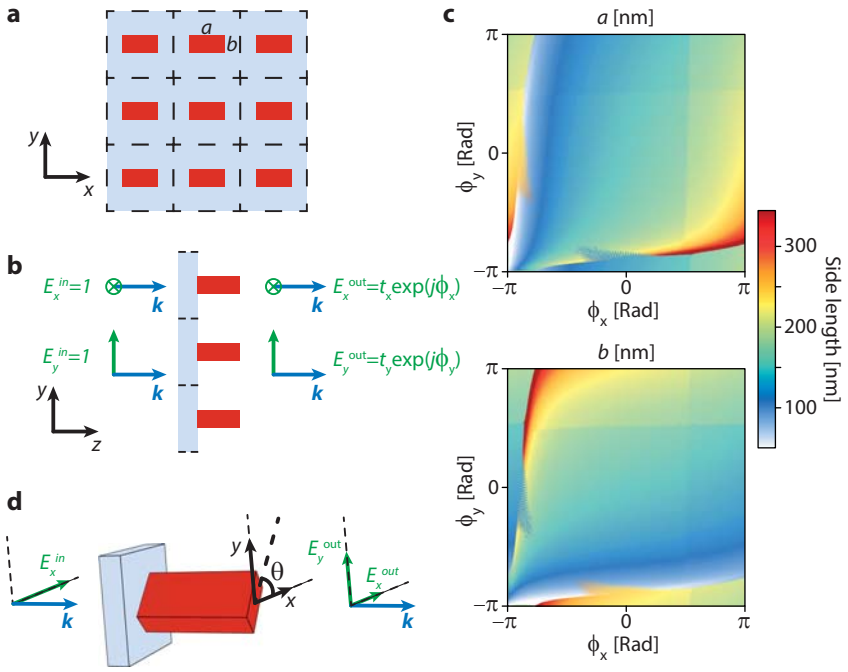

Figure 2.8: **Metasurface structure and design graphs. (a)** Schematics of a uniform lattice of dielectric nano-posts showing the post dimensions. **(b)** Side-view of the uniform array of nano-posts, showing the transmission parameters along the x and y axes. With a proper choice of the material, lattice constant, and post height, ϕ_x and ϕ_y can be fully and independently controlled to cover the whole 0–2π range. **(c)** Chosen values of a and b as functions of ϕ_x and ϕ_y. **(d)** Simultaneous control of the output polarization and phase through rotating the nano-post with correspondingly chosen dimensions. The nano-post can generate an output field with any arbitrary polarization and phase from any given input polarization.

As discussed above, the metasurface structure of Fig. **2.8**, has the ability to control the phase and polarization of output light independently on a subwavelength lattice. Specifically, when the transmittance of the metasurface is close to unity, the transmission of the nanopost shown in Fig. **2.8d** can be modeled as $\mathbf{E}^{\text{out}} = \mathbf{T}\mathbf{E}^{\text{in}}$, where the Jones matrix $\mathbf{T}$ is given by Eq. 2.1. Once the input and output electric field vectors are known at each point on the metasurface, the corresponding Jones matrix can be calculated from Eq. 2.2. Then, the required rotation angle θ and phase pairs, $\phi_{x'}$ and $\phi_{y'}$, can be calculated using Eq. 2.1. The data in Fig. **2.8c** can then be used to find the nanopost that provides the required phases.

Experimental results

Finally, in order to experimentally investigate the capability of the proposed method and structure to generate polarization holograms, we designed and fabricated two different polarization holograms that project the data in two color images. The original, simulated, and measured color images are shown in Figs. **2.9a** and **2.9b** for the two images. Both holograms are about 30 degrees in height, corresponding to a diagonal NA of 0.36 for the hologram in Fig. **2.9a**. The design process was exactly similar for the two images, and started by calculating the Stokes parameters from the RGB data, as shown in Figs. **2.6a** and **2.6b**, which correspond to the hologram of Fig. **2.9a**. The initial electric field distribution on the hologram was then calculated from the Stokes parameters [Fig. **2.6d**], and the modified GS algorithm was used to calculate the required metasurface electric field distributions as well as the simulated polarization holograms, shown in Figs. **2.9a** and **2.9b**, middle. Assuming an input electric field polarized along the x axis, the corresponding nanoposts were found through the process explained in the previous paragraph.

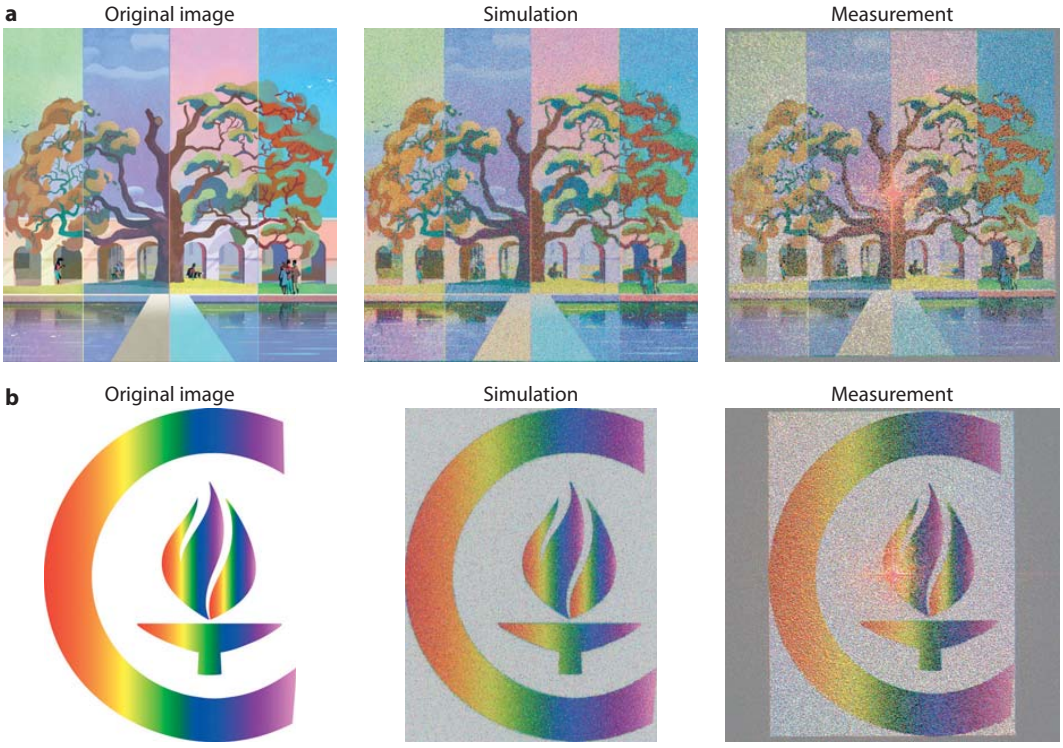

Figure 2.9: **Simulation and measurement results (a)** and **(b)** The original target image along with simulated and measured polarization holograms converted to false-color images. Both holograms are about 30-degrees tall, corresponding to a diagonal NA of 0.36 for the holograms in panel **a**.

The process used to fabricate the devices is mostly similar to the fabrication process of the polarization camera, and it is explained in Appendix 2.3 in more detail. In short, a layer of α-Si was deposited on the fused silica substrate. The metasurface pattern was defined using electron-beam lithography and reversed through evaporation and lift-off of an aluminum oxide (Al_2O_3) layer. This layer was used as a hard mask in dry etching of α-Si and was dissolved after the etch step.

To measure the hologram, we used a custom-built microscope that imaged the back-focal plane of the objective lens on the image sensor, using a simple 4-f system. We used an LP to set the input polarization along the x axis. In addition, a polarization analyzer composed of a QWP and an LP was used inside the 4-f system to measure the hologram Stokes parameters. The measured Stokes parameters were then converted back to RGB data and combined to form the measured holograms plotted in Figs. **2.9a** and **2.9b**, right.

It is worth noting here that a free normalization parameter exists in the conversion of the Stokes parameters to the RGB data that determines the light intensity corresponding to *white* color. In addition, different linear transformations might be used for the conversion to map specific colors to specific intensities. Here, using 8-bit color images where the RGB values change from 0 to 255 for each color, we simply used the linear relation $S_i = (X - 128)/128$, where i can be 1, 2, or 3 and X denotes R, G, or B, respectively. However, one might want to have a different color mapping, for instance convert black to an intensity of zero. This might simply be possible either through using only half of the possible existing polarization states, i.e., by setting $S_i \geq 0$, or using a more complicated mapping.

An alternative design method is possible where all the nanoposts have the same rotation axis (i.e., all nano-posts have $\theta = \theta_0$). In that design, there is no conversion between the two linear polarizations along the two axes of the nanoposts, which we can call x and y without loss of generality. As a result, the input and output x-polarized (as well as y-polarized) powers should be equal, which means that the input polarization should be chosen based on the axes directions and the desired hologram. In addition, the normalization step in the hologram design algorithm would be slightly different for this method. We simulated the same polarization holograms using this alternative method as well, and didn't observe any significant difference in their performance.

The unprecedented capabilities of dielectric metasurfaces in simultaneous control of phase and polarization allow for implementation of new categories of devices with

no conventional counterparts. Here, we discussed vectorial holograms that generate polarization patterns of almost arbitrary complexity, designed using a modified GS algorithm. The devices operate in the near infrared and are based on an α-Si birefringent metasurface. The same method and structure can readily be used in other wavelength ranges using various materials [68, 212, 216]. While the demonstrated concepts and methods can be used to make holograms with enhanced security and added data storage capabilities, we expect that they spur more important applications in advanced structured illumination schemes or vectorial beam generation.

Appendix 2.1: Simulation, fabrication, and measurement details of polarization cameras

Simulation and design. To design the DoFP metasurface mask, we first calculated the two phase profiles required for the two polarization states [Fig. **2.2d**]. The phase profiles correspond to decentered aspheric lenses that focus each polarization at the center of one image sensor pixel. These phases are then used in Eq. 2.3 along with the known input polarization states to calculate the Jones matrix. To find the nano-post corresponding to each Jones matrix, the matrix is diagonalized according to Eq. 2.1, and the two phases, $\phi_{x'}$ and $\phi_{y'}$, and the rotation angle θ are then extracted. The dimensions of the nano-post providing the required pair of phases is then found using the data in Fig. **2.2b**.

The polarization target used for the imaging experiments in Fig. **2.4** was designed in a slightly different manner since in this case only the output polarization is of interest. Assuming an x-polarized input light, the output polarization at each point on the mask was chosen according to Fig. **2.4a**. In the general case, the mask can then be designed using the Jones matrix found from Equation 2.2. In this special case, however, the device is a set of nano-posts acting as quarter or half wave-plates. Therefore, we designed the nano-posts in a manner similar to [132] to make it robust to fabrication errors.

To find the transmission amplitude and phase for the nano-posts [Fig. **2.A1**] we simulated a uniform array of nano-posts with rectangular cross-sections under normally incident x- and y-polarized light using the rigorous coupled-wave analysis (RCWA) technique [217]. The resulting complex transmissions were then used to find the best nano-post that provides each required phase pair through minimizing the Euclidean distance between $[e^{i\phi_x}, e^{i\phi_y}]$ and $[t_x, t_y]$, where ϕ_x and ϕ_y are the desired phase values, and t_x and t_y are complex nano-post transmissions. The optimized

nano-post dimensions are plotted in Fig. 2.2**b**.

Fabrication. The fabrication process is the same for both the DoFP metasurface mask and the polarization imaging target. The fabrication started with deposition of a 650-nm-thick layer of α-Si on a 500-μm-thick fused silica substrate. The metasurface pattern is defined in a ~300-nm-thick ZEP-520A positive electron-beam resist using EBL. After development of the resist, a ~70-nm-thick layer of Al_2O_3 is deposited on the sample using electron-beam evaporation and lifted off to invert the pattern. The Al_2O_3 is then used as a hard mask in the reactive ion etching of the α-Si layer. Finally, the Al_2O_3 mask is removed in a solution of hydrogen peroxide and ammonium hydroxide.

Measurement. The measurement setups (including part models) are schematically illustrated in Fig. 2.A2 for different parts of the characterization process. To characterize the DoFP super-pixel performance, light from an LED was passed through an LP and a QWP to set the input polarization state. The six different polarization states [Fig. 2.3**a**] were generated using this combination. The intensity distribution patterns at the focal plane after the DoFP metasurface mask were then imaged using a custom-built microscope. The data was analyzed by calculating the Stokes parameters measured by each super-pixel, and averaging over all the super-pixels that fit within the field of view. A 10-nm bandwidth filter with a center wavelength of 850 nm was inserted in the path to characterize the narrow-band operation, and was then removed to acquire the results for a wider-bandwidth source.

The imaging polarimetry experiments were performed in a similar way. For these experiments, the polarization target was illuminated by x-polarized light out of a supercontinuum laser source (filtered by the same 10-nm bandwidth filter). The target was imaged onto the DoFP metasurface mask plane using a secondary custom-built microscope (operating as relay optics). The intensity distribution at the focal plane after the DoFP metasurface mask was then imaged and analyzed to generate the polarization images plotted in Fig. 2.4**d**. For comparison, the DoFP metasurface mask was removed and a polarization analyzer (i.e., a QWP and an LP) was inserted into the system to form the reference polarization images plotted in Fig. 2.4**c**.

Appendix 2.2: Supporting figures for polarization cameras

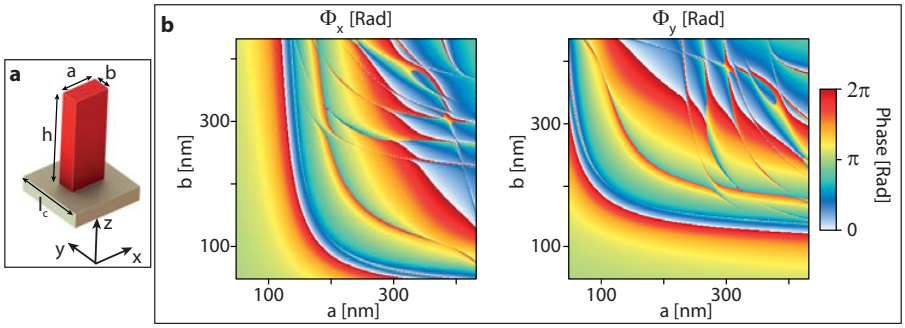

Figure 2.A1: **Transmission phase of the birefringent nano-posts. (a)** Schematic illustration of an α-Si nano-post showing its dimensions. **(b)** Simulated transmission phases for the x- and y-polarized light at the wavelength of 850 nm. The posts are 650 nm tall, and the lattice constant is 480 nm.

Appendix 2.3: Simulation, fabrication, and measurement details of polarization holograms

Simulation. The RCWA technique [217] was used to calculate the transmission amplitude and phase of the rectangular nanoposts. The refractive indices of α-Si and fused silica were assumed to be 3.6 and 1.45 at the operation wavelength of 850 nm. The sizes of nanoposts that provide a specific phase pair plotted in Fig. **2.8c** are found through minimizing the total complex error $|t_x - \exp(i\phi_x)|^2 + |t_2 - \exp(i\phi_y)|^2$. The holograms are designed using Eqs. 2.4-2.6, where the fast Fourier transform technique is used to calculate the discrete Fourier transforms. The algorithm converged to the final designs in less than 20 iterations in all cases.

Sample fabrication. The α-Si layer was deposited on the fused silica substrate using the plasma enhanced chemical vapor deposition to a final thickness of 682 nm. The metasurface pattern was generated using an EBPG5200 electron beam lithography machine in a positive electron resist (ZEP-520A). An electron beam evaporated Al_2O_3 layer was used to reverse the generated pattern with a lift-off process, and was then used as a hard mask for dry etching the α-Si layer. The Al_2O_3 layer was then dissolved in a mixture of hydrogen peroxide and ammonium hydroxide.

Measurement procedure. The metasurface was illuminated by an x-polarized collimated beam from an ~850-nm laser diode. An objective lens (LMPlanFl 20×, NA=0.4; Olympus) was used to form a Fourier transform of the metasurface hologram in its back focal plane. A $4f$ system (LB1471-B, f=50 mm and LB1437-B, f=150 mm; Thorlabs Inc.) was then used to image the back focal plane onto a

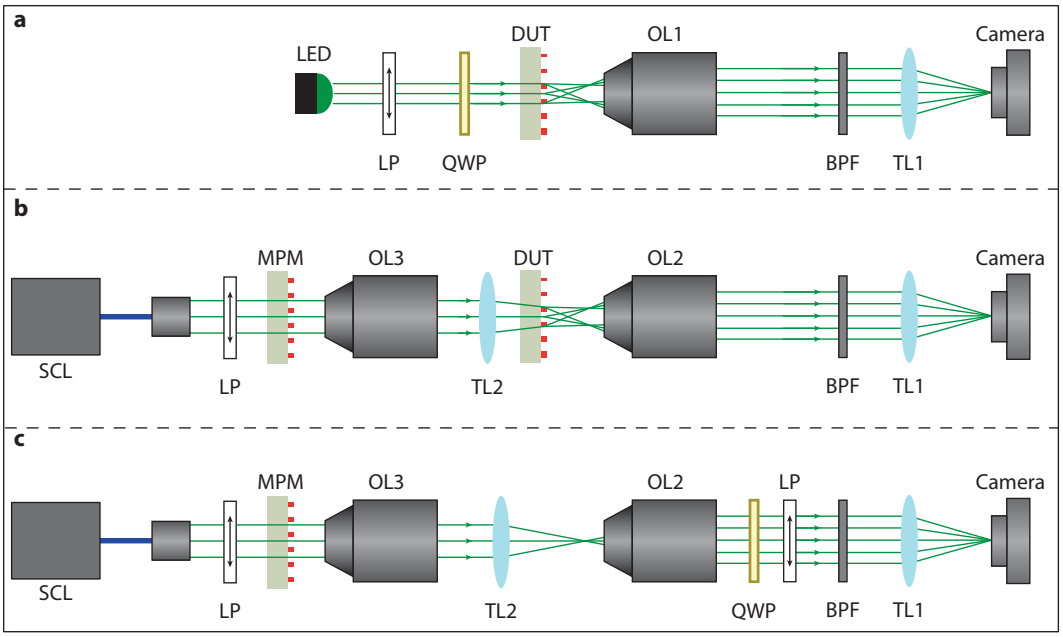

Figure 2.A2: **Measurement setups for polarization camera.** **(a)** Schematics of the measurement setup used to characterize the superpixels of the DoFP metasurface mask. **(b)** Schematics of the measurement setup used to capture polarimetric images using the DoFP metasurface mask. **(c)** Schematics of the measurement setup used to capture polarimetric images using the conventional method. LP: Linear polarizer; QWP: Quarter wave-plate; DUT: Device under test; OL: Objective lens; BPF: Bandpass filter; TL: Tube lens; SCL: Supercontinuum laser; MPM: Metasurface polarization mask. (OL1: Olympus UMPlanFl 100×, NA = 0.95; OL2: LMPlanFl 20×, NA = 0.4; OL3: Mitutoyo M Plan Apo 10, NA = 0.28; BPF: Thorlabs FL850-10; TL1: Thorlabs AC254-200-B-ML; TL2: Thorlabs LB1723-B; LP: Thorlabs LPVIS100-MP2; QWP: Thorlabs AQWP10M-980; SCL: Fianium WhiteLase micro.)

charge-coupled device (CCD) image sensor (CoolSNAP K4; Photometrics). A polarization state analyzer formed from a QWP (AQWP10M-980; Thorlabs Inc.) and an LP (LPVIS100-MP2; Thorlabs Inc.), placed inside the $4f$ system was used to measure the Stokes parameters of the holograms. The measured Stokes parameters were numerically combined and converted to color data to form the final false-color holograms.

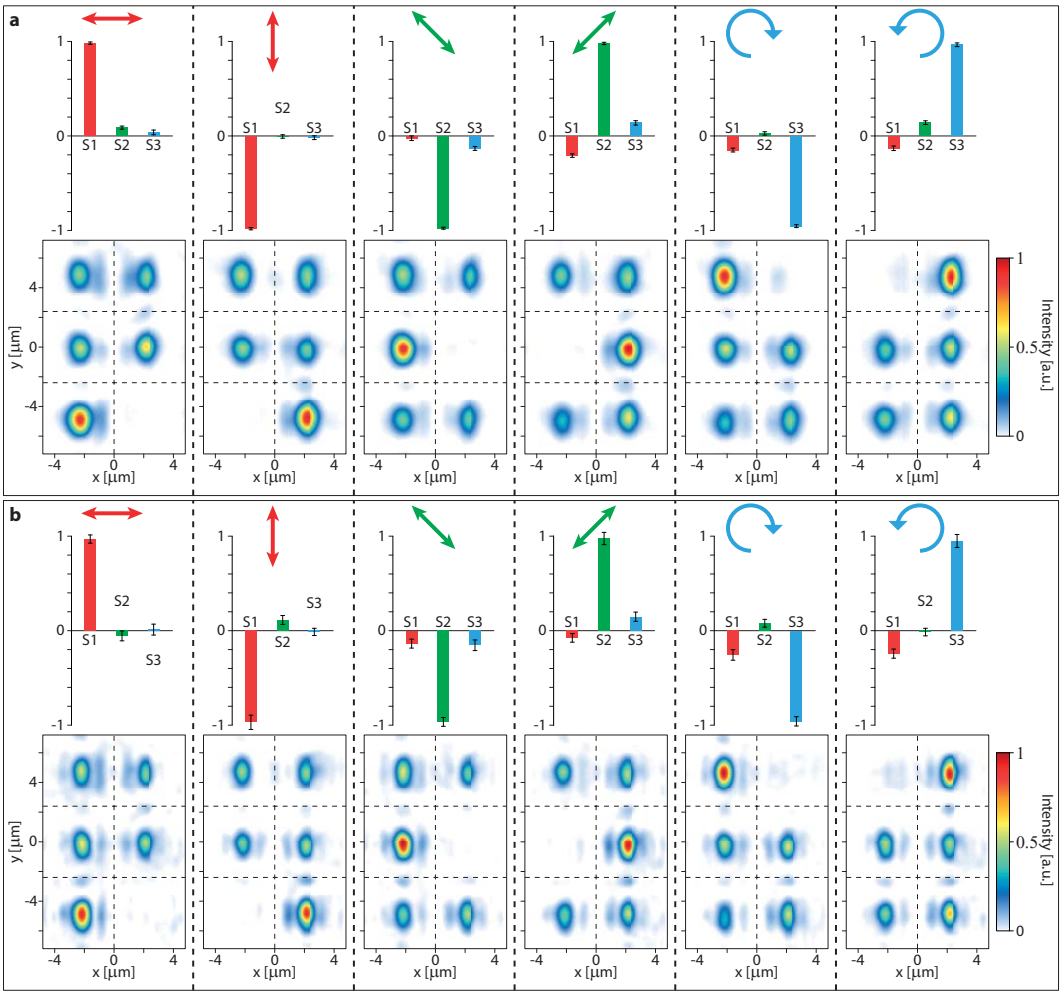

Figure 2.A3: **Superpixel characterization of the DoFP metasurface mask with 4.8-µm pixels.** **(a)** Calculated average Stokes parameters for different input polarizations (top) and the corresponding intensity distributions of a sample superpixel (bottom). The Stokes parameters are averaged over about 120 superpixels (limited by the microscope field of view), and the error bars demonstrate the statistical standard deviations. The measurements are performed with an 850-nm LED filtered by a bandpass filter (center: 850 nm, FWHM: 10 nm) as the light source. **(b)** Same as **a**, with the bandpass filter removed from the setup. The results shown in **a** are the same as the ones presented in Figs. **2.3a** and **2.3b** and are shown here for comparison with the results shown in **b**. When using the band-pass filter, the iris in front of the LED has a larger diameter to compensate for the lower power of the filtered light. This results in the focal spots being tighter without the band-pass filter.

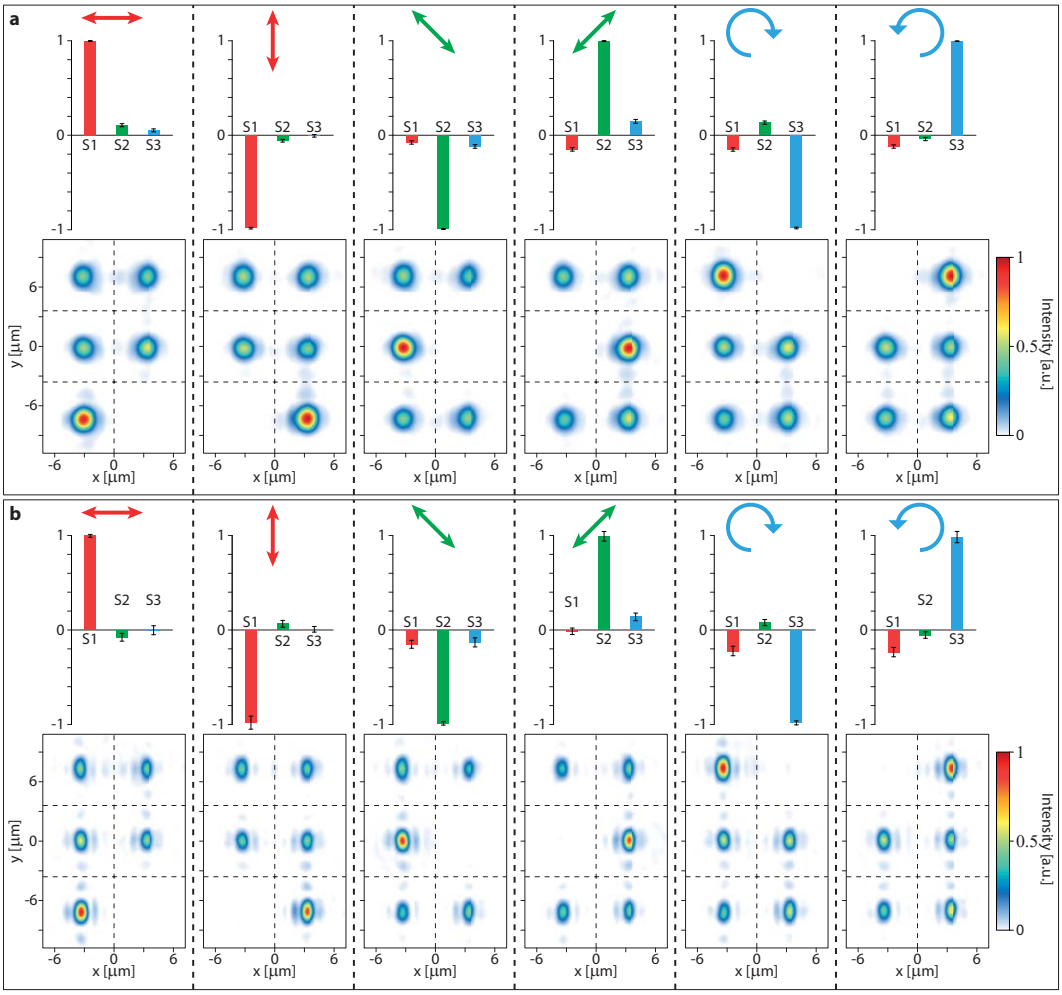

Figure 2.A4: **Superpixel characterization of the DoFP metasurface mask with 7.2-μm pixels. (a)** Calculated average Stokes parameters for different input polarizations (top) and the corresponding intensity distributions of a sample superpixel (bottom). The Stokes parameters are averaged over more than 50 superpixels (limited by the microscope field of view), and the error bars demonstrate the statistical standard deviations. The measurements are performed with an 850-nm LED filtered by a bandpass filter (center: 850 nm, FWHM: 10 nm) as the light source. **(b)** Same as **a**, with the bandpass filter removed from the setup.

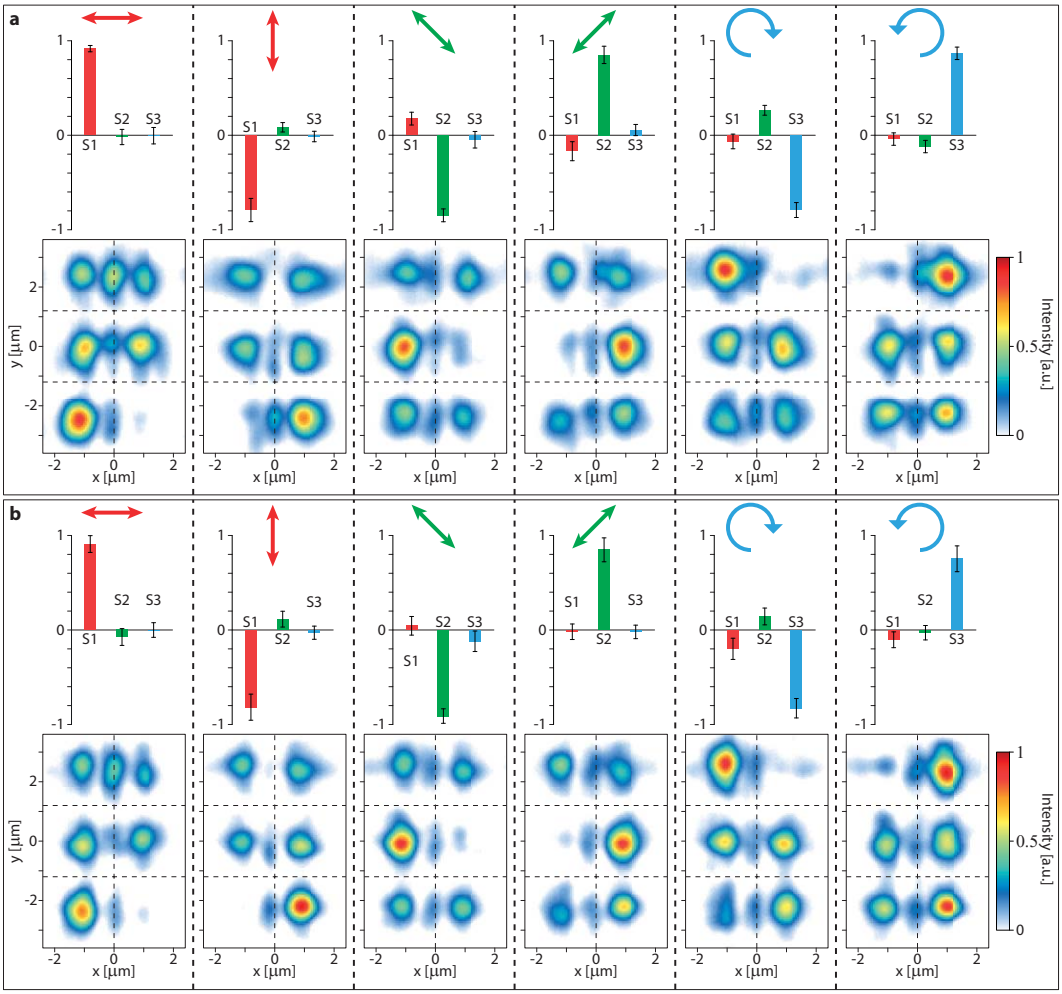

Figure 2.A5: **Superpixel characterization of the DoFP metasurface mask with 2.4-μm pixels.** **(a)** Calculated average Stokes parameters for different input polarizations (top) and the corresponding intensity distributions of a sample superpixel (bottom). The Stokes parameters are averaged over about 370 superpixels (limited by the microscope field of view), and the error bars demonstrate the statistical standard deviations. The measurements are performed with an 850-nm LED filtered by a bandpass filter (center: 850 nm, FWHM: 10 nm) as the light source. **(b)** Same as **a**, with the bandpass filter removed from the setup.

Chapter 3

MULTIWAVELENGTH METASURFACES

The material in this chapter was in part presented in [135–137, 212].

3.1 Introduction

One main drawback of almost all of metasurface devices, particularly the ones with spatially varying phase profiles like lenses and gratings, is their chromatic dispersion: their performance changes as the wavelength is varied [218–220]. Refractive optical elements also suffer from chromatic dispersion; however, their chromatic dispersion, which stems from material dispersion, is substantially smaller than those of the diffractive elements [219, 220]. An ideal refractive lens made of a dispersionless material will show no chromatic aberration. On the other hand, the chromatic aberration of diffractive elements mainly comes from the geometrical arrangement of the device. Early efforts focused on making achromatic diffractive lenses by cascading them in the form of doublets and triplets [221–224], but it was later shown that it is fundamentally impossible to make a converging achromatic lens which has a paraxial solution (i.e., is suitable for imaging) by only using diffractive elements [225]. Although diffractive-refractive combinations have successfully been implemented to reduce chromatic aberrations, they are mostly useful in deep ultraviolet (DUV) and X-ray wavelengths where materials are significantly more dispersive [27, 226].

Truly achromatic diffractive devices are very challenging to demonstrate, and therefore many efforts have focused on demonstration of multiwavelength devices that work at a few distinct wavelengths. For proper operation, a multiwavelength metasurface should provide independent phase control at the desired wavelengths. Multiple resonances of meta-atoms formed from two rectangular dielectric resonators have been used in an effort to provide this phase coverage at three wavelengths in [227, 228]. However, the demonstrated cylindrical lens that has a few Fresnel zones and a numerical aperture of NA = 0.04, still exhibits multiple focal points. Multiwavelength lenses based on plasmonic metasurfaces have been demonstrated in [229, 230]. These devices, in addition to the low efficiency of plasmonic metasurfaces [51], have multiple focuses and are polarization dependent. An achromatic metasurface design is proposed in [231] based on the idea of dispersionless meta-atoms (i.e., meta-atoms

that impart constant delays). However, this idea only works for metasurface lenses with one Fresnel zone, limiting the size and numerical aperture of the lenses. For a typical lens with tens of Fresnel zones, dispersionless meta-atoms will not reduce the chromatic dispersion as we will shortly discuss. In the following we briefly discuss the reason for chromatic dispersion of metasurface lenses, and then propose three methods for designing multiwavelength metasurfaces. The first method is based on correcting the lens behavior at distinct wavelengths through complete and independent phase coverage at the design wavelengths. The second method is based on spatial multiplexing of multiple metasurfaces designed for different wavelengths. In the third technique, we have utilized the birefringence of asymmetric nano-posts (like elliptical or rectangular ones) to control the phases of light with two different wavelengths and polarizations independently. Finally, we show that this method can be used to implement a double wavelength metasurface lens (DW-ML) that can replace an objective lens in a TPM system.

3.2 Root of chromatic dispersion in metasurfaces

In diffractive lenses, chromatic dispersion mainly manifests itself through a significant change of focal length as a function of wavelength [27]. This change is schematically shown in Fig. **3.1a**, along with a schematic metasurface lens assumed to be corrected to have the same focal distance at a few wavelengths. To better understand the underlying reasons for this chromatic dispersion, we consider a hypothetical aspheric metasurface lens. The lens is composed of different meta-atoms which locally modify the phase of the transmitted light to generate the desired wavefront. We assume that the meta-atoms are dispersionless in the sense that their associated phase changes with wavelength as $\phi(\lambda) = 2\pi L/\lambda$ like a piece of dielectric with a constant refractive index. Here λ is the free space wavelength and L is an effective parameter associated with the meta-atoms that controls the phase (L can be an actual physical parameter or a function of physical parameters of the meta-atoms). We assume that the full 2π phase needed for the lens is covered using different meta-atoms with different values of L. The lens is designed to focus light at λ_0 [Fig. **3.1b**] to a focal distance f_0, and its phase profile in all Fresnel zones matches the ideal phase profile at this wavelength. Because of the specific wavelength dependence of the dispersionless meta-atoms (i.e., proportionality to $1/\lambda$), at a different wavelength, λ_1, the phase profile of the lens in the first Fresnel zone follows the desired ideal profile needed to maintain the same focal distance [Fig. **3.1b**]. However, outside the first Fresnel zone,

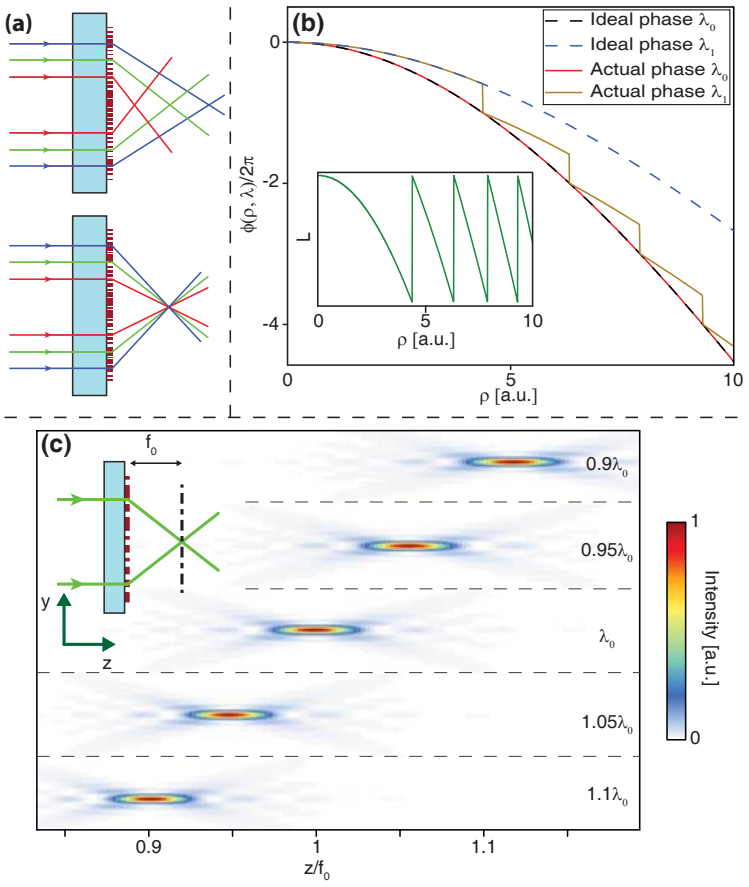

Figure 3.1: **Chromatic dispersion of metasurface lenses.** **(a)** Schematic illustration of a typical metasurface lens focusing light of different wavelengths to different focal distances (top), and schematic of a metasurface lens corrected to focus light at specific different wavelengths to the same focal distance (bottom). **(b)** The phase profile of a hypothetical aspheric metasurface lens at the design wavelength λ_0 and a different wavelength λ_1 as a function of the distance to the center of the lens (ρ). (Inset) Plot of the parameter of the meta-atoms controlling phase (named L). The Fresnel zone boundaries happen at the integer multiples of 2π in the λ_0 phase curve. These zone boundaries coincide with the jumps in the actual phase at λ_1 and L. **(c)** Intensity of light at different wavelengths in the axial plane after passing through the lens showing considerable chromatic dispersion rising from phase jumps at the boundaries between different Fresnel zones.

the actual phase profile of the lens deviates substantially from the desired phase profile. Due to the jumps at the boundaries between the Fresnel zones, the actual phase of the lens at λ_1 is closer to the ideal phase profile at λ_0 than the desired phase profile at λ_1. In the inset of Fig. **3.1b** the effective meta-atom parameter L is plotted as a function of distance to the center of the lens ρ. The jumps in L coincide with the jumps in the phase profile at λ_1. In Fig. **3.1c**, the simulated intensity profile of the same hypothetical lens is plotted at a few wavelengths close to λ_0. The focal distance changes approximately proportional to $1/\lambda$. This wavelength dependence is also observed in Fresnel zone plates [27, 232, 233], and for lenses with wavelength independent phase profiles [219, 220] (the $1/\lambda$ dependence is exact in the paraxial limit, and approximate in general). This behavior confirms the previous observation that the phase profile of the lens at other wavelengths approximately follows the phase profile at the design wavelength. Therefore, the chromatic dispersion of metasurface lenses mainly stems from wrapping the phase, and the dependence of the phase on only one effective parameter (e.g., L) whose value undergoes sudden changes at the zone boundaries. As we show in the following, using two parameters to control metasurface phase at two wavelengths can resolve this issue, and enable lenses with the same focal length at two different wavelengths. With more than two control parameters that enable independent phase control at more wavelengths, this idea can be generalized to more than two wavelengths.

3.3 Multiwavelength metasurfaces with meta-molecules

Concept and design

The metasurface platform we use here is based on α-Si nano-posts on a fused silica substrate [Figs. **3.2a** and **3.2b**. The nano-posts are placed on the vertices of a hexagonal lattice, and locally sample the phase to generate the desired phase profile [67]. For a fixed height, the transmission phase of a nano-post can be controlled by varying its diameter. The post height can be chosen such that at a certain wavelength the whole 2π phase shift is covered, while keeping the transmission amplitude high. Each nano-post has multiple resonances that are excited and contribute to the scattered field with various strengths [125]. Since many resonances play an important role in the response of nano-posts, we find that explaining their response based on these resonances does not provide an intuitive understanding of their operation. Instead, these nano-posts can be better understood as truncated multi-mode waveguides [77, 125]. To design a metasurface that works at two different wavelengths, a unit cell

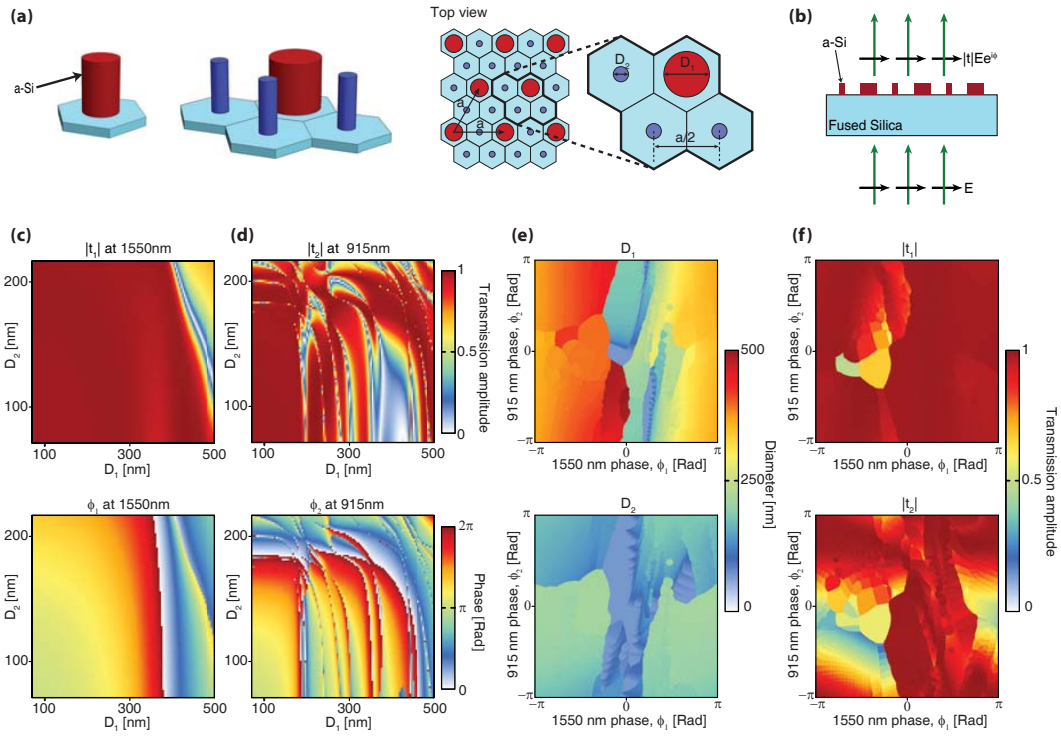

Figure 3.2: **Meta-molecule design and its transmission characteristics.** **(a)** A single scattering element composed of an α-Si nano-post on a fused silica substrate (left). The unit cell composed of four scattering elements that provide more control parameters for the scattering phase (center), and placement of the meta-molecules on a hexagonal lattice with lattice constant a (right). **(b)** Cross sectional schematic of a uniform array of meta-molecules, showing the transmission amplitude and phase definitions. **(c)** and **(d)** Transmission amplitude (top) and phase (bottom) as a function of the two diameters in the unit cell for 1550 nm and 915 nm. **(e)** Selected values of D_1 (top) and D_2 (bottom) as functions of phases at 1550 nm (ϕ_1) and 915 nm (ϕ_2). **(f)** Transmission amplitude at 1550 nm (top) and 915 nm (bottom) for the selected meta-molecules as a function of phase shifts, showing high transmission for almost all phases.

consisting of four different nano-posts [Fig. 3.2**a**] was chosen because it has more parameters to control the phases at the two wavelengths almost independently. Due to the weak coupling between the nano-posts [67], they behave like individual scatterers with high cross-section as shown in our previous works [14, 67, 125]. As molecules consisting of multiple atoms form the units for more complex materials, we call these unit cells with multiple meta-atoms *meta-molecules*. The meta-molecules can also form a periodic lattice (in this case hexagonal), and effectively sample the desired phase profiles simultaneously at two wavelengths. The lattice is subwavelength at both wavelengths of interest; therefore, the non-zero diffraction orders are not excited. In general, the four nano-posts can each have different diameters and distances from each other. However, to make the design process more tractable, we choose three of the four nano-posts with the same diameter D_2 and the fourth post with diameter D_1, and place them in the centers of the hexagons at a distance $a/2$ (as shown in Fig. 3.2**a**). Therefore, each meta-molecule has two parameters, D_1 and D_2, to control the phases at the two wavelengths. For this demonstration, we chose two wavelengths of 1550 nm and 915 nm, because of the availability of lasers at these wavelengths. A periodic array of meta-molecules was simulated to find the transmission amplitude and phase (see Appendix 3.1 for simulation details). The simulated transmission amplitudes and phases for 1550 nm ($|t_1|$ and ϕ_1) and 915 nm ($|t_2|$ and ϕ_2) are plotted as functions of D_1 and D_2 in Figs. 3.2**b** and 3.2**c**. In these simulations the lattice constant (a) was set to 720 nm and the posts were 718 nm tall. Since the two wavelengths are not close, the ranges of D_1 and D_2 must be very different in order to properly control the phases at 1550 nm and 915 nm. For each desired combination of the phases ϕ_1 and ϕ_2 in the $(-\pi, \pi)$ range at the two wavelengths, there is a corresponding D_1 and D_2 pair that minimizes the total transmission error which is defined as $\epsilon = |\exp(i\phi_1) - t_1|^2 + |\exp(i\phi_2) - t_2|^2$. These pairs are plotted in Fig. 3.2**d** as a function of ϕ_1 and ϕ_2. Using the complex transmission coefficients (i.e., t_1 and t_2) in error calculations results in automatically avoiding resonance areas where the phase might be close to the desired value, but transmission is low. The corresponding transmission amplitudes for the chosen meta-molecules are plotted in Fig. 3.2**e** , and show this automatic avoidance of low transmission meta-molecules. In the lens design process, the desired transmission phases of the lens are sampled at the lattice points at both wavelengths resulting in a (ϕ_1, ϕ_2) pair at each lattice site. Using the plots in Fig. 3.2**d**, values of the two post diameters are found for each lattice point. Geometrically, the values of the two diameters are limited by $D_1 + D_2 < a$. Besides, we set a minimum value of 50 nm for the gaps between the posts to facilitate the

metasurface fabrication.

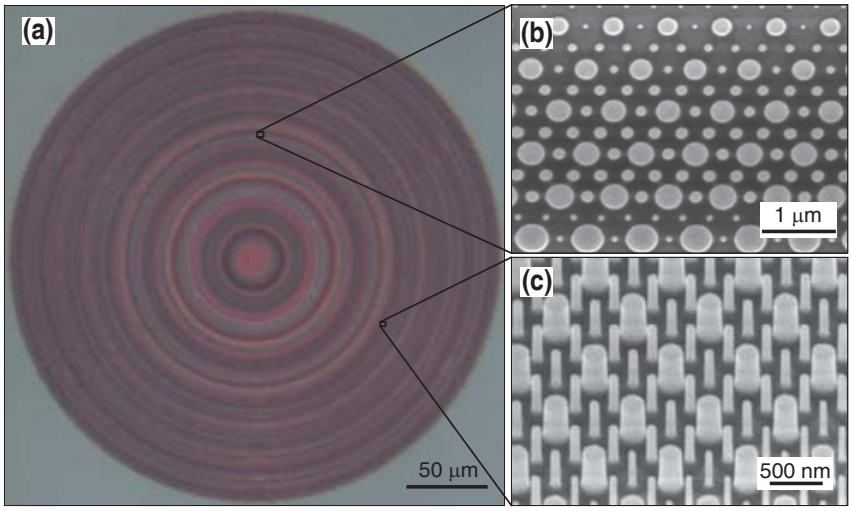

Figure 3.3: **Fabricated device images.** **(a)** Optical microscope image of the fabricated device. **(b)** and **(c)** Scanning electron micrographs of parts of the fabricated device from top **b** and with a 30 degree tilt **c**.

Experimental results

A double wavelength aspheric lens was designed using the proposed platform to operate at both 1550 nm and 915 nm. The lens has a diameter of 300 μm and focuses the light emitted from single mode fibers at each wavelength to a focal plane 400 μm away from the lens surface (the corresponding paraxial focal distance is 286 μm, thus the nNA is 0.46). The lens was fabricated using standard nano-fabrication techniques: a 718-nm-thick layer of α-Si was deposited on a fused silica substrate, the lens pattern was generated using EBL and transferred to the α-Si layer using Al_2O_3 as a hard mask (see Appendix 3.1 for fabrication details). Optical and scanning electron microscope images of the lens and nano-posts are shown in Fig. **3.3**. The smallest diameter of the nano-posts and gap sizes used in the design and fabrication of the metasurfaces were 72 nm and 50 nm, respectively. For characterization, the fabricated metasurface lens was illuminated by light emitted from the end facet of a single mode fiber, and the transmitted light intensity was imaged at different distances from the lens using a custom built microscope (see Appendix 3.1 and Fig. **3.A1** for measurement setup and details). Measurement results for both wavelengths are plotted in Figs. **3.4a**–**3.4d**. Figures **3.4a** and **3.4b** show the measured (left) and simulated (right) intensity profiles in the focal plane at 915 nm and 1550 nm. The measured FWHM is 1.9 μm at 915 nm, and 2.9 μm at 1550 nm. The intensity

measured at the two axial plane cross sections are plotted in Fig. **3.4c** for the two wavelengths. A nearly diffraction-limited focus is observed in the measurements, and no other secondary focal points with comparable intensity is seen. To confirm the diffraction-limited behavior, a perfect phase mask was simulated using the same illumination used in the measurements. The simulated FWHMs were 1.6 μm and 2.75 μm for 915 nm and 1550 nm, respectively (see Appendix 3.1 for simulation details). Focusing efficiencies of 22% and 65% were measured at 915 nm and 1550 nm, respectively. Focusing efficiency is defined as the ratio of the power passing through a 20-μm-diameter disk around the focus to the total power incident on the lens. As expected from the lattice and lens symmetries, no measurable change in the focus pattern or efficiency of the lens was observed as the incident light polarization was varied. Another lens with a longer focal distance of 1000 μm (thus a lower NA of 0.29) was fabricated and measured with the same platform and method. Measurement results for those devices are presented in Fig. **3.A2**. Slightly higher focusing efficiencies of 25% and 72% were measured at 915 nm and 1550 nm for those devices. For comparison, a lens designed with the same method and based on the same metasurface platform is simulated using finite difference time domain (FDTD) method with a freely available software (MEEP) [234]. To reduce the computational cost, the simulated lens is four times smaller and focuses the light at 100 μm distance. Because of the equal numerical apertures of the simulated and fabricated devices, the focal intensity distributions and the focal depths are comparable. The simulation results are shown in Figs. **3.4a**, **3.4b**, and **3.4c**. Figures **3.4a** and **3.4b** show the simulated focal plane intensity of the lens at 915 nm and 1550 nm, respectively. The simulated FWHM is 1.9 μm at 915 nm and 3 μm at 1550 nm, both of which are in accordance with their corresponding measured values. Also, the simulated intensity distributions in the axial cross section planes, which are shown in Fig. **3.4d**, demonstrate only one strong focal point. The focusing efficiency was found to be 32% at 915 nm, and 73% at 1550 nm. We attribute the difference in the simulated and measured efficiencies to fabrication imperfections and measurement artifacts (see Appendix 3.1 for measurement details).

Discussion

The efficiency at 915 nm is found to be lower than expected both in measurements and FDTD simulations. While the average power transmission of the selected meta-molecules is about 73% as calculated from Fig. **3.2e**, the simulated focusing efficiency is about 32%. To better understand the reasons for this difference, two blazed gratings

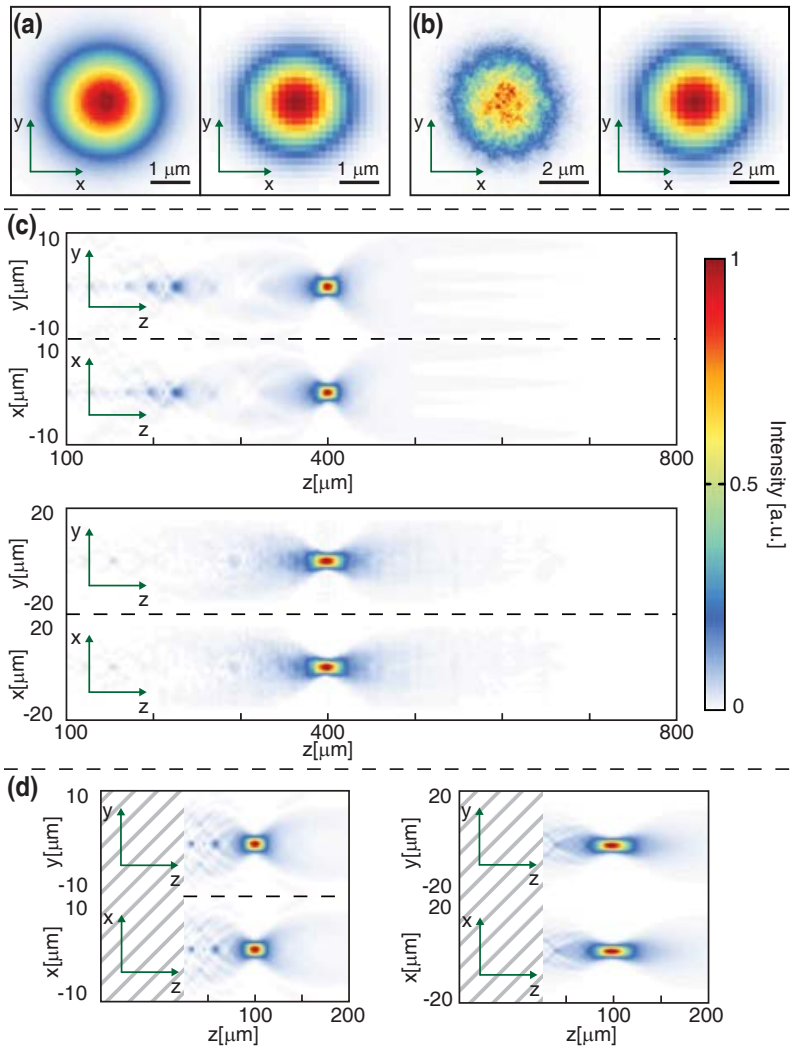

Figure 3.4: **Measurement and simulation results of the double-wavelength lenses with meta-molecules.** **(a)** Measured (left) and simulated (right) focal plane intensities at 915 nm. The simulated lens has the same numerical aperture as the measured one, but is four times smaller. One-dimensional cross sections of the measured and simulated intensity profiles are shown in the bottom. The red arrows denote the FWHMs which are both ~1.9 μm. **(b)** Same results as in **a** for 1550 nm. The high frequency fluctuations seen in the measured intensity are caused by the highly non-uniform sensitivity of the phosphorous coated CCD camera. The FWHMs are ~2.9 μm and ~3 μm for measurement and simulation, respectively. **(c)** Intensity measured in the axial planes of the lens for 915 nm (top) and 1550 nm (bottom). The high frequency noise of the camera at 1550 nm is filtered to generate a smooth distribution. **(d)** Simulated intensity profiles in the axial planes at 915 nm (left) and 1550 nm (right) for the four times smaller lens.

with different angles were designed and simulated for both wavelengths using the same meta-molecules (see Appendix 3.1 and Fig. **3.A3**). It is observed that for the gratings (that are aperiodic), a significant portion of the power is diffracted to other angles both in reflection and transmission. Besides, the power lost into diffractions to other angles is higher for the grating with larger deflection angle. The main reason for the large power loss to other angles is the relatively large lattice constant. The chosen lattice constant of $a = 720$ nm is just slightly smaller than $a_{\max} = \frac{2}{\sqrt{3}n_g}\lambda = 727$ nm, the lattice constant at which the first order diffracted light starts to propagate in the glass substrate (refractive index: $n_g = 1.452$) for a perfectly periodic structure. Thus, even a small deviation from perfect periodicity can result in light being diffracted to propagating orders. Besides, the lower transmission of some meta-molecules reduces the purity of the plane wave wavefronts diffracted to the design angle. Furthermore, the desired phase profile of high numerical aperture lenses cannot be sampled at a high enough resolution using large lattice constants. Therefore, as shown in this work, a lens with a lower numerical aperture has a higher efficiency. There are a few methods to increase the efficiency of the lenses at 915 nm: the lattice constant is bound by the geometrical and fabrication constraint: $D_1 + D_2 + 50\text{nm} < a$, hence the smallest value of $D_1 + D_2$ that gives full phase coverage at the longer wavelength sets the lower bound for the lattice constant. This limit can usually be decreased by using taller posts, however, that would result in a high sensitivity to fabrication errors at the shorter wavelength. Thus, a compromise should be made here, and higher efficiency designs might be possible by more optimum selections of the post height and the lattice constant. The lattice constant can also be smaller if less than the full 2π phase shift is used at 1550 nm (thus slightly lower efficiency at 1550 nm). In addition, as explained earlier, in minimizing the total transmission error equal weights are used for 915 nm and 1550 nm. A higher weight for 915 nm might result in higher efficiency at this wavelength, probably at the expense of 1550 nm efficiency. For instance, if we optimize the lens only for operation at 915 nm, devices with efficiencies as high as 80% are possible [14, 67].

Utilizing more degrees of freedom in the unit cell can be used to increase the number of wavelengths with independent phase control. While each different diameter of the nano-posts in the unit cell can be used to add an additional wavelength with independent control, other geometrical parameters in the unit cell might enable additional control. Increasing the number of wavelengths will probably result in a decreased efficiency at each wavelength, as the transmission phase and amplitude errors at each individual wavelength will probably increase. We reserve a more

detailed study of these effects for later work.

The approach presented here cannot be directly used to correct for chromatic dispersion over a continuous bandwidth; the multiwavelength lenses still have chromatic dispersion much like normal metasurface lenses in narrow bandwidths around the corrected wavelengths. For achieving zero chromatic dispersion over a narrow bandwidth, the meta-atoms should independently control the phase at two very close wavelengths. High quality factor resonances must be present for the meta-atom phase to change rapidly over a narrow bandwidth, and such resonances will result in high sensitivities to fabrication errors that would make the metasurface impractical.

The meta-molecule platform, used here to multiwavelength metasurfaces, can also be used for applications where different functionalities at different wavelengths are desired. For instance, it can be used to implement a lens with two given focal distances at two wavelengths, or a lens converging at one wavelength and diverging at the other. In addition, given the generality of the meta-molecule concept, it can be applied to other areas of interest in metasurfaces, such as nonlinear [108, 109, 111] and microwave [34, 57] metasurfaces. Here we have used only two of the degrees of freedom of the meta-molecules, but increased functionalities at more than two wavelengths can be achieved by making use of all the degrees of freedom. Operation at more than two wavelengths enables applications in color display technologies or more complex fluorescence imaging techniques.

3.4 Multiwavelength metasurfaces based on spatial multiplexing

Spatial multiplexing is a simple technique that has been used for enhancing the number of operation wavelengths [180, 235] or adding new functionalities to optical devices [236] for a long time. In this section, we discuss multiwavelength metasurface lenses based on spatial multiplexing with two different approaches: large scale aperture division and meta-atom interleaving. We use dielectric transmitarrays based on amorphous silicon α-Si to implement the two different methods, and experimentally demonstrate lenses that focus light with wavelengths of 915 nm and 1550 nm to the same distance. The methods introduced here can readily be generalized to more than two wavelengths, or to devices that perform different functions at different wavelengths, or at the same wavelength.

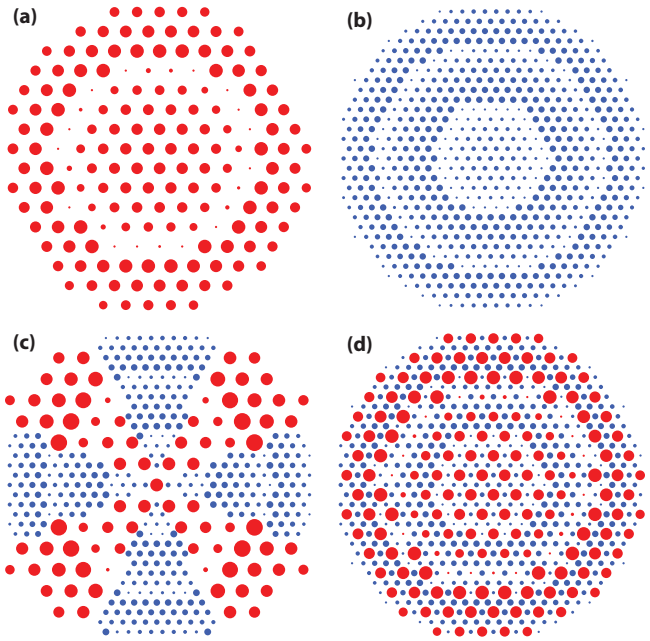

Figure 3.5: **Spatial multiplexing scheme.** **(a)** Schematic of a metasurface lens designed to focus light with wavelength λ_1, and **(b)** wavelength λ_2 to a distance f. **(c)** Double-wavelength metasurface lenses formed by lens aperture division, and **(d)** by interleaving meta-atoms.

Concept and metasurface structure

Two metasurface lenses designed for two different wavelengths [Figs. 3.5**a** and 3.5**b**] can be combined through dividing the metasurface aperture into macroscopic areas, resulting in a multi-sector device as shown in Fig. 3.5**c**. A less obvious method is to interleave the meta-atoms of the two lenses as shown in Fig. 3.5**d**. If the phase change introduced by the meta-atoms is local (i.e., the coupling between the meta-atoms is small), we can expect light scattered by each group of meta-atoms (one group corresponds to one lens) to interfere constructively in their respective focal spot at the design wavelength.

We use the HCTA platform for implementation of the devices. The platform consists of α-Si nano-posts on a fused silica substrate [Fig. 3.6**a**] that can form a hexagonal lattice [Fig. 3.6**b**]. For proper choices of the nano-posts height and lattice constant, full phase coverage can be achieved at a design wavelength by changing the diameters of the nano-posts [67]. The nano-posts behave like multi-mode truncated waveguides with many resonant modes around the wavelength of interest [77, 125]. Superposition of the scattered fields of these resonant modes can result in full 2π phase coverage, while maintaining a high transmission amplitude. Since the structure needs to be

fabricated with a single step electron beam lithography, the nano-post heights should be the same at both wavelengths (which we have chosen to be 915 nm and 1550 nm due to availability of laser sources). In addition, since the two wavelengths are relatively far apart, we choose the 1550 nm lattice constant to be twice that of the 915 nm [Figs. 3.7**a** and 3.7**b**]. With this choice, the two metasurfaces can be interleaved by simply replacing one out of four 915-nm meta-atoms by a 1550-nm one as shown in Fig. 3.7**c**.

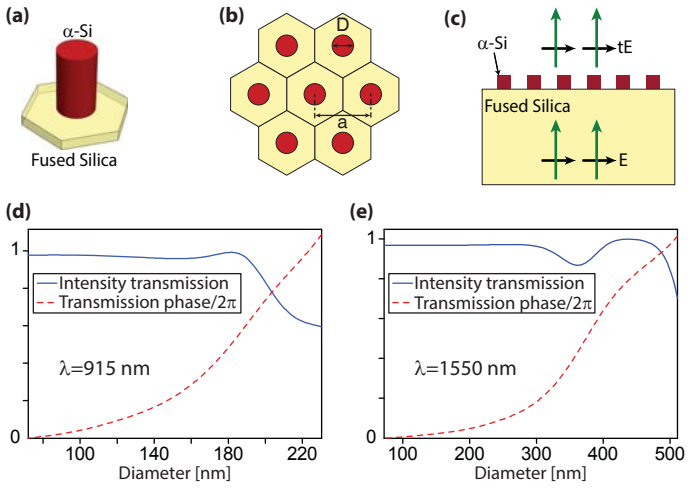

Figure 3.6: **Metasurface structure with simulated amplitude and phase curves.** **(a)** Schematic of an α-Si cylindrical nano-post on a fused silica substrate. **(b)** Top view of the meta-atoms on a hexagonal lattice showing geometrical parameters. **(c)** Schematic of the simulated structure. **(d)** Intensity transmission, and phase of the transmission coefficient at $\lambda = 915$ nm, and **(e)** at $\lambda = 1550$ nm. The lattice constant is 360 nm for $\lambda = 915$ nm, and 720 nm for the $\lambda = 1550$ nm structure. The α-Si layer is 718 nm thick in both cases.

Taking these considerations into account, we find that a post height of 718 nm, lattice constants of 360 nm at $\lambda = 915$ nm, and 720 nm at $\lambda = 1550$ nm, enable full phase coverage with high transmission at both wavelengths. The simulated intensity transmission ($|t|^2$) and transmission phase ($\angle t$) for such uniform lattices are plotted in Figs. 3.6**d** and 3.6**e** at 915 nm and 1550 nm, respectively. For simulations, a uniform array of meta-atoms with a given diameter is illuminated with a plane wave at the wavelength of interest [Fig. 3.6**c**], and the transmission amplitude and phase are calculated. We have used RCWA [217] to perform the simulations.

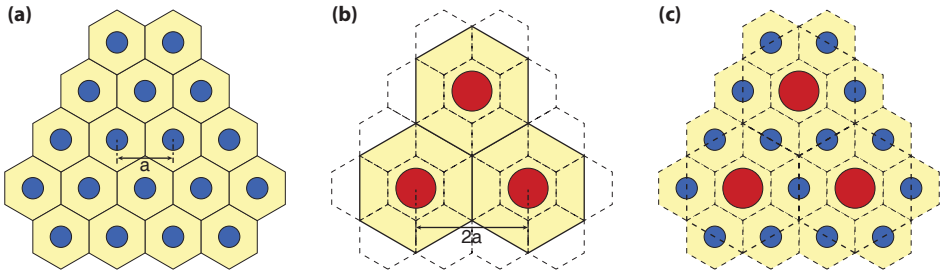

Figure 3.7: **Interleaved lattice schematics.** **(a)** Schematic of the short-wavelength metasurface lattice with a lattice constant of a. **(b)** Schematic of the long-wavelength lattice with a lattice constant of $2a$, overlaid on the unit-cell boundaries of the short-wavelength meta-atoms. **(c)** Schematic of the interleaved lattice resulting from replacing one out of four short-wavelength meta-atoms with a long-wavelength one.

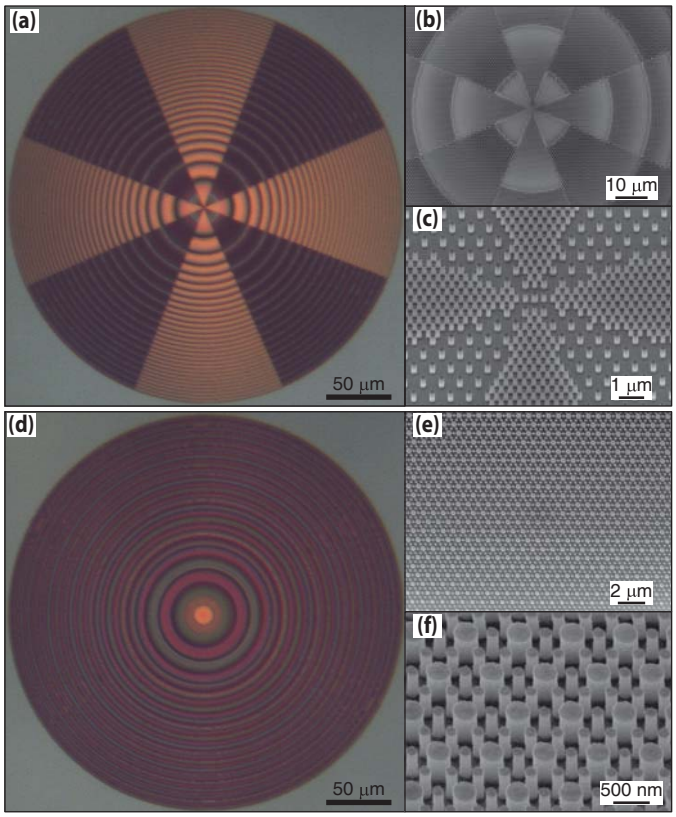

Figure 3.8: **Fabricated device images.** **(a)** Optical and **(b, c)** scanning electron microscope images of the multi-sector lens. **(d)** Optical and **(e, f)** scanning electron microscope images of the interleaved lens.

Experimental results

For experimental demonstration, we have designed and fabricated a multi-sector and an interleaved lens that focus light from single mode fibers at 915 nm and 1550 nm to a focal point 400 μm away from the lens surface without spherical aberrations. The lenses are 300 μm in diameter, and the single mode fiber is placed 600 μm away from the backside of the ~500-μm-thick substrate of the lens (resulting in a focal distance of 286 μm, and a numerical aperture of 0.46, similar to the meta-molecule lens). The multi-sector lens is formed by dividing two single wavelength lenses designed for 915 nm and 1550 nm to 8 radial sectors and combining them similar to Fig. **3.5c**, and the interleaved lens is formed from combining the two single wavelength lenses in the manner shown in Fig. **3.7**. The single wavelength lenses are designed using the metasurface platforms described above. The smallest nano-post diameter is set to 72 nm in all the designs. For the interleaved lens, a minimum gap of ~50 nm is set between the adjacent nano-posts to facilitate their fabrication. This resulted in the maximum nano-post diameters of 200 and 420 nm for the 915 nm and 1550 nm lenses, respectively, thus the highest achievable phase delay was $\sim 1.6\pi$ at each wavelength. The less than 2π phase coverage leads to small wavefront errors and lowers the focusing efficiencies of the lenses. In the design process, the best nano-post for each lattice site was chosen by minimizing the complex transmission error defined as $|exp(i\phi) - t|$, where ϕ is the desired phase at the lattice site and t is the complex transmission coefficient of the nano-posts. Using this design procedure, and assuming that the lenses require a uniform distribution of nano-posts with various phases from 0 to 2π, we find that the incomplete phase coverage achieved here results in a less than 3% reduction in the lens efficiency.

The devices were fabricated by depositing a 718-nm-thick layer of α-Si on a fused silica substrate using the PECVD technique. The device pattern was written on an electron beam resist using EBL, and was transferred to an Al_2O_3 layer using a lift-off process. The Al_2O_3 layer served as a hard mask for etching the α-Si layer in a dry etch process, and was removed in a solution of hydrogen peroxide and ammonium hydroxide. Optical and scanning electron microscope images of both the multi-sector and interleaved devices are shown in Fig. **3.8**.

The lenses were characterized by measuring the intensity distributions in the focal plane, and in many planes parallel to the focal plane using custom built microscopes with $\sim \times 100$ magnification. Schematics of measurement setups are shown in Fig. **3.9**. Measured intensities in axial and focal planes at both wavelengths are plotted in

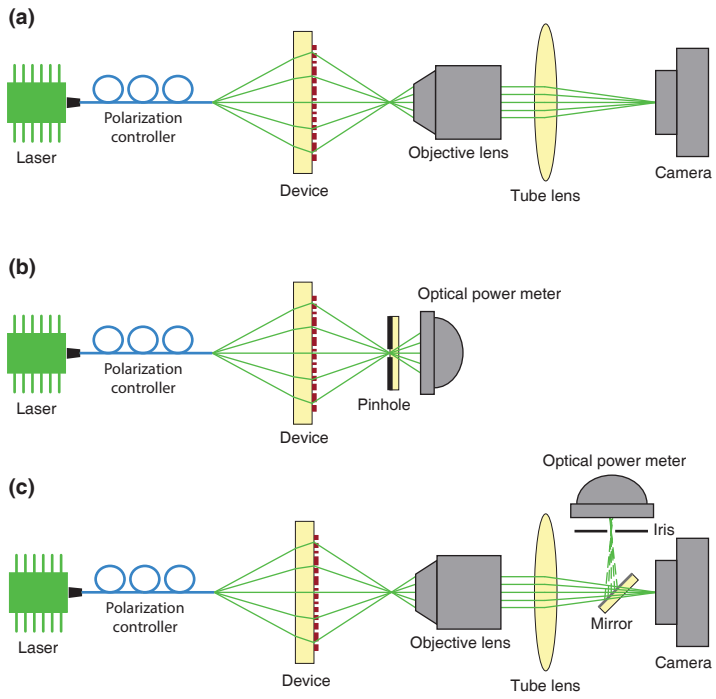

Figure 3.9: **Measurement setup schematics. (a)** Schematics of the measurement setup used for measuring the optical intensity distribution patterns in different planes at 915 nm. **(b)** Schematics of the setup used for measuring the focusing efficiency of the lens at 915 nm. **(c)** Schematics of the setup used for characterizing the devices at 1550 nm. The flip mirror, iris, and optical power meter were used to measure the focusing efficiencies.

Figs. 3.10**a**–3.10**d** for the multi-sector lens and in Figs. 3.10**i**–3.10**l** for the interleaved lens. The polarization of incident light was changed using the polarization controllers shown in Fig. 3.9, and no polarization dependence was observed. Measured axial plane intensities for the multi-sector lens are plotted in Figs. 3.10**a** and 3.10**c**, where a single strong focus is observed at both wavelengths. The intensity distributions in the focal plane are plotted in Figs. 3.10**b** and 3.10**d**, and show features that are caused by the division of the lens aperture into multiple sectors. The high frequency fluctuations observed in the 1550 nm focal plane measurements are caused by the highly non-uniform responsivity of the phosphorous coated CCD used. To achieve smoother intensity distributions in the axial plane, these high frequency fluctuations are filtered through removing all components with spatial frequencies higher than the free space propagation constant. For comparison, a lens designed with the same method and NA, but with all dimensions and distances four times smaller than the fabricated device was simulated using the FDTD method in MEEP [234]. The smaller size of the simulated device was necessary to make the simulations

feasible with the available computational resources. Figures **3.10e**–**3.10h** show the simulated intensities for this device at both wavelengths in the axial and focal planes. The illumination was linearly polarized in simulations, and the symmetry of the structure ensures the same behavior for other incident polarizations. A very good agreement is observed between simulated and measured focal depths and the focal plane intensities. Focusing efficiency is defined as the ratio of the power focused by the device, to the output power of the fiber, and is measured at 915 nm and 1550 nm with setups schematically shown in Figs. **3.9b** and **3.9c**, respectively. The pinhole used at 915 nm has a diameter of 20 μm, and the iris used for 1550 nm is 2 mm in diameter, which translates to a ~20-μm diameter in the object plane. Simulated and measured efficiencies and FWHMs, in addition to the diffraction-limited FWHMs are summarized in Tables 3.1 and 3.2, respectively. The diffraction-limited FWHMs are found via simulation of a perfect phase mask at each wavelength, with the same optical fiber illuminations that are used to design and measure the lenses.

Measurement results for the interleaved lens are plotted in Figs. **3.10i**–**3.10l**. Unlike 1550 nm, at 915 nm a second focus is observed at $z \approx 220$ μm, with the peak intensity approximately 1.8 times, and a power 1.2 times those of the main focus. Similar to the multi-sector lens case, a four times smaller interleaved lens designed using the same platform is simulated for comparison, and the simulated intensities are plotted in Figs. **3.10m**–**3.10p**. A weak second focus is observed around $z \approx 50$ μm in the simulations as well. It is worth noting that these devices are multi-order (similar to multi-order gratings), and have multiple focal points (like a Fresnel zone plate lens). These higher order focal points can be seen in all four axial plane measurements in Figs. **3.10a**, **3.10c**, **3.10i**, and **3.10k**. The higher order focal points have low intensities in all cases except for Fig. **3.10i**. If the "*blazing*" of the lens is perfect (i.e., the phase profile is equal to its ideal case), all of the power will be directed towards the designed focal distance. However, if some error is introduced to the phase profile, a portion of the power will be directed towards higher order focal points. As this error increases, the power in the main focus will decrease. The 1550 nm nano-posts are optically large and support many resonant modes around 915 nm, resulting in some error in the phase of the total transmitted field at 915 nm. Besides, as we will shortly discuss, the coupling between 1550 nm and 915 nm posts is not negligible at 915 nm. These errors result in a significant portion of the power going to the higher order focus at 915 nm for the interleaved lens. Measured and simulated efficiencies and FWHMs are summarized in Tables 3.1 and 3.2, respectively.

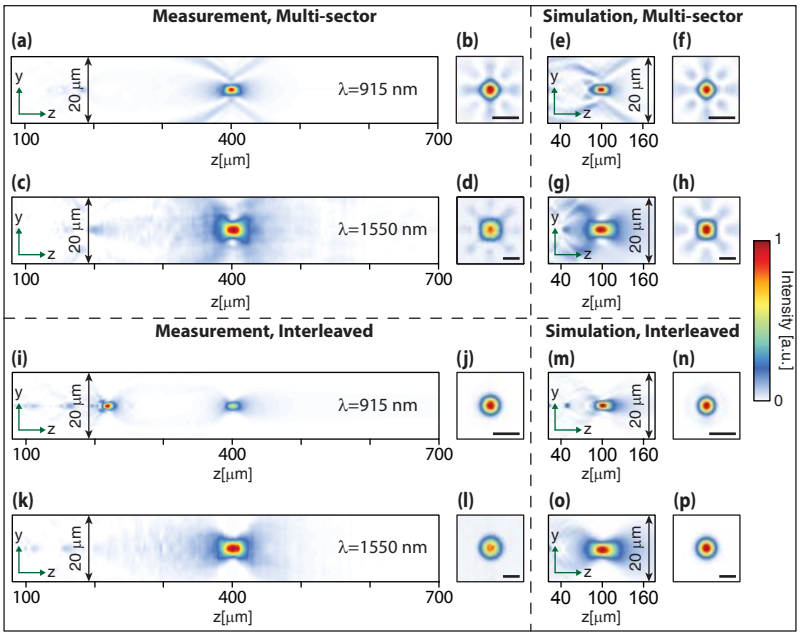

Figure 3.10: **Measured and simulated intensity profiles.** **(a)** Intensity measured in the axial plane and **(b)**, in the focal plane at 915 nm for the multi-sector lens. **(c)** and **(d)** Same measurements as **a** and **b** at 1550 nm. The high frequency intensity fluctuations observed in the measured focal intensity at 1550 nm is caused by the high non-uniformity in the responsivity of pixels in the phosphorous coated CCD used in 1550 nm measurements. This nonphysical fluctuation is filtered for the axial plane plots to acquire a smoother distribution. **(e)–(h)** FDTD simulated intensities for a similar multi-sector lens with a four times smaller size and focal distance. **(i)–(l)** Similar results to **a–d**, but for the interleaved lens. **(m)–(p)** FDTD simulated intensities for a four times smaller interleaved lens. Scale bars: 4 μm.

To determine the origin of the focus observed at $z \approx 220$ μm, we use paraxial imaging equations by considering the fiber tip as an object and the focal plane intensity as its image. We find that the effective object distance from the lens is 1003 μm using the $f_1 = 286$ μm focal distance, and the 400 μm image distance. Therefore, the focal distance corresponding to the focus observed at $z \approx 220$ μm is $f_3 \approx 180$ μm. We represent this focal distance by f_3, because there is also a secondary focal distance $f_2 = 485$ μm arising from the 1550 nm nano-posts, as they also form a lens at 915 nm. The focal distance of the lens formed from 1550 nm nano-posts is given by $f_2 = \frac{1550}{915} \times 286$ μm $= 485$ μm at 915 nm [135]. We note that we have $1/f_3 = 1/f_1 + 1/f_2$. This means that the equivalent transmission mask of the lens contains a term proportional to $\exp\{-i\frac{2\pi}{\lambda}(\frac{1}{f_1} + \frac{1}{f_2})\sqrt{x^2 + y^2}\}$. This term is the result of the addition of two phase profiles generated by the 915-nm and 1550-nm nano-posts, and indicates coupling between these nano-posts (this term cannot exist if

915 nm and 1550 nm posts operate completely independently). Therefore, at 915 nm the coupling between the interleaved nano-posts cannot be completely neglected. For an improved design, this coupling can be taken into account if unit cells formed from combining the two nano-post groups are analyzed together [135].

Table 3.1: Measured and simulated efficiencies for the multi-sector and interleaved lenses

Wavelength	915 nm		1550 nm	
	Measured	Simulated	Measured	Simulated
Multi-sector	37 ±1%	40.6%	30 ±1%	36.8%
Interleaved	10 ±0.5%	27%	58 ±1%	75.8%

Table 3.2: Measured, simulated, and diffraction-limited FWHM focal spot sizes for the multi-sector and interleaved lenses

Wavelength	915 nm		
	Measured	Simulated	Limit
Multi-sector	1.85±0.05 μm	1.7 μm	1.6 μm
Interleaved	1.85±0.05 μm	1.7 μm	1.6 μm
Wavelength	1550 nm		
	Measured	Simulated	Limit
Multi-sector	3.3±0.2 μm	3 μm	2.75 μm
Interleaved	3.3±0.2 μm	3 μm	2.75 μm

Discussion

The efficiency of the interleaved lens at 915 nm is significantly lower than 1550 nm, both in measurements and simulations. Two factors play important roles in this difference between the efficiencies at the two wavelengths. First, the interleaved lens has an effective lattice constant of 720 nm [Fig. **3.7c**], which is close to $a_{\max} = \frac{2}{\sqrt{3}n_g}\lambda = 727$ nm, the lattice constant above which higher diffraction orders will be propagating in the glass substrate at 915 nm (here $n_g = 1.452$ is the refractive index of glass). Therefore, the non-periodicity of the lens structure results in higher order diffractions propagating inside the substrate. In contrast, this lattice constant is subwavelength enough at 1550 nm such that no higher diffraction orders are present. Second, the 915-nm nano-posts are optically small at 1550 nm, whereas the 1550-nm nano-posts are optically large and support many resonances around 915 nm. Therefore, while adding the 915-nm nano-posts to the 1550-nm lens results in a relatively small phase error at 1550 nm, introducing the large 1550-nm nano-posts to the 915-nm lens changes the phase profile significantly, and for some nano-post

diameters it also reduces the transmission amplitude. In addition, the measured efficiency for the interleaved lens at 915 nm (10%) is lower than the simulated value of 27%. The transmission phase of the device at 915 nm is more sensitive to errors in the nano-post diameters because of the larger aspect ratio of the nano-posts, and fabrication errors have degraded the phase profile of the lens and its efficiency by directing a significant portion of power to the higher order focus around 220 μm.

Efficiencies of the multi-sector device at the two wavelengths are closer to each other than the interleaved lens. The sum of simulated efficiencies at 915 nm and 1550 nm for these devices is always less than 100%. The interleaved design, in contrary, can have a sum of efficiencies at 915 nm and 1550 nm that is higher than 100% as evidenced by the simulation results. This is because the high-index nano-posts can have an optical cross-section significantly larger than the geometrical area of the metasurface pixel that they occupy. Besides, the efficiency of the interleaved lens can be increased, and its sensitivity to fabrication errors can be decreased using the meta-molecule concept and a concurrent design of the nano-posts for the two wavelengths [135]. In addition, the division of the aperture to multiple macroscopic sectors changes the shape of the input aperture of the lens and thus the shape of its focal spot. The interleaved design on the other hand, does not cause this issue.

The demonstrated multiwavelength lenses can be used in applications where simultaneous operation at a few discrete wavelengths is required, such as two photon fluorescence microscopy. While conventional refractive achromatic lenses could have a better performance (specifically a higher efficiency) in such applications, they are bulky, more expensive to fabricate, and harder to customize. Besides, multiple metasurfaces can be monolithically integrated in order to correct various aberrations, add functionalities, or be directly integrated with electronics to form compact electro-optical systems [139]. Nevertheless, multiwavelength lenses are demonstrated here only as a proof of concept example for the general method of spatial multiplexing of metasurfaces for implementing multiwavelength multifunctional optical devices. The introduced methods can be directly applied to designing metasurfaces with different functionalities at different wavelengths. For instance, a metasurface can be designed to operate as a lens at one wavelength, and as a grating at the other one. It can also be applied to making metasurfaces that perform multiple functions simultaneously at a single wavelength. It would be very challenging, if at all possible, to fabricate such devices with the conventional refractive optics platform.

We have shown that by spatially multiplexing metasurface lenses that are designed

for operation at two different wavelengths, we can realize lenses that simultaneously operate at both wavelengths. We designed, fabricated, and characterized DW-MLs based on macroscopic aperture division (i.e., the multi-sector lens), and meta-atom interleaving. Although here we used this concept to demonstrate double-wavelength lenses, the idea can be readily generalized to devices with more operation wavelengths, or devices that perform different functions at different wavelengths, or even at the same wavelength. Therefore, spatial multiplexing introduces a simple route towards multiwavelength and multi-functional metasurfaces.

3.5 Double-wavelength metasurface lens based on structurally birefringent nano-posts

Concept and design

In this section we demonstrate DW-MLs that focus two wavelengths of light with perpendicular linear polarizations to the same focal distance, as schematically shown in Fig. **3.11b** (e.g., the x-polarized light at a wavelength λ_1 and y-polarized light at a different wavelength λ_2 are focused to the same distance). We experimentally demonstrate lenses with large NAs values up to 0.7 and high efficiencies at both wavelengths ($\eta \sim 65\% - 92\%$) with nearly diffraction-limited operation. In the next section, we demonstrate how a similar DW-ML can be used as an objective lens for TPM. In addition to lenses, this concept can be applied to other metasurfaces to independently control the wavefronts at two different wavelengths for orthogonal polarizations, and provide different functionalities at those wavelengths.

We have previously shown that metasurfaces based on α-Si nano-posts with elliptical cross sections [Fig. **3.11**(c)] can independently control the phases of two orthogonal polarizations at a single wavelength in 2 [14]. These metasurfaces are composed of nano-posts placed at the vertices of a uniform lattice like the one shown in Fig. **3.11**(d). For proper choices of the lattice constant ($\sim 0.5\lambda$) and the height of the nano-posts ($\sim 0.6\lambda$), the phase of light for two linear polarizations oriented along the nano-post axes can be controlled independently by changing the ellipse diameters [14]. We have also demonstrated broadband operation of non-deflecting metasurfaces (e.g., spatially varying wave plates) composed of elliptical nano-posts [132], but the approach is not applicable to the metasurfaces operating based on light deflection (e.g., lenses). In this section, we show that the two control parameters (i.e., the axis lengths) of nano-posts with elliptical cross-sections can be utilized to independently control the wavefronts of optical waves with two different wavelengths and orthogonal

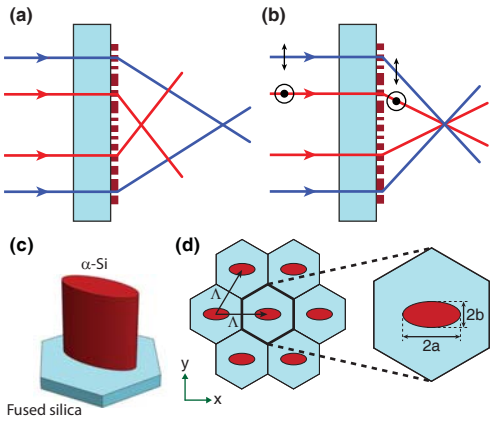

Figure 3.11: **DW-ML concept based on birefringent nano-posts. (a)** Normal chromatic dispersion of a metasurface lens, resulting in different focal distances for different wavelengths (schematically shown by red and blue rays), and **(b)** schematics of a metasurface corrected to focus light with two different wavelengths and orthogonal linear polarizations to the same focal distance. **(c)** An α-Si nano-post with elliptical cross-section exhibiting birefringence. **(d)** A metasurface formed by arraying elliptical nano-posts in a periodic lattice.

polarizations. For instance, the phase profile of the device can be independently controlled for x-polarized light at a wavelength λ_1, and for y-polarized light at a different wavelength λ_2. The behavior of the device for cross polarized light (e.g., y-polarized light at λ_1) will be governed through the regular chromatic dispersion of diffractive devices (see for instance [135, 219]).

Figures **3.12a** and **3.12b** show simulated transmission amplitude (top) and phase (bottom) at 915 nm and 780 nm for x and y-polarized light, respectively (ellipse diameters $2a$ and $2b$, and the axis directions are shown in Fig. **3.11d**). Here, the meta-atoms are assumed to be 553 nm tall, the lattice constant is 500 nm, and the wavelengths are chosen to match available laser sources in our lab. The RCWA was used for the simulations [217]. The nano-posts operate as truncated multimode optical waveguides with multiple resonances around the operation wavelengths [67, 77, 125]. The ellipticity, results in an effective birefringence and a phase difference for light polarized along the two axes of the ellipse [14]. Therefore, the two ellipse diameters provide two phase control parameters that enable independent control of phase for light polarized along the two axes [14]. Figure **3.12** shows that the independent phase control is possible even if the two orthogonal polarizations of light have different wavelengths. Using the simulated transmission amplitude and phase data, we find the corresponding ellipse diameters that provide any desired phase

pairs at both wavelengths, ϕ_1 and ϕ_2, while keeping both transmission amplitudes high. To simultaneously achieve the desired phases and high transmission amplitudes at both wavelengths, we minimize the total complex amplitude error defined as $\epsilon = |\exp(i\phi_1) - t_1|^2 + |\exp(i\phi_2) - t_2|^2$. Here ϕ_1 and ϕ_2 are the desired phases at the two wavelengths, and t_1 and t_2 are complex transmissions of nano-posts at the two wavelengths for the corresponding orthogonal linear polarizations. The corresponding values of the chosen diameters are plotted in Fig. **3.12c** as functions of the phases at the two wavelengths. As Fig. **3.12c** shows, the axis length $2a$ dominantly controls the phase of x-polarized light, and the phase of y-polarized light is mostly controlled by the axis length $2b$. Amplitudes and phases of these chosen nano-posts are plotted in Figs. **3.12d** and **3.12e**, showing that this independent phase control is achieved with very high accuracy and high transmission. Using this independent control, any two arbitrary phase profiles for orthogonal linearly polarized light at the two wavelengths can be realized.

Experimental results

We designed, fabricated, and characterized five lenses with the same diameter of 200 μm and NAs ranging from 0.12 to 0.7 that simultaneously work at 915 nm and 780 nm, for x and y-polarized light, respectively. The fabrication process was similar to [14]: a 553-nm α-Si layer was deposited on a fused silica substrate using PECVD. The metasurface pattern was generated with an EBL system. A ~70-nm Al_2O_3 layer was deposited using electron beam evaporation, and was lifted off, leaving a hard mask defining the nano-posts. The hard mask was used to etch the α-Si layer in a dry etching step, and was then removed. SEM images of the fabricated devices are shown in Fig. **3.13**.

Figure **3.14** shows schematics of the measurement setups used to characterize the devices. A custom built microscope with a $\sim \times 100$ magnification, shown schematically in Fig. **3.14a**, was used to perform the intensity distribution measurements. Figure **3.15** summarizes the measurement results for the five lenses. Axial and focal plane intensities are plotted in Figs. **3.15a** and **3.15b** for 780 nm and 915 nm, respectively. At both wavelengths and for all lenses, one single focus is observed close to the designed distances of 100, 200, 400, 600, and 800 μm. As denoted by Fig. **3.15c**, all lenses have a nearly diffraction-limited focus (measured FWHMs at both wavelengths and for all NA values are less than 7% larger than their diffraction-limited values). The measured FWHMs in the axial plane are plotted in Fig. **3.15d**, along with the theoretical values calculated from $2\pi w^2/\lambda$, with w denoting the diffraction-limited

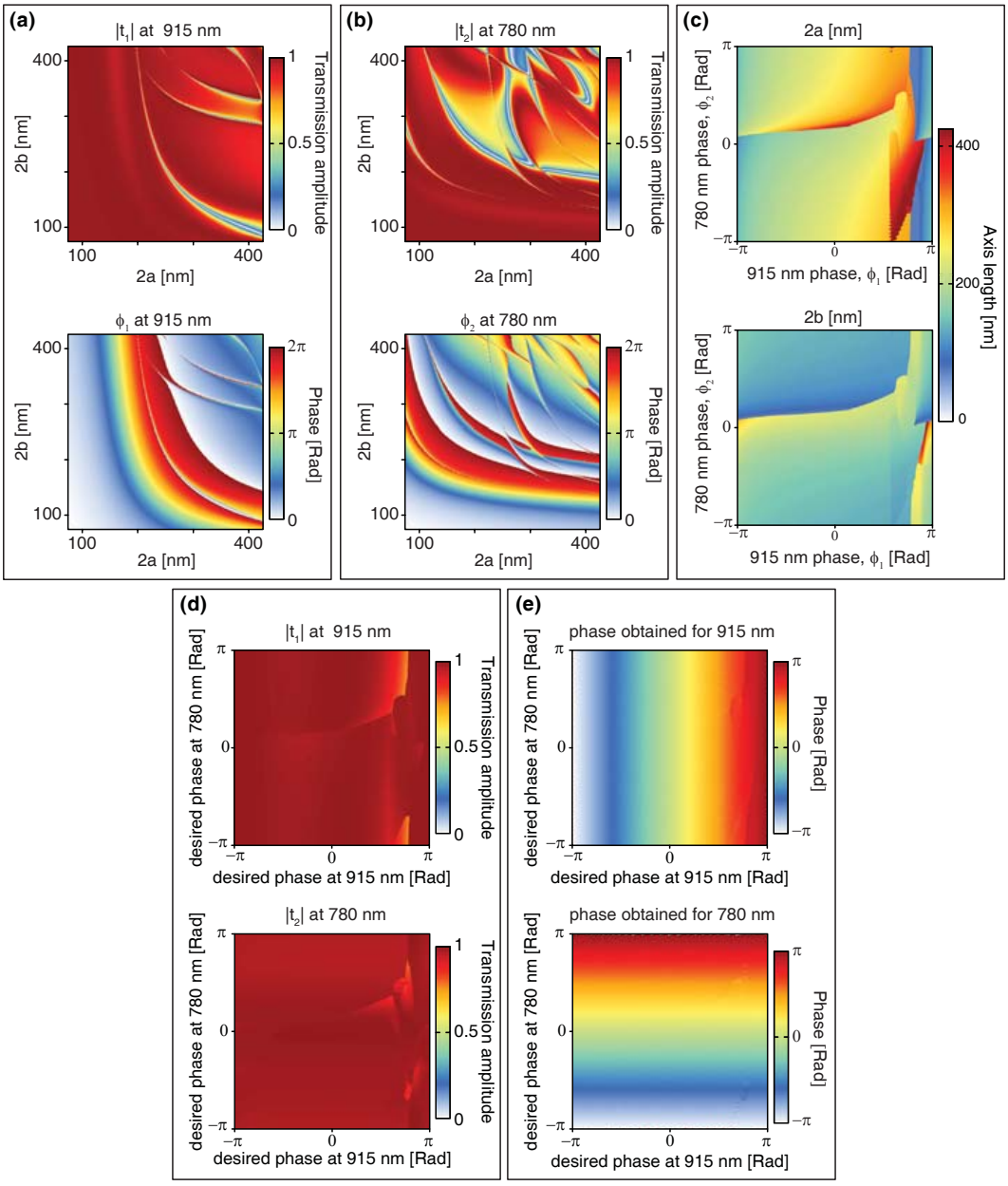

Figure 3.12: **DW-ML simulation and design graphs. (a)** Transmission amplitude (top) and phase (bottom) of the meatasurface at 915 nm for *x*-polarized light versus ellipse diameters. **(b)** The same plots as **a**, but for *y*-polarized light at 780 nm. **(c)** Optimal values of diameters $2a$ and $2b$ that provide phase pairs (ϕ_1, ϕ_2) for complete phase coverage at the two wavelengths. **(d)** Transmission amplitude, and **(e)** phase at both wavelengths for the corresponding optimal diameters shown in **c**.

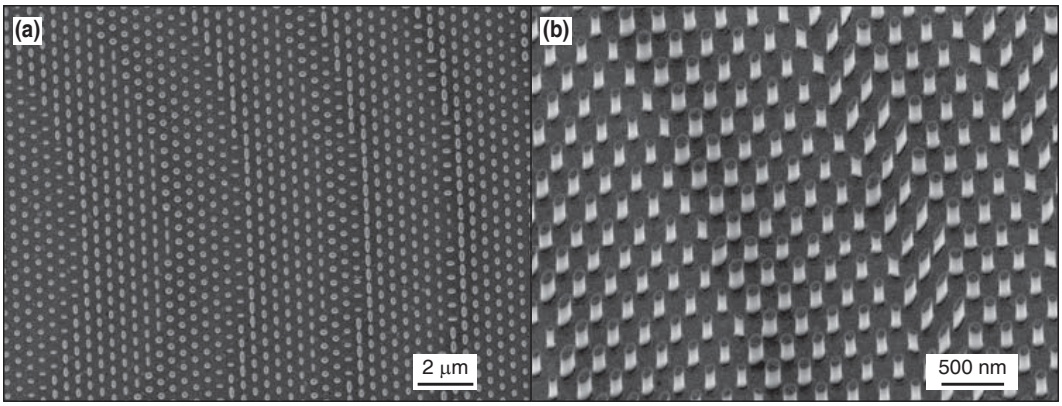

Figure 3.13: **SEM images of fabricated DW-MLs. (a)** Scanning electron micrograph of a fabricated device viewed normally, and **(b)** at a tilt angle.

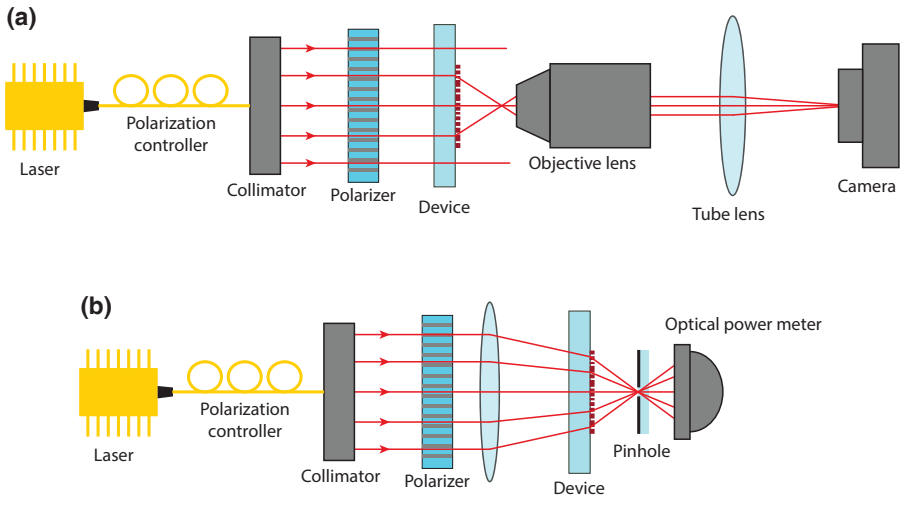

Figure 3.14: **Measurement setup schematics. (a)** Schematic of the measurement setup used for measuring intensity profiles, and **(b)** focusing efficiencies.

transverse FWHM. Efficiency was defined as the measured power in focus, divided by the total power incident on the lens. The setup used to measure the efficiencies is schematically shown in Fig. 3.14**b**. Since the diameter of the collimated beam (~2.3 mm, using the $1/e^2$ intensity definition) is much larger than the size of the metasurface lenses, for efficiency measurements the beam was partially focused using a lens with a focal distance of 200 mm to have a diameter of ~134 μm at the metasurface lenses (such that 99% of the beam power passes through the lens aperture). The radius of curvature of the beam at the metasurfaces is ~16 mm, which is much larger than the focal distances of the metasurface lenses, making the curvature of the beam almost negligible. The measured efficiencies are plotted in

Fig. 3.15**e** for both wavelengths, and are seen to be above 65% for all NAs at both wavelengths. Similar to our previous works [67], efficiency generally decreases with increasing NA. A set of fabricated pinholes were used to filter out-of-focus light for efficiency measurements. Diameters of the used pinholes were 6, 6, 10, 15, and 20 μm for different lenses in decreasing NA order. We attribute the lower efficiency at 780 nm to higher sensitivity of its phase to fabrication errors.

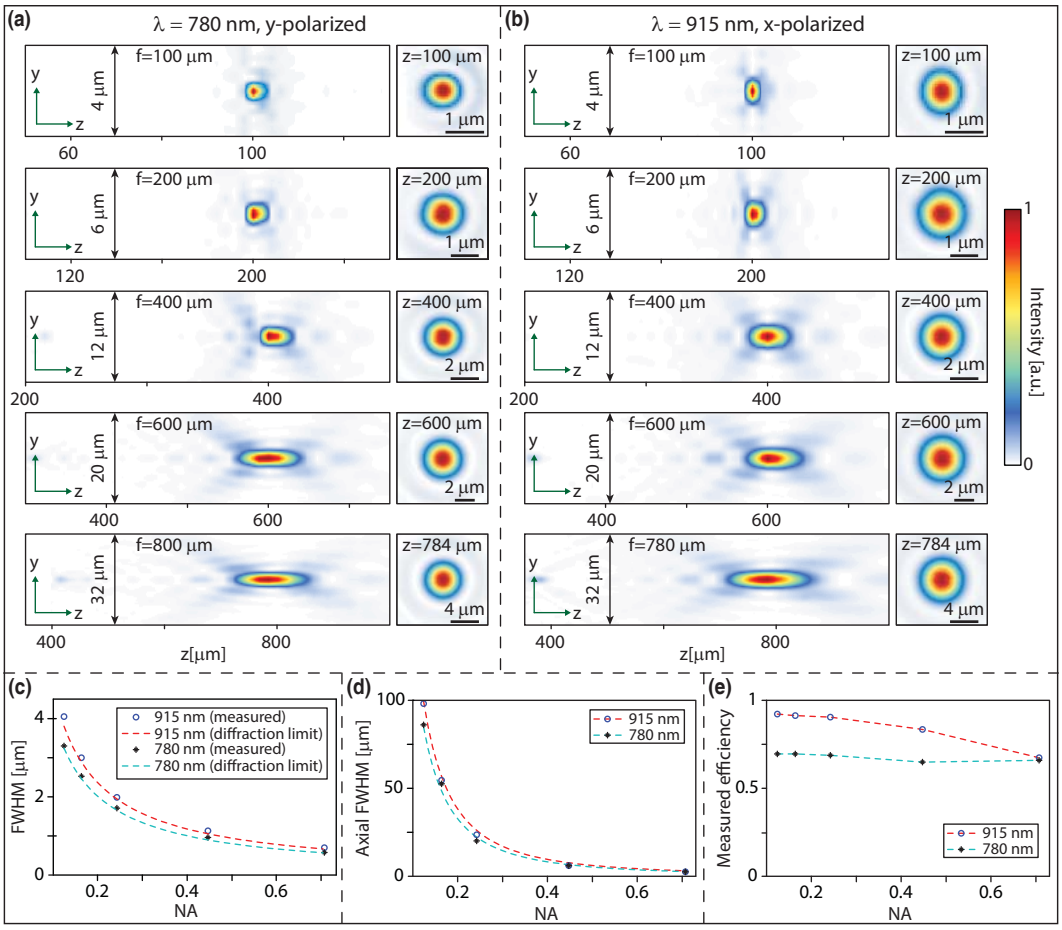

Figure 3.15: **Co-polarized measurement results of the DW-ML. (a)** Measured axial (left) and focal (right) plane intensities for *y*-polarized light at 780 nm. Results are in increasing focal distance order from top to bottom. **(b)** Same measurement results as in **a** for *x*-polarized light at 915 nm. **(c)** Measured FWHMs in the focal plane versus NA. The corresponding theoretical diffraction limits at both wavelengths are denoted via dashed lines. **(d)** Measured axial plane FWHMs along with their corresponding theoretical values. **(e)** Measured efficiencies of the metasurface lenses at both wavelengths. Dashed lines show eye-guides.

We have also characterized the operation of the devices under illumination with

cross-polarized light (i.e., y-polarized light at 915 nm, and x-polarized light at 780 nm). In cross-polarized operation, the devices also exhibit Fresnel phase zones but these zones are not optimized for focusing to a tight spot. Indeed, the cross-polarization measurement results summarized in Fig. **3.16** show that the devices focus cross-polarized light as well, but with lower efficiency, higher distortions, and to focal distances different from the corresponding co-polarized values. It is worth noting that these devices operate as diffractive lenses with different phase profiles for x- and y-polarized light. Also, for each polarization they follow the regular chromatic dispersion of diffractive lenses, and therefore their focal distance changes with wavelength proportional to $1/\lambda$ [23, 135, 219]. Since cross-polarized light is focused to a different focal distance, it can be considered as loss when the device focuses unpolarized light. When the devices are used for imaging applications, the excitation and the collected paths need to be passed through polarizers. Otherwise, the image will exhibit elevated background and/or imaging artifacts depending on the exact lens design.

Discussion

The high-NA and high efficiency, in addition to the fact that the working wavelengths can be arbitrarily close, make this platform attractive for single and multi-photon fluorescence microscopy where the two working wavelengths (i.e., the excitation and emission wavelengths of the fluorophores) are not very far [237]. In addition, these lenses can be used for light collection in cases where the sample is tagged with two different fluorophores with close emission spectra. It should be noted, however, that the efficiencies of the lenses will be 50% lower for unpolarized light, as the cross-polarized light will be focused to a different focal distance than the co-polarized light [Figs. **3.15** and **3.16**]. Besides, the lenses discussed here are aspherical and suffer from aberrations for off-axis imaging and focusing. This problem can be solved by designing lens doublets that are corrected for the off-axis monochromatic aberrations [139].

The maximum distance between the two operating wavelengths of the proposed metasurface platform is limited by practical considerations. The nano-posts height should be large enough to provide the required 2π phase at the longer wavelength. This results in higher sensitivity of the phases of nano-posts at the shorter wavelength to fabrication errors, which in turn decreases device efficiency at that wavelength. This lower efficiency at the shorter wavelength is already observed in this work. Thus, the maximum wavelength distance is limited mostly by practical considerations and

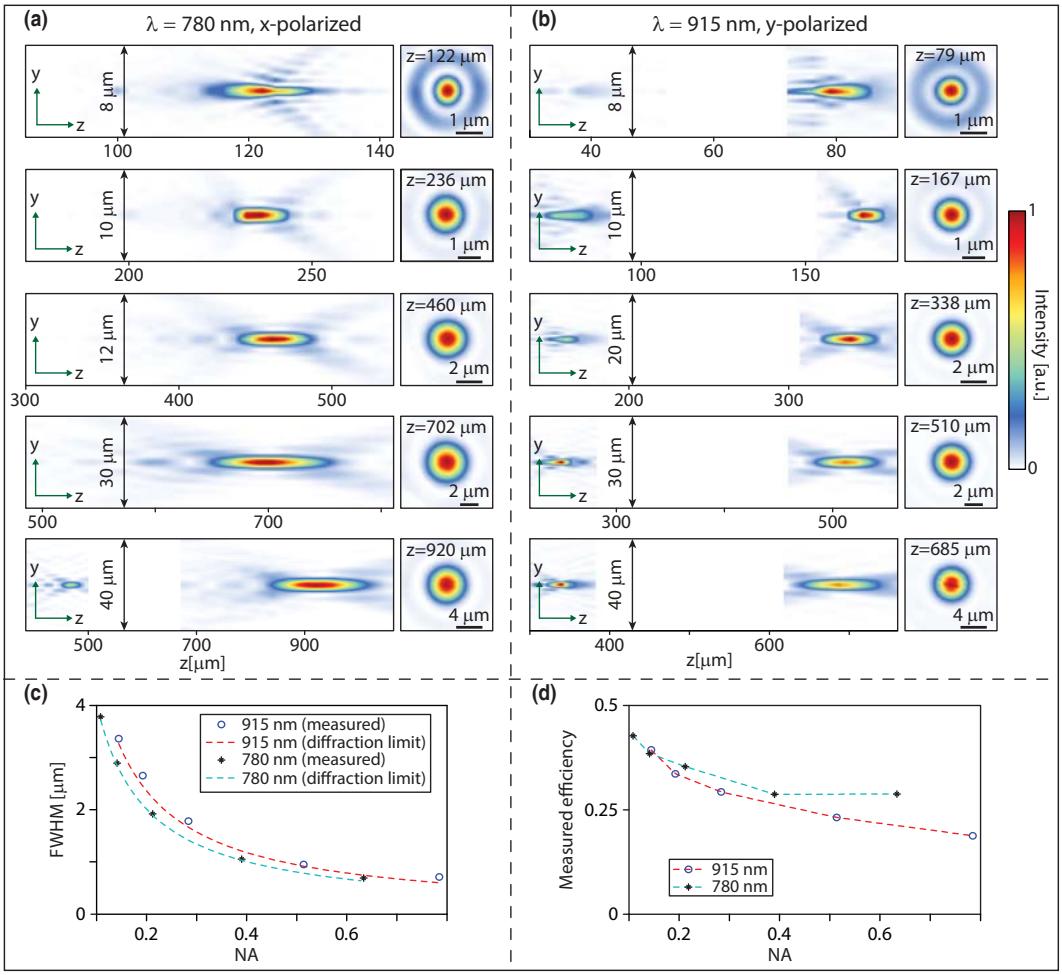

Figure 3.16: **Measurement results under illumination with cross-polarized light. (a)** Measured axial (left) and focal (right) plane intensities for *x*-polarized light at 780 nm. Results are in increasing co-polarized focal distance order from top to bottom. We have verified that no other points of comparable intensity are present in areas not shown in the axial measurements. **(b)** Same measurement results as in **a** for *y*-polarized light at 915 nm. **(c)** Measured FWHMs in the focal plane (focal distances labeled in **a** and **b**) versus NA. The corresponding theoretical diffraction limits at both wavelengths are denoted via dashed lines. **(d)** Measured efficiencies of the metasurface lenses at both wavelengths for cross-polarized light. Dashed lines show eye-guides.

the achievable fabrication tolerances.

In conclusion, birefringent elliptical nano-posts can be used to independently control optical wavefronts at two different wavelengths with orthogonal linear polarizations. This control can be utilized to generate any desired wavefronts at both wavelengths, resulting in an optical behavior at each wavelength independent from the other one. Using these meta-atoms, we demonstrated double-wavelength metasurface lenses that focus x and y-polarized light at 915 and 780 nm, respectively, to the same focal distance. Lenses with NA values up to 0.7 were experimentally demonstrated to have nearly diffraction-limited operation and efficiencies above 65%. This method can also be combined with the demonstrated meta-molecule concept [135] to achieve more phase control parameters, and chromatically corrected lenses at four or more wavelengths.

3.6 Two-photon microscopy with a double-wavelength metasurface objective lens

TPM is widely used for deep tissue imaging in various areas of life sciences [238–241]. The method utilizes the lower scattering of near-IR light inside tissues, the higher transverse and lateral resolution, and the lower level of background fluorescence in two-photon excitation to form high-quality images hundreds of microns deep inside tissues [240, 241]. Development of compact low-weight TPMs for *in vivo* imaging of brain activity has been of great interest in recent years [242–247]. For compactness and low-weight, most of these systems use graded index objective lenses with optical qualities inferior to the conventional refractive objectives.

Dielectric metasurfaces enable high-end optical elements with high efficiencies, and with a thin and light-weight form factor. Metasurface devices integrated in thin layers [36, 248] and on membranes [140] have milligram and microgram weights. Therefore, the weight of optics will not be a significant factor in the total weight of systems that employ metasurface optics. In addition, because of their novel capabilities [14, 15, 125, 210, 249–253] and manufacturability with conventional nano-fabrication techniques, metasurfaces have attracted a great deal of attention in the past few years, especially for imaging applications [71, 139, 254]. Fluorescence microscopy is an especially suitable area for meta-lenses as the fluorescence bandwidth is usually limited and predetermined. Despite this, meta-lenses have not previously been employed for single- or multi-photon fluorescence

microscopy. The reason lies in the fact that they are conventionally designed for a single operation wavelength, while in fluorescence microscopy the focal positions at the excitation and emission wavelengths can be far apart due to the chromatic dispersion [23, 119, 219, 232]. This can significantly reduce the excitation–collection efficiency in the system.

Here we propose and experimentally demonstrate TPM with a DW-ML working as the objective lens. We use a birefringent dichroic dielectric metasurface platform to make the DW-ML that is designed to have the same focal distance at the excitation and emission wavelengths, similar in concept to the DW-MLs discussed in previous chapter. We show that the DW-ML forms images that are qualitatively comparable to those taken with a refractive objective.

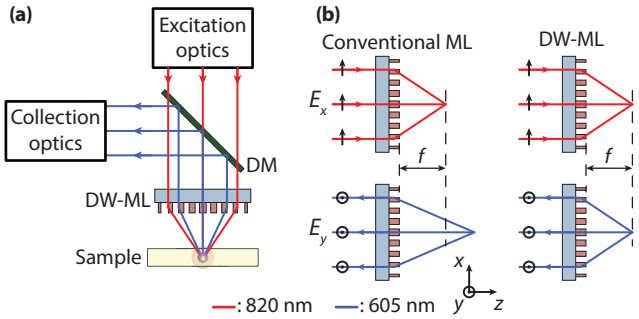

Figure 3.17: **Schematic illustration of TPM with a metasurface objective lens.** **(a)** Schematic of a TPM employing a metasurface objective lens. A pulsed laser source is focused inside a sample using the excitation optics and a metasurface objective. The same metasurface lens along with the collection optics collects the light that is emitted by the sample through a two-photon fluorescence process. DM: Dichroic mirror. **(b)** Schematic illustration of a conventional metasurface lens focusing light with different wavelengths to distinct focal lengths, and the DW-ML designed to focus 820-nm *x*-polarized light and 605-nm *y*-polarized light to the same focal distance of f.

A simplified schematic of a TPM employing the DW-ML is shown in Fig. 3.17**a**. "Long-wavelength" light from a high–peak power pulsed laser is collimated using the excitation optics, passes through a dichroic mirror and is focused inside the fluorescent sample using the DW-ML. At the focal point inside the fluorescent sample, "short-wavelength" photons are emitted upon the absorption of pairs of the long-wavelength photons. The DW-ML collimates the emitted fluorescent light which is then reflected off the dichroic mirror and detected by a photodetector through the collection optics. The DW-ML should be designed to focus both the excitation and emission wavelengths to the same distance. To achieve this goal, we use the

birefringent dichroic meta-atom technique discussed in the previous section. This is schematically shown in Fig. **3.17b**, where the DW-ML focuses horizontally polarized light at the long wavelength, and vertically polarized light at the short wavelength to the same focal distance, f.

Considering the available pulsed laser, the TPM setup, and the fluorescent molecules used, we chose the operation wavelengths to be 820 nm for excitation and 605 nm for emission (see Appendix 3.3 and Fig. **3.A4** for specifics of the measurements and the TPM setup). To implement the DW-ML, we used p-Si because it has a high-index and a low loss at the chosen operation wavelengths. The metasurface is composed of p-Si nano-posts with a rectangular cross section, located at the vertices of a square lattice on a fused silica substrate. As schematically shown in Fig. **3.18a**, the structure is covered by an SU-8 polymer capping layer which provides mechanical robustness and protects the metasurface. The asymmetric structure of the nano-posts generates structural birefringence, resulting in different transmission phases and amplitudes for x- and y-polarized light [14]. For proper choices of the nano-post height and the lattice constant, the two phases along the two meta-atom axes can be controlled fully and independently. As we have previously shown, the same holds true if the two orthogonal polarizations have similar [14] or different [137] wavelengths. To provide the full 2π phase coverage at both wavelengths, the nano-post height was chosen to be 407 nm, and the lattice constant was set to 310 nm. The transmission amplitude and phase at both wavelengths are plotted in Fig. **3.A5** as a function of the widths of the nano-posts, w_x and w_y. Using this data, we have found the post sizes that minimize the weighted complex transmission errors for the two wavelengths (see Appendix 3.3 for more details). The chosen values for w_x and w_y are plotted in Figs. **3.18b** and **3.18c** versus the required phases at 820 nm and 605 nm.

Using the data in Figs. **3.18b** and **3.18c**, we designed the DW-ML with a diameter of 1.6 mm, and an NA of 0.5 (with a focal distance f ~1.386 mm at 820 nm and 605 nm wavelengths). The 0.5 NA value is chosen to match that of the conventional objective lens used in the TPM measurements. The lens is designed to focus light at both wavelengths to a tight spot without spherical aberrations. Fig. **3.19a** shows an SEM image of a part of the fabricated DW-ML, before capping with the SU-8 layer. An optical image of the finished device is shown in the inset of Fig. **3.19a**.

To characterize the DW-ML we used a measurement setup and procedure similar to the ones used in our previous report [137]. The lens was illuminated by a collimated laser beam, and the optical intensity distribution was captured in several planes parallel

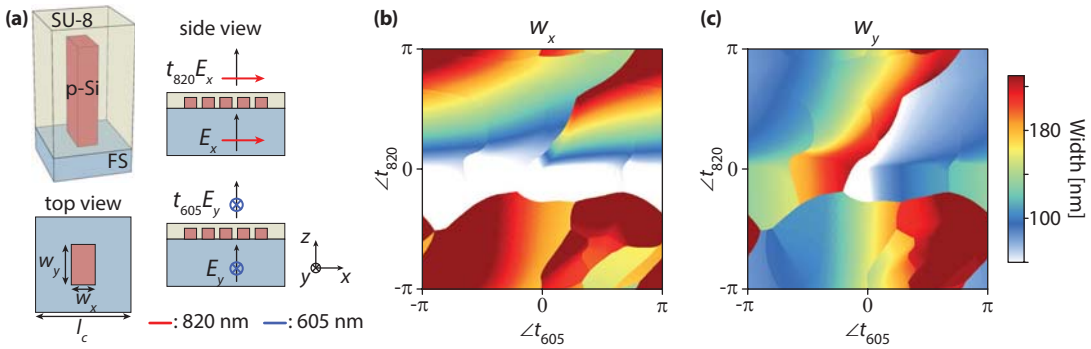

Figure 3.18: **Meta-atom design for TPM. (a)** Schematic illustration of the meta-atom, consisting of a polycrystalline silicon (p-Si) nano-post with a rectangular cross-section sitting on a fused silica substrate and covered by an SU-8 layer. Top and side views of the nano-posts showing the dimensions and illumination conditions. Tuning the nano-post dimensions, w_x and w_y, allows for independent control of transmission phase of *x*-polarized light at 820 nm and *y*-polarized light at 605 nm. **(b)** The chosen values of w_x and **(c)** w_y versus the required phases for the two wavelengths. The nano-posts height is 407 nm and the lattice constant is 310 nm.

to the focal plane using a custom-built microscope (for details of the measurement procedure and setup see Appendix 3.3 and Fig. **3.A6**). For characterization at the two wavelengths of interest we used two different light sources. An 822-nm laser diode was used as the excitation close to 820 nm, and a supercontinuum laser with a bandpass filter centered at 600 nm and a 10-nm FWHM was used for the measurements close to 605 nm. The measured intensity distributions in the axial and focal planes are shown in Fig. **3.19b** and **3.19c** for the long and short wavelengths, respectively. The measured FWHMs in the focal plane are ~0.93 μm and ~0.68 μm at 822 nm and 600 nm. They are both close to their corresponding diffraction-limited values of 0.85 μm and 0.62 μm. The DW-ML shows similar focal lengths at both wavelengths, with maximum intensities in the 1376 μm and 1380 μm planes at 822 nm and 600 nm, respectively. These values are close to the designed focal distance of ~1386 μm. The long depth of focus and the elevated background in Fig. **3.19c** (for the 600-nm case) are caused by the considerable bandwidth of the source, and the diffractive chromatic dispersion of the metasurface lens [119, 255]. Resulting from this chromatic dispersion, the difference between the focal distance at the side wavelengths of 595 nm and 605 nm (corresponding to the measurement bandwidth) is about 20 μm. This causes a significant portion of the total light power to be out of focus in each plane around the focal distance.

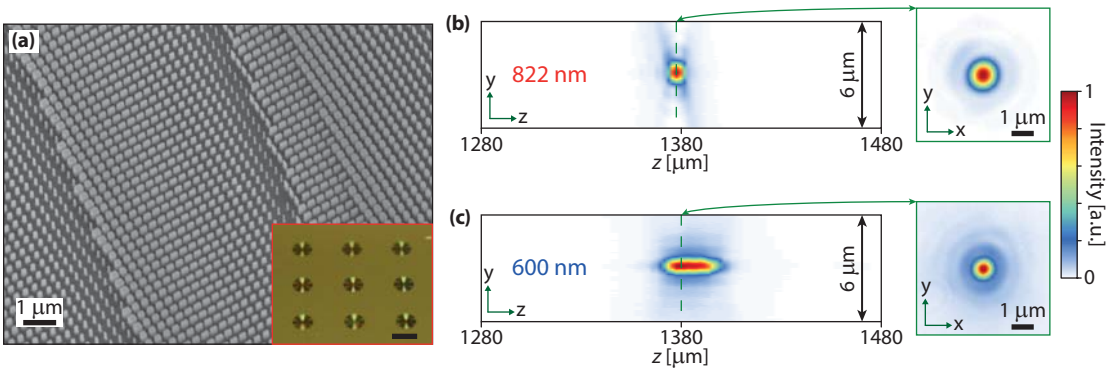

Figure 3.19: **Characterization of the metasurface lens.** **(a)** SEM image of a portion of the fabricated DW-ML. Inset: Optical image of a few fabricated lenses. Scale bar: 2 mm. **(b)** Measured light intensity in the axial (left) and focal (right) planes for *x*-polarized 822-nm illumination. **(c)** Same results as **b** for a *y*-polarized light source with a center wavelength of 600 nm and FWHM of approximately 10 nm.

To measure the focusing efficiency, we used the setup shown in Fig. **3.A6b**. To block the out-of-focus light, irises with ~1.1 mm and ~0.55 mm diameters (for 822 nm and 600 nm wavelengths, respectively) were placed in front of the photodetector in the image plane of the microscope. These correspond to 10-µm and 5-µm diameter apertures in the focal plane of the DW-ML, respectively. The focusing efficiencies, defined as the ratio of the power passing through the irises to the total incident power, were measured to be 61% and 27% at 822 nm and 600 nm, respectively. We should mention here that the 10-nm bandwidth of the 600-nm measurement source resulted in the reduced measured efficiency through the enhanced depth of focus. The measured 27% "broadband" efficiency would correspond to a single-wavelength efficiency of ~45% around 600 nm (see Appendix 3.3 for discussion and simulation results of the efficiency).

Finally, we characterized the operation of the DW-ML by using it as the objective in a TPM for imaging a fluorophore-coated polyethylene microsphere ~90 µm in diameter (see Appendix 3.3 and Fig. **3.A4** for the microscope setup and details). **3.20**a shows a regular image of the microsphere captured with the conventional objective. The two-photon fluorescent images captured by the DW-ML and the conventional objective are shown in Figs. **3.20b** and **3.20c**, respectively.

The two images are qualitatively similar and almost all fluorescent clusters visible in Fig. **3.20c** can also be seen in Fig. **3.20b**. The exact focal planes in the two setups might be slightly different, and this may account for some of the discrepancies

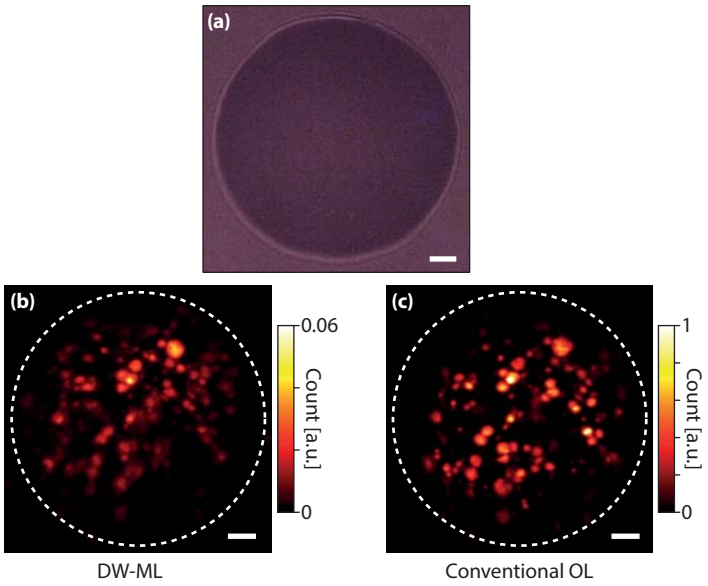

Figure 3.20: **TPM with the DW-ML. (a)** Regular microscope image of a fluorescent polyethylene microsphere. **(b)** Two-photon fluorescent microscope image of the microsphere in **a** captured using the DW-ML, and **(c)** captured using a conventional refractive objective. Scale bars: 10 μm.

between the two images. In addition, there are some important differences that are innate to the use of the DW-ML. The collected photon count is about 15× lower for the DW-ML (the colormaps in Figs. **3.20b** and **3.20c** are in the same unit), while the excitation beam power for the DW-ML was ~4.7× larger than for the conventional objective. A few factors contribute to the effectively lower efficiency of the DW-ML for the combined excitation–collection process. First, the excitation efficiency is lower because of the lower focusing efficiency of the DW-ML at 820 nm (~61%). The collection efficiency is also limited by the 45% focusing efficiency close to 605 nm. For the unpolarized light emitted by the fluorophores, the collection efficiency is reduced to half of this value (~22.5%). In addition, the chromatic dispersion of the DW-ML results in lower peak intensity in focus, which further reduces the two-photon fluorescence rate (see Appendix 3.3). Finally, the broad emission bandwidth of the fluorescence emission and the chromatic dispersion result in a lower collection efficiency, arising from the emitting molecule being out-of-focus because it has a wavelength other than 605 nm.

As discussed above, a few different factors determine the efficiency of TPM with the DW-ML. The single-wavelength focusing efficiencies at the excitation and emission spectra limit the collected power. As previously demonstrated [137], using a high-

index material with lower loss that has a larger index contrast with the capping layer results in higher focusing efficiencies. Moreover, employing more advanced optimization and design methods [256] can help realize higher focusing efficiencies. The diffractive chromatic dispersion of the DW-ML is another factor that decreases both the peak excitation intensity and the collection efficiency. We should note that the absolute value of chromatic dispersion (that is the absolute change in the focal distance for a given change in the operation wavelength) is linearly proportional to the focal distance. Therefore, a metasurface lens with the same NA but shorter focal distance has a wider operation bandwidth [139]. Moreover, the resolution and the collection efficiency only depend on the numerical aperture, not the absolute physical aperture size or the focal distance. Therefore, metasurface lenses are more suited for two-photon applications with shorter focal distances and smaller apertures (keeping the NA constant). Such characteristics are very attractive for miniaturized TPMs [242–247]. Moreover, the ability to independently control the function of the DW-ML at the two operation wavelengths allows for integration of the lens and the dichroic mirror in the same device. One method of implementing this is through separating the excitation and collection paths by designing the lens to collimate the emitted light in an off-axis direction. This can further reduce the total weight, size, complexity, and cost of the TPM.

The DW-ML can be tuned using various techniques [36, 140, 248, 257] to enable axial scanning for fast three-dimensional scanning. In addition, the singlet DW-ML has large off-axis geometric aberrations that limit its field of view significantly. To mitigate this problem, the corrected metasurface doublet scheme can be employed [139, 169].

Most fluorophores have higher emission efficiency if the two-photon excitation wavelength is slightly shorter than twice their emission spectrum peak. However, it is very challenging to design high efficiency DW-MLs where the two wavelengths are far apart using the birefringent meta-atoms utilized here. In such cases the meta-molecule method [135], the spatial multiplexing technique [136, 181, 258], or the topological optimization method [256] might be more promising.

In conclusion, we used the birefringent dichroic dielectric metasurface platform to realize a DW-ML. Using the DW-ML as the objective lens, we demonstrated TPM with image qualities comparable to a conventional microscope objective. The effect of the large diffractive chromatic dispersion of the DW-ML was considered and discussed. As a proof of concept, this work demonstrates the capabilities and limitations of the dielectric metasurface platform in multi-photon microscopy. With

the great interest in the development of more compact TPMs, we believe metasurfaces can play a significant role in this field.

Appendix 3.1: Additional information and discussion for meta-molecule based devices

Simulation. To find the transmission amplitude and phase of a multi-element metasurface, the RCWA technique was used [217]. A normally incident plane wave at each wavelength was used as the excitation, and the amplitude and phase of the transmitted wave were extracted. Since the lattice is subwavelength for normal incidence at both wavelengths, only the zeroth order diffracted light is nonzero. This justifies the use of only one transmission value at each wavelength to describe the behavior of meta-molecules. The lattice constant was chosen as 720 nm, and the α-Si posts were 718-nm tall. Refractive indices of 3.56 and 3.43 were assumed for α-Si at 915 nm and 1550 nm, respectively.

The paraxial focal distance of the two lenses were calculated to be 286 μm and 495 μm for the lenses that focus light from the fiber to 400 μm and 1000 μm, respectively, by fitting a parabola to the phase profiles of the lenses. For a fitted parabola $y = \alpha x^2$, the paraxial focal distance can be calculated using $f = 2\pi/2\alpha\lambda$. The corresponding numerical apertures can then found to be 0.46 and 0.29 for the two lenses.

The perfect phase mask (that also served as the goal phase profile for the designed devices) was calculated from the illuminating field and the aspherical desired phase profile using the method described in supplementary information of [67]. The illuminating field was calculated by propagating the output fields of single mode fibers at each wavelength using the plane wave expansion (PWE) method up to the metasurface layer. The perfect phase mask was then applied to the field, and the result was propagated using the PWE method to the focal point. The diffraction-limited FWHM was then calculated from the intensity profile at the focal plane.

Full wave simulation of a full lens was done using FDTD in MEEP [234]. A lens with a diameter of 75 μm and a focal length of 100 μm was designed with the same method as the fabricated device. The lens focuses the light emitted from a single mode fiber (with mode diameters of 10.4 μm at 1550 nm and 6 μm at 915 nm) placed 150 μm away from a 125 μm thick fused silica substrate (all of the geometrical dimensions were chosen 4 times smaller than the values for the experimentally measured device). The distances to fibers were chosen such that more than 99% of the total power emitted by the fiber passes through the lens aperture. At both wavelengths, the light

from the fibers was propagated through air, air-glass interface, and through glass up to a plane about a wavelength before the metasurface using a PWE code. Electric and magnetic field distributions at this plane were used as sources for FDTD simulation of the lenses, and fields were calculated at about a wavelength after the metasurface using MEEP. The PWE code was used again to further propagate these fields to the focal plane and beyond [Figs. **3.4d**]. The focusing efficiencies were calculated by dividing the power in a 20-μm-diameter disk around the focus, to the total power incident on the lens.

Sample fabrication. A 718-nm-thick hydrogenated α-Si layer was deposited on a fused silica substrate using the PECVD technique with a 5% mixture of silane in argon at 200 °C. An EBPG5000+ EBL system was used to define the metasurface pattern in the ZEP-520A positive resist (~300 nm, spin coated at 5000 rpm for 1 minute). The pattern was developed in a resist developer for 3 minutes (ZED-N50 from Zeon Chemicals). An approximately 100-nm-thick Al_2O_3 layer was deposited on the sample using electron beam evaporation, and was lifted off reversing the pattern. The patterned Al_2O_3 hard mask was then used to dry etch the α-Si layer in a 3:1 mixture of SF_6 and C_4F_8 plasma. After etching, the mask was removed using a 1:1 solution of ammonium hydroxide and hydrogen peroxide at 80° C.

Measurement procedure. Devices were measured using a fiber placed ~1100 μm away from the metasurface (500 μm substrate thickness plus 600 μm distance between the fiber and the substrate), and a custom built microscope with ~ ×100 magnification (Fig. **3.A1**). At 915 nm, a fiber coupled semiconductor laser with a single mode fiber with an angled polished connector was used for illumination. Fiber tip angle was adjusted to correct for the angled connector cut. A ×100 objective lens (×100 UMPlanFl NA=0.95, Olympus) and a tube lens (AC254-200-B-ML, Thorlabs) with a focal distance of 20 cm were used to image intensity at planes of interest to a CCD camera (CoolSNAP K4, Photometrics). A calibration sample with known feature sizes was measured to find the pixel-size transferred to the object plane. The objective was moved with a translation stage to image different planes around the focus. The plotted axial plane intensities are upsampled 2:1 in the axial direction (4 μm adjacent measurement planes distance to 2 μm) to achieve a smoother graph. For focusing efficiency measurement at 915 nm, a 20-μm-diameter pinhole was placed in the focal plane of the metasurface lens to only let the focused light pass through. The pinhole was made by wet etching a 20 μm hole in a thick layer of chrome deposited on a fused silica substrate. A power meter (PM100D, with photodetector head S122C,

Thorlabs) was then used to measure the power after the pinhole, and the output power of the fiber. The efficiency was calculated as the ratio of these two powers. The reported measured efficiency is therefore a lower bound on the actual efficiency as it does not include reflection from the substrate, and two reflections from the two sides of the pinhole glass substrate. A similar setup was used for measurements at 1550 nm: a tunable 1550 nm laser (Tunics-Plus, Photonetics) was used with a single mode fiber for illumination. The same ×100X objective was used with a 20-cm tube lens (AC254-200-C-ML, Thorlabs) to image the intensity in the object plane to a camera (Digital CamIR 1550, Applied Scintillation Technologies). The camera has a significantly non-uniform sensitivity for different pixels which leads to high noise level of the images captured by the camera (as seen in Fig. **3.4b**). The nonphysical high frequency noise of the images (noise with frequencies higher than twice the free space propagation constant) was removed numerically to reduce the noise in the axial intensity patterns. The intensity pattern was also upsampled in the axial direction from the actual 4 μm distance between adjacent measurement planes, to 2 μm to achieve a smoother intensity profile. To find the focused power, the focal plane of the lens was imaged using the microscope to a photodetector. A 2-mm iris in the image plane (corresponding to 20 μm in the object plane) was used to limit the light reaching the photodetector. The input power was measured by imaging the fiber facet to the photodetector using the same setup and without the iris. The efficiency was obtained by dividing the focused power by the input power.

Discussion of deflection efficiency of blazed gratings designed with the proposed meta-molecule platform. To understand the reasons behind the low efficiency of the lenses at 915 nm, two double wavelength blazed gratings were designed using the proposed meta-molecule scheme. One grating with a small deflection angle (5 degrees) and another one with a larger angle (20 degrees) were simulated at 915 nm using MEEP, and power loss channels were analyzed in both cases (Fig. **3.A3**). Both gratings were chosen to be 2 meta-molecules wide in the y direction, so that periodic boundary conditions in this direction can be used in FDTD. The 5-degree grating is 322 lattice constants long in the x direction, while the 20-degree one is 146 lattice constants. The lengths are chosen such that the grating phases at 915 nm and 1550 nm are both almost repeated after the chosen lengths [Fig. **3.A3a**]. An x-polarized plane-wave normally incident from the fused silica side was used as excitation in both simulations, and the transmitted and reflected electric and magnetic field intensities were calculated about a wavelength apart from the meta-molecules. The transmitted fields were further propagated using a plane wave expansion program,

and the resulting fields in an area of length 30 μm around the center can be seen in Figs. **3.A3b** and **3.A3c** for 5-degree and 20-degree gratings, respectively. The field distributions outside of the areas shown here look similar to the ones shown. In both cases, a dominant plane wave propagating in the design direction is observed, along with some distortions. Angular distribution of power in transmission and reflection is analyzed using the Fourier transform of the fields. The resulting power distributions are shown in Figs. **3.A3d** and **3.A3e** for 5 degrees and 20 degrees, respectively. While the average power transmission of meta-molecules used in both gratings (found from the data in Fig. **3.2e**) is slightly above 73%, only 36% and 22% of the incident power is directed to 5 and 20 degrees for the corresponding gratings. The actual total transmitted powers are 56% and 50% for the 5- and 20-degree gratings, showing that an additional ~20% of the power gets reflected as a result of the introduced aperiodicity. Because of the relatively large lattice constant, even a small aperiodicity can result in generation of propagating modes in the substrate, thus the reflection is considerably higher for the gratings than for a perfectly periodic lattice. From the 56% transmitted power in the 5 degree grating, 20% is lost to diffraction to other angles. From Figs. **3.A3b** and **3.A3c** we can see there are distortions in the transmitted field. These distortions, mainly due to the low transmission amplitude of some of the meta-molecules and their phase errors, result in the transmitted power being diffracted to other angles. Also, it is seen that power loss to other angles both in reflection and transmission is higher for larger grating angles. This is due to the need for finer sampling of the wave front for waves with steeper angles. The lower efficiency for gratings with larger angles results in lower efficiency of lenses with higher numerical apertures which need bending light with larger angles.

Appendix 3.2: Supporting figures for meta-molecule based devices

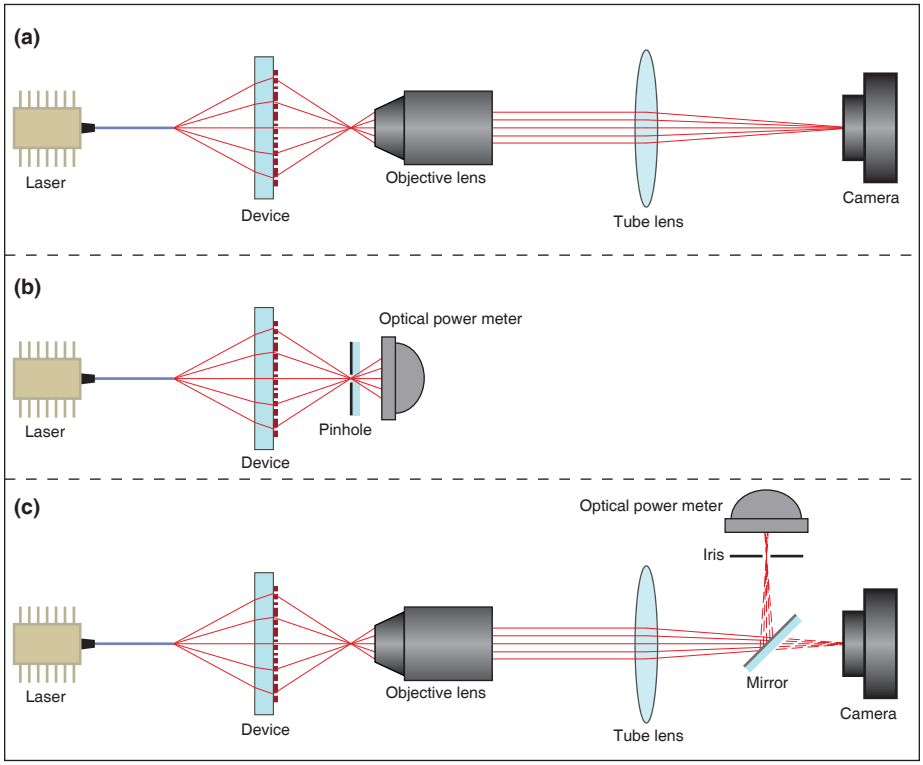

Figure 3.A1: **Measurement setups.** **(a)** Schematic of the measurement setup used to capture the focus pattern and the intensity distribution in different planes around focus. The laser source, fibers, tube lens, and camera were different in the 915-nm and 1550-nm measurements. **(b)** The measurement setup for measuring the efficiency of the lenses at 915 nm using a 20-μm pinhole in the focal plane. **(c)** The setup for measuring focusing efficiency of the lens at 1550 nm using a 2-mm iris in the image plane of a ~ ×100 microscope.

Appendix 3.3: Additional information and discussion for TPM

Simulation. The transmission amplitude and phase of the nano-posts [Fig. **3.A5**] were acquired by simulating a uniform array of nano-posts on a square lattice using the RCWA technique [217]. The p-Si nano-posts were 407 nm tall, the lattice constant was 310 nm, and the refractive index of p-Si was 3.7231+0.0078i at 820 nm, and 3.9984+0.0282i at 605 nm. For the SU-8 layer, we used refractive index values of 1.58 and 1.595 at 820 nm and 605 nm, respectively. A normally incident plane-wave was used as the excitation.

Sample fabrication. A 458-nm thick layer of hydrogenated α-Si was deposited on a 1-mm-thick fused silica substrate using PECVD. The layer was then annealed in a furnace to form the 407-nm-thick p-Si layer. The metasurface patterns were

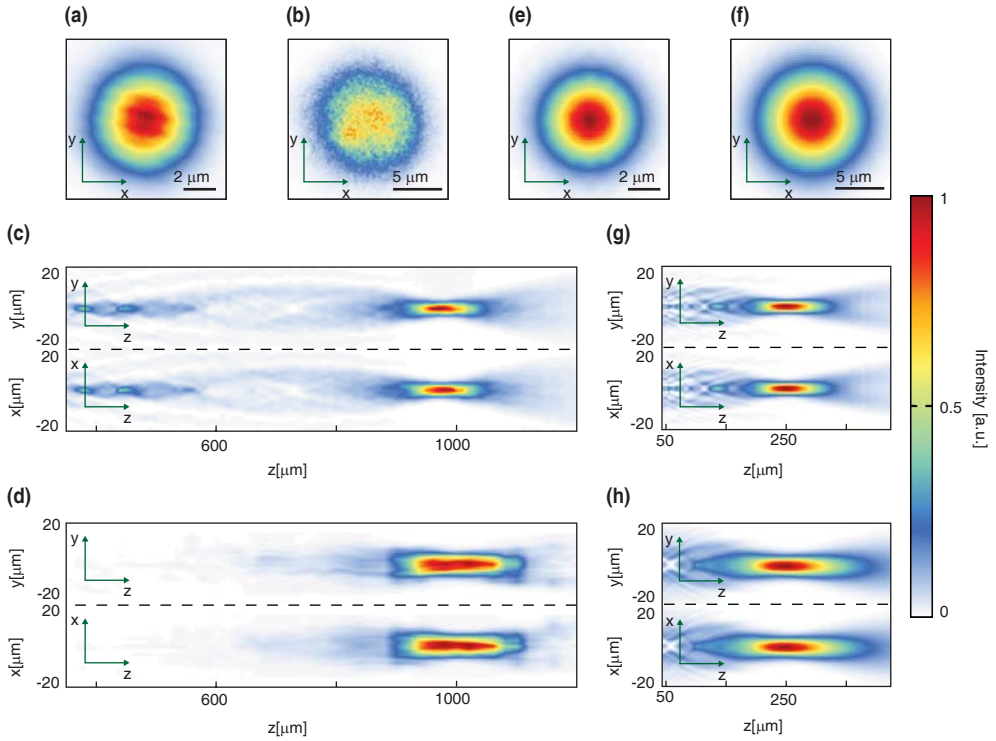

Figure 3.A2: **Measurement and simulation results for the lenses with a lower NA. (a)** and **(b)** Measured intensity in the focal plane of a double wavelength lens (1000-μm focal length, 300-μm diameter) at 915 nm **a**, and 1550 nm **b**. At 915 nm the lens actually focuses the light 980 μm away from its surface, so the focal spot shown here is imaged at ≈980 μm away from the surface. The error in focal distance is probably due to the approximation made in the mode diameter of the fiber (see Fig. **3.A1**S1), which affects the focusing distance of a low-NA lens more than that of a high-NA lens. **(c)** Intensity measured in the axial planes of the lens for 915 nm. **(d)** The same axial plots for 1550 nm. **(e)** and **(f)** Simulated focal plane intensity of a lens with the same NA as the one shown in (**a**–**d**) but with a diameter of 75 μm at wavelengths of 915 nm **(e)**, and 1550 nm **(f)**. **(g)** and **(h)** Simulated intensity profiles in the axial planes at 915 nm and 1550 nm, respectively, calculated for the same lens described in **e**.

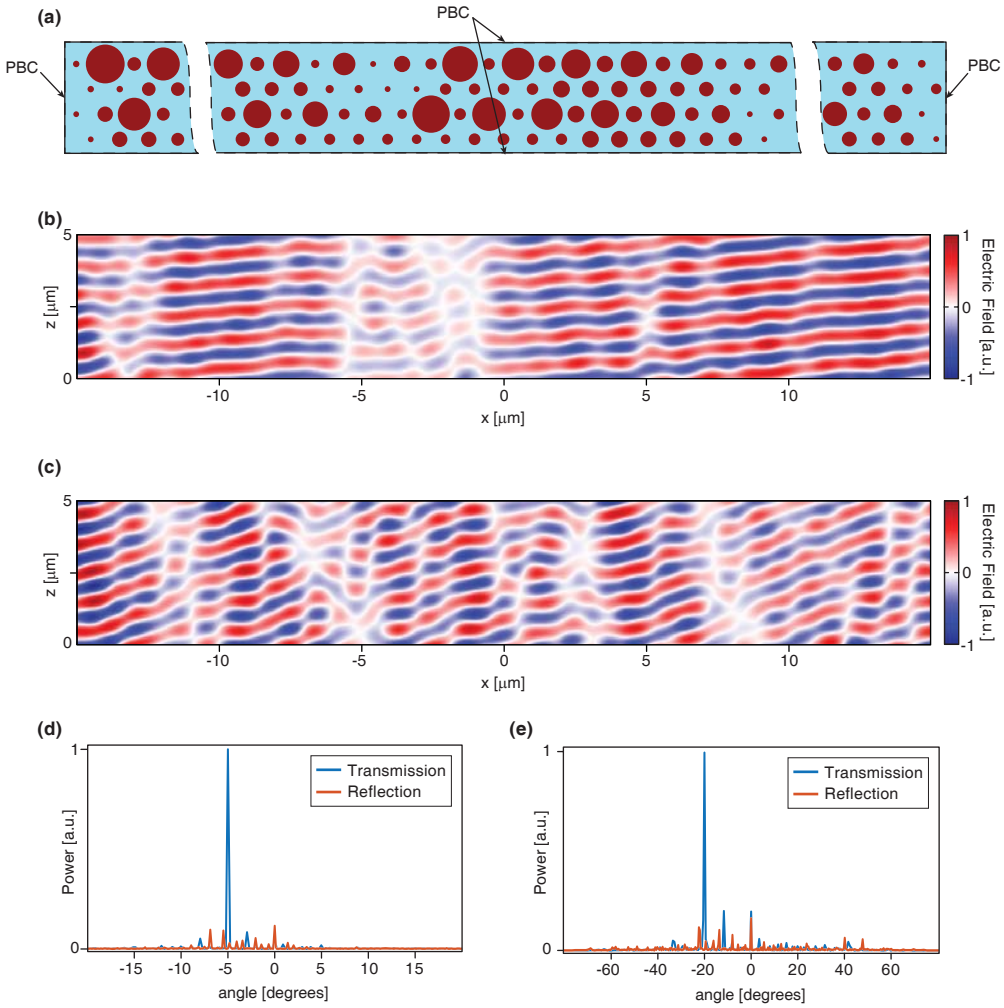

Figure 3.A3: **Double wavelength blazed gratings based on the meta-molecule design. (a)** Schematic of the simulated grating. The 5 degree grating is 322 meta-molecules long, while the 20-degree one is 146 meta-molecules long. Periodic boundary conditions were used in side boundaries and perfectly matched layers were used to terminate the simulation domain in top and bottom directions. **(b)** and **(c)** Real part of the electric field a few wavelengths after the 5-degree **b**, and 20-degree **c** gratings. **(d)** and **(e)** Distribution of transmitted and reflected power in different angles for the 5-degree **d**, and 20-degree **e** gratings.

generated with EBL in a positive electron-beam resist. An Al_2O_3 layer was deposited on the generated pattern after development, and was used to reverse the pattern through lift-off. The patterned Al_2O_3 layer was then used as a hard mask in the dry etching process of the p-Si layer. Finally, a ~2-μm-thick layer of SU-8 was spin coated on the metasurface, and a gold aperture was deposited around the lens to reduce the background light.

Measurement procedure. The setup in Fig. **3.A6** was used for the DW-ML characterization measurements. A collimated beam was used to illuminate the DW-ML and the intensity distribution was imaged at multiple planes around the focal plane and parallel to it. These images were compiled to form the axial intensity distribution profiles of Figs. **3.19b** and **3.19c**. The two-photon image in Fig. **3.20b** is captured by replacing the objective lens in a TPM by the DW-ML. The DW-ML was oriented in such a way that the excitation axis of the metasurface (corresponding to the 820-nm wavelength) overlapped with the polarization direction of the excitation laser. The details of the TPM are shown in Fig. **3.A4**. Both the DW-ML and the refractive objective are used to image a polyethylene microsphere about 90 μm in diameter and coated with a fluorophore (UVPMS-BR-0.995 10-90m μm, Cospheric).

Effects of chromatic dispersion on efficiency. In this section we first study the effect of the finite bandwidth of the light used to characterize the DW-ML at 605 nm. Second, we estimate the effect of the bandwidth of the pulsed laser on the excitation efficiency of the two-photon imaging. In both cases, we model the lens as a transmission mask with constant amplitude and phase over the bandwidth. This model results in an upper-bound for the efficiency, as it only takes the diffractive chromatic dispersion into account, and overlooks the wavelength dependence of the nano-posts over the bandwidth of the pulse.

To estimate the apparent reduction in measured efficiency due to the finite bandwidth of the 600-nm source, we simulated the focusing of the DW-ML at 41 wavelengths (580 nm to 620 nm, at 1-nm separations). This bandwidth was chosen to completely cover the pass-band of the used filter. The simulation was performed through modeling the DW-ML as a complex transmission mask, and propagating the fields after the DW-ML using a PWE code. To get the total intensity in the focal plane, the weighted intensities (using the transmission values of the bandpass filter) were added for all the wavelengths. The integral of this total intensity in a disk with a 5-μm diameter was divided to the total power before the DW-ML to achieve a ~38% focusing efficiency. In addition, we calculated the efficiency at the center

wavelength of 600 nm to be ~63%. Therefore, we estimated the experimental single wavelength focusing efficiency to be ~45%. As expected from our previous work, the experimental focusing efficiency at the shorter wavelength is more sensitive to fabrication errors [137].

The excitation efficiency in the two-photon process is proportional to the intensity squared. To estimate the ratio of the peak intensity squared for the DW-ML and the conventional objective lens, we simulated both cases using the method explained above. We modeled the DW-ML by its transmission mask at 820 nm, and modeled the objective as a perfect aspheric phase mask. The pulsed laser has a $\lessapprox$120 fs width, and assuming a bandwidth-limited Gaussian pulse, we find that it has a $\gtrapprox$9 nm bandwidth. We calculated the electric field distribution in the focal plane for both the DW-ML and the conventional objective for all the wavelengths. Since the exact waveform of the pulse after passing through the setup is not known, we calculated the peak intensity ratio in two extreme cases. First, we assumed that all different wavelengths add up in phase in the focal plane (corresponding to a case with the shortest possible pulse width and the largest peak-to-average power ratio). Second, we assumed that the pulse is completely broadened (with a peak-to-average power ratio of one). To model this, we added the simulated intensities of different wavelengths in the focal plane. With equal input powers for the DW-ML and the conventional objective, the peak intensity ratios in the two cases were ~12.7 and ~4.9, respectively. In reality, the ratio must be between these two values because the pulse reaching the focal point is broadened due to dispersion, yet it's not completely incoherent.

Using these pieces of data, we can estimate the contribution of different factors to the lower excitation-collection efficiency of the DW-ML compared to the conventional objective. As observed in Figs. **3.20b** and **3.20c**, the collected power with the DW-ML is about 0.06 of the collected power with the objective. In addition, the excitation laser power with the DW-ML is about 4.7 times larger than the objective. The collected power is proportional to the peak excitation intensity squared, and the collection efficiency. Therefore we can write

$$\frac{P_{\mathrm{OL}}^{\mathrm{Col}}}{P_{\mathrm{DW-ML}}^{\mathrm{Col}}} = \frac{\eta_{\mathrm{OL}}^{\mathrm{Col}}}{\eta_{\mathrm{DW-ML}}^{\mathrm{Col}}}\left(\frac{P_{\mathrm{OL}}^{\mathrm{Exc}}}{P_{\mathrm{DW-ML}}^{\mathrm{Exc}}}\frac{I_{\mathrm{OL}}^{p}}{I_{\mathrm{DW-ML}}^{p}}\right)^{2}, \tag{3.1}$$

where the subscripts determine the utilized lens (OL denoting the conventional objective lens), Col and Exc denote collection and excitation, and I^p is the peak intensity for the lenses calculated with equal excitation powers. Using this equation

and the 22.5% collection efficiency of the DW-ML, we can estimate the $\frac{I^p_{\mathrm{OL}}}{I^p_{\mathrm{DW-ML}}}$ ratio to be ~9.1. This ratio falls well within the 4.9-12.7 range that was calculated.

Appendix 3.4: Supporting figures for TPM

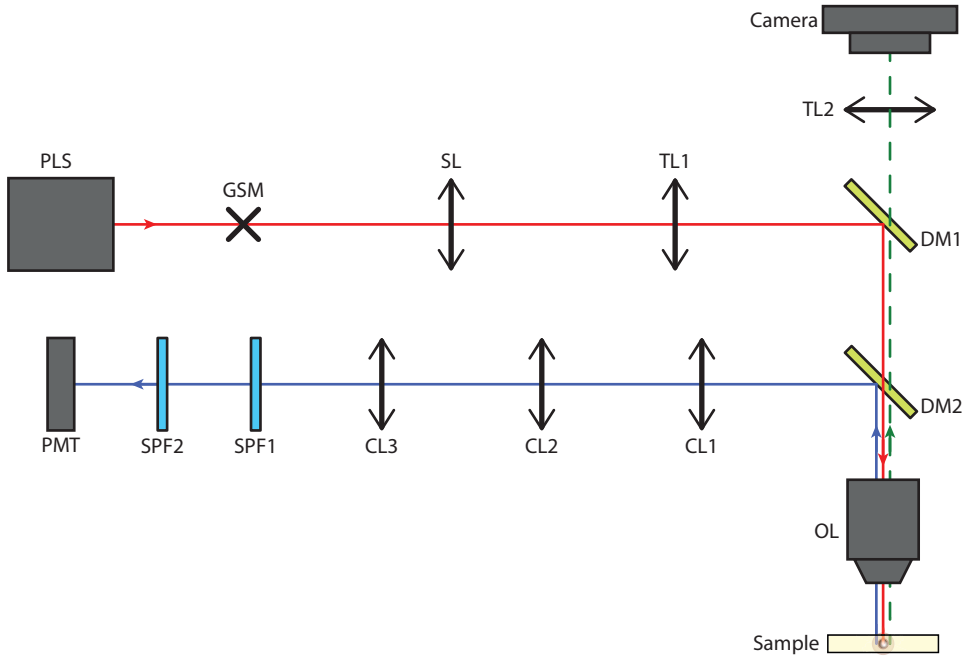

Figure 3.A4: **Schematics of the TPM setup.** PLS: Pulsed laser source, Spectra-Physics InSight DS+. GSM: Galvanometer scanning mirror, Cambridge Tech 6215H. SL: Scan lens $f = 54$ mm, Thorlabs LSM54-1050. TL1: Tube lens $f = 200$ mm, Thorlabs ITL200. DM1: Dichroic mirror, reflects >805 nm, Thorlabs DMSP805L. DM2: Dichroic mirror, reflects 500–700 nm, Chroma T600/200dcrb. OL: Objective lens 20×/NA = 0.5, Zeiss EC Epiplan-Neofluar (this objective is replaced by the DW-ML). CL1: Collection lens $f = 100$ mm, Thorlabs AC508-100. CL2: Collection lens $f = 50$ mm, Thorlabs LA1119. CL3: Collection lens $f = 30$ mm, Thorlabs LA1085. SPF1: Short-pass filter <680 nm, Chroma ET680SP-2P8. SPF2: Short-pass filter <700 nm, Thorlabs FESH0700. PMT: Photomultiplier tube, Hamamatsu R3896. TL2: Tube lens $f = 75$ mm, Thorlabs AC508-075. Camera: AmScope HD205-WU. The camera is only used to find the part of the sample that is of interest and bring it in focus.

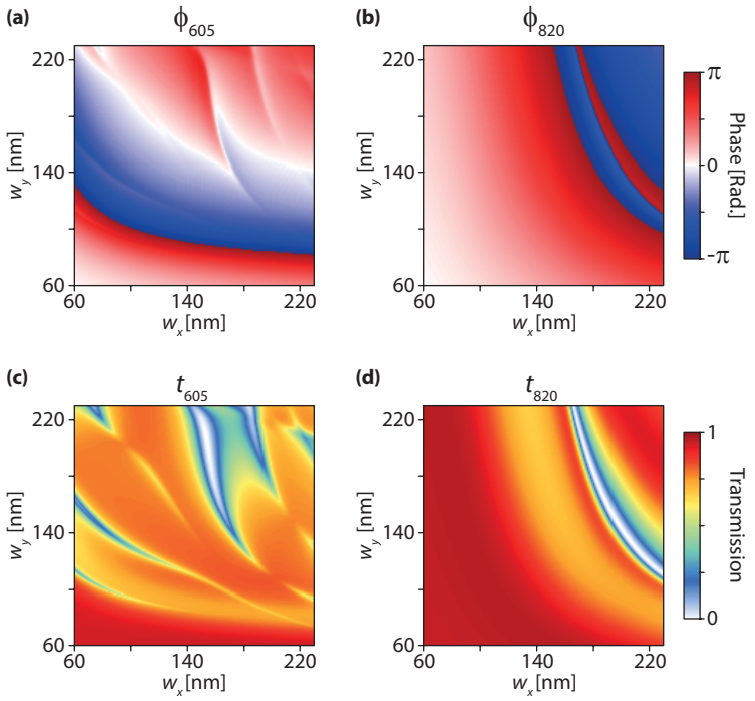

Figure 3.A5: **Simulated transmission phase and amplitude of a uniform array of nano-posts. (a)** Simulated transmission phase of a uniform array of nano-posts at 605 nm, and **(b)** at 820 nm. **(c)** Simulated transmission amplitude of a uniform array of nano-posts at 605 nm, and **(d)** at 820 nm. Material loss contributes to the lower transmittance at 605 nm.

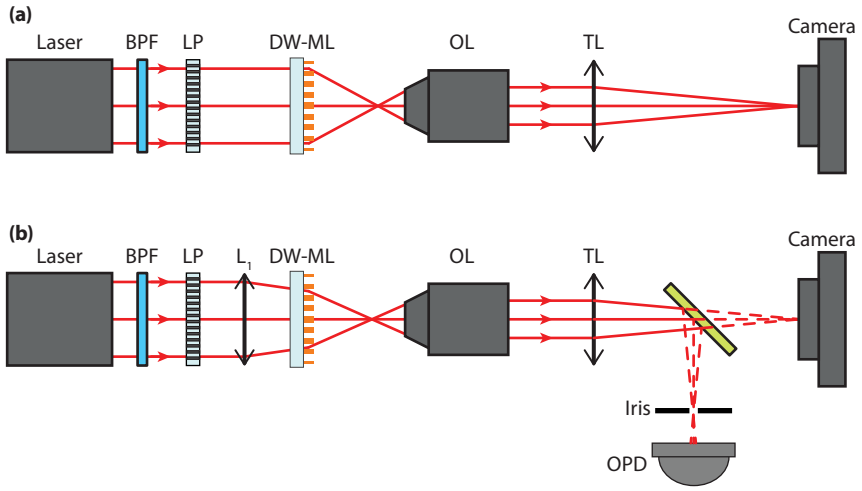

Figure 3.A6: **Schematics of the setups used to characterize the DW-ML. (a)** Schematics of the setup used to capture the intensity distribution patterns of Fig. **3.19**. Laser: ~822-nm laser diode for measurements at 820 nm, and Fianium WhiteLase Micro supercontinuum laser for characterization at 605 nm. BPF: Band-pass filter with a center wavelength of ~600 nm and FWHM of 10 nm (used only with the supercontinuum), Thorlabs FB600-10. LP: Linear polarizer, Thorlabs LPVIS100-MP2. OL: Objective lens 100×/NA = 0.95, Olympus UMPlanFl. TL: Tube lens $f = 20$ cm, Thorlabs AC254-200-B-ML. Camera: Photometrics Coolsnap K4. **(b)** Schematic of the setup used to measure the focusing efficiency of the DW-ML. L_1: Lens. $f = 200$ mm, Thorlabs AC254-200-B-ML. OPD: Optical power detector, Thorlabs PM100D with photodetector head Thorlabs S122C. L_1 is only used to partially focus light such that it has a ~550-μm FWHM at the DW-ML plane. This way, more than 99% of the input light power passes through the lens. The iris diameter is 1.1 mm for 820 nm and 0.55 mm at 605 nm.

Chapter 4

CONTROLLING THE DIFFRACTIVE CHROMATIC DISPERSION WITH METASURFACES

The material in this chapter was in part presented in [119].

Diffraction gratings disperse light in a rainbow of colors with the opposite order than refractive prisms, a phenomenon known as negative dispersion. While refractive dispersion can be controlled via material refractive index, diffractive dispersion is fundamentally an interference effect dictated by geometry. In this chapter, we show that this fundamental property can be altered using dielectric metasurfaces, and we experimentally demonstrate diffractive gratings and focusing mirrors with positive, zero, and hyper negative dispersion. These optical elements are implemented using a reflective metasurface composed of dielectric nano-posts that provide simultaneous control over phase and its wavelength derivative. In addition, as the first practical application, we demonstrate a focusing mirror that exhibits a fivefold reduction in chromatic dispersion, and thus an almost three-times increase in operation bandwidth compared to a regular diffractive element. This concept challenges the generally accepted dispersive properties of diffractive optical devices and extends their applications and functionalities.

4.1 Introduction

Most optical materials have positive (normal) dispersion, which means that the refractive index decreases at longer wavelengths. As a consequence, blue light is deflected more than red light by dielectric prisms [Fig. **4.1a**]. The reason why diffraction gratings are said to have negative dispersion is because they disperse light similar to hypothetical refractive prisms made of a material with negative (anomalous) dispersion [Fig. **4.1b**]. For diffractive devices, dispersion is not related to material properties, and it refers to the derivative of a certain device parameter with respect to wavelength. For example, the angular dispersion of a grating that deflects normally incident light by a positive angle θ is given by $\mathrm{d}\theta/\mathrm{d}\lambda = \tan(\theta)/\lambda$ (see [219] and Appendix 4.2). Similarly, the wavelength dependence of the focal length (f) of a diffractive lens is given by $\mathrm{d}f/\mathrm{d}\lambda = -f/\lambda$ [23, 219]. Here we refer to diffractive

devices that follow these fundamental chromatic dispersion relations as "*regular*". Achieving new regimes of dispersion control in diffractive optics is important both at the fundamental level and for numerous practical applications. Several distinct regimes can be differentiated as follows. Diffractive devices are dispersionless when the derivative is zero (i.e., $\mathrm{d}\theta/\mathrm{d}\lambda = 0$, $\mathrm{d}f/\mathrm{d}\lambda = 0$ shown schematically in Fig. **4.1c**), have positive dispersion when the derivative has opposite sign compared to a regular diffractive device of the same kind (i.e., $\mathrm{d}\theta/\mathrm{d}\lambda < 0$, $\mathrm{d}f/\mathrm{d}\lambda > 0$) as shown in Fig. **4.1d**, and are hyper-dispersive when the derivative has a larger absolute value than a regular device (i.e., $|\mathrm{d}\theta/\mathrm{d}\lambda| > |\tan(\theta)/\lambda|$, $|\mathrm{d}f/\mathrm{d}\lambda| > |-f/\lambda|$) as seen in Fig. **4.1e**. Here we show that these regimes can be achieved in diffractive devices based on optical metasurfaces.

Similar to other diffractive devices, metasurfaces that locally change the propagation direction (e.g., lenses, beam deflectors, holograms) have negative chromatic dispersion [23, 135, 219, 259]. This is because most of these devices are divided in Fresnel zones whose boundaries are designed for a specific wavelength [135, 233], as discussed in 3. This chromatic dispersion is an important limiting factor in many applications and its control is of great interest. Metasurfaces with zero and positive dispersion would be useful for making achromatic singlet and doublet lenses, and the larger-than-regular dispersion of hyper-dispersive metasurface gratings would enable high resolution spectrometers. We emphasize that the devices with zero chromatic dispersion discussed here are fundamentally different from the multiwavelength metasurface gratings and lenses recently reported [74, 135–137, 181, 227–229, 233, 235, 260], similar to the ones discussed in 3. Multiwavelength devices have several diffraction orders, which result in lenses (gratings) with the same focal length (deflection angle) at a few discrete wavelengths. However, at each of these focal distances (deflection angles), the multi-wavelength lenses (gratings) exhibit the regular negative diffractive chromatic dispersion (see [135, 233], Appendix 4.2 and Fig. **4.A1**).

4.2 Theory

Here we argue that simultaneously controlling the phase imparted by the meta-atoms composing the metasurface (ϕ) and its derivative with respect to frequency ω ($\phi' = \partial\phi/\partial\omega$ which we refer to as chromatic phase dispersion or dispersion for brevity) makes it possible to dramatically alter the fundamental chromatic dispersion of diffractive components. This, in effect, is equivalent to simultaneously

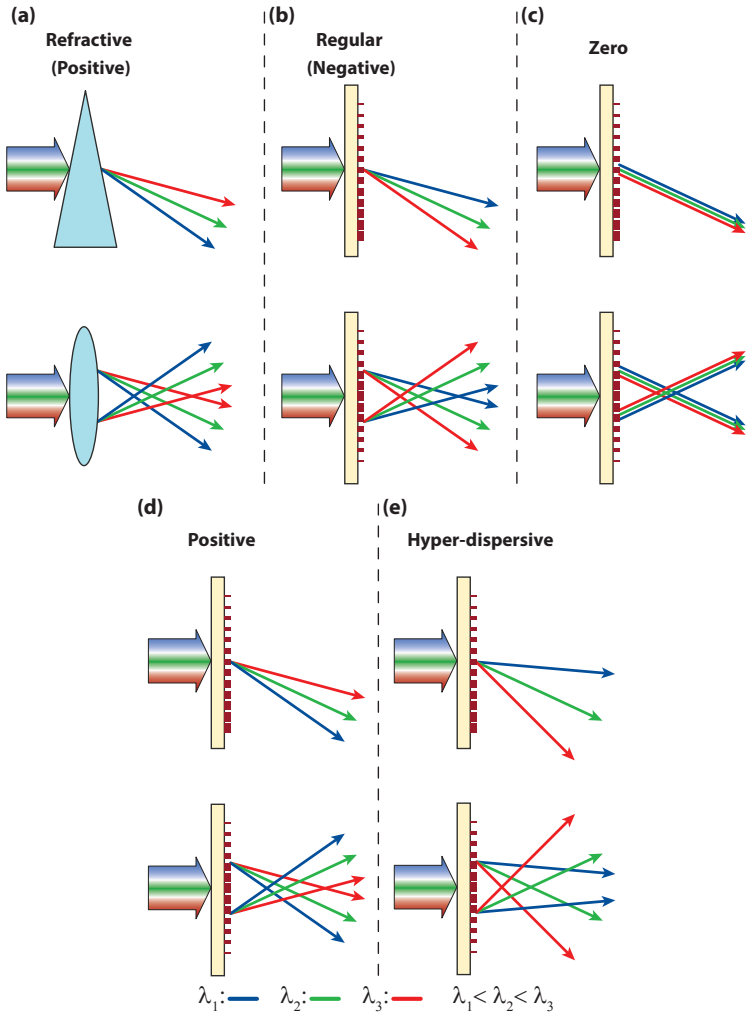

Figure 4.1: **Schematic illustrations of different dispersion regimes. (a)** Positive chromatic dispersion in refractive prisms and lenses made of materials with normal dispersion. **(b)** Regular (negative) dispersion in typical diffractive and metasurface gratings and lenses. **(c)** Schematic illustration of zero, **(d)** positive, and **(e)** hyper dispersion in dispersion-controlled metasurfaces. Only three wavelengths are shown here, but the dispersions are valid for any other wavelength in the bandwidth. The diffractive devices are shown in transmission mode for ease of illustration, while the actual devices fabricated in this chapter are designed to operate in reflection mode.

controlling the "effective refractive index" and "chromatic dispersion" of the meta-atoms. We have used this concept to demonstrate metasurface focusing mirrors with zero dispersion [261] in NIR. Using the concept introduced in [261], here we experimentally show metasurface gratings and focusing mirrors that have positive, zero, and hyper chromatic dispersions. We also demonstrate an achromatic focusing mirror with a highly diminished focal length chromatic dispersion, resulting in an almost three-times increase in its operation bandwidth.

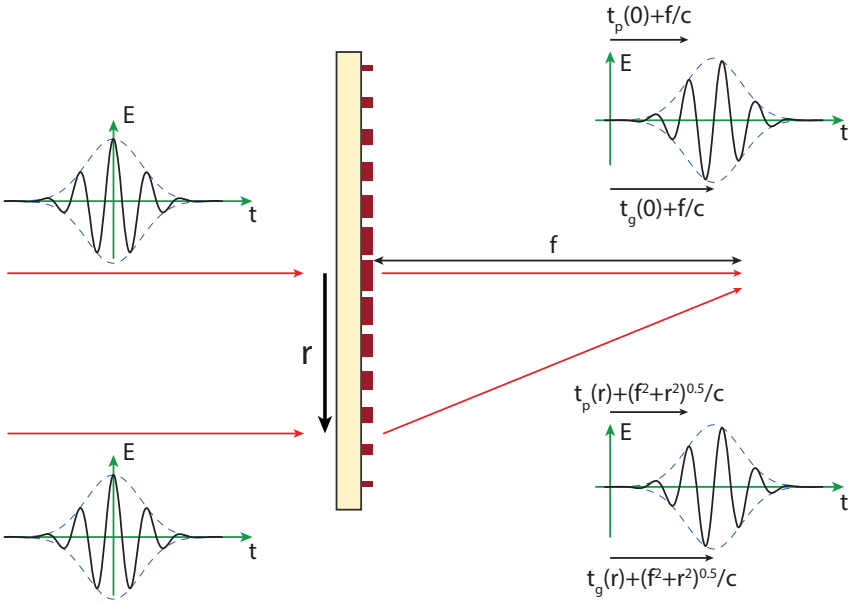

Figure 4.2: **Phase and group delays in focusing.** Schematics of focusing of a light pulse to the focal distance of a flat lens. The E vs t graphs show schematically the portions of the pulse passing through the center and at a point at a distance r away from center both before the lens, and when arriving at focus. The portions passing through different parts of the lens should acquire equal group delays and arrive at the focal point in phase for dispersionless operation.

First, we consider the case of devices with zero chromatic dispersion. In general for truly frequency independent operation, a device should impart a constant delay for different frequencies (i.e., demonstrate a true time delay behavior), similar to a refractive device made of a non-dispersive material [219]. Therefore, the phase profile will be proportional to the frequency:

$$\phi(x, y; \omega) = \omega T(x, y), \tag{4.1}$$

where $\omega = 2\pi c/\lambda$ is the angular frequency (λ: wavelength, c: speed of light) and $T(x, y)$ determines the function of the device (for instance $T(x, y) = -x \sin\theta_0/c$ for

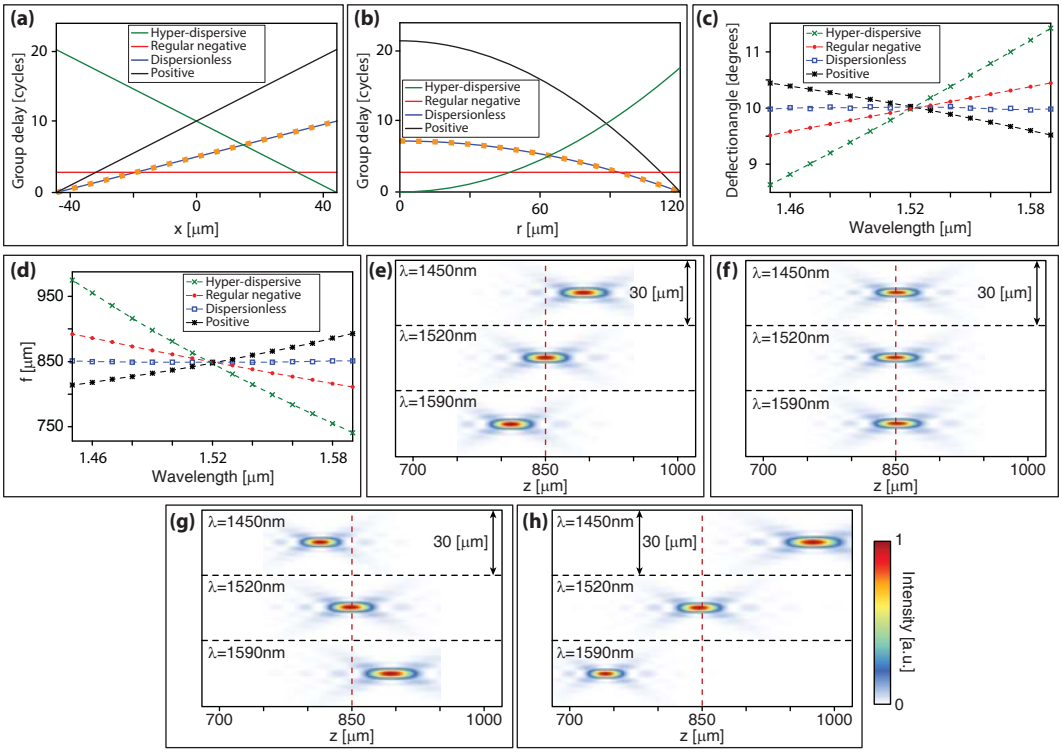

Figure 4.3: **Required phase and group delays and simulation results of dispersion-engineered metasurfaces based on hypothetical meta-atoms. (a)** Required values of group delay for gratings with various types of chromatic dispersion. The dashed line shows the required phase delay for all devices, which also coincides with the required group delay for the dispersionless gratings. The gratings are ~90 μm wide, and have a deflection angle of 10 degrees in their center wavelength of 1520 nm. **(b)** Required values of group delay for aspheric focusing mirrors with various types of chromatic dispersion. The dashed line shows the required phase delay for all devices. The mirrors are 240 μm in diameter, and have a focal distance of 650 μm at their center wavelength of 1520 nm. **(c)** Simulated deflection angles for gratings with regular, zero, positive, and hyper dispersions. The gratings are 150 μm wide and have a 10-degree deflection angle at 1520 nm. **(d)** Simulated focal distances for metasurface focusing mirrors with different types of dispersion. The mirrors are 500 μm in diameter and have a focal distance of 850 μm at 1520 nm. All gratings and focusing mirrors are designed using hypothetical meta-atoms that provide independent control over phase and dispersion (see Appendix 4.1 for details). **(e)** Intensity in the axial plane for the focusing mirrors with regular negative, **(f)** zero, **(g)** positive, and **(h)** hyper dispersions plotted at three wavelengths (see Fig. **4.A3** for other wavelengths).

a grating that deflects light by angle θ_0; $T(x, y) = -\sqrt{x^2 + y^2 + f^2}/c$ for a spherical-aberration-free lens with a focal distance f). Since the phase profile is a linear function of ω, it can be realized using a metasurface composed of meta-atoms that control the phase $\phi(x, y; \omega_0) = T(x, y)\omega_0$ and its dispersion $\phi' = \partial\phi(x, y; \omega)/\partial\omega = T(x, y)$. The bandwidth of dispersionless operation corresponds to the frequency interval over which the phase locally imposed by the meta-atoms is linear with frequency ω. For gratings or lenses, a large device size results in a large $|T(x, y)|$, which means that the meta-atoms should impart a large phase dispersion. Since the phase values at the center wavelength $\lambda_0 = 2\pi c/\omega_0$ can be wrapped into the 0 to 2π interval, the meta-atoms only need to cover a rectangular region in the *phase-dispersion* plane bounded by $\phi = 0$ and 2π lines, and $\phi' = 0$ and ϕ'_{max} lines, where ϕ'_{max} is the maximum required dispersion which is related to the device size (see Appendix 4.5 and Fig. **4.A2**). The required phase-dispersion coverage means that, to implement devices with various phase profiles, for each specific value of the phase we need various meta-atoms providing that specific phase, but with different dispersion values.

Considering the simple case of a flat dispersionless lens (or focusing mirror) with radius R, we can get some intuition to the relations found for phase and dispersion. Dispersionless operation over a certain bandwidth $\Delta\omega$ means that the device should be able to focus a transform limited pulse with bandwidth $\Delta\omega$ and carrier frequency ω_0 to a single spot located at focal length f [Fig. **4.2**]. To implement this device, part of the pulse hitting the lens at a distance r from its center needs to experience a pulse delay (i.e., group delay $t_g = \partial\phi/\partial\omega$) smaller by $(\sqrt{r^2 + f^2} - f)/c$ than part of the pulse hitting the lens at its center. This ensures that parts of the pulse hitting the lens at different locations arrive at the focus at the same time. Also, the carrier delay (i.e., phase delay $t_p = \phi(\omega_0)/\omega_0$) should also be adjusted so that all parts of the pulse interfere constructively at the focus. Thus, to implement this phase delay and group delay behavior, the lens needs to be composed of elements, ideally with sub-wavelength size, that can provide the required phase delay and group delay at different locations. For a focusing mirror, these elements can take the form of sub-wavelength one-sided resonators, where the group delay is related to the quality factor Q of the resonator (see Appendix 4.7) and the phase delay depends on the resonance frequency. We note that larger group delays are required for lenses with larger radius, which means that elements with higher quality factors are needed. If the resonators are single mode, the Q imposes an upper bound on the maximum bandwidth $\Delta\omega$ of the pulse that needs to be focused. The operation bandwidth can be expanded by using one-sided resonators with multiple resonances that partially

overlap. As we will show later in the chapter, these resonators can be implemented using silicon nano-posts backed by a reflective mirror.

To realize metasurface devices with non-zero dispersion of a certain parameter $\xi(\omega)$, phase profiles of the following form are needed:

$$\phi(x, y; \omega) = \omega T(x, y, \xi(\omega)). \tag{4.2}$$

For instance, the parameter $\xi(\omega)$ can be the deflection angle of a diffraction grating $\theta(\omega)$ or the focal length of a diffractive lens $f(\omega)$. As we show in the Appendix 4.4, to independently control the parameter $\xi(\omega)$ and its chromatic dispersion $\partial\xi/\partial\omega$ at $\omega = \omega_0$, we need to control the phase dispersion at this frequency in addition to the phase. The required dispersion for a certain parameter value $\xi_0 = \xi(\omega_0)$, and a certain dispersion $\partial\xi/\partial\omega|_{\omega=\omega_0}$ is given by:

$$\frac{\partial\phi(x, y; \omega)}{\partial\omega}|_{\omega=\omega_0} = T(x, y, \xi_0) + \partial\xi/\partial\omega|_{\omega=\omega_0}\omega_0\frac{\partial T(x, y, \xi)}{\partial\xi}|_{\xi=\xi_0}. \tag{4.3}$$

This dispersion relation is valid over a bandwidth where a linear approximation of $\xi(\omega)$ is valid. One can also use Fermat's principle to get similar results to Eq. 4.3 for the local phase gradient and its frequency derivative (see Appendix 4.6).

We note that discussing these types of devices in terms of phase $\phi(\omega)$ and phase dispersion $\partial\phi/\partial\omega$, which we mainly use in this chapter, is equivalent to using the terminology of phase delay ($t_p = \phi(\omega_0)/\omega_0$) and group delay ($t_g = \partial\phi/\partial\omega$). The zero dispersion case discussed above corresponds to a case where the phase and group delays are equal. Figures **4.3a** and **4.3b** show the required phase and group delays for blazed gratings and focusing mirrors with various types of dispersion, demonstrating the equality of phase and group delays in the dispersionless case. In microwave-photonics, the idea of using sets of separate optical cavities for independent control of the phase delay of the optical carrier, and group delay of the modulated RF signal has previously been proposed [262] to achieve dispersionless beam steering and resemble a true time delay system over a narrow bandwidth. For all other types of chromatic dispersion, the phase and group delays are drastically different, as shown in Figs. **4.3a** and **4.3b**.

Assuming hypothetical meta-atoms that provide independent control of phase and dispersion up to a dispersion of -150 Rad/μm (to adhere to the commonly used convention, we report the dispersion in terms of wavelength) at the center wavelength of 1520 nm, we have designed and simulated four gratings with different chromatic dispersions (see Appendix 4.1 for details). The simulated deflection angles as

functions of wavelength are plotted in Fig. **4.3c**. All gratings are 150 μm wide, and have a deflection angle of 10 degrees at their center wavelength of 1520 nm. The positive dispersion grating exhibits a dispersion equal in absolute value to the negative dispersion of a regular grating with the same deflection angle, but with an opposite sign. The hyper-dispersive design is three-times more dispersive than the regular grating, and the dispersionless beam deflector shows almost no change in its deflection angle. Besides gratings, we have also designed focusing mirrors exhibiting regular, zero, positive, and hyper dispersions. The focusing mirrors have a diameter of 500 μm and a focal distance of 850 μm at 1520 nm. Hypothetical meta-atoms with a maximum dispersion of -200 Rad/μm are required to implement these focusing mirror designs. The simulated focal distances of the four designs are plotted in Fig. **4.3d**. The axial plane intensity distributions at three wavelengths are plotted in Figs. **4.3e**–**4.3h** (for intensity plots at other wavelengths see Fig. **4.A3**). To relate to our previous discussion of dispersionless focusing mirrors depicted in Fig. **4.2**, a focusing mirror with a diameter of 500 μm and a focal distance of 850 μm would require meta-atoms with a maximum group delay of ~24 λ_0/c, with λ_0=1520 nm. To implement this device we used hypothetical meta-atoms with maximum dispersion of ~-100 Rad/μm which corresponds to a group delay of ~24 λ_0/c. The hypothetical meta-atoms exhibit this almost linear dispersion over the operation bandwidth of 1450 nm to 1590 nm.

4.3 Metasurface design

An example of meta-atoms capable of providing 0 to 2π phase coverage and different dispersions is shown in Fig. **4.4a**. The meta-atoms are composed of a square cross-section α-Si nano-post on a low refractive index silicon dioxide (SiO_2) spacer layer on an aluminum reflector that play the role of the multi-mode one sided resonators mentioned above. They are located on a periodic square lattice [Fig. **4.4a**, middle]. The simulated dispersion versus phase plot for the meta-atoms at the wavelength of $\lambda_0 = 1520$ nm is depicted in Fig. **4.4b**, and shows a partial coverage up to the dispersion value of ~ -100 Rad/μm. The nano-posts exhibit several resonances which enable high dispersion values over the 1450 nm to 1590 nm wavelength range. The meta-atoms are 725 nm tall, the SiO_2 layer is 325 nm thick, the lattice constant is 740 nm, and the nano-post side length is varied from 74 to 666 nm at 1.5 nm steps. Simulated reflection amplitude and phase for the periodic lattice are plotted in Figs. **4.4c** and **4.4d**, respectively. The reflection amplitude over the bandwidth of

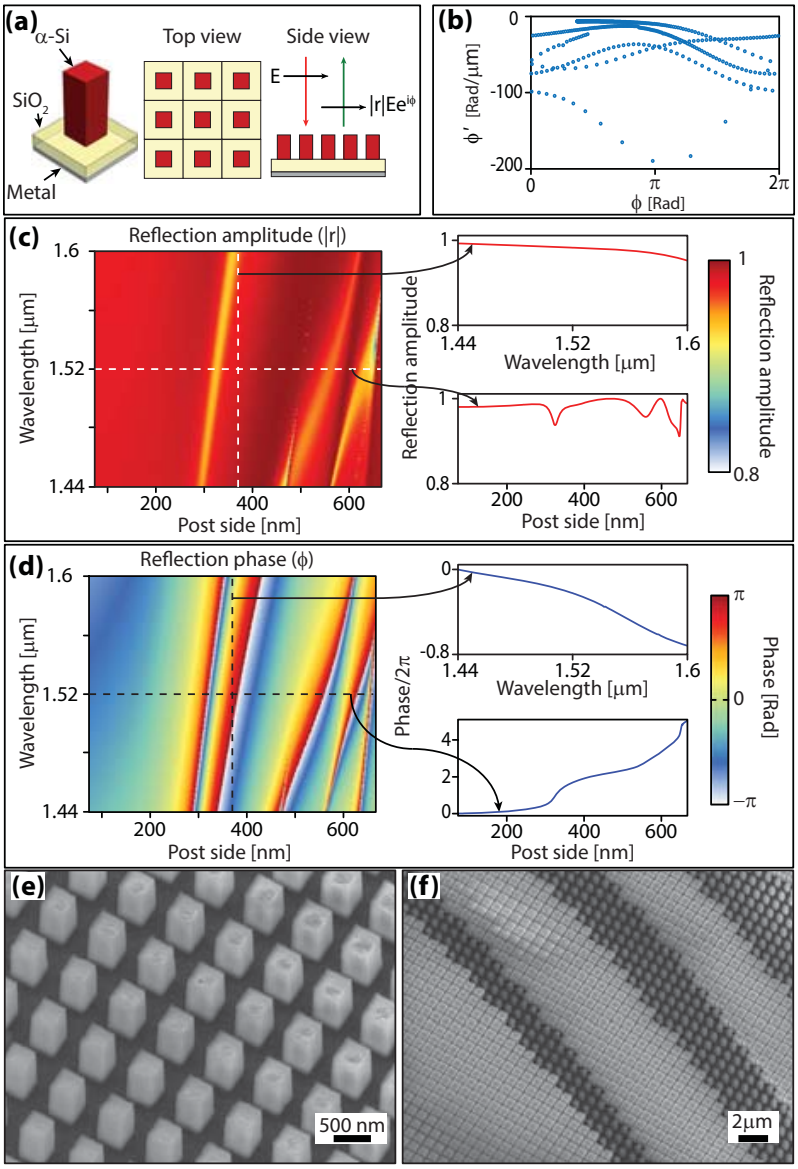

Figure 4.4: **High-dispersion silicon meta-atoms. (a)** A meta-atom composed of a square cross-section α-Si nano-post on a silicon dioxide layer on a metallic reflector. Top and side views of the meta-atoms arranged on a square lattice are also shown. **(b)** Simulated dispersion versus phase plot for the meta-atom shown in **a** at λ_0 =1520 nm. **(c)** Simulated reflection amplitude, and **(d)** phase as a function of the nano-post side length and wavelength. The reflection amplitude and phase along the dashed lines are plotted on the right. **(e)** and **(f)** Scanning electron micrographs of the fabricated nano-posts and devices.

interest is close to one for all nano-post side lengths. The operation of the nano-post meta-atoms is best intuitively understood as truncated multi-mode waveguides with many resonances in the bandwidth of interest [77, 125]. By going through the nano-post twice, light can obtain larger phase shifts compared to the transmissive operation mode of the metasurface (i.e., without the metallic reflector). The metallic reflector keeps the reflection amplitude high for all sizes, which makes the use of high quality factor resonances possible. As discussed before, high quality factor resonances are necessary for achieving large dispersion values, because, as we have shown in Appendix 4.7, dispersion is given by $\phi' \approx -Q/\lambda_0$, where Q is the quality factor of the resonance.

Using the dispersion-phase parameters provided by this metasurface, we designed four gratings operating in various dispersion regimes. The gratings are ~90 μm wide and have a 10-degree deflection angle at 1520 nm. They are designed to operate in the 1450 to 1590 nm wavelength range, and have regular negative, zero, positive, and hyper (three-times-larger negative) dispersion. Since the phase of the meta-atoms does not follow a linear frequency dependence over this wavelength interval [Fig. **4.4d**, top right], we calculate the desired phase profile of the devices at 8 wavelengths in the range (1450 to 1590 nm at 20 nm steps), and form an 8×1 complex reflection coefficient vector at each point on the metasurface. Using Figs. **4.4c** and **4.4d**, a similar complex reflection coefficient vector is calculated for each meta-atom. Then, at each lattice site of the metasurface, we place a meta-atom whose reflection vector has the shortest weighted Euclidean distance to the desired reflection vector at that site. The weights allow for emphasizing different parts of the operation bandwidth, and can be chosen based on the optical spectrum of interest or other considerations. Here, we used an inverted Gaussian weight ($\exp((\lambda - \lambda_0)^2/2\sigma^2)$, σ = 300 nm), which values wavelengths farther away from the center wavelength of λ_0 = 1520 nm. The same design method is used for the other devices discussed in the chapter. The designed devices were fabricated using standard semiconductor fabrication techniques as described in Appendix 4.1. Figures **4.4e** and **4.4f** show scanning electron micrographs of the nano-posts, and some of the devices fabricated using the proposed reflective meta-atoms. Figure **4.A6** shows the chosen post side lengths and the required as well as the achieved phase and group delays for the gratings with different dispersions. Required phases and the values provided by the chosen nano-posts are plotted at three wavelengths for each grating in Fig. **4.A6**.

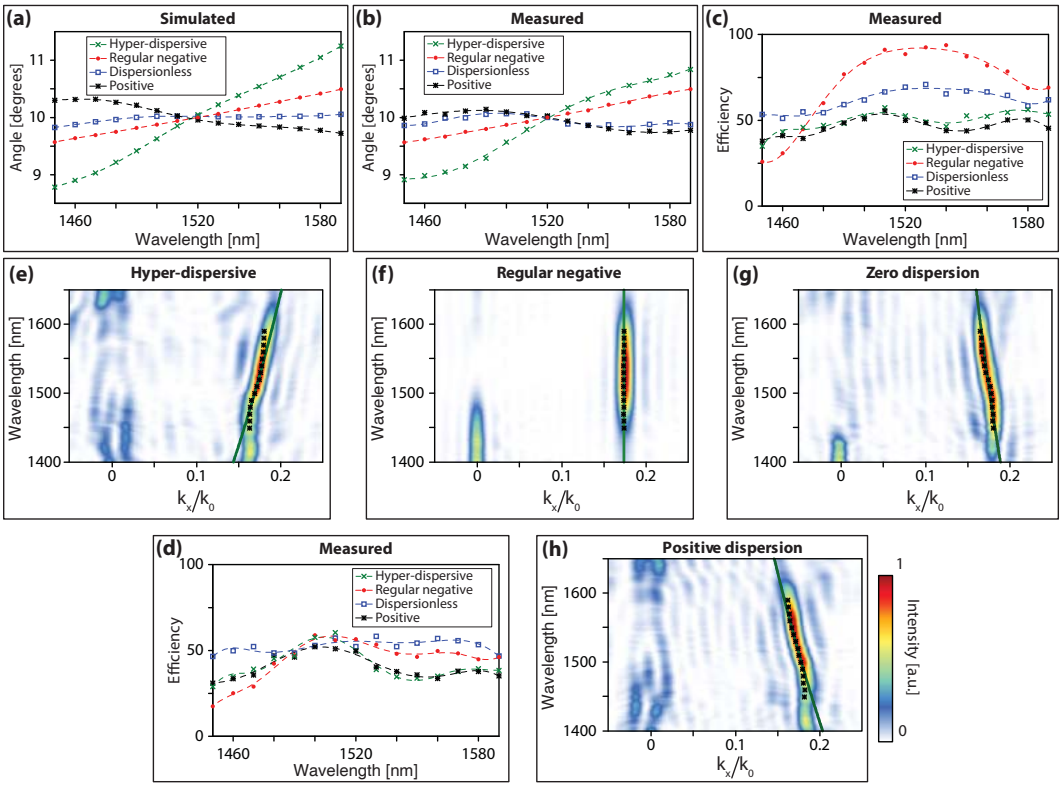

Figure 4.5: **Simulation and measurement results of gratings in different dispersion regimes.** **(a)** Simulated deflection angles for gratings with different dispersions, designed using the proposed reflective meta-atoms. **(b)** Measured deflection angles for the same grating. **(c)** Measured deflection efficiency for the gratings under TE, and **(d)** TM illumination. **(e)**–**(h)** Comparison between FDTD simulation results showing the intensity distribution of the diffracted wave as a function of normalized transverse wave-vector (k_x/k_0, $k_0 = 2\pi/\lambda_0$, and λ_0 =1520 nm) and wavelength for different gratings, and the measured peak intensity positions plotted with black stars. All simulations here are performed with TE illumination. The green lines show the theoretically expected maximum intensity trajectories.

4.4 Experimental results

Figures **4.5a** and **4.5b** show the simulated and measured deflection angles for gratings, respectively. The measured values are calculated by finding the center of mass of the deflected beam 3 mm away from the grating surface (see Appendix 4.1 and Fig. **4.A8** for more details about the measurement). As expected, the zero-dispersion grating shows an apochromatic behavior resulting in a reduced dispersion, the positive grating shows positive dispersion in the ~1490–1550 nm bandwidth, and the hyper-dispersive one shows an enhanced dispersion in the measurement bandwidth. This can also be viewed from the grating momentum point of view: a regular grating has a constant momentum set by its period, resulting in a constant transverse wave-vector. In contrary, the momentum of the hyper-dispersive grating increases with wavelength, while that of the zero and positive gratings decreases with it. This means that the effective period of the non-regular gratings changes with wavelength, resulting in the desired chromatic dispersion. Figures **4.5e**–**4.5h** show good agreement between simulated intensities of these gratings versus wavelength and transverse wave-vector (see Appendix 4.1 for details) and the measured beam deflection (black stars). The change in the grating pitch with wavelength is more clear in Fig. **4.A6**, where the required and achieved phases are plotted for three wavelengths. The green line is the theoretical expectation of the maximum intensity trajectory. Measured deflection efficiencies of the gratings, defined as the power deflected by the gratings to the desired order, divided by the power reflected from a plain aluminum reflector (see Appendix 4.1 and Fig. **4.A8** for more details) are plotted in Figs. **4.5c** and **4.5d** for TE and TM illuminations, respectively. A similar difference in the efficiency of the gratings for TE and TM illuminations has also been observed in previous works [67, 125].

As another example for diffractive devices with controlled chromatic dispersion, four spherical-aberration-free focusing mirrors with different chromatic dispersions were designed, fabricated and measured using the same reflective dielectric meta-atoms. The mirrors are 240 μm in diameter and are designed to have a focal distance of 650 μm at 1520 nm. Figure **4.A7** shows the chosen post side lengths and the required as well as the achieved phase and group delays for the focusing mirrors with different dispersions. Figures **4.6a** and **4.6b** show simulated and measured focal distances for the four focusing mirrors (see Figs. **4.A9**, **4.A10**, and **4.A11** for detailed simulation and measurement results). The positive dispersion mirror is designed with dispersion twice as large as a regular mirror with the same focal distance, and the

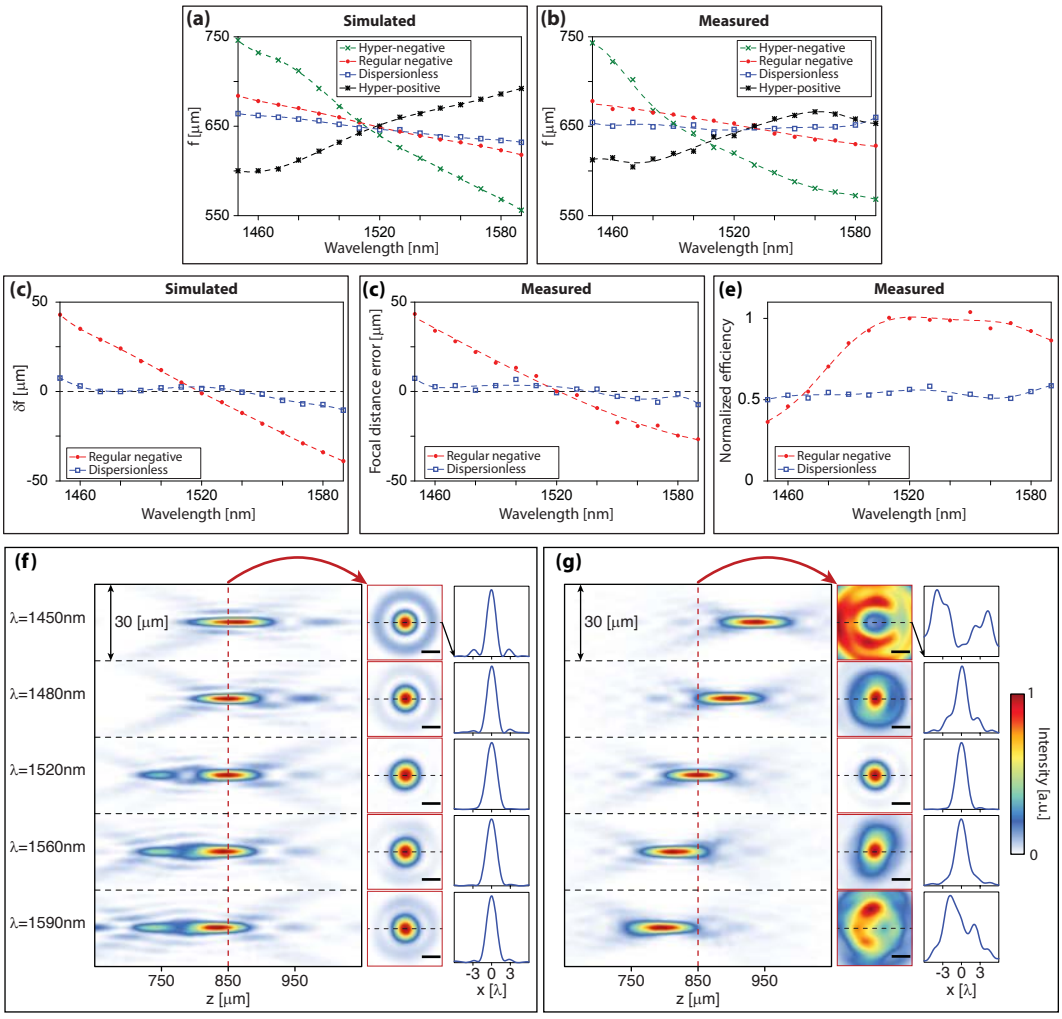

Figure 4.6: **Simulation and measurement results for focusing mirrors with different dispersion regimes. (a)** Simulated focal distance for focusing mirrors with different dispersions, designed using the reflective meta-atoms (see Fig. **4.A9** for axial plane intensity distributions). The mirrors are 240 μm in diameter and have a focal distance of 650 μm at 1520 nm. **(b)** Measured focal distances of the same focusing mirrors (see Figs. **4.A10** and **4.A11** for axial plane intensity distributions). **(c)** Simulated and **(d)** measured focal distance deviation from its design value of 850 μm as a function of wavelength for the dispersionless and regular mirrors (see Figs. **4.A12** and **4.A13** for extended simulation and measurement results). **(e)** Measured efficiency for the regular and dispersionless mirrors normalized to the efficiency of the regular device at its center wavelength of 1520 nm. **(f)** Measured intensity in the axial plane of the dispersionless metasurface mirror at five wavelengths (left). Intensity distributions measured in the desired focal plane (i.e., 850 μm away from the mirror surface) at the same wavelengths are shown in the center, and their one dimensional profiles along the *x* axis are plotted on the right. **(g)** Same plots as in **f** but for the regular mirror. Scale bars: 2λ.

hyper-dispersive mirror has a negative dispersion three and a half times larger than a regular one. The zero dispersion mirror shows a significantly reduced dispersion, while the hyper-dispersive one shows a highly enhanced dispersion. The positive mirror shows the expected dispersion in the ~1470–1560 nm range.

As an application of diffractive devices with dispersion control, we demonstrate a spherical-aberration-free focusing mirror with increased operation bandwidth. For brevity, we call this device dispersionless mirror. Since the absolute focal distance change is proportional to the focal distance itself, a relatively long focal distance is helpful for unambiguously observing the change in the device dispersion. Also, a higher NA value is preferred because it results in a shorter depth of focus, thus making the measurements easier. Having these considerations in mind, we have chosen a diameter of 500 μm and a focal distance of 850 μm (NA≈0.28) for the mirror, requiring a maximum dispersion of $\phi'_{\max} \approx -98$ Rad/μm which is achievable with the proposed reflective meta-atoms. We designed two dispersionless mirrors with two σ values of 300 and 50 nm. For comparison, we also designed a regular metasurface mirror for operation at $\lambda_0 = 1520$ nm and with the same diameter and focal distance as the dispersionless mirrors. The simulated focal distance deviations (from the designed 850 μm) for the regular and dispersionless ($\sigma = 300$ nm) mirrors are plotted in Fig. **4.6**(c), showing a considerable reduction in chromatic dispersion for the dispersionless mirror. Detailed simulation results for these mirrors are plotted in Fig. **4.A12**.

Figures **4.6d**–**4.6g** summarize the measurement results for the dispersionless and regular mirrors (see Appendix 4.1 and Fig. **4.A8** for measurement details and setup). As Figs. **4.6d** and **4.6g** show, the focal distance of the regular mirror changes almost linearly with wavelength. The dispersionless mirror, however, shows a highly diminished chromatic dispersion. Besides, as seen from the focal plane intensity measurements, while the dispersionless mirrors are in focus in the 850 μm plane throughout the measured bandwidth, the regular mirror is in focus only from 1500 to 1550 nm (see Figs. **4.A13** and **4.A14** for complete measurement results, and the Strehl ratios). Focusing efficiencies, defined as the ratio of the optical power focused by the mirrors to the power incident on them, were measured at different wavelengths for the regular and dispersionless mirrors (see Appendix 4.1 for details). The measured efficiencies were normalized to the efficiency of the regular metasurface mirror at its center wavelength of 1520 nm (which is estimated to be ~80%–90% based on Fig. **4.4**, measured grating efficiencies, and our previous works [67]). The

normalized efficiency of the dispersionless mirror is between 50% and 60% in the whole wavelength range and shows no significant reduction in contrast to the regular metasurface mirror.

4.5 Discussion

The reduction in efficiency compared to a mirror designed only for the center wavelength (i.e., the regular mirror) is caused by two main factors. First, the required region of the phase-dispersion plane is not completely covered by the reflective nano-post meta-atoms. Second, the meta-atom phase does not change linearly with respect to frequency in the relatively large bandwidth of 140 nm as would be ideal for a dispersionless metasurface. Both of these factors result in deviation of the phase profiles of the demonstrated dispersionless mirrors from the ideal ones. Furthermore, dispersionless metasurfaces use meta-atoms supporting resonances with high quality factors, thus leading to higher sensitivity of these devices to fabrication errors compared to the regular metasurfaces.

Equation 4.3 is basically a Taylor expansion of Eq. 4.2 kept to the first order. As a result, this equation is accurate only over the range of linearity of the phase given in Eq. 4.2. To increase the validity bandwidth, one can generalize the method to keep higher order terms of the series. Another method to address this issue is the Euclidean distance minimization method that was used in the design process of the devices presented here.

In conclusion, we demonstrated that independent control over phase and dispersion of meta-atoms can be used to engineer the chromatic dispersion of diffractive metasurface devices over continuous wavelength regions. This is in effect similar to controlling the "material dispersion" of meta-atoms to compensate, over-compensate, or increase the structural dispersion of diffractive devices. In addition, we developed a reflective dielectric metasurface platform that provides this independent control. Using this platform, we experimentally demonstrated gratings and focusing mirrors exhibiting positive, negative, zero, and enhanced dispersions. We also corrected the chromatic aberrations of a focusing mirror resulting in a ~3 times bandwidth increase (based on an Strehl ratio > 0.6, see Fig. **4.A14**). In addition, the introduced concept of metasurface design based on dispersion-phase parameters of the meta-atoms is general and can also be used for developing transmissive dispersion engineered metasurface devices.

Appendix 4.1: Simulation, fabrication, and measurement details

Simulation and design. The gratings with different dispersions discussed in Fig. **4.3c** were designed using hypothetical meta-atoms that completely cover the required region of the phase-dispersion plane. We assumed that the meta-atoms provide 100 different phase steps from 0 to 2π, and that for each phase, 10 different dispersion values are possible, linearly spanning the 0 to -150 Rad/μm range. We assumed that all the meta-atoms have a transmission amplitude of 1. The design began with constructing the ideal phase masks at eight wavelengths equally spaced in the 1450–1590 nm range. This results in a vector of eight complex numbers for the ideal transmission at each point on the metasurface grating. The meta-atoms were assumed to form a two dimensional square lattice with a lattice constant of 740 nm, and one vector was generated for each lattice site. The optimum meta-atom for each site was then found by minimizing the Euclidean distance between the transmission vector of the meta-atoms and the ideal transmission vector for that site. The resulting phase mask of the grating was then found through a two-dimensional interpolation of the complex valued transmission coefficients of the chosen meta-atoms. The grating area was assumed to be illuminated uniformly, and the deflection angle of the grating was found by taking the Fourier transform of the field after passing through the phase mask, and finding the angle with maximum intensity. A similar method was used to design and simulate the focusing mirrors discussed in Figs. **4.3d**–**4.3h**. In this case, the meta-atoms are assumed to cover dispersion values up to -200 Rad/μm. The meta-atoms provide 21 different dispersion values distributed uniformly in the 0 to -200 Rad/μm range. The focusing mirrors were designed and the corresponding phase masks were found in a similar manner to the gratings. A uniform illumination was used as the source, and the resulting field after reflection from the mirror was propagated in free space using a plane wave expansion method to find the intensity in the axial plane. The focal distances plotted in Fig. **4.3d** show the distance of the maximum intensity point from the mirrors at each wavelength. The gratings and focusing mirrors discussed in Figs. **4.5a**, **4.6a**, and **4.6c** are designed and simulated in exactly the same manner, except for using actual dielectric meta-atom reflection amplitudes and phases instead of the hypothetical ones.

If the actual meta-atoms provided an exactly linear dispersion (i.e., if their phase was exactly linear with frequency over the operation bandwidth), one could use the required values of the phase and dispersion at each lattice site to choose the best meta-atom (knowing the coordinates of one point on a line and its slope would suffice to determine the line exactly). The phases of the actual meta-atoms, however, do not

follow an exactly linear curve [Fig. **4.4d**]. Therefore, to minimize the error between the required phases, and the actual ones provided by the meta-atoms, we have used a minimum weighted Euclidean distance method to design the devices fabricated and tested in the chapter: at each point on the metasurface, we calculate the required complex reflection at eight wavelengths (1450–1590 nm, at 20 nm distances). We also calculate the complex reflection provided by each nano-post at the same wavelengths. To find the best meta-atom for each position, we calculate the weighted Euclidean distance between the required reflection vector, and the reflection vectors provided by the actual nano-posts. The nano-post with the minimum distance is chosen at each point. As a result, the chromatic dispersion is indirectly taken into account, not directly. The weight function can be used to increase or decrease the importance of each part of the spectrum depending on the specific application. In this work, we have chosen an inverted Gaussian weight function ($\exp((\lambda - \lambda_0)^2/2\sigma^2)$, $\lambda_0 = 1520$ nm, $\sigma = 300$ nm) for all the devices to slightly emphasize the importance of wavelengths farther from the center. In addition, we have also designed a dispersionless lens with $\sigma = 50$ nm (the measurement results of which are provided in Figs. **4.A13** and **4.A14**) for comparison. The choice of 8 wavelengths to form and compare the reflection vectors is relatively arbitrary; however, the phases of the nano-posts versus wavelength are smooth enough, such that they can be well approximated by line segments in 20 nm intervals. In addition, performing the simulations at 8 wavelengths is computationally not very expensive. Therefore, 8 wavelengths are enough for a 150 nm bandwidth here, and increasing this number may not result in a considerable improvement in the performance.

Reflection amplitude and phase of the meta-atoms were found using rigorous coupled wave analysis technique [217]. For each meta-atom size, a uniform array on a subwavelength lattice was simulated using a normally incident plane wave. The subwavelength lattice ensures the existence of only one propagating mode which justifies the use of only one amplitude and phase for describing the optical behavior at each wavelength. In the simulations, the α-Si layer was assumed to be 725 nm thick, the SiO_2 layer was 325 nm, and the aluminum layer was 100 nm thick. A 30-nm-thick Al_2O_3layer was added between the Al and the oxide layers (this layer served as an etch stop layer to avoid exposing the aluminum layer during the etch process). Refractive indices were set as follows in the simulations: SiO_2: 1.444, Al_2O_3: 1.6217, and Al: 1.3139-i13.858. The refractive index of α-Si used in the simulations is plotted in Fig. **4.A15**.

The FDTD simulations of the gratings [Figs. **4.5e**–**4.5h**] were performed using a normally incident plane-wave illumination with a Gaussian amplitude in time (and thus a Gaussian spectrum) in MEEP [234]. The reflected electric field was saved in a plane placed one wavelength above the input plane at time steps of 0.05 of the temporal period. The results in Figs. **4.5e**–**4.5h** are obtained via Fourier transforming the fields in time and space resulting in the reflection intensities as a function of frequency and transverse wave-vector.

Sample fabrication. A 100-nm aluminum layer and a 30-nm Al_2O_3 layer were deposited on a silicon wafer using electron beam evaporation. This was followed by deposition of 325 nm of SiO_2 and 725 nm of α-Si using the PECVD technique at 200 °C. A ~300 nm thick layer of ZEP-520A positive electron-beam resist was spun on the sample at 5000 rpm for 1 minute, and was baked at 180 °C for 3 minutes. The pattern was generated using a Vistec EBPG5000+ EBL system, and was developed for 3 minutes in the ZED-N50 developer (from Zeon Chemicals). A ~70-nm Al_2O_3 layer was subsequently evaporated on the sample, and the pattern was reversed with a lift off process. The Al_2O_3 hard mask was then used to etch the α-Si layer in a 3:1 mixture of SF_6 and C_4F_8 plasma. The mask was later removed using a 1:1 solution of ammonium hydroxide and hydrogen peroxide at 80° C.

Measurement procedure. The measurement setup is shown in Fig. **4.A8a**. Light emitted from a tunable laser source (TUNICS-Plus, Photonetics) was collimated using a fiber collimation package (F240APC-1550, Thorlabs), passed through a 50/50 beamsplitter (BSW06, Thorlabs), and illuminated the device. For grating measurements a lens with a 50-mm focal distance was also placed before the grating at a distance of ~45 mm to partially focus the beam and reduce the beam divergence after being deflected by the grating in order to decrease the measurement error (similar to Fig. **4.A8b**). The light reflected from the device was redirected using the same beamsplitter, and imaged using a custom built microscope. The microscope consists of a ×50 objective lens (LMPlanFL N, NA=0.5, Olympus), a tube lens with a 20-cm focal distance (AC254-200-C-ML, Thorlabs), and an InGaAs camera (320HX-1.7RT, Sensors Unlimited). The grating deflection angle was found by calculating the center of mass for the deflected beam imaged 3 mm away from the gratings surface. For efficiency measurements of the focusing mirrors, a flip mirror was used to send light towards an iris (2 mm diameter, corresponding to an approximately 40 μm iris in the object plane) and a photodetector (PM100D with an S122C head, Thorlabs). The efficiencies were normalized to the efficiency of the

regular mirror at its center wavelength by dividing the detected power through the iris by the power measured for the regular mirror at its center wavelength. The measured intensities were up-sampled using their Fourier transforms in order to achieve smooth intensity profiles in the focal and axial planes. To measure the grating efficiencies, the setup shown in Fig. **4.A8b** was used, and the photodetector was placed ~50 mm away from the grating, such that the other diffraction orders fall outside its active area. The efficiency was found by calculating the ratio of the power deflected by the grating to the power normally reflected by the aluminum reflector in areas of the sample with no grating. The beam-diameter on the grating was calculated using the setup parameters, and it was found that ~84% of the power was incident on the 90 μm wide gratings. This number was used to correct for the lost power due to the larger size of the beam compared to the grating.

Appendix 4.2: Chromatic dispersion of diffractive devices.

Chromatic dispersion of a regular diffractive grating or lens is set by its function. The grating momentum for a given order of a grating with a certain period is constant and does not change with changing the wavelength. If we denote the size of the grating reciprocal lattice vector of interest by k_G, we get

$$\sin(\theta) = \frac{k_G}{2\pi/\lambda} \Rightarrow \theta = \sin^{-1}(\frac{k_G}{2\pi/\lambda}), \tag{4.4}$$

where θ is the deflection angle at a wavelength λ for normally incident beam. The chromatic angular dispersion of the grating ($\mathrm{d}\theta/\mathrm{d}\lambda$) is then given by

$$\frac{\mathrm{d}\theta}{\mathrm{d}\lambda} = \frac{k_G/2\pi}{\sqrt{1-(k_G\lambda/2\pi)^2}} = \frac{\tan(\theta)}{\lambda}, \tag{4.5}$$

and in terms of frequency

$$\frac{\mathrm{d}\theta}{\mathrm{d}\omega} = -\frac{\tan(\theta)}{\omega}. \tag{4.6}$$

Therefore, the dispersion of a regular grating only depends on its deflection angle and the wavelength. Similarly, focal distance of one of the focal points of diffractive and metasurface lenses changes as $\mathrm{d}f/\mathrm{d}\lambda = -f/\lambda$ (thus $\mathrm{d}f/\mathrm{d}\omega = f/\omega$ ([135, 219, 233]).

Appendix 4.3: Chromatic dispersion of multiwavelength diffractive devices.

As it is mentioned in the main text, multiwavelength diffractive devices ([135, 227, 233]) do not change the dispersion of a given order in a grating or lens. They are essentially multi-order gratings or lenses, where each order has the regular (negative)

diffractive chromatic dispersion. These devices are designed such that at certain distinct wavelengths of interest, one of the orders has the desired deflection angle or focal distance. If the blazing of each order at the corresponding wavelength is perfect, all of the power can be directed towards that order at that wavelength. However, at wavelengths in between the designed wavelengths, where the grating or lens is not corrected, the multiple orders have comparable powers, and show the regular diffractive dispersion. This is schematically shown in Fig. **4.A1a**. Figure **4.A1b** compares the chromatic dispersion of a multi-wavelength diffractive lens to a typical refractive apochromatic lens.

Appendix 4.4: Generalization of chromatic dispersion control to nonzero dispersions.

Here we present the general form of equations for the dispersion engineered metasurface diffractive devices. We assume that the function of the device is set by a parameter $\xi(\omega)$, where we have explicitly shown its frequency dependence. For instance, ξ might denote the deflection angle of a grating or the focal distance of a lens. The phase profile of a device with a desired $\xi(\omega)$ is given by

$$\phi(x, y, \xi(\omega); \omega) = \omega T(x, y, \xi(\omega)), \tag{4.7}$$

which is the generalized form of the Eq. 4.1. We are interested in controlling the parameter $\xi(\omega)$ and its dispersion (i.e., derivative) at a given frequency ω_0. $\xi(\omega)$ can be approximated as $\xi(\omega) \approx \xi_0 + \partial\xi/\partial\omega|_{\omega=\omega_0}(\omega - \omega_0)$ over a narrow bandwidth around ω_0. Using this approximation, we can rewrite Eq. 4.7 as

$$\phi(x, y; \omega) = \omega T(x, y, \xi_0 + \partial\xi/\partial\omega|_{\omega=\omega_0}(\omega - \omega_0)). \tag{4.8}$$

At ω_0, this reduces to

$$\phi(x, y; \omega)|_{\omega=\omega_0} = \omega_0 T(x, y, \xi_0), \tag{4.9}$$

and the phase dispersion at ω_0 is given by

$$\frac{\partial\phi(x, y; \omega)}{\partial\omega}|_{\omega=\omega_0} = T(x, y, \xi_0) + \partial\xi/\partial\omega|_{\omega=\omega_0}\omega_0\frac{\partial T(x, y, \xi)}{\partial\xi}|_{\xi=\xi_0}. \tag{4.10}$$

Based on Eqs. 4.9 and 4.10, the values of ξ_0 and $\partial\xi/\partial\omega|_{\omega=\omega_0}$ can be set independently, if the phase $\phi(x, y, \omega_0)$ and its derivative $\partial\phi/\partial\omega$ can be controlled simultaneously and independently. Therefore, the device function at ω_0 (determined by the value

of ξ_0) and its dispersion (determined by $\partial\xi/\partial\omega|_{\omega=\omega_0}$) will be decoupled. The zero dispersion case is a special case of Eq. 4.10 with $\partial\xi/\partial\omega|_{\omega=\omega_0} = 0$. In the following we apply these results to the special cases of blazed gratings and spherical-aberration-free lenses (also correct for spherical-aberration-free focusing mirrors).

For a 1-dimensional conventional blazed grating we have $\xi = \theta$ (the deflection angle), and $T = -x\sin(\theta)$. Therefore the phase profile with a general dispersion is given by

$$\phi(x;\omega) = -\omega x \sin[\theta_0 + D(\omega - \omega_0)], \tag{4.11}$$

where $D = \partial\theta/\partial\omega|_{\omega=\omega_0} = \nu D_0$, and $D_0 = -\tan(\theta_0)/\omega_0$ is the angular dispersion of a regular grating with deflection angle θ_0 at the frequency ω_0. We have chosen to express the generalized dispersion D as a multiple of the regular dispersion D_0 with a real number ν to benchmark the change in dispersion. For instance, $\nu = 1$ corresponds to a regular grating, $\nu = 0$ represents a dispersionless grating, $\nu = -1$ denotes a grating with positive dispersion, and $\nu = 3$ results in a grating three-times more dispersive than a regular grating (i.e., hyper-dispersive). Various values of ν can be achieved using the method of simultaneous control of phase and dispersion of the meta-atoms, and thus we can break this fundamental relation between the deflection angle and angular dispersion. The phase derivative necessary to achieve a certain value of ν is given by

$$\frac{\partial\phi(x;\omega)}{\partial\omega}|_{\omega=\omega_0} = -x/c\sin(\theta_0)(1-\nu), \tag{4.12}$$

or in terms of wavelength

$$\frac{\partial\phi(x;\lambda)}{\partial\lambda}|_{\lambda=\lambda_0} = \frac{2\pi}{{\lambda_0}^2} x\sin(\theta_0)(1-\nu). \tag{4.13}$$

For a spherical-aberration-free lens we have $\xi = f$ and $T(x,y,f) = -\sqrt{x^2+y^2+f^2}/c$. Again we can approximate f with its linear approximation $f(\omega) = f_0 + D(\omega-\omega_0)$, with $D = \partial f/\partial\omega|_{\omega=\omega_0}$ denoting the focal distance dispersion at $\omega = \omega_0$. The regular dispersion for such a lens is given by $D_0 = f_0/\omega_0$. Similar to the gratings, we can write the more general form for the focal distance dispersion as $D = \nu D_0$, where ν is some real number. In this case, the required phase dispersion is given by

$$\frac{\partial\phi(x,y;\omega)}{\partial\omega}|_{\omega=\omega_0} = -\frac{1}{c}[\sqrt{x^2+y^2+{f_0}^2} + \frac{\nu {f_0}^2}{\sqrt{x^2+y^2+{f_0}^2}}], \tag{4.14}$$

which can also be expressed in terms of wavelength

$$\frac{\partial\phi(x,y;\lambda)}{\partial\lambda}|_{\lambda=\lambda_0} = \frac{2\pi}{{\lambda_0}^2}[\sqrt{x^2+y^2+{f_0}^2} + \frac{\nu {f_0}^2}{\sqrt{x^2+y^2+{f_0}^2}}]. \tag{4.15}$$

Appendix 4.5: Maximum meta-atom dispersion required for controlling chromatic dispersion of gratings and lenses.

Since the maximum achievable dispersion is limited by the meta-atom design, it is important to find a relation between the maximum dispersion required for implementation of a certain metasurface device, and the device parameters (e.g., size, focal distance, deflection angle, etc.). Here we find these maximums for the cases of gratings and lenses with given desired dispersions.

For the grating case, it results from Eq. 4.13 that the maximum required dispersion is given by

$$\max\left(\frac{\partial\phi(x;\lambda)}{\partial\lambda}|_{\lambda=\lambda_0}\right) = k_0 X \frac{\sin(\theta_0)}{\lambda_0}(1-\nu), \tag{4.16}$$

where X is the length of the grating, and $k_0 = 2\pi/\lambda_0$ is the wavenumber. It is important to note that based on the value of ν, the sign of the meta-atom dispersion changes. However, in order to ensure a positive group velocity for the meta-atoms, the dispersions should be negative. Thus, if $1-\nu > 0$, a term should be added to make the dispersion values negative. We can always add a term of type $\phi_0 = kL_0$ to the phase without changing the function of the device. This term can be used to shift the required region in the phase-dispersion plane. Therefore, it is actually the difference between the minimum and maximum of Eqs. 4.13 and 4.15 that sets the maximum required dispersion. Using a similar procedure, we find the maximum necessary dispersion for a spherical-aberration-free lens as

$$\phi'_{\max} = -\frac{k_0 f}{\lambda_0}\begin{cases} \frac{\Theta+\nu}{\sqrt{\Theta}} - 1 - \nu & \nu < 1 \\ \frac{\Theta+\nu}{\sqrt{\Theta}} - 2\sqrt{\nu} & 1 < \nu < \sqrt{\Theta} \\ (1-\sqrt{\nu})^2 & \sqrt{\Theta} < \nu < \Theta \\ -(\frac{\Theta+\nu}{\sqrt{\Theta}} - 1 - \nu) & \Theta < \nu \end{cases}, \tag{4.17}$$

where f is the focal distance of the lens, and $\Theta = (f^2+R^2)/f^2 = 1/(1-\mathrm{NA}^2)$ (R: lens radius, NA: numerical aperture). $\log\left[\phi'_{\max}/(-k_0 f/\lambda_0)\right]$ is plotted in Fig. **4.A2a** as a function of NA and ν. In the simpler case of dispersionless lenses (i.e., $\nu = 0$), Eq. 4.17 can be further simplified to

$$\phi'_{\max} = -\frac{k_0 R}{\lambda}\frac{1-\sqrt{1-\mathrm{NA}^2}}{\mathrm{NA}} \approx -\frac{k_0 R \mathrm{NA}}{2\lambda}, \tag{4.18}$$

where R is the lens radius and the approximation is valid for small values of NA. The maximum required dispersion for the dispersionless lens is normalized to $-k_0 R/\lambda_0$ and is plotted in Fig. **4.A2b** as a function of NA.

Appendix 4.6: Fermat's principle and the phase dispersion relation.

Phase only diffractive devices can be characterized by a local grating momentum (or equivalently phase gradient) resulting in a local deflection angle at each point on their surface. Here we consider the case of a 1D element with a given local phase gradient (i.e., $\phi_x = \partial\phi/\partial x$) and use Fermat's principle to connect the frequency derivative of the local deflection angle (i.e., chromatic dispersion) to the frequency derivative of ϕ_x (i.e., $\partial\phi_x/\partial\omega$). For simplicity, we assume that the illumination is close to normal, and that the element phase does not depend on the illumination angle (which is in general correct in local metasurfaces and diffractive devices).

Considering Fig. **4.A16a**, we can write the phase acquired by a ray going from point A to point B, and passing the interface at x as

$$\Phi(x,\omega) = \frac{\omega}{\mathrm{c}}[\mathrm{n}_1\sqrt{x^2 + {y_A}^2} + \mathrm{n}_2\sqrt{(d-x)^2 + {y_B}^2}] + \phi(x,\omega), \tag{4.19}$$

To minimize this phase we need

$$\frac{\partial\Phi(x,\omega)}{\partial x} = \frac{\omega}{\mathrm{c}}[\frac{\mathrm{n}_1 x}{\sqrt{x^2 + {y_A}^2}} + \frac{\mathrm{n}_2(d-x)}{\sqrt{(d-x)^2 + {y_B}^2}}] + \phi_x = 0. \tag{4.20}$$

For this minimum to occur at point O (i.e., $x = 0$)

$$\phi_x(\omega) = \frac{\omega}{\mathrm{c}}\frac{\mathrm{n}_2 d}{r} = \frac{\mathrm{n}_2\omega}{\mathrm{c}}\sin(\theta(\omega)), \tag{4.21}$$

which is a simple case of the diffraction equation, and where $r = \sqrt{d^2 + {y_B}^2}$ is the OB length. At $\omega + \mathrm{d}\omega$, we get the following phase for the path from A to B' [Fig. **4.A16**(b)]

$$\begin{aligned}\Phi(x,\omega+\mathrm{d}\omega) =& \frac{\omega+\mathrm{d}\omega}{\mathrm{c}}[\mathrm{n}_1\sqrt{x^2 + {y_A}^2} \\ &+ \mathrm{n}_2\sqrt{(d-x+\mathrm{d}x)^2 + (y_B+\mathrm{d}y)^2}] + \phi(x,\omega+\mathrm{d}\omega),\end{aligned} \tag{4.22}$$

where we have chosen B' such that OB and OB' have equal lengths. Minimizing the path passing through O

$$\phi_x(\omega+\mathrm{d}\omega) = \frac{\omega+\mathrm{d}\omega}{\mathrm{c}}\frac{\mathrm{n}_2(d+dx)}{r} = \frac{\mathrm{n}_2(\omega+\mathrm{d}\omega)}{\mathrm{c}}\sin(\theta(\omega+\mathrm{d}\omega)), \tag{4.23}$$

subtracting 4.21 from 4.23, and setting $\phi_x(\omega+\mathrm{d}\omega) - \phi_x(\omega) = \frac{\partial\phi_x}{\partial\omega}\mathrm{d}\omega$, we get

$$\frac{\partial\phi_x}{\partial\omega} = \frac{\mathrm{n}_2}{c}\sin(\theta(\omega)) + \frac{\mathrm{d}\theta}{\mathrm{d}\omega}\frac{\mathrm{n}_2\omega}{c}\cos(\theta(\omega)). \tag{4.24}$$

One can easily recognize the similarity between Eqs. 4.24 and 4.10.

Appendix 4.7: Relation between dispersion and quality factor of highly reflective or transmissive meta-atoms.

Here we show that the phase dispersion of a meta-atom is linearly proportional to the stored optical energy in the meta-atoms, or equivalently, to the quality factor of the resonances supported by the mata-atoms. To relate the phase dispersion of transmissive or reflective meta-atoms to the stored optical energy, we follow an approach similar to the one taken in chapter 8 of [263] for finding the dispersion of a single port microwave circuit. We start from the frequency domain Maxwell's equations

$$\begin{aligned} \nabla \times E &= i\omega\mu H, \\ \nabla \times H &= -i\omega\epsilon E, \end{aligned} \tag{4.25}$$

and take the derivative of the Eq. 4.25 with respect to frequency

$$\nabla \times \frac{\partial E}{\partial \omega} = i\mu H + i\omega\mu \frac{\partial H}{\partial \omega}, \tag{4.26}$$

$$\nabla \times \frac{\partial H}{\partial \omega} = -i\epsilon E - i\omega\epsilon \frac{\partial E}{\partial \omega}. \tag{4.27}$$

Multiplying Eq. 4.26 by H^* and the conjugate of Eq. 4.27 by $\partial E/\partial\omega$, and subtracting the two, we obtain

$$\nabla \cdot (\frac{\partial E}{\partial \omega} \times H^*) = i\mu|H|^2 + i\omega\mu \frac{\partial H}{\partial \omega} \cdot H^* - i\omega\epsilon \frac{\partial E}{\partial \omega} \cdot E^*. \tag{4.28}$$

Similarly, multiplying Eq. 4.27 by E^* and the conjugate of Eq. 4.26 by $\partial H/\partial\omega$, and subtracting the two we find

$$\nabla \cdot (\frac{\partial H}{\partial \omega} \times E^*) = -i\epsilon|E|^2 - i\omega\epsilon \frac{\partial E}{\partial \omega} \cdot E^* + i\omega\mu \frac{\partial H}{\partial \omega} \cdot H^*. \tag{4.29}$$

Subtracting Eq. 4.29 from Eq. 4.28 we get

$$\nabla \cdot (\frac{\partial E}{\partial \omega} \times H^* - \frac{\partial H}{\partial \omega} \times E^*) = i\mu|H|^2 + i\epsilon|E|^2. \tag{4.30}$$

Integrating both sides of Eq. 4.30, and using the divergence theorem to convert the left side to a surface integral leads to

$$\oint_{\partial V} (\frac{\partial E}{\partial \omega} \times H^* - \frac{\partial H}{\partial \omega} \times E^*) = i \int_V (\mu|H|^2 + \epsilon|E|^2) dv = 2iU, \tag{4.31}$$

where U is the total electromagnetic energy inside the volume V, and ∂V denotes the surrounding surface of the volume. Now we consider a metasurface composed

of a subwavelength periodic array of meta-atoms as shown in Fig. **4.A17**. We also consider two virtual planar boundaries Γ_1 and Γ_2 on both sides on the metasurface (shown with dashed lines in Fig. **4.A17**). The two virtual boundaries are considered far enough from the metasurface that the metasurface evanescent fields die off before reaching them. Because the metasurface is periodic with a subwavelength period and preserves polarization, we can write the transmitted and reflected fields at the virtual boundaries in terms of only one transmission t and reflection r coefficients. The fields at these two boundaries are given by

$$\begin{aligned} E_1 &= E + rE \\ H_1 &= -\hat{z} \times (\frac{E}{\eta_1} - r\frac{E}{\eta_1}) \\ E_2 &= tE \\ H_2 &= -t\hat{z} \times \frac{E}{\eta_2} \end{aligned}, \tag{4.32}$$

where E is the input field, E_1 and E_2 are the total electric fields at Γ_1 and Γ_2, respectively, and η_1 and η_2 are wave impedances in the materials on the top and bottom of the metasurface.

Inserting fields from Eq. 4.32 to Eq. 4.31, and using the uniformity of the fields to perform the integration over one unit of area, we get

$$\frac{\partial r}{\partial \omega} r^* \frac{|E|^2}{\eta_1} + \frac{\partial t}{\partial \omega} t^* \frac{|E|^2}{\eta_2} = i\tilde{U}, \tag{4.33}$$

where $\tilde{U}$ is the optical energy per unit area that is stored in the metasurface layer. For a loss-less metasurface that is totally reflective (i.e., $t = 0$ and $r = e^{i\phi}$), we obtain

$$\frac{\partial \phi}{\partial \omega} = \frac{\tilde{U}}{P_{\text{in}}}, \tag{4.34}$$

where we have used $P_{\text{in}} = |E|^2/\eta_1$ to denote the per unit area input power. Finally, the dispersion can be expressed as

$$\frac{\partial \phi}{\partial \lambda} = \frac{\partial \phi}{\partial \omega}\frac{\partial \omega}{\partial \lambda} = -\frac{\omega}{\lambda}\frac{\tilde{U}}{P_{\text{in}}}. \tag{4.35}$$

We used Eq. 4.35 throughout the work to calculate the dispersion from solution of the electric and magnetic fields at a single wavelength, which reduced simulation time by a factor of two. In addition, in steady state the input and output powers are equal $P_{\text{out}} = P_{\text{in}}$, and therefore we have

$$\frac{\partial \phi}{\partial \lambda} = -\frac{1}{\lambda}\frac{\omega \tilde{U}}{P_{\text{out}}} = -\frac{Q}{\lambda}, \tag{4.36}$$

where we have assumed that almost all of the stored energy is in one single resonant mode, and Q is the quality factor of that mode. Therefore, in order to achieve large dispersion values, resonant modes with high quality factors are necessary.

Appendix 4.8: Supporting figures.

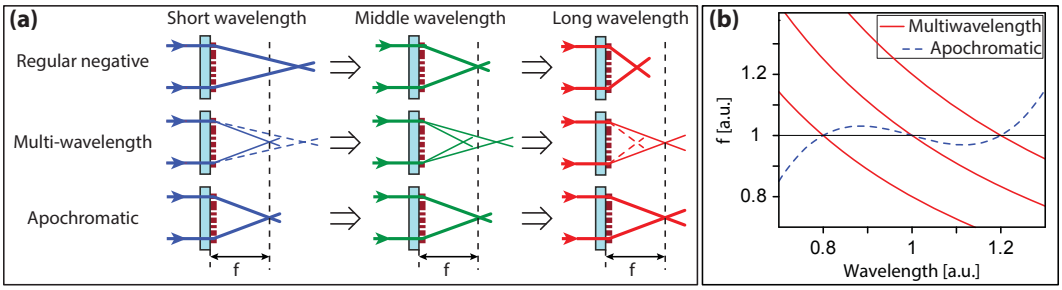

Figure 4.A1: **Comparison of regular, multi-wavelength, and apochromatic lenses. (a)** Schematic comparison of a regular, a multi-wavelength, and an apochromatic metasurface lens. The multi-wavelength lens is corrected at a short and a long wavelength to have a single focal point at a distance f, but it has two focal points at wavelengths in between them, none of which is at f. The apochromatic lens is corrected at the same short and long wavelengths, and in wavelengths between them it will have a single focus very close to f. **(b)** Focal distances for three focal points of a multiwavelength lens corrected at three wavelengths, showing the regular dispersion (i.e., $f \propto 1/\lambda$) of each focus with wavelength. For comparison, focal distance for the single focus of a typical apochromatic lens is plotted.

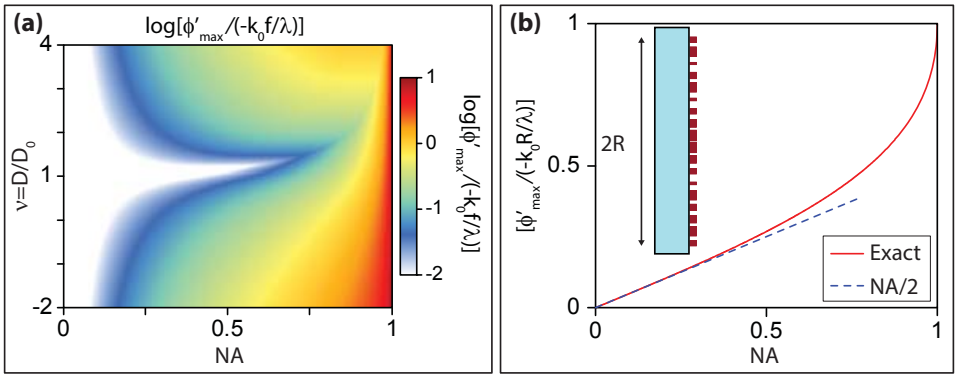

Figure 4.A2: **Maximum required dispersion of meta-atoms for lenses. (a)** Maximum meta-atom dispersion necessary to control the dispersion of a spherical-aberration-free lens. The maximum dispersion is normalized to $-k_0 f/\lambda_0$ and is plotted on a logarithmic scale. **(b)** Normalized (to $-k_0 R/\lambda_0$) maximum dispersion required for a dispersionless lens. R is the radius, f is the focal distance, and NA is the numerical aperture of the lens.

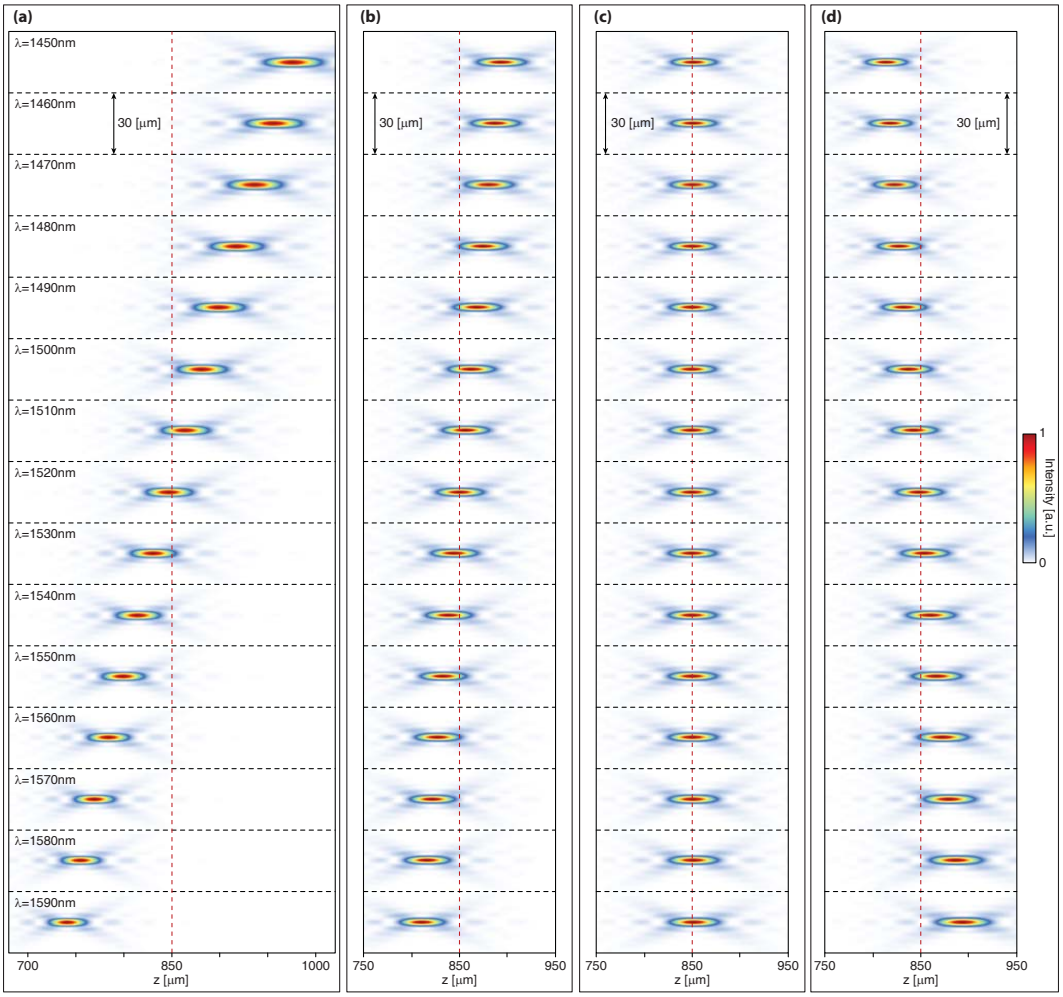

Figure 4.A3: **Simulated axial intensity distribution for focusing mirrors with different dispersions designed using hypothetical meta-atoms.** **(a)** Hyper-dispersive mirror. **(b)** Mirror with regular dispersion. **(c)** Mirror with zero dispersion. **(d)** Mirror with positive dispersion.

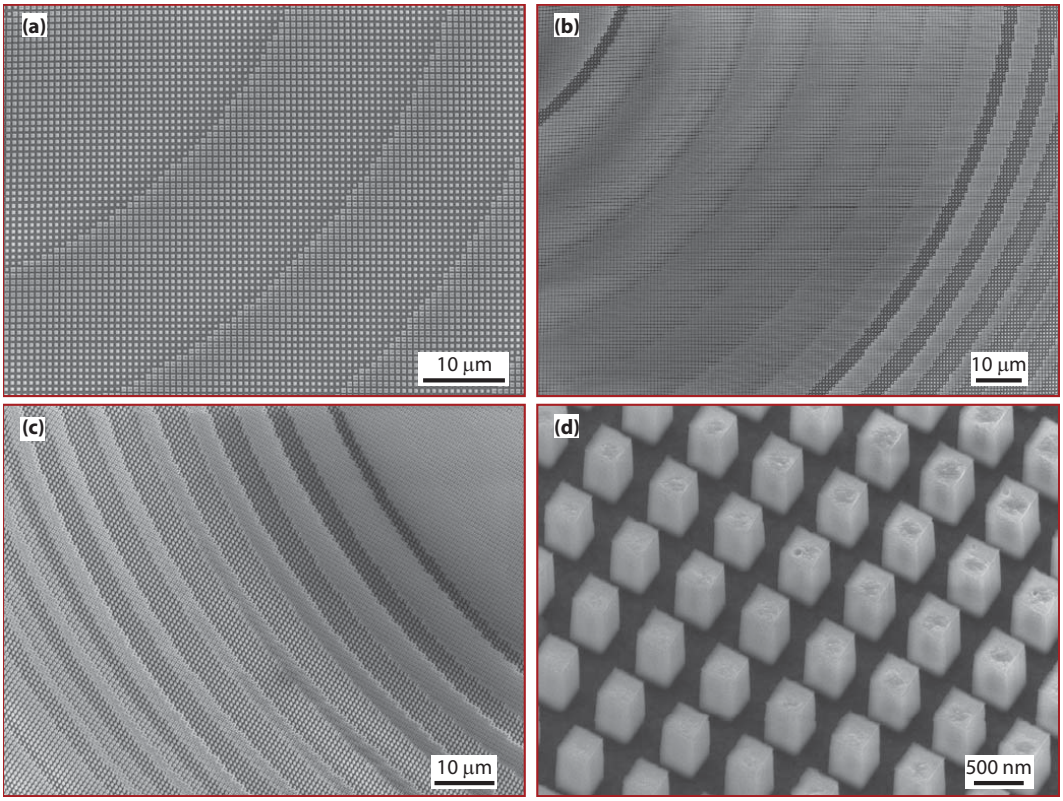

Figure 4.A4: **Scanning electron micrographs of metasurface focusing mirrors with 850 μm focal distance.** **(a)** Regular metasurface mirror. **(b)** Dispersionless metasurface mirror with $\sigma = 300$ nm, and **(c)** $\sigma = 50$ nm. **(d)** Fabricated meta-atoms.

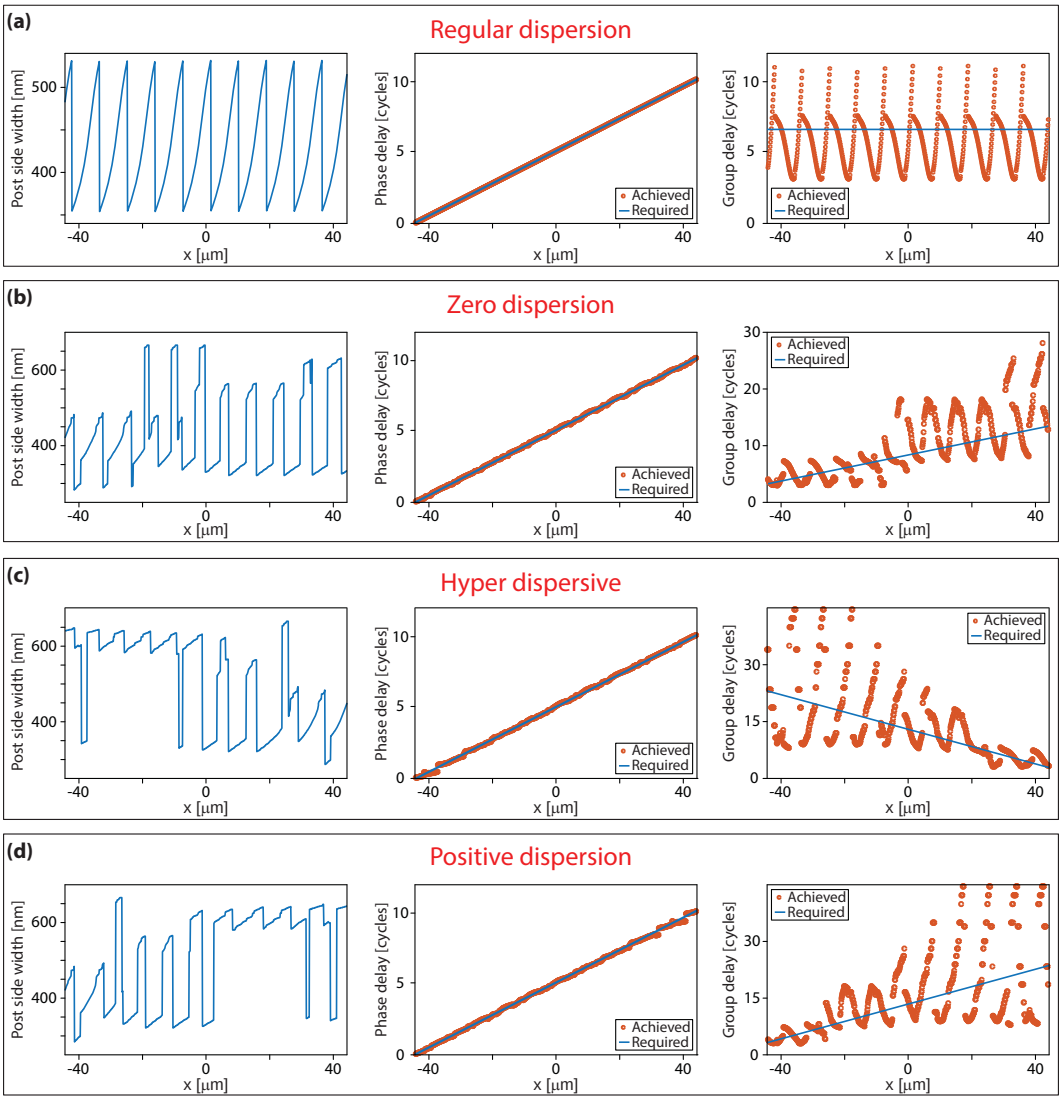

Figure 4.A5: **Chosen nano-post side lengths for gratings and their corresponding phase and group delays. (a)** The chosen nano-post side length (left), phase delay (center), and group delay (right) at 1520 nm for the fabricated regular grating. **(b)–(d)** Same as **a** for the dispersionless, hyper-dispersive, and positive-dispersion gratings respectively.

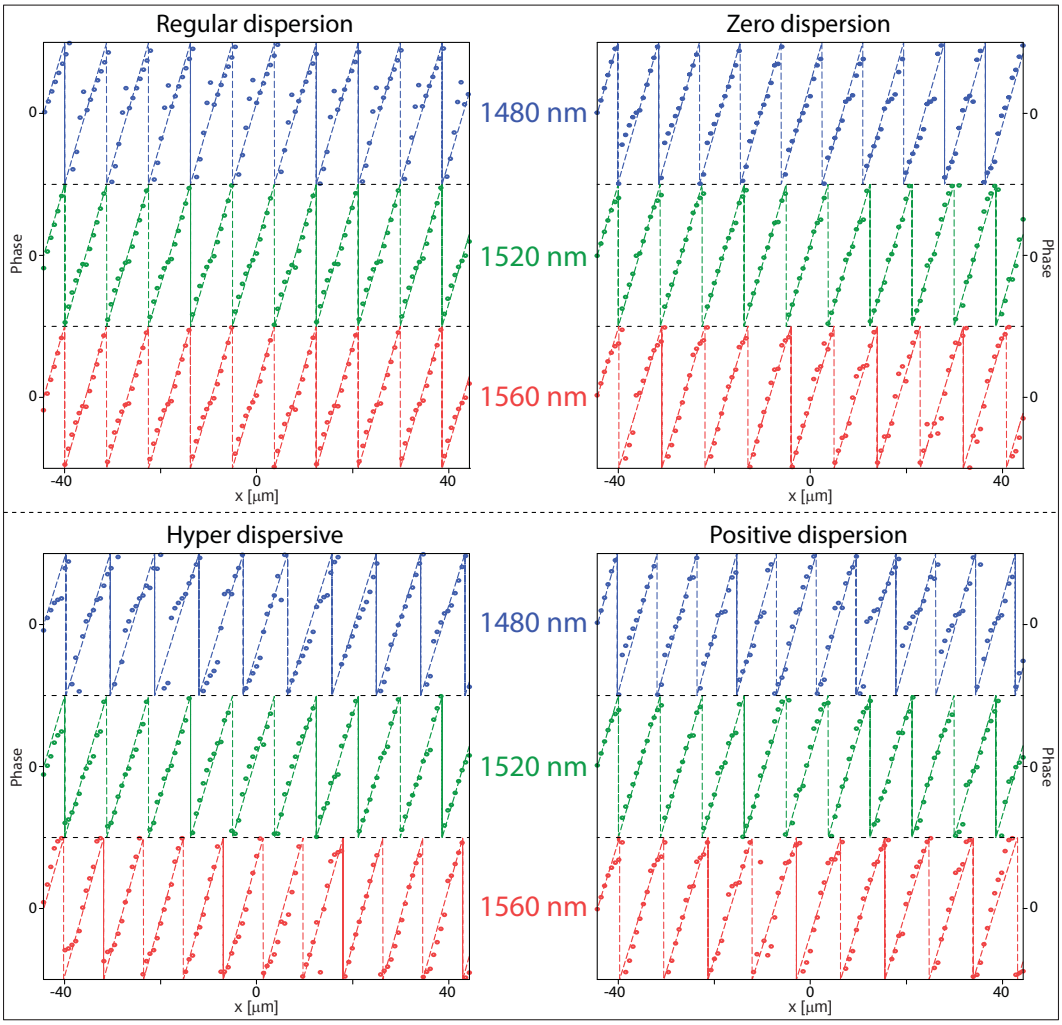

Figure 4.A6: **Required and achieved phase values for gratings at three wavelengths.** The phase delays are wrapped to the $-\pi$ to π range. While the effective grating pitch is constant for the regular grating, it changes with wavelength in all other cases.

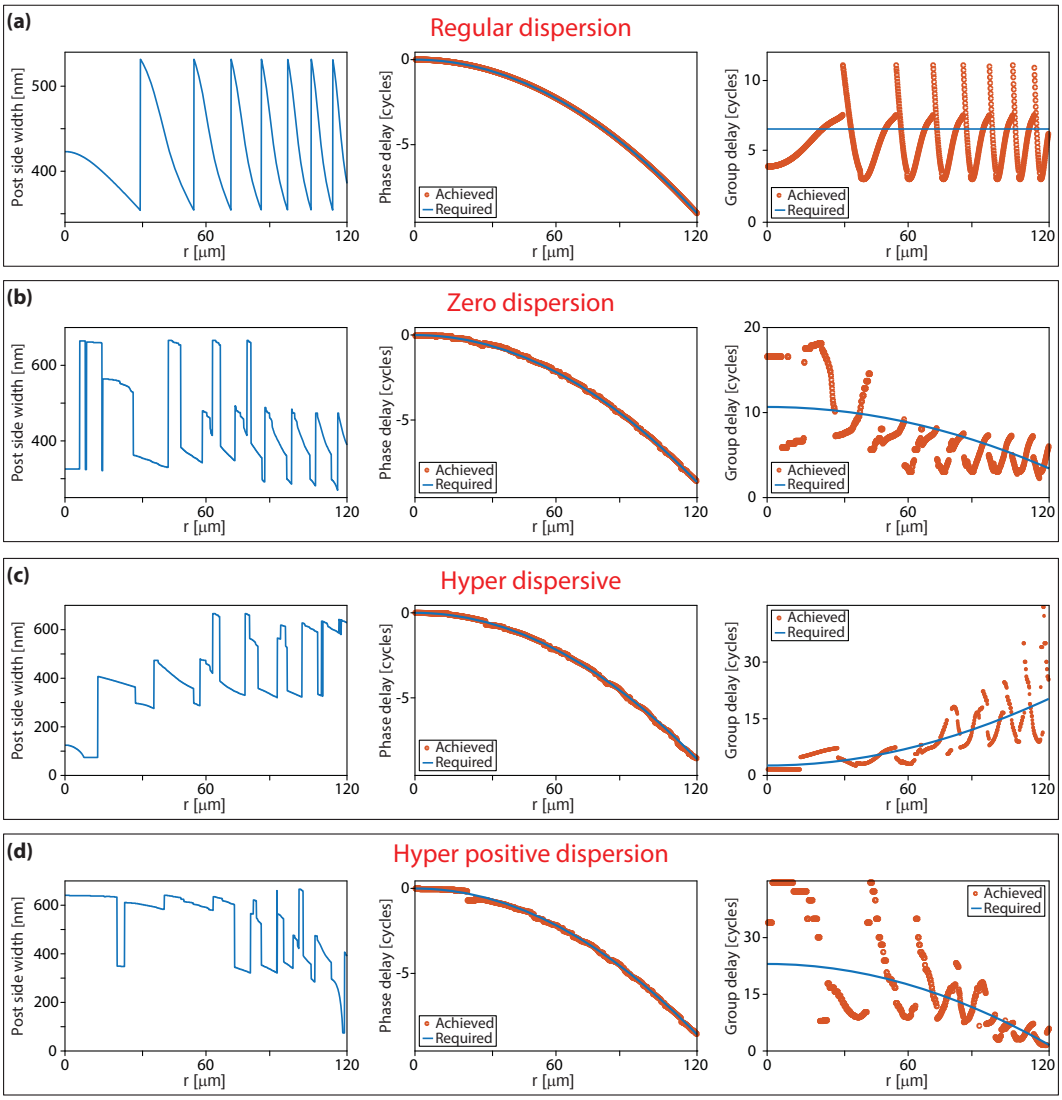

Figure 4.A7: **Chosen nano-post side lengths for focusing mirrors and their corresponding phase and group delays. (a)** The chosen nano-post side length (left), phase delay (center), and group delay (right) at 1520 nm for the fabricated 240 μm regular focusing mirror. **(b)**–**(d)** Same as **a** for the dispersionless, hyper-dispersive, and positive-dispersion focusing mirrors respectively.

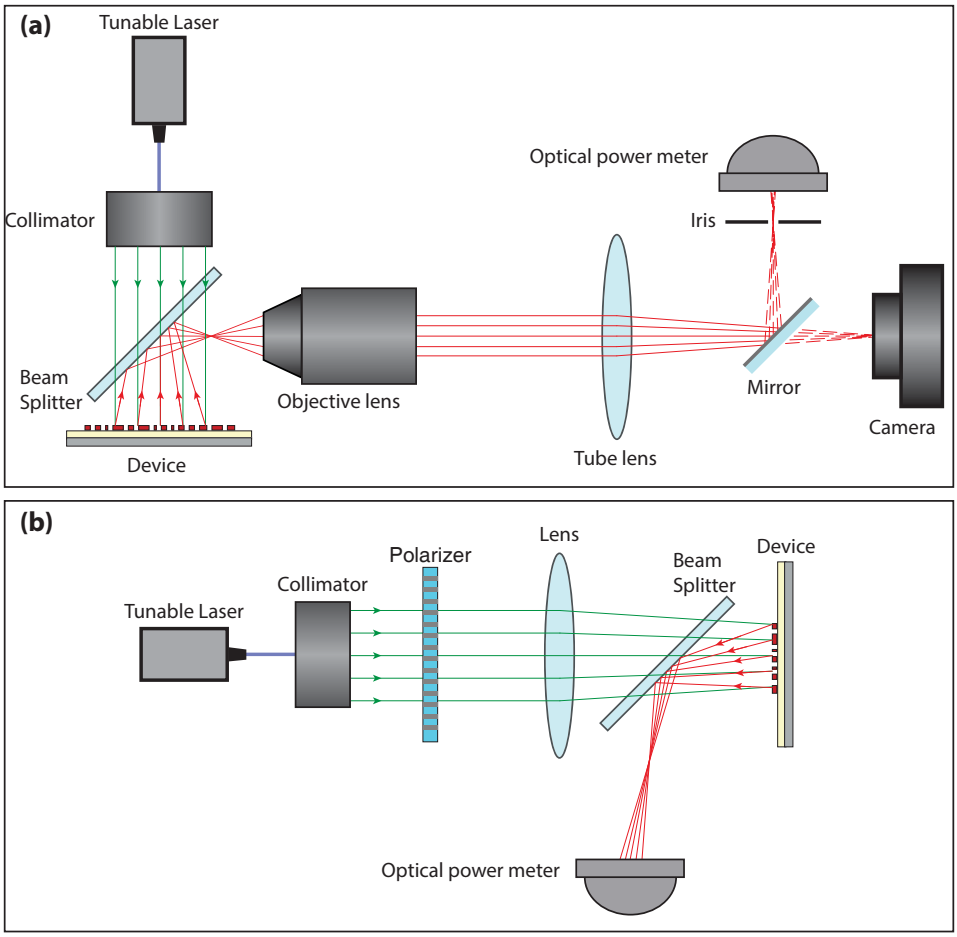

Figure 4.A8: **Measurement setups. (a)** Schematic illustration of the setup used to measure the deflection angles of gratings, and focus patterns and axial plane intensity distributions of focusing mirrors at different wavelengths. To measure the efficiency of the focusing mirrors, the flip mirror, iris, and optical power meter were used. **(b)** The setup used to measure the efficiencies of the gratings. The power meter was placed at a long enough distance such that the other diffraction orders fell safely outside its active aperture area.

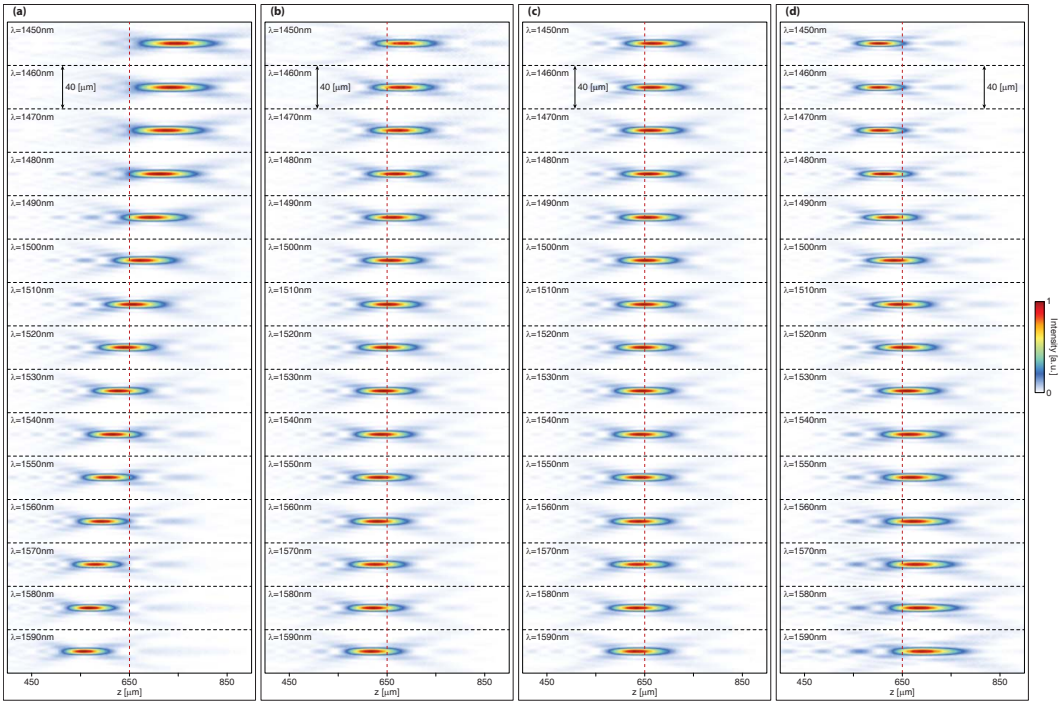

Figure 4.A9: **Simulated axial intensity distribution for focusing mirrors with different dispersions** designed using the reflective α-Si nano-posts discussed in Fig. **4.6a**. **(a)** Hyper-dispersive mirror. **(b)** Mirror with regular dispersion. **(c)** Mirror with zero dispersion. **(d)** Mirror with a positive dispersion with an amplitude twice the regular negative dispersion.

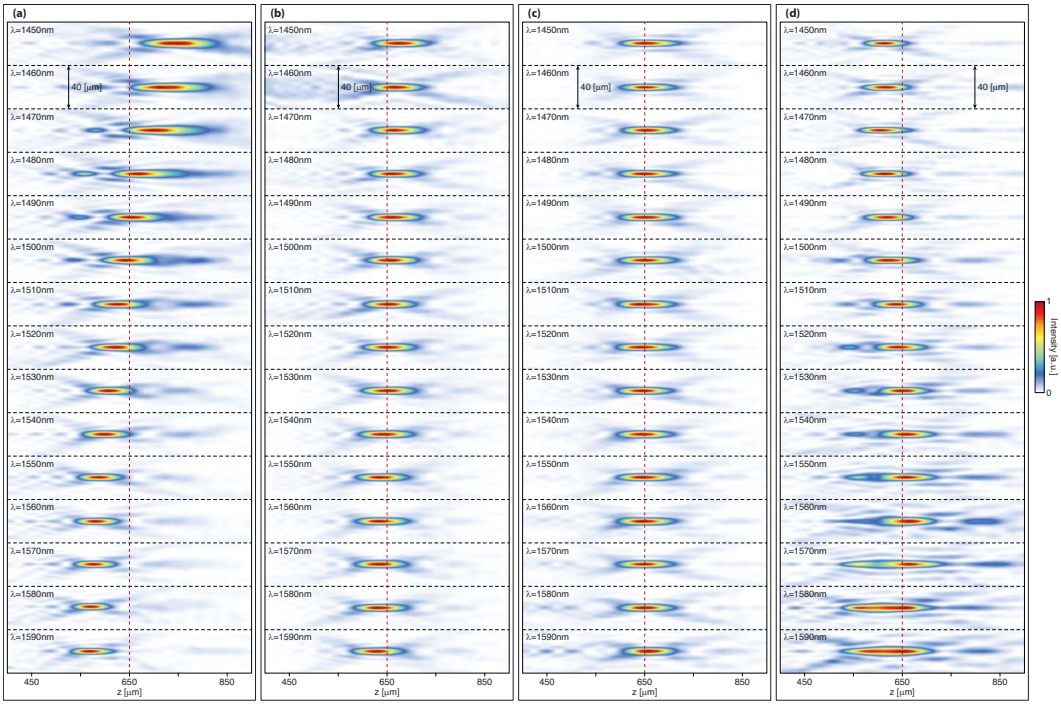

Figure 4.A10: **Measured axial intensity distributions for focusing mirrors with different dispersions** designed using the reflective α-Si nano-posts discussed in Fig. **4.6b**. **(a)** Hyper-dispersive mirror. **(b)** Mirror with regular dispersion. **(c)** Mirror with zero dispersion. **(d)** Mirror with a positive dispersion with an amplitude twice the regular negative dispersion.

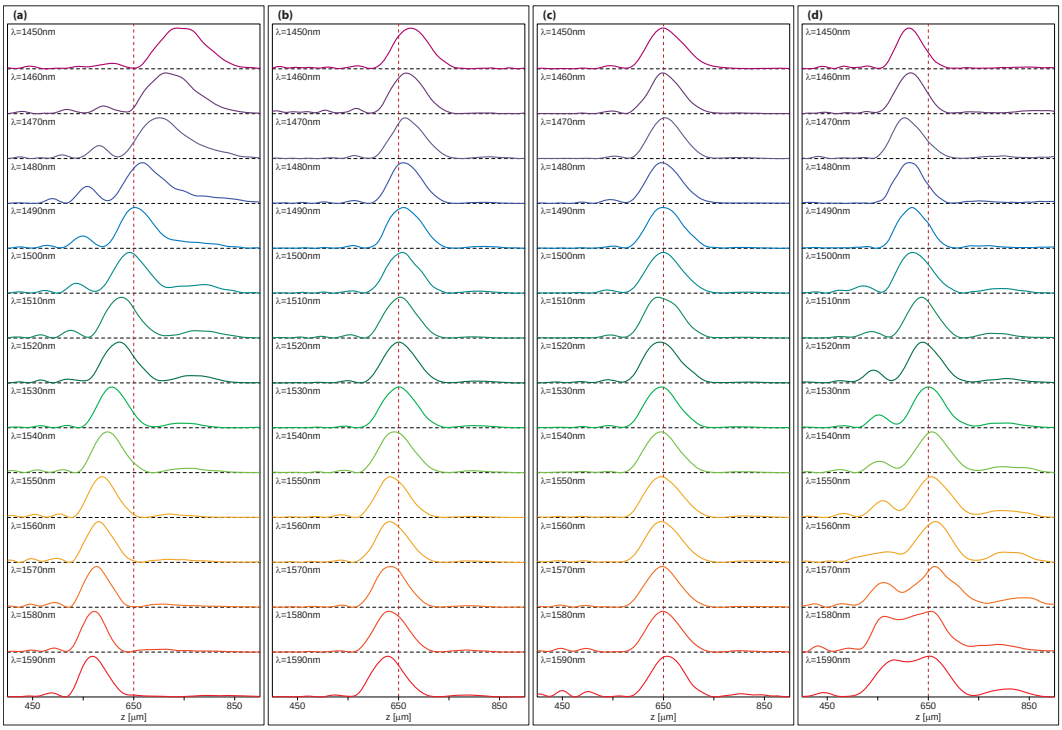

Figure 4.A11: **One-dimensional cuts of the measured axial intensities plotted in Fig. 4.A10. (a)** Hyper-dispersive mirror. **(b)** Mirror with regular dispersion. **(c)** Mirror with zero dispersion. **(d)** Mirror with a positive dispersion with an amplitude twice the regular negative dispersion.

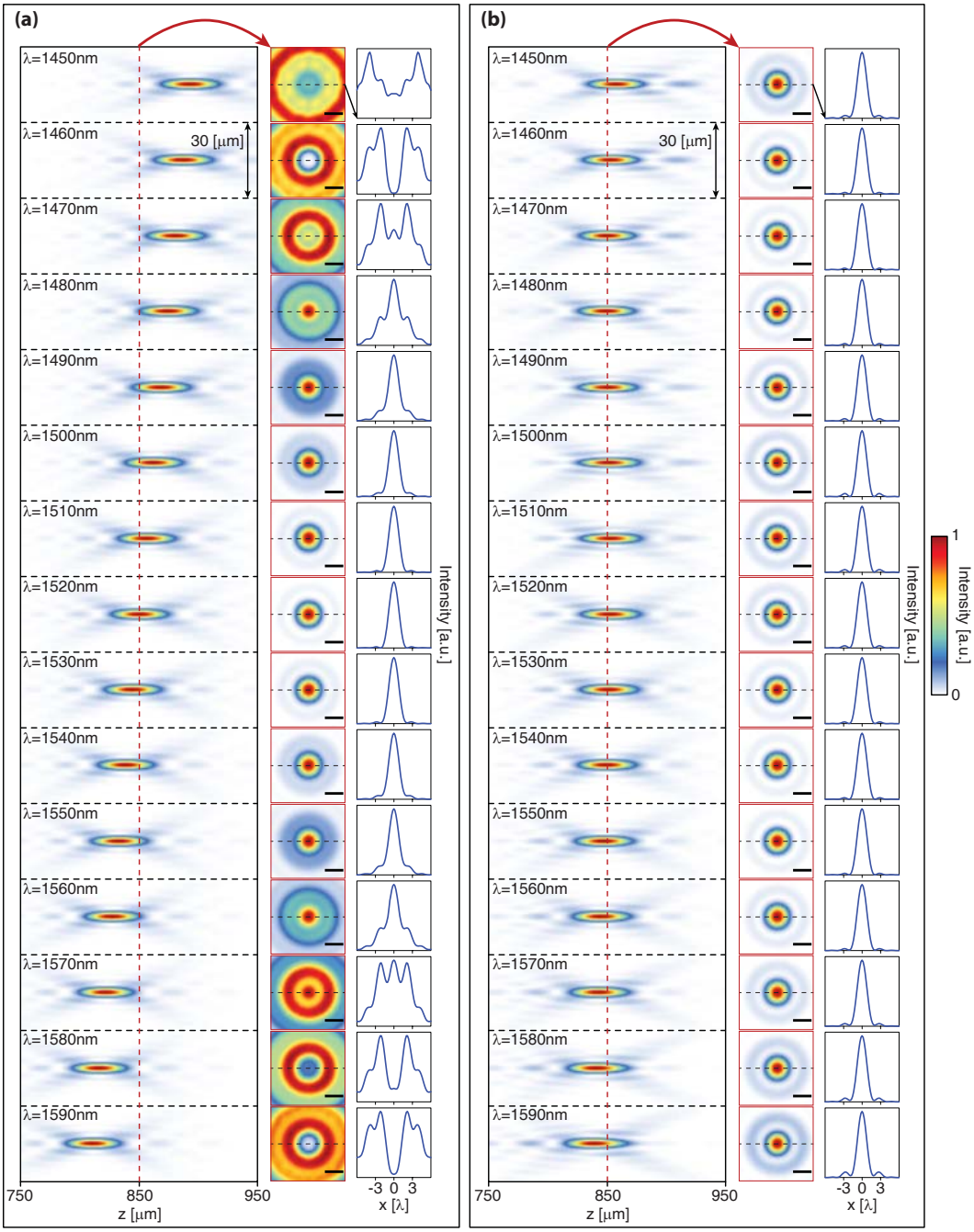

Figure 4.A12: **Extended simulation results for the regular and dispersionless mirrors discussed in Figs. 4.6c–4.6g. (a)** Simulated axial plane (left) and focal plane (center) intensities for a regular metasurface focusing mirror designed using the proposed reflective dielectric meta-atoms. One-dimensional cross-sections of the focal plane intensity is plotted on the right. The focusing mirror has a diameter of 500 μm and a focal distance of 850 μm at 1520 nm. **(b)** Similar results for a focusing mirror with the same parameters designed to have a minimal dispersion in the bandwidth. Scale bars: 2λ.

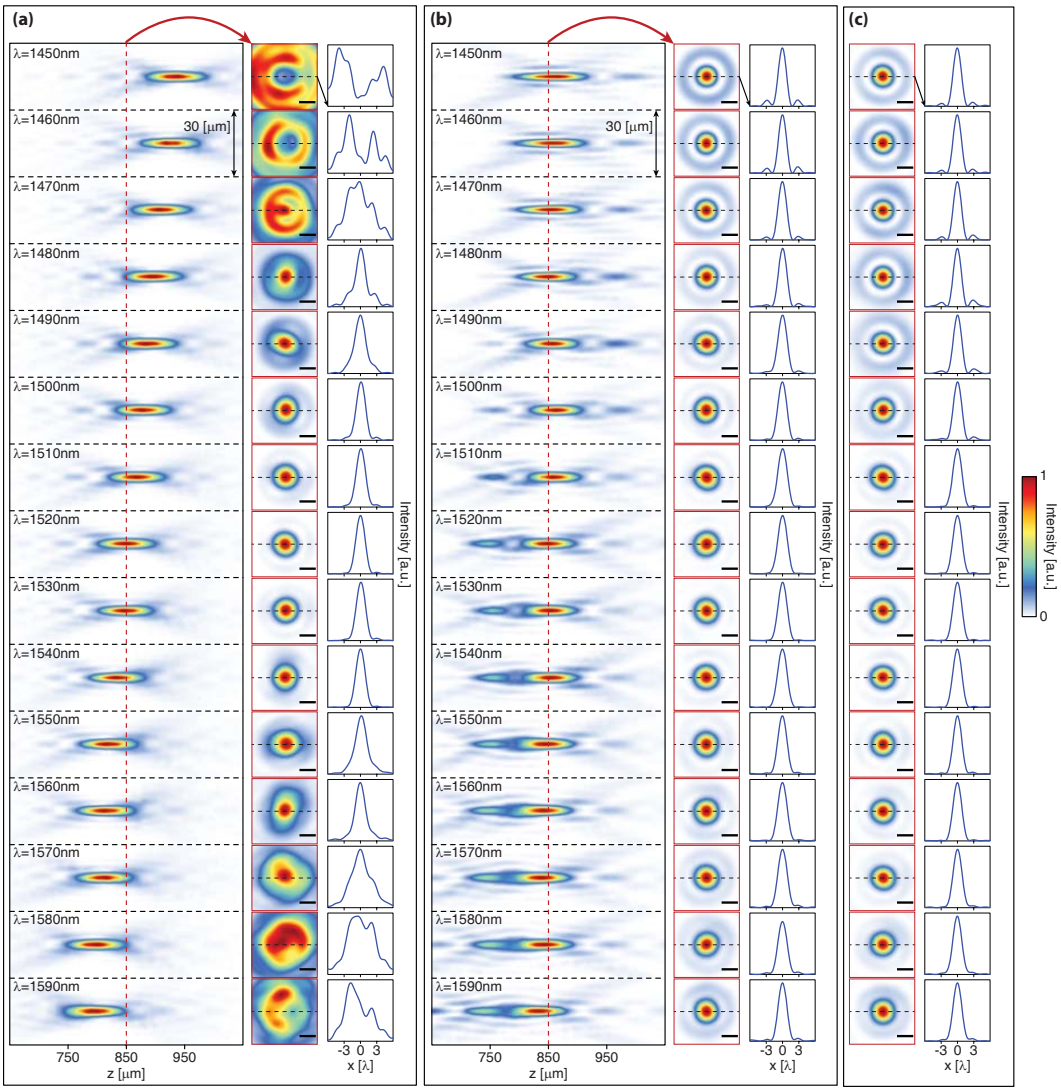

Figure 4.A13: **Complete measurement results for the dispersionless and regular mirrors discussed in Figs. 4.6c–4.6g. (a)** Measured intensities for the regular metasurface mirror. The axial plane intensities are shown on the left, the measured intensities in the 850 μm plane are plotted in the middle, and one dimensional cuts of the focal plane measurements are shown on the right. **(b)** Same as **a** but for the dispersionless mirror design with σ = 300 nm. **(c)** Measured intensities in the plane 850 μm away from the surface of the dispersionless mirror with σ = 50 nm. One-dimensional cuts of the measured intensities are shown on the right. Scale bars: 2λ.

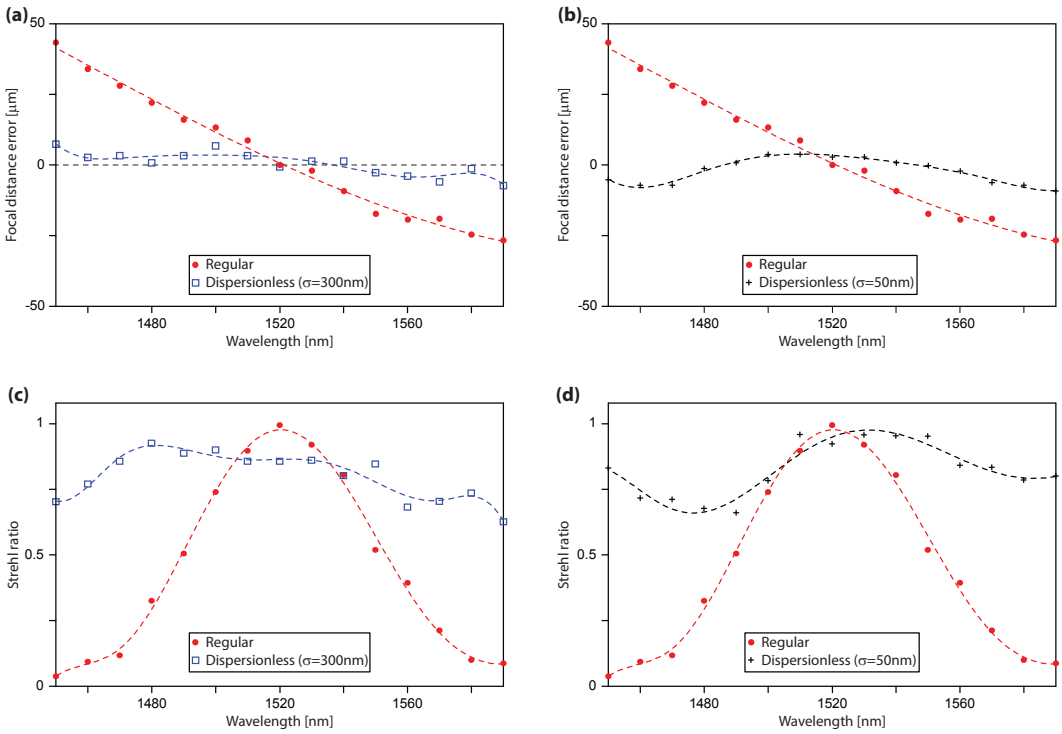

Figure 4.A14: **Measured focal distances and Strehl ratios for the regular and dispersionless mirrors.** **(a)** Measured focal distances for the regular and disperisonless (σ = 300 nm) mirrors (same as Fig. **4.6d**). **(b)** Measured focal distances for the regular and disperisonless (σ = 50 nm) mirrors. **(c)** Strehl ratios calculated from the measured two dimensional modulation transfer functions (MTF) of the regular and dispersionless (σ = 300 nm) metasurface mirrors. To find the Strehl ratio, the volume enclosed by the normalized two dimensional MTF is calculated at each wavelength. **(d)** The same graph as in **c**, calculated and plotted for the σ = 50 nm dispersionless mirror. In both cases, a clear flattening of the Strehl ratio, which is a measure of the contrast of an image formed by the mirror, is observed compared to the regular metasurface mirror.

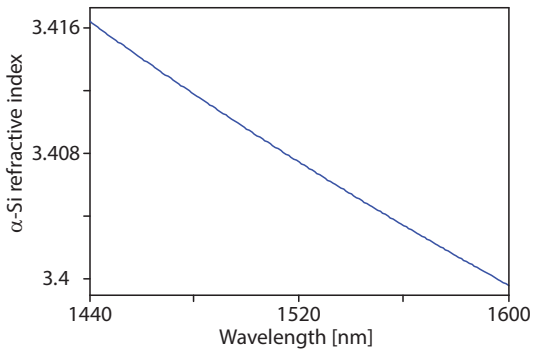

Figure 4.A15: **Refractive index of α-Si.** The refractive index values were obtained using spectroscopic ellipsometry.

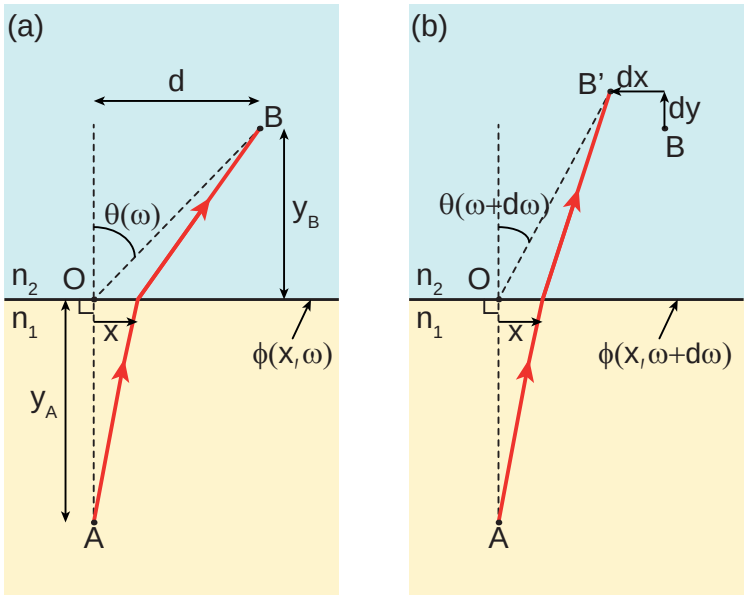

Figure 4.A16: **Schematic of light deflection at a gradient phase surface. (a)** A gradient phase surface between two materials with indices n_1 and n_2. At frequency ω a ray of light going from A to B, passes the interface at a point with coordinate x. **(b)** The same structure with a ray of light at $\omega + d\omega$ that goes from A to B′.

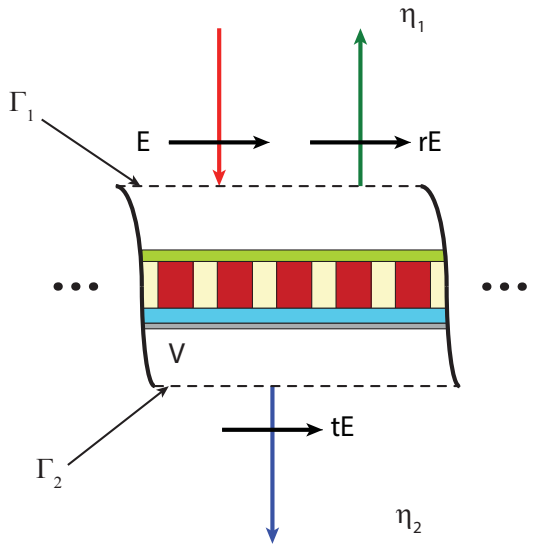

Figure 4.A17: **Schematic of a generic metasurface.** The metasurface is between two uniform materials with wave impedances of η_1 and η_2, and it is illuminated with a normally incident plane wave from the top side. Virtual planar boundaries Γ_1 and Γ_2 are used for calculating field integrals on each side of the metasurface.

Chapter 5

METASYSTEMS

The material in this chapter was in part presented in [120, 139–141, 264].

So far, we have only focused on *single-metasurface components*. The true potentials of metasurfaces, however, can only be reached when multiple metasurfaces are co-designed and combined to make *metasystems*. In this chapter, we showcase this capability through several examples of metasystems that provide functionalities that are not achievable with single metasurfaces. In the first two sections, we discuss how vertical integration of multiple metasurfaces can be used for correcting geometric aberrations of imaging and projection lenses to make compact wide field of view (FOV) cameras [139] and light engines for augmented reality (AR) headsets [264]. The third section discusses the potentials of integration of metasurfaces and the MEMS technology to fabricate compact, fast, and highly tunable lenses [140]. Section 4 introduces the folded metasurface optics platform, and demonstrates how this platform can be utilized to design and implement complicated optical systems such as spectrometers in very small form factors [141]. Finally, in section 5 we discuss how viewing metasurfaces as platforms for implementing various mathematical operations allows for the design of non-conventional optical elements like flat retroreflectors [120].

5.1 Miniature optical planar camera based on a wide-angle metasurface doublet corrected for monochromatic aberrations

Vertically cascaded metasurface stacks can perform sophisticated image corrections and can be directly integrated with image sensors. In this section, we demonstrate this concept with a miniature flat camera integrating a monolithic metasurface lens doublet corrected for monochromatic aberrations, and an image sensor. The doublet lens, which acts as a fisheye photographic objective, has a small f-number of 0.9, an angle-of-view larger than 60°×60°, and operates at 850 nm wavelength with 70% focusing efficiency. The camera exhibits nearly diffraction-limited image quality, which indicates the potential of this technology in the development of optical systems

for microscopy, photography, and computer vision.

Introduction

Optical systems such as cameras, spectrometers, and microscopes are conventionally made by assembling discrete bulk optical components like lenses, gratings and filters. The optical components are manufactured separately using cutting, polishing and grinding, and have to be assembled with tight alignment tolerances, a process that is becoming more challenging as the optical systems shrink in size. Furthermore, the continuous progress of mobile, wearable, and portable consumer electronics and medical devices has rapidly increased the demand for high-performance and low-cost miniature optical systems. Optical metasurfaces offer an alternative approach for realization of optical components [3, 4, 6, 265, 266]. Recent advances have increased their efficiency and functionalities, thus allowing metasurface diffractive optical components with comparable or superior performance than conventional optical components [14, 66–68, 267]. The main advantage of metasurfaces stems from the capability to make sophisticated planar optical systems composed of lithographically stacked electronic and metasurface layers. The resulting optical system is aligned lithographically, thus eliminating the need for post-fabrication alignments.

The development of the optoelectronic image sensor has been a significant step towards the on-chip integration of cameras [268]; however, the camera lenses are yet to be fully integrated with the image sensor. The freedom in controlling the metasurface phase profiles has enabled implementation of spherical-aberration-free flat lenses that focus normally incident light to diffraction-limited spots [32, 33, 41, 67]. Such lenses have been used in applications requiring focusing of an optical beam or collimating emission from an optical fiber [65] or a semiconductor laser [68]. However, the metasurface lenses suffer from other monochromatic aberrations (i.e., coma and astigmatism), which reduce their FOV and hinder their adoption in imaging applications where having a large FOV is an essential requirement. A metasurface lens can be corrected for coma if it is patterned on the surface of a sphere [28, 269, 270], but direct patterning of nano-structures on curved surfaces is challenging. Although conformal metasurfaces might provide a solution [125], the resulting device would not be flat. As we show here, another approach for correcting monochromatic aberrations of a metasurface lens is through cascading and forming a metasurface doublet lens.

Here, we show a doublet lens formed by cascading two metasurfaces can be corrected

over a wide range of incident angles. We also demonstrate an ultra-slim, low f-number camera, composed of two metasurface lenses placed on top of an image sensor. The camera represents an example of the optical systems enabled by the metasurface vertical integration platform.

Design and optimization of the metasurface doublet lens

Figure **5.1a** schematically shows focusing by a spherical-aberration-free metasurface lens. Simulated focal spots for such a lens are shown in Fig. **5.1b**, exhibiting diffraction-limited focusing for normal incident and significant aberrations for incident angles as small as a few degrees. The proposed doublet lens [Fig. **5.1c**] is composed of two metasurfaces behaving as polarization insensitive phase plates which are patterned on two sides of a single transparent substrate. The aberrations of two cascaded phase plates surrounded by vacuum have been studied previously in the context of holographic lenses, and it has been shown that such a combination can realize a fisheye lens with significantly reduced monochromatic aberrations [30]. We used the ray tracing approach to optimize the phase profiles of the two metasurfaces when they are separated by a 1-mm-thick fused silica substrate. Simulation results of the focal plane spot for different incident angles (θ) are presented in Fig. **5.1d**, showing nearly diffraction-limited focusing by the doublet up to almost 30° incident angle. The doublet lens has an input aperture diameter of 800 μm and a focal length of 717 μm corresponding to an f-number of 0.9. In the optimum design, the first metasurface operates as a corrector plate and the second one performs the significant portion of focusing; thus, we refer to them as correcting and focusing metasurfaces, respectively. The metasurfaces are designed for the operation wavelength of 850 nm, and are implemented using the dielectric nano-post metasurface platform shown in Fig. **5.2a** [67]. The metasurfaces are composed of hexagonal arrays of α-Si nano-posts with different diameters which rest on a fused silica substrate and are covered by the SU-8 polymer. The nano-posts behave as truncated waveguides with circular cross sections supporting Fabry-Pérot resonances [14, 67, 125]. The high refractive index between the nano-posts and their surroundings leads to weak optical coupling among the nano-posts and allows for the implementation of any phase profile with subwavelength resolution by spatially varying the diameters of the nano-posts. Simulated intensity transmission and phase of the transmission coefficient for different nano-post diameters are presented in Fig. **5.2b**, showing that 2π phase coverage is achieved with an average transmission over 96% (see Appendix 5.1 for details).

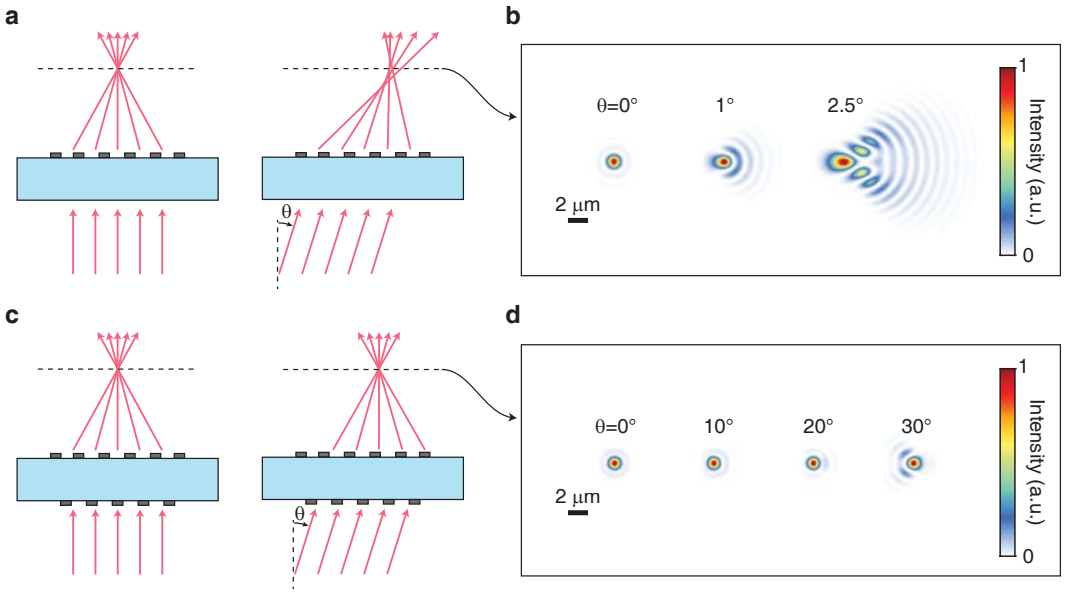

Figure 5.1: **Focusing by metasurface singlet and doublet lenses. (a)** Schematic illustration of focusing of on-axis and off-axis light by a spherical-aberration-free metasurface singlet lens. **(b)** Simulated focal plane intensity for different incident angles. Scale bar: 2 μm. **(c)** and **(d)** Similar illustration and simulation results as presented in **a** and **b** but for a metasurface doublet lens corrected for monochromatic aberrations. Scale bar: 2 μm. Both lenses have aperture diameter of 800 μm and focal length of 717 μm (f-number of 0.9) and the simulation wavelength is 850 nm. See Appendix 5.1 for details.

Device fabrication

We fabricated the metasurfaces on both sides of a fused silica substrate by depositing α-Si and defining the nano-post pattern using EBL and dry etching (see Appendix 5.1 for the details). First, the correcting metasurfaces were patterned on the top side of the substrate, and then the focusing metasurfaces were aligned and patterned on the substrate's bottom side (as schematically shown in Fig. 5.2**c**). To protect the metasurfaces while processing the other side of the substrate, the metasurfaces were cladded by a layer of cured SU-8 polymer. Aperture and field stops were formed by depositing and patterning opaque metal layers on the top and bottom sides of the substrate, respectively, and anti-reflection layers were coated on both sides of the device. Photos of the top and bottom sides of a set of fabricated metasurface doublet lenses are shown in Fig. 5.2**c**. SEM images of the nano-posts are shown in Fig. 5.2**d**.

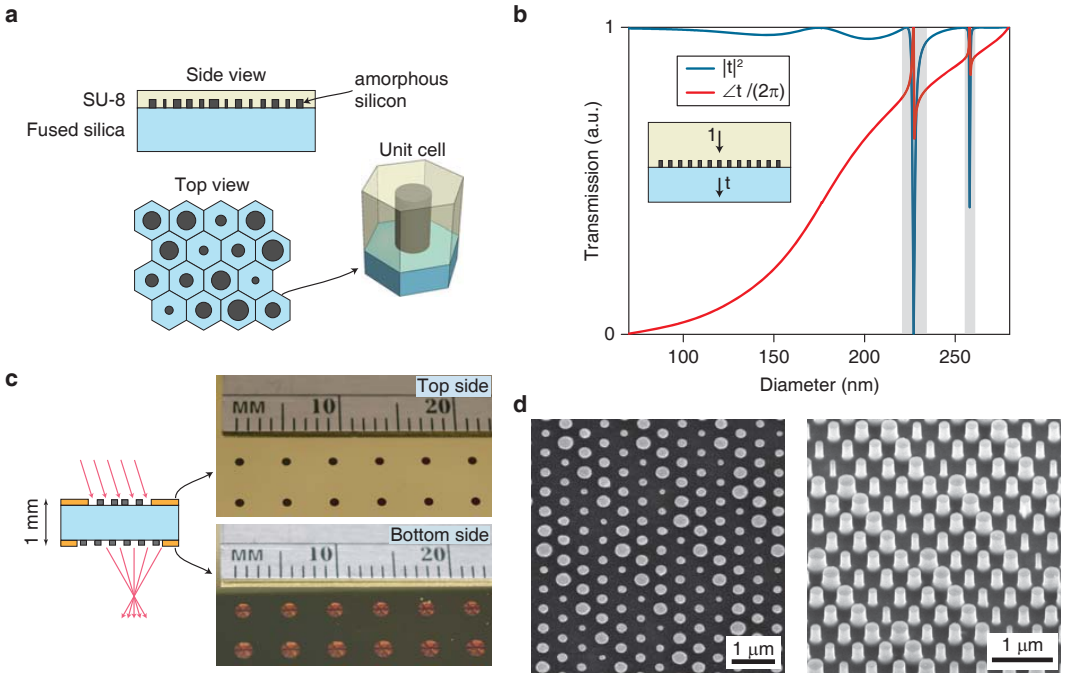

Figure 5.2: **Monolithic metasurface doublet lens. (a)** A schematic illustration of the dielectric metasurface used to implement the metasurface doublet lens. The metasurface is composed of an array of α-Si nano-posts covered with a layer of SU-8 polymer and arranged in a hexagonal lattice. **(b)** Simulated intensity transmission ($|t|^2$) and the phase of transmission coefficient ($\angle t$) of the metasurface shown in **a** with identical nano-posts as a function of the nano-posts' diameter. The diameters with low transmission values, which are highlighted by two grey rectangles, are excluded from the designs. The nano-posts are 600 nm tall, the lattice constant is 450 nm, and the simulation wavelength is 850 nm. **(c)** Schematic drawing of the monolithic metasurface doublet lens composed of two metasurfaces on two sides of a 1-mm-thick fused silica substrate, an aperture stop, and a field stop. The photographs of the top and bottom sides of an array of doublet lenses are also shown. **(d)** Scanning electron micrographs showing a top and an oblique view of the α-Si nano-posts composing the metasurfaces. Scale bars: 1 μm.

Focal spot and focusing efficiency characterizations

We characterized the fabricated metasurface doublet by illuminating it with an 850-nm laser beam at different incident angles (as shown in Fig. **5.3a**), and measuring its focal spot and focusing efficiency. For comparison, a spherical-aberration-free singlet metasurface lens with the same aperture diameter and focal length as the doublet lens (phase profile $\phi(\rho) = -(2\pi/\lambda)\sqrt{\rho^2 + f^2}$, ρ: radial coordinate, f=717 μm: focal length, D=800 μm: aperture diameter) was also fabricated and characterized. The focal spots of the metasurface doublet and singlet lenses were measured with two different polarizations of incident light and are shown along with the corresponding simulation results in Figs. **5.3b** and **5.3c**, respectively (see Appendix 5.1 for details). The doublet lens has a nearly diffraction-limited focal spot for incident angles up to more than 25° (with the criterion of Strehl ratio of larger than 0.9, see Fig. **5.A1**) while the singlet exhibits significant aberrations even at incident angles of a few degrees. As Figs. **5.3b** and **5.3c** show, simulated and measured spot shapes agree well. For the doublet lens, a small asymmetry in the 0° spot shape and slightly larger aberrations are observed in the measured spots compared to the simulation results, which we attribute to a misalignment (estimated ~2 μm along both x and y directions) between the top and bottom side patterns (see Fig. **5.A2**).

The focusing efficiency (i.e., ratio of the focused power to the incident power) for the metasurface doublet lens is shown in Fig. **5.3d**, and is ~70% for normally incident light. The focusing efficiency is polarization dependent, and its value for unpolarized light drops at the rate of ~1% per degree as the incident angle increases. The measured focusing efficiency at normal incidence is lower than the average of the transmission shown in Fig. **5.2b** because of the large NA of the focusing metasurface [67], undesired scattering due to the sidewall roughness of the nano-posts, residual reflection at the air/SU-8 interfaces, and measurement artefacts (see Appendix 5.1 for details). The metasurfaces are polarization insensitive at normal incidence, but their diffraction efficiency depends on the polarization of incident light for non-zero incident angles. The focusing efficiency is lower for the transverse magnetic (TM) polarized light compared with the transverse electric (TE) polarized light because of the excitation of some resonances of the nano-posts with the axial component of the electric field of the incident light [125]. This also causes the slight difference between the TE and TM spot shapes for the 30° incident light shown in Fig. **5.3b**. We measured a focusing efficiency of ~75% for the singlet, and did not observe a detectable difference between the focal spots measured with TE and TM polarizations. The measured relative location of the doublet lens focal

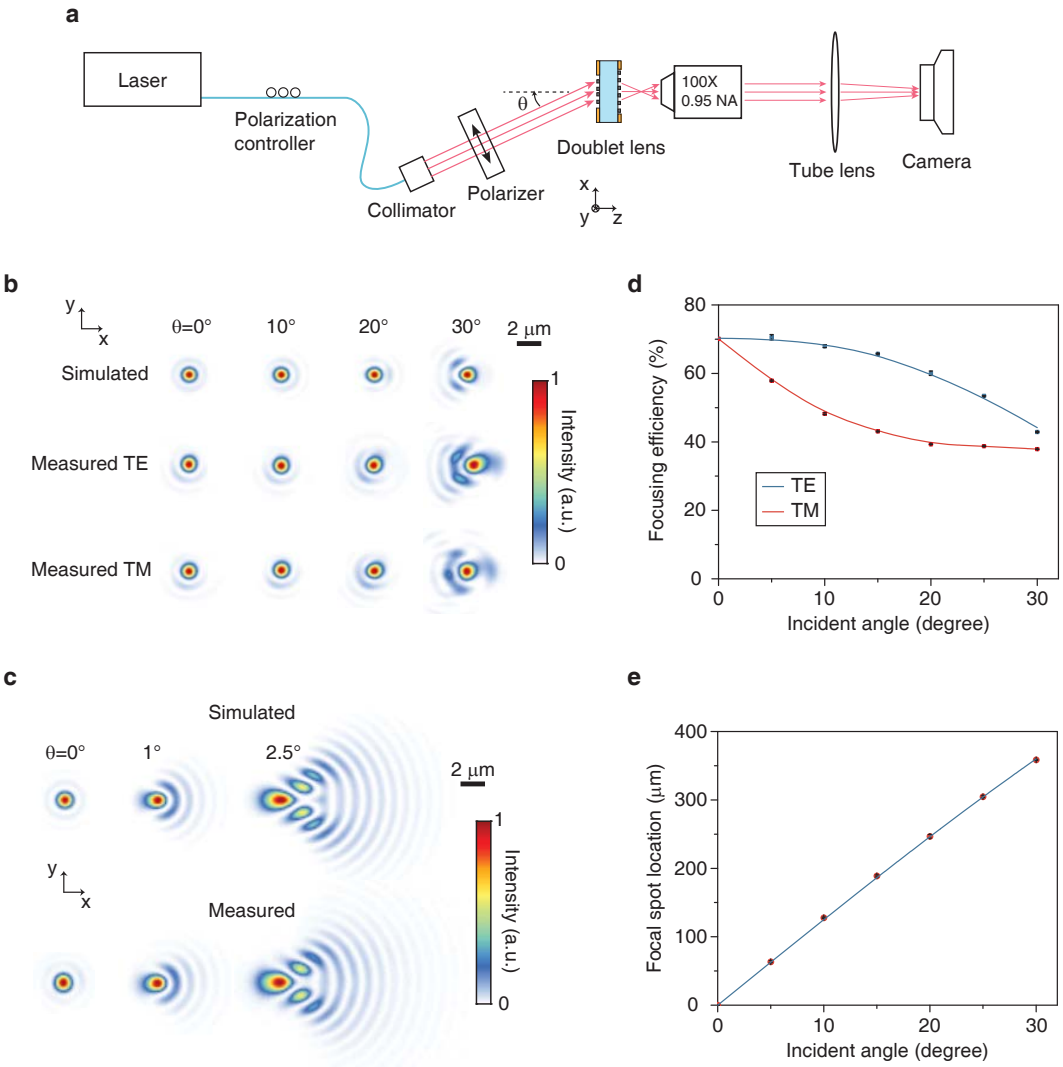

Figure 5.3: **Measured and simulated focal spots of the metasurface doublet and singlet lenses. (a)** Schematic drawing of the measurement setup. **(b)** Simulated and measured focal plane intensity profiles of the metasurface doublet lens for different incident angles (θ). Scale bar: 2 μm. **(c)** Simulated and measured focal plane intensity profiles for a metasurface singlet with the same aperture diameter and focal length as the metasurface doublet. For the range of angles shown, the measured intensity distributions are polarization insensitive. Scale bar: 2 μm. **(d)** Measured focusing efficiency of the metasurface doublet for TE and TM polarized incident light as a function of incident angle. The measured data points are shown by the symbols and the solid lines are eye guides. **(e)** Transverse location of the focal spot for the doublet lens as a function of incident angle. The measured data points are shown by the symbols and the solid line shows the $f\sin(\theta)$ curve, where $f = 717$ μm is the focal length of the metasurface doublet lens.

spot as a function of incident angle is shown in Fig. **5.3e** along with the $f\sin(\theta)$ curve. The good agreement between the measured data and the curve indicates that the metasurface doublet lens can be used as an orthographic fisheye lens or a wide angle Fourier transform lens [30]. Also, the specific $f\sin(\theta)$ fisheye distortion of the image leads to a uniform brightness over the image plane [271].

Imaging performance

We characterized the imaging performance of the metasurface doublet lens using the experimental setup shown in Fig. **5.4a**. A pattern printed on a letter-size paper was used as an object. The object was placed ~25 cm away from the metasurface doublet lens and was illuminated by an LED (center wavelength: 850 nm, bandwidth: 40 nm, spectrum shown in Fig. **5.A3**). The image formed by the doublet lens was magnified by ~10× using an objective and a tube lens and captured by a camera. A bandpass filter with 10 nm bandwidth (see Fig. **5.A3** for the spectrum) was used to spectrally filter the image and reduce the effect of chromatic aberration on the image quality. Figure **5.4b** shows the image captured by the camera, and its insets depict the zoomed-in views of the image at 0°, 15°, and 30° view angles. For comparison, an image captured using the same setup but with the metasurface singlet lens is shown in Fig. **5.4c**. The objective lens used for magnifying the images has a smaller NA than the metasurface lenses and limits the resolution of the captured images (see Fig. **5.A4** for an image taken with a higher NA objective).

Any imaging system can be considered as a low pass spatial filter whose transfer function varies across the FOV. For incoherent imaging systems, the transfer function for each point in the FOV can be obtained by computing the Fourier transform of the focal spot intensity. The modulus of this transfer function is referred to as the MTF and represents the relative contrast of the image versus the spatial details of the object. The MTFs for the metasurface doublet and singlet lenses were computed using the measured focal spots (Figs. **5.3b** and **5.3c**) and are shown in Figs. **5.4d** and **5.4e**, respectively. Both the images and the MTFs shown in Figs.**5.4b**–**5.4d** demonstrate the effectiveness of correction achieved by cascading two metasurfaces, and the diffraction-limited performance of the metasurface doublet lens over a wide FOV.

Miniature metasurface camera

To further demonstrate the use of this technology in imaging applications, we realized a miniature planar camera by using a metasurface doublet lens and a complementary

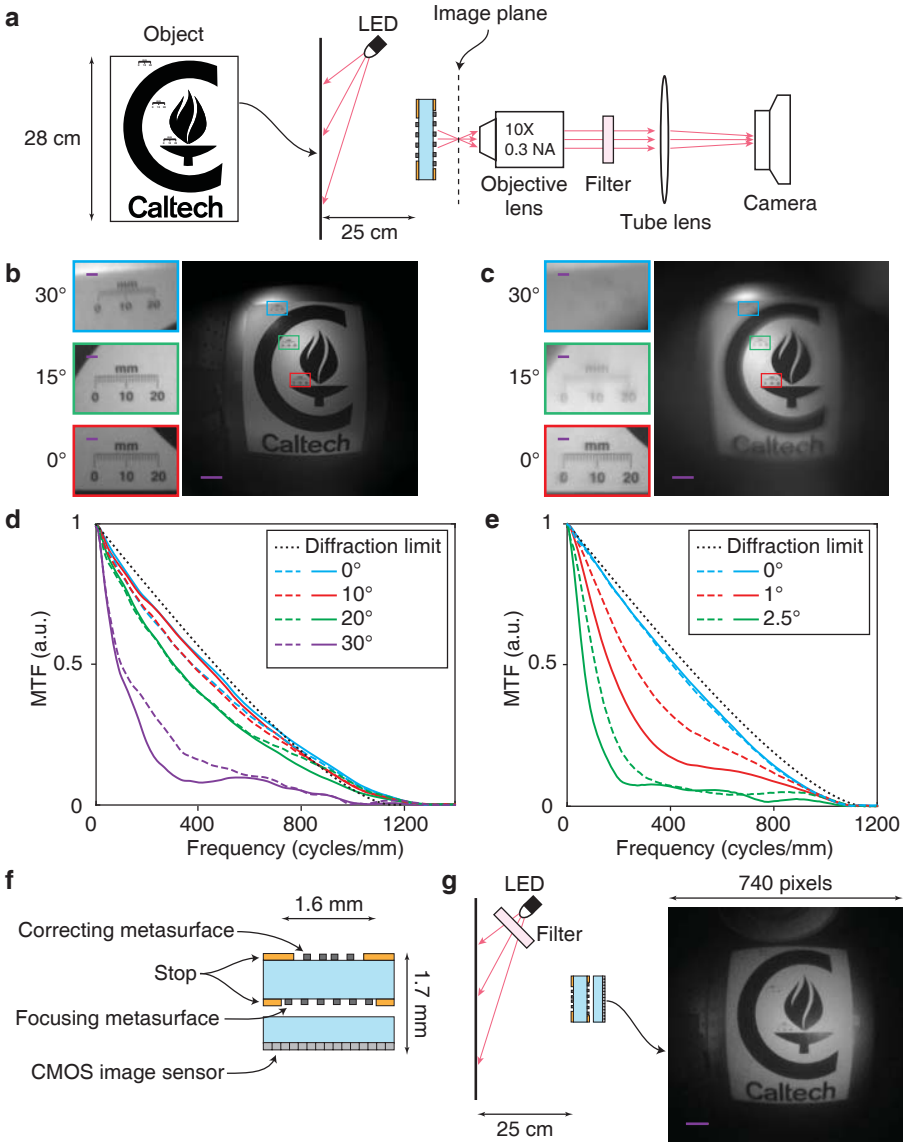

Figure 5.4: **Imaging with the metasurface doublet lens.** **(a)** Schematic of the measurement setup. **(b)** Image taken with the metasurface doublet lens, and **(c)** with the spherical-aberration-free metasurface singlet lens. Scale bar: 100 μm. The insets show zoomed-in views of the images at the locations indicated by the rectangles with the same outline colors which correspond to viewing angles of 0°, 15°, and 30°. Scale bar: 10 μm. **(d)** and **(e)** MTF of the metasurface doublet and singlet lenses, respectively. The solid and dashed lines show the MTF in the tangential plane (along x in Fig. **5.3b**) and sagittal plane (along y in Fig. **5.3b**), respectively. **(f)** Schematic drawing of a miniature planar camera realized using a metasurface doublet lens and a CMOS image sensor. **(g)** Imaging setup and the image captured by the miniature camera. Scale bar: 100 μm.

metal oxide transistor (CMOS) image sensor as schematically shown in Fig. 5.4**f**. To compensate for the light propagating through the cover glass protecting the image sensor, another doublet lens was optimized (see Metasurface Doublet Lens II in Fig. 5.A5). The total dimensions of the camera (including the image sensor) are 1.6 mm×1.6 mm ×1.7 mm. The miniature camera was characterized using the setup shown in Fig. 5.4**g** and by imaging the object shown in Fig. 5.4**a** which was illuminated by a filtered LED (center wavelength: 850 nm, bandwidth: 10 nm, see Fig. 5.A3 for the spectrum). The image captured by the image sensor is also shown in Fig. 5.4**g** which shows a wide FOV. The camera's image quality is reduced by the nonuniform responsivity of the image sensor pixels to the 850 nm light due to the color filters, and by its larger-than-optimal pixel size. Therefore, the image quality can be improved by using a monochromatic image sensor with a smaller pixel size (the optimum pixel size for the miniature camera is ~0.4 μm based on the MTFs shown in Fig. 5.4**d**). Thus, the miniature camera benefits from the current technological trend in pixel size reduction.

The intensity of the image formed by a camera only depends on the NA of its lens (it is proportional to $1/f$-number^2=4NA^2 [272]); therefore, the metasurface miniature camera collects a small optical power but forms a high brightness image. Furthermore, the metasurface doublet lens is telecentric in the image space, and light is incident on the image sensor with the uniform angular distribution (see Fig. 5.A5), and thus removing the need for the variable incident angle correction in the image sensor.

Correcting chromatic abberations

The metasurface doublet lens suffers from chromatic aberrations that reduce the image quality of the miniature camera as the illumination bandwidth increases. Simulated focal spots of the metasurface doublet lens for different illumination bandwidths and the corresponding MTFs are shown in Figs. 5.5**a** and 5.5**b**, respectively. See Fig. 5.A6 for the off-axis MTFs. As it can be seen from the MTFs, the imaging resolution decreases as the illumination bandwidth increases. This effect can be seen as reduced contrast and lower resolution in the image shown in Fig. 5.5**c** (40 nm bandwidth illumination) compared with the image shown in Fig. 5.5**d** (10 nm bandwidth illuminations). For the imaging purpose, the fractional bandwidth of a metasurface lens is proportional to $\lambda/(f\text{NA}^2)$ (see Appendix 5.1) and can be increased by reducing the NA of the metasurface lens and its focal length. Also, since the MTFs of the metasurface doublet lens shown in Fig. 5.5**b** have significant

high frequency components, the unfavourable effect of chromatic aberration can to some extent be corrected using Wiener deconvolution [273]. Figure **5.5e** shows the deconvolution results of the image shown in Fig. **5.5c** that is taken with a 40-nm-bandwidth illumination (see Appendix 5.1 for the details). As expected, the deconvolved image appears sharper and has a higher contrast than the original image; however, deconvolution also amplifies the noise, limiting its applicability for correcting the chromatic aberrations over a significantly wider bandwidth.

Discussion

The metasurface doublet lens and camera can be further miniaturized by reducing the thickness of the substrate, the diameters of the metasurface lenses, the focal length of the lens, and the distance to the image sensor by the same scale factor, while using the same nano-post metasurface design presented in Fig. **5.2**. For example, a 10× smaller camera (160 μm×160 μm×170 μm) can be designed and fabricated using a similar procedure on a 100-μm-thick fused silica substrate. Such a camera would have 10× larger bandwidth compared to the miniature camera presented here, the same image plane intensity, but with 10× smaller image and 100× lower number of distinguishable pixels (94×94 pixels instead of 940×940). Compared to other miniature lenses reported previously [274–276] and Awaiba NanEye camera (`http://www.awaiba.com`), the metasurface doublet offers significantly smaller f-number and better correction for monochromatic aberrations which lead to brighter images with higher resolution; however, they have larger chromatic aberration (i.e., narrower bandwidth).

The miniature metasurface camera concept can be extended for color and hyperspectral imaging by using a set of metasurfaces that are designed for different center wavelengths and fabricated side by side on the same chip. Each of the metasurface doublet lenses forms an image on a portion of a single monochromatic image sensor. High quality thin-film color filters with different center wavelengths can be directly deposited on the correcting metasurface of each doublet lens, and the color filter efficiency issues associated with small size color filters will be avoided [277, 278]. Also, multiwavelength metasurface lenses which work at multiple discrete wavelengths have been demonstrated [135–137, 227]. However, the multiwavelength metasurfaces exhibit the same chromatic dispersion (i.e., $\mathrm{d}f/\mathrm{d}\lambda$) and thus similar chromatic aberrations as the single wavelength metasurface lenses. The α-Si metasurfaces have negligible absorption loss for wavelengths above 650 nm. For shorter wavelength, materials with lower absorption loss such as p-Si, gallium

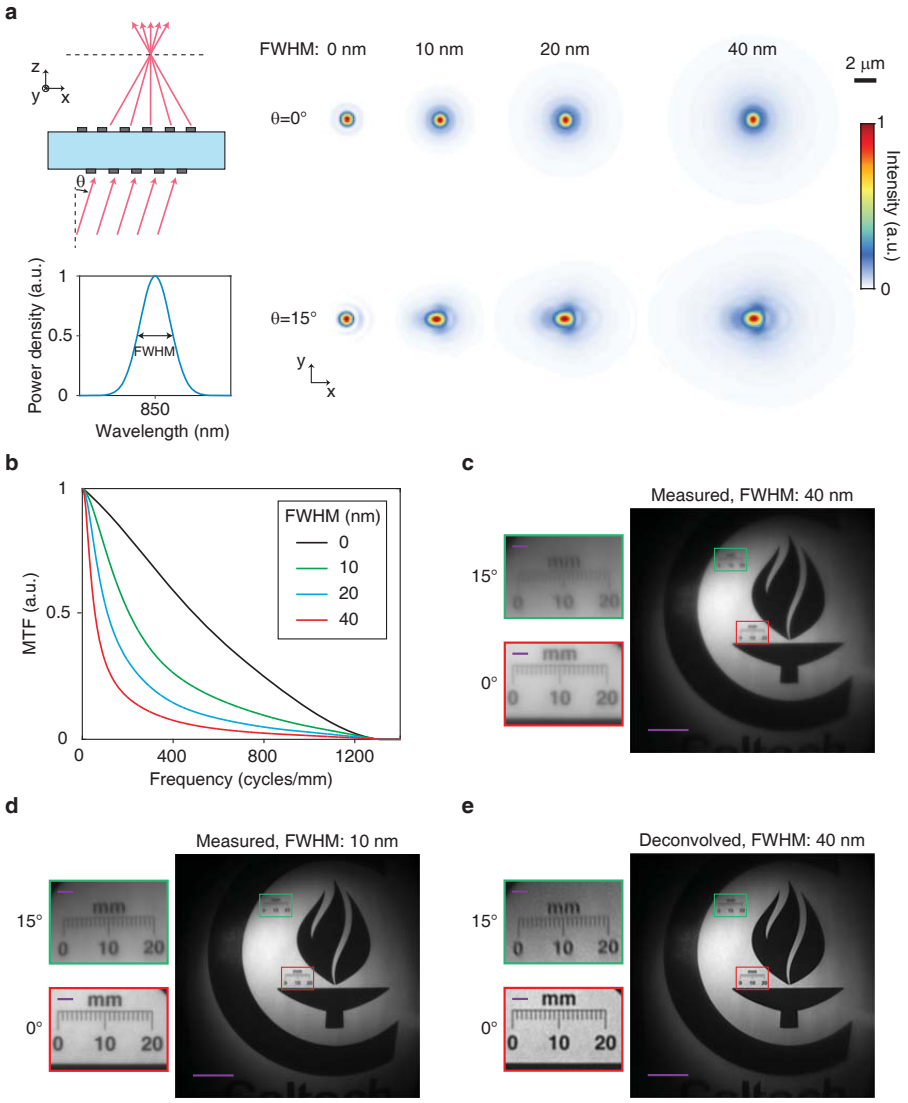

Figure 5.5: **Chromatic aberration of metasurface doublet lens and its correction.** **(a)** Illustration of focusing of wideband light by a metasurface doublet lens. The spectrum of the incident light (shown at the bottom) is assumed as a Gaussian function centered at the design wavelength of the doublet lens. Scale bar: 2 μm. **(b)** On-axis MTF of the metasurface doublet lens for different bandwidths of incident light. **(c)** Image formed by the metasurface doublet lens with an unfiltered LED illumination (40-nm FWHM), and **(d)** with filtered LED illumination (10-nm FWHM). Scale bar: 100 μm. See Fig. **5.A3** for the spectra. The images are captured using the setup shown in Fig. **5.4a** but with a higher magnification objective (20×, 0.4 NA). **(e)** Chromatic aberration correction for the image shown in **d**. Scale bar: 100 μm. The insets in **c**–**e** show zoomed-in views of the images at the locations indicated by the rectangles with the same outline colors corresponding to viewing angles of 0° (red border) and 15° (green border), and the scale bars shown in the insets represent 10 μm.

phosphide, TiO_2 [76, 78], or SiN_x [69, 279] can be used.

The metasurface-enabled camera we reported here has a flat and thin form factor, small f-number, exhibits nearly diffraction-limited performance over a large FOV. From a manufacturing standpoint, the metasurface doublets have several advantages over conventional lens modules. Conventional lens modules are composed of multiple lenses which are separately manufactured and later aligned and assembled together to form the module. On the other hand, the metasurface doublets are batch manufactured with simultaneous fabrication of tens of thousands of doublets on each wafer, and with the metasurfaces aligned to each other using lithographic steps during fabrication. Furthermore, the assembly of the conventional lens modules with the image sensors has to be done in a back-end step, but the metasurface doublet can be monolithically stacked on top of image sensors. More generally, this work demonstrates a vertical on-chip integration architecture for designing and manufacturing optical systems, which is enabled through high performance metasurfaces. This architecture will enable low-cost realization of conventional optical systems (e.g., spectrometers, 3D scanners, projectors, microscopes, etc.), and systems with novel functionalities in a thin and planar form factor with immediate applications in medical imaging and diagnostics, surveillance, and consumer electronics.

5.2 Metasurface-based compact light engine for augmented reality headsets

Introduction

Despite the great advances, potentials of augmented reality to fundamentally transform the way people use computers is partially hindered by the size and weight of the AR headsets. In waveguide-based devices, the light engine constitutes a significant portion of the total volume and weight. Dielectric metasurfaces can be used to demonstrate various high performance optical elements like blazed gratings and wide FOV lenses, similar to the ones shown in the previous section, with small thicknesses, high efficiencies, and little stray light. In this section, we discuss how the same principles and design strategies used to make a wide FOV lens can be utilized to design a compact light engine, integrated with three monochrome μ-LED displays for red, green, and blue. The metasurfaces image the μ-LEDs on the prism or grating couplers. This design avoids an important shortcoming of μ-LEDs and metasurface lenses, i.e., that each work well only for a single wavelength. As examples, we present designs for 532 nm, with over 3000 resolved angular points in an 8-mm-diameter

FOV, and a total volume less than 0.65 cc (<2 cc for the three wavelengths). Limited by the total internal reflection region inside a waveguide with a 1.78 refractive index, the light engine can produce an image with over 1500×1500 points over a FOV slightly larger than 85°×85° in air.

Powered by the great advancements in electronics, computer science, and compact refractive and diffractive micro-optics [280], headmounted AR displays have in recent years become a new category of consumer electronics. With many great proposals and demonstrations based on various technologies including visor and waveguide based systems [281–284], many products from different companies are now hitting the market. Among various designs, waveguide-based designs seem more suitable for compact AR headsets with wide FOVs. In these devices, the light engine constitutes a significant portion of the volume and weight of the device, and can even limit its performance by not providing the whole FOV and resolution supported by the waveguide optics.

Here we present the proposal and design of a compact light engine based on three monochrome μ-LED displays imaged using multi-metasurface optical systems corrected for wide FOVs. Since each μ-LED display has its own metasurface optics, this design significantly avoids the main challenge facing both μ-LEDs and metasurfaces, that is, they each work well when designed for a single color. This shortcoming has so far prevented the use of μ-LEDs in AR headsets because the pixel size is significantly increased when μ-LEDs of different colors are combined to provide full RGB coverage on the same chip. On the other hand, hindered by the size and weight of optical elements, it has not been practical to use three separate μ-LED displays as each of them would require its own imaging optics.

The proposed design overcomes this issue since the imaging optics for each color can be separate, while keeping the total volume and weight of the optics low (i.e., to lower than 2 cubic centimeters and less than 3 grams for the optics of the three colors combined). More specifically, we demonstrate a five layer metasurface design with a corrected FOV of 8 mm (close to 90° inside a glass with a refractive index of 1.78) to provide near diffraction-limited focusing with about 3000 resolved points. The optics has a collection NA of 0.25, and delivers the collimated beams with root mean square (RMS) wavefront errors lower than 0.25 across its field to an aperture with a diameter of 2.1 mm. Capped by the total internal reflection region of the waveguide (i.e., 35°-80°, for an index of 1.78) the optics can deliver over 1500×1500 points for each color, within a FOV just above 85°×85° in air. If the use of glass

substrates with ultra-high indices (e.g., n≈1.95) is possible, it is possible to make the device even more compact with a larger FOV in air, as we show in a secondary design with FOV=105°×105°, and collection NA=0.4. We also present metasurface designs based on crystalline silicon nano-scatterers that can implement the proposed metasurfaces at all wavelengths of interest (480 nm, 532 nm, and 635 nm). In the end, we discuss the main challenges faced by this technology including the chromatic dispersion and point potential methods of mitigation. While the concept of metasurfaces has previously been proposed for use in AR devices [285, 286], it has generally been limited to their application as periodic grating couplers. Being the first proposal and demonstration of its kind, we believe that this work will pave the way and encourage the exploration of potentials of metasurface optical elements for integration into compact optical systems used in AR headsets.

Concept

Figure 5.6 schematically shows the concept of the metasurface based light engine AR display. As shown in Fig. 5.6**a**, light from monochrome μ-LED displays is collimated and directed to the waveguide, using the multi-metasurface optical systems. Based on whether the eye box expanders and the out-coupling gratings can be combined for different colors or not (e.g., using volumetric Bragg gratings), one, two, or three waveguides might be used in the actual design. Here, for the sake of simplicity, we assume that the waveguides can be combined and therefore show only one waveguide. As seen in Fig. 5.6**b**, light engines for the three colors combined can be smaller than 3 cubic centimeters (with about 2 mm of thickness reserved for the μ-LED displays and their electrical circuitry). Figure 5.6**c** schematically shows a zoomed-in view of the light engine for the red color μ-LED display. The multiple metasurface system images each pixel of the μ-LED display into the grating coupler aperture with a corrected wavefront. To better visualize the compactness of the proposed platform, a schematic illustration of the whole metasurface-based light engine mounted on a typical pair of glasses is shown in Fig. 5.6**d**.

Metasurface design

The nano-post based metasurface platform that can be used to implement the metasurfaces is shown in Fig. 5.7**a**. In order to better suppress higher order diffractions and unwanted scattering, the nano-posts are generally patterned on a uniform lattice, for instance a square lattice like Fig. 5.7**b**. In addition, the lattice should be subwavelength and satisfy the Nyquist sampling rate for the used

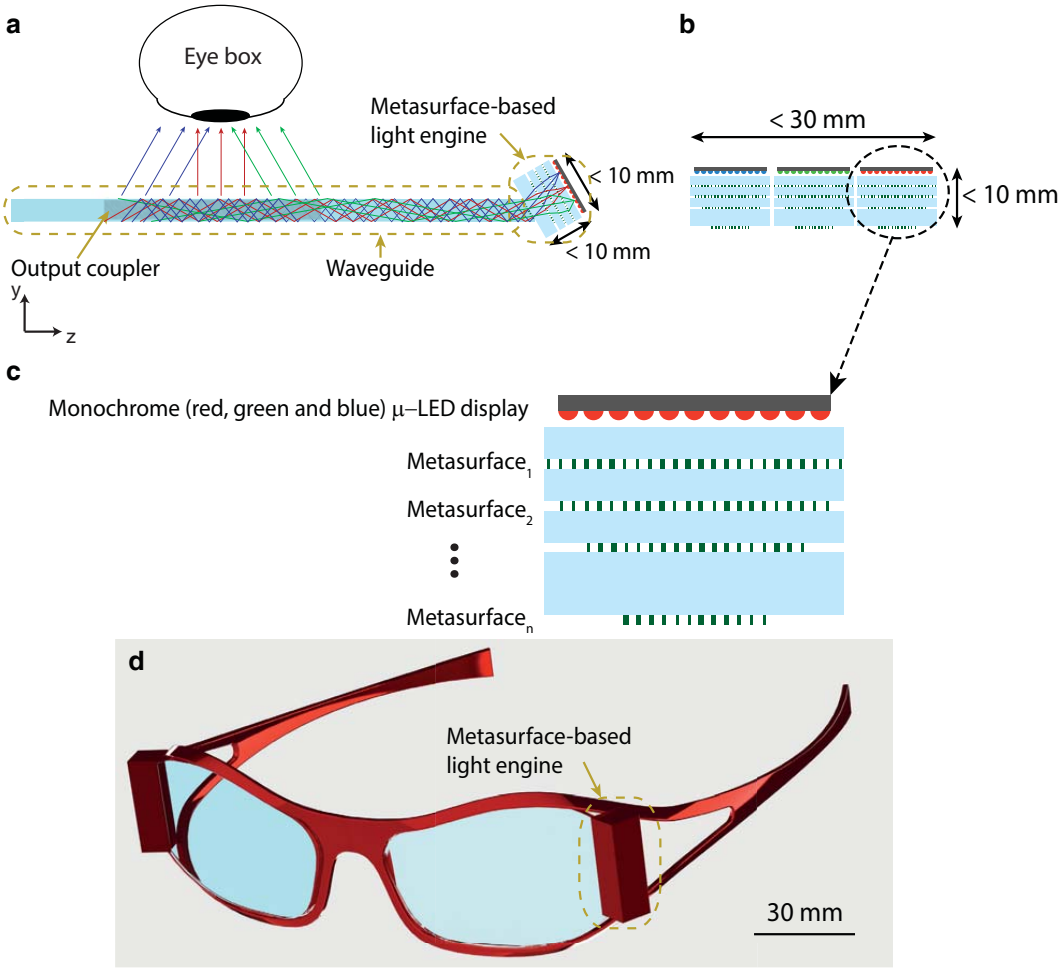

Figure 5.6: **Concept of μ-LED and metasurface-based light engines for AR glasses based on waveguides. (a)** Schematic top-view of the glass, showing relative locations of the waveguide, light engine, and the eye box. The metasurface-based optics collimates light from the monochrome μ-LED displays and directs it to the prism coupler. Inside the waveguide, light is expanded by the eye box expander and is finally out-coupled using holographic volume gratings that could increase the FOV. **(b)** Schematics of the side view of the μ-LED displays and the metasurface based optics, showing all three colors at the same time. The whole light engine is smaller than $30\text{mm} \times 10\text{mm} \times 10\text{mm}$, with the total volume of the optics smaller than 2 cubic centimeters. **(c)** Zoomed-in view of the μ-LED display and typical metasurfaces forming the light engine optics for the red color. **(d)** Schematic illustration of the whole metasurface-based light engine mounted on a typical pair of glasses.

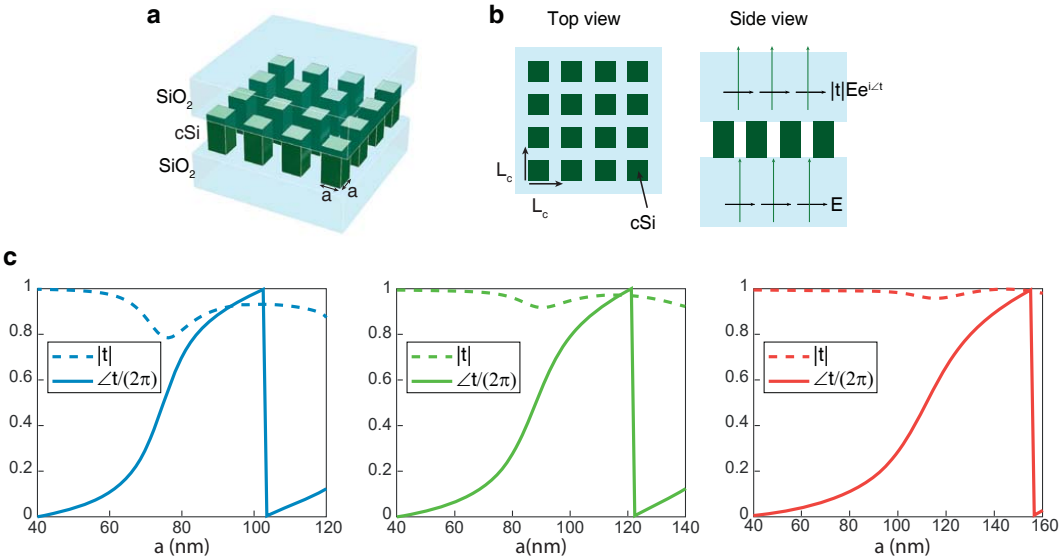

Figure 5.7: **Schematics and design graphs for dielectric metasurfaces based on c-Si. (a)** Schematic illustration of the proposed metasurface structure that is composed of c-Si nano-posts with square cross sections, sandwiched between two low-index substrates. For fabrication considerations, one of the substrates can actually be fabricated by spin coating a thick spin-on glass or polymer layer that does not fill in the nano-post gaps. **(b)** Top and side views of the proposed metasurface structure, showing the lattice constant L_c, and the complex transmission t. The optimal metasurface structure will have different thicknesses and lattice constants for the three different colors. **(c)** The simulated transmission amplitudes and phases for metasurfaces designed for blue (left, 480 nm), green (middle, 532 nm), and red (right, 635 nm). The metasurfaces have thicknesses of 224 nm, 270 nm, and 340 nm, and lattice constants of 180 nm, 200 nm, and 240 nm for blue, green, and red, respectively. Measured refractive indices of c-Si on quartz was used for the simulations. The used index values are $4.413 - 0.04033j$, $4.136 - 0.01027j$, and $3.874 - 0.008432j$ at wavelengths of 480 nm, 532 nm, and 635 nm, respectively. The graphs ensure full 2π phase coverage at all required wavelengths with high transmission. In addition, the high refractive index of c-Si ensures the ability to optimize metasurfaces for large deflection angles with high diffraction efficiencies.

material systems and transmission functions that are implemented [36]. With proper design, the nano-post array can have very high transmission efficiencies (80%-100%, depending on the material losses), while at the same time providing full 0-2π phase coverage with changing the nano-post dimensions [66, 67, 76]. Figure **5.7c** shows the transmission phases and amplitudes for three arrays with different lattice constants and nano-post thicknesses designed for blue, green, and red (480 nm, 532 nm, and 635 nm, respectively). In order to use the same material system for all colors, all metasurfaces are designed using crystalline silicon (c-Si). This way, the metasurfaces for all three colors can be fabricated on the same substrates, increasing the mechanical robustness and decreasing the required packaging volume and weight significantly. The three graphs in Fig. **5.7c** show the clear ability of the designed nano-post arrays to provide full phase coverage with high transmission. One important property of this type of metasurface is the very low coupling between adjacent nano-posts as the the high index contrast between the nano-posts and the surrounding media results in almost all of the optical energy being confined inside the nano-posts [67, 76]. As a result, sizes of the nano-posts can be changed without significantly altering the transmission phases and amplitudes of its neighbors. This enables high efficiency beam deflection to large angles, which in turn results in thin high-efficiency lenses with large NAs [33, 67].

Ray optics design of the light engine

While a single-layer metasurface lens has the ability to focus light to a point without spherical aberrations [41, 212], multiple metasurface layers are required in order to correct for other monochromatic aberrations as discussed in the previous section [30, 139]. Figure **5.8** summarizes the results of one such design, where 5 metasurface layers are cascaded to provide near-diffraction-limited imaging of the green μ-LED to the input aperture of the waveguide (i.e., the prism edge). As seen in Fig. **5.8a**, the first four metasurfaces have radii of 4.5 mm, and are each separated 1 mm from the previous surface, where the spacing glasses each have a refractive index of ~1.5. The fifth glass layer is 4 mm thick and has an index of ~1.78, to match that of the waveguide. The fifth metasurface has a diameter of 2.1 mm, resulting in an input aperture of 2.1 mm at the coupling prism. The total thickness of the device is 8 mm, and it could be fitted inside a 9mm × 9mm × 8mm cube, and thus it will occupy a volume of less than 0.65 cubic centimeters (i.e., <2 cubic centimeters for the three wavelengths combined). In addition, the total glass volume is about $3 \times 0.4 = 1.2$ cubic centimeters, so the total weight of the glass would be about 3 grams (assuming

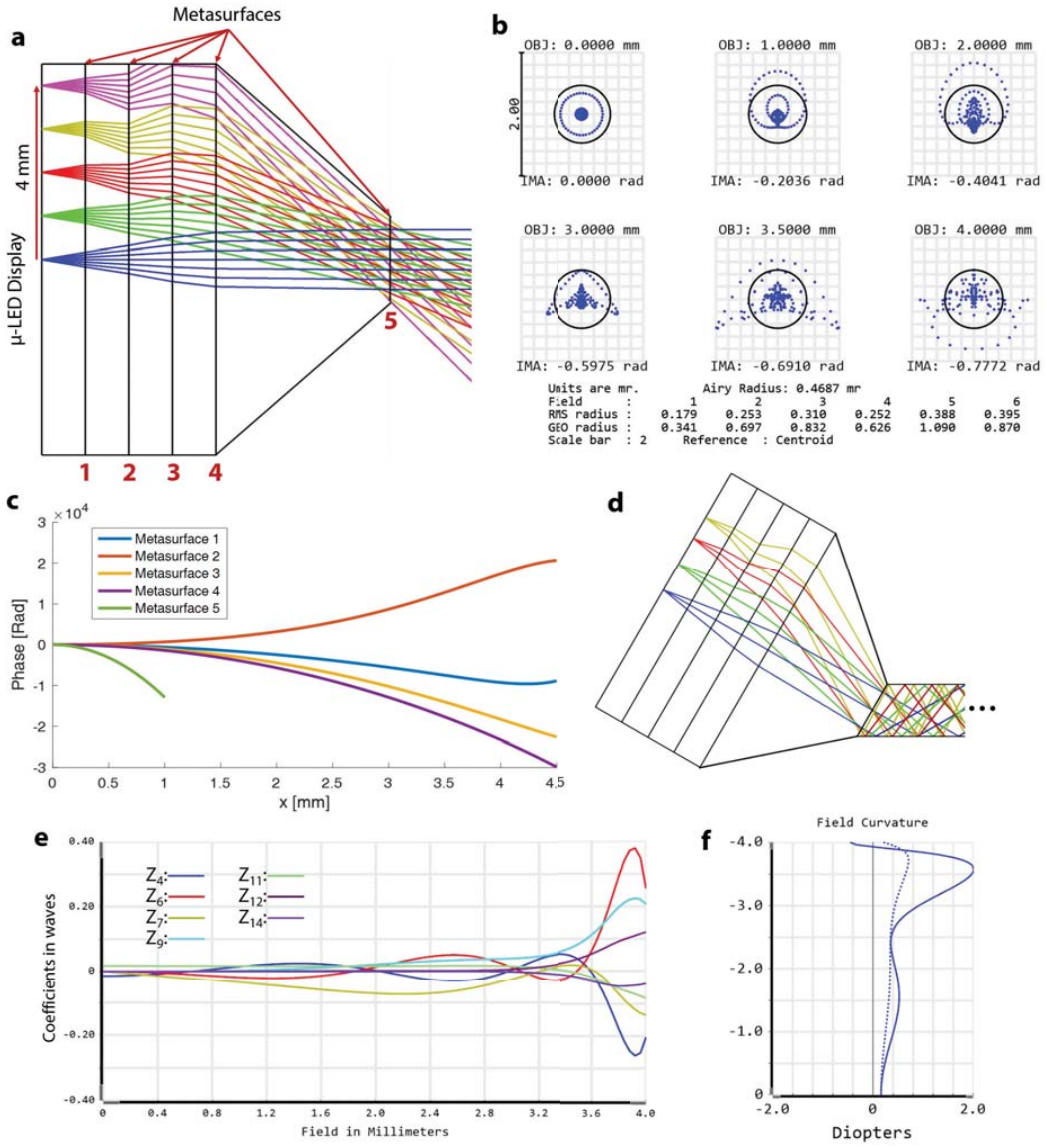

Figure 5.8: **Design of a 5-layer metasurface based light engine. (a)** A five-layer metasurface design with a FOV of 8 mm (diameter) and collection NA of 0.25. Locations of the metasurfaces are denoted with the numbered vertical lines. The system includes 4 glass layers of 1 mm thickness each, and a fifth layer that is 4 mm thick (the conical layer). The first 4 layers have refractive indices of ~1.5, and the fifth layer has an index of ~1.78 to match that of the prism and the waveguide. **(b)** Spot diagram simulations for six different points in the FOV. **(c)** Optimized phase profiles for the five metasurfaces, numbered from left to the right according to panel **a**. **(d)** Schematic of the light engine mounted on a 57.5-degree prism-coupled waveguide. **(e)** Nonzero standard Zernike coefficients 4-14 versus the FOV, calculated for an aperture diameter of 2.1 mm. **(f)** The field curvature versus FOV, showing less than 2 diopters of curvature, and also showing that the dominant aberration is astigmatism.

a density of 2.5 grams/cc).

As seen from the spot diagram simulations of Fig. **5.8b**, the system has a near-diffraction-limited focusing up to a FOV of 4 mm, corresponding to an angle of ~44 degrees (0.77 Rad). Considering the ~1.5 Rad FOV, the optics has more than 3000 resolvable points along the diagonal (corresponding to more than 2000×2000 points). The light at the object plane is telecentric and is collected up to an NA of 0.25 for most of the surface, except very close to 4 mm where the effective collection NA is slightly less. The optimized phase profiles for the five metasurfaces are plotted in Fig. **5.8c**. It is worth noting that for two of the metasurfaces the maximum required OPD is about 5000 waves, which corresponds to a thickness of more than 3 mm (assuming a glass with an index of 1.78). Figure **5.8d** schematically shows the light engine integrated with a waveguide that has a prism with a 57.5-degree edge, and therefore a thickness just below 1.8 mm. Assuming a waveguide index of 1.78 (similar to the one used here), angles from 35 to 80 degrees can be used for coupling as they are bounded by total internal reflection inside the waveguide. This means that an angular area of 45°×45° can be directly coupled inside the waveguide. Given the smaller than 0.5 mRad angular resolution, this corresponds to a resolution of more than 1500×1500 points for each color. With the three wavelengths combined, this means a total of more than 7 megapixels. On the μ-LED display, this roughly corresponds to a FOV of 4mm × 4mm. Given that μ-LED displays with pixel sizes of about 3 μm have already been demonstrated [287, 288], it seems reasonable to think that ones with pixel pitches of about 2.5 μm are feasible too. We should also note here that for such a smaller FOV, the metasurface optics can also have smaller diameter (about 7 mm) and smaller total volume (about 1.2 cc for the three wavelengths combined). In addition, the 45°×45° FOV inside the waveguide translates to a larger than 85°×85° FOV in air.

Figures **5.8e** and **5.8f** show the first nonzero standard Zernike coefficients (Z_4 to Z_14) and the field curvature, respectively. As seen from both graphs, the dominant aberration is astigmatism. Nevertheless, the RMS wavefront error (calculated from rays in reference to the centroid) is smaller than 0.25 waves over the whole FOV, and is smaller than 0.1 waves for field values below 3 mm. Calculated from the Zernike coefficients, the wavefront error peaks at slightly above 0.4 waves close to 3.9 mm, and is smaller than 0.25 waves below 3 mm.

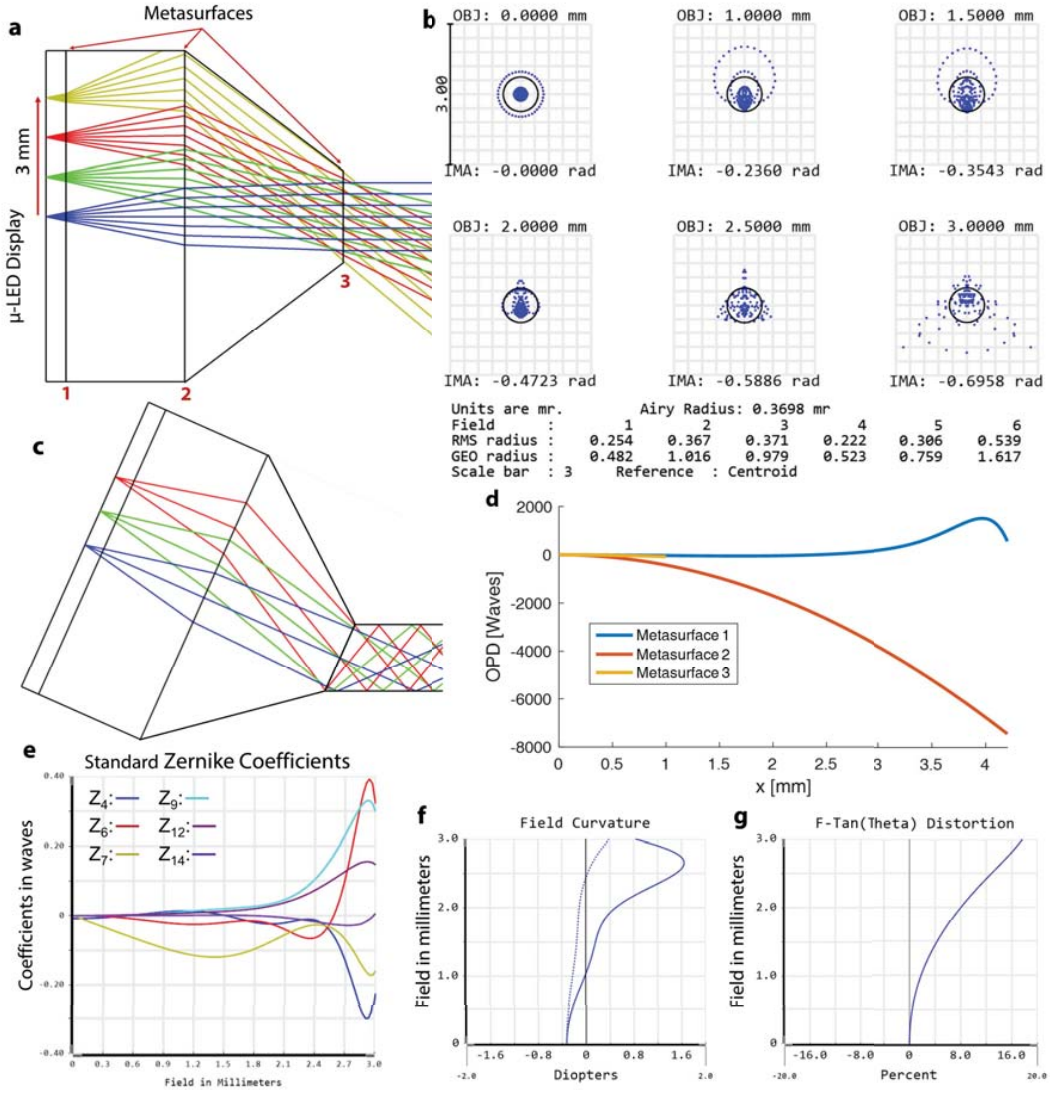

Figure 5.9: **Design of a more compact metasurface based light engine with 3 layers.** **(a)** A three-layer metasurface design with a FOV of 6 mm (diameter) and collection NA of 0.4. The three glass substrates and the waveguide have refractive indices of ~1.95, and are 0.5, 3, and 4 mm thick from left to right, respectively. **(b)** Spot diagram simulations for six different points in the FOV. **(c)** Schematic of the light engine mounted on a 60-degree prism-coupled waveguide. **(d)** Optimized phase profiles for the five metasurfaces, numbered from left to the right according to panel **a**. **(e)** Nonzero standard Zernike coefficients 4-14 versus the FOV, calculated for an aperture diameter of 2 mm. **(f)** The field curvature, and **(g)** distortion versus FOV.

Discussion

Like any other optical system, the design of the metasurface light engine optics involves various compromises. For instance, the collection NA and the angular resolution of the optics can be increased at the expense of FOV (with the same volume constraints). One example of such an alternative design is summarized in Fig. **5.9**. If high-index glass substrates are available (e.g., n≈1.95) and smaller physical FOVs are desired, more compact designs are possible similar to the one shown in Fig. **5.9**. This design has three metasurface layers, and can support a diagonal FOV of 6 mm on the display. The total optics size is smaller than 6mm × 6mm × 7.5mm, and it can deliver over 2000×2000 resolved points over a 105°×105° FOV in air. Other designs that are closer to the perfect human eye resolution of 0.3 mRad are possible with a FOV smaller than 6 mm diagonal. In addition, the number of metasurface layers is inversely proportional to the system efficiency, while it is possible to increase the collection NA with more layers. Therefore, a compromise should be made that maximizes the total system efficiency in this regard as well.

The main drawback of using metasurface optics is their large chromatic dispersion, which unlike refractive optics does not mainly originate from material dispersion and as such, unlike the case of refractive element, it cannot be solved using combination of different materials. While it is possible (and in fact relatively straight forward) to design metasurfaces that have high diffraction efficiencies over bandwidths of more than 10% [141, 289], similar to other diffractive devices [233], metasurfaces, have a large negative dispersion resulting from a phase profile that is almost constant with wavelength [135]. As a result, the regular chromatic dispersion of the metasurfaces can significantly decrease the achievable resolution and degrade the device performance. For instance, while the exact amount of degradation depends on the actual LED linewidth, for a typical value of 30-40 nm the resolution might drop by more than a factor of ten for the design in Fig. **5.9**. Despite the modest success of the independent group delay-phase delay control method in addressing the chromatic dispersion issue in metasurfaces [119, 255, 290], its applicability is severely limited to devices with miniature sizes (i.e., a couple of hundred microns in diameter) because of the requirement for extremely high quality factor resonances in millimeter scale devices. As a result, the two main approaches for addressing the chromatic dispersion issue are using metasurface diffractive/refractive combinations [27, 232, 280], and decreasing the emission bandwidth of μ-LEDs. With these methods, it might be possible to decrease the effect of chromatic dispersion to levels that are acceptable for the human eye.

The unique properties of metasurfaces enable a few platforms for tunable, conformal, and folded optical elements and systems that are more difficult to achieve with other technologies. For instance, various types of tunable metasurface devices, either based on stretchable substrates [36, 291] or micro-electro-mechanically tunable doublets [140] have been recently demonstrated that can potentially be integrated into the light engine optics to enable time-multiplexed multi-focus image rendering. Obviously, other types of flat tunable lenses, such as liquid crystal ones [197] can also be used for this purpose. Conformal metasurfaces [125, 292] provide additional design degrees of freedom by allowing for the metasurface to be non-planar. In addition to higher diffraction efficiencies and lower stray light, one of their main advantages over their conventional Fresnel counterparts is that the metasurface phase profile does not need to have the same symmetries of the underlying surface since the phase profile is defined lithographically in a different step. Finally, the folded metasurface optical platform can be used to reduce the total volume of the optics by using the metasurface substrate multiple times as propagation space [141]. While requiring more complicated design strategies (and potentially having a poorer optical quality), the folded metasurface platform can result in more compact devices with less complicated fabrication steps as most of the alignment steps can be eliminated.

Finally, while the use of low-throughput high-end patterning techniques like electron beam lithography is possible for proof of concept demonstrations and design rounds, it is essential to use low-cost high-throughput techniques such as nano-imprint lithography [293, 294] for mass production. Using such techniques and material systems like silicon for which high-quality etching processes are available can potentially reduce the fabrication cost of the optics.

In this section we proposed a design for a compact light engine composed of three monochrome μ-LED displays imaged using multi-metasurface optical systems corrected over a wide FOV. This design avoids the main challenge faced by both small μ-LED displays and metasurfaces, i.e., their operation is limited to one color range. As a proof of principle, we designed a five-layer and a three-layer metasurface optical system with a corrected FOV of 8 mm diagonal (close to 90° angular inside a glass with a refractive index of 1.78), with a close to diffraction-limited operation over the whole FOV. With a total size smaller than 2 cubic centimeters, the metasurface optics has the ability to generate 2000×2000 diffraction-limited points within its FOV. The same optics can be coupled to a waveguide delivery system and provide a wide FOV of >85°×85° in air. While several fundamental and technical challenges such as

the chromatic dispersion, alignment of different colors, and fabrication tolerances need to be investigated, we believe that this work demonstrates a clear potential for metasurfaces to address some of the challenges faced in the design of compact light engines for headmounted AR displays.

5.3 Micro-electro-mechanically tunable metasurface lens

Varifocal lenses, conventionally implemented by changing the axial distance between multiple optical elements, have a wide range of applications in imaging and optical beam scanning. The use of conventional bulky refractive elements makes these varifocal lenses large, slow, and limits their tunability. Metasurfaces, on the other hand, enable thin and lightweight optical elements with precisely engineered phase profiles. In this section, we demonstrate tunable metasurface doublets based on MEMS, with more than 60 diopters (about 4‰) change in the optical power upon a 1-μm movement of one metasurface, and a scanning frequency that can potentially reach a few kHz. They can also be integrated with a third metasurface to make compact microscopes (~1 mm thick) with a large corrected FOV (~500 μm or 40 degrees) and fast axial scanning for 3D imaging. This paves the way towards MEMS integrated metasurfaces as a platform for tunable and reconfigurable optics.

Introduction

Lenses are ubiquitous optical elements present in almost all imaging systems. Compact lenses with tunable focal/imaging distance have many applications, and therefore several methods have been developed to make such devices [36, 257, 291, 295–309]. Deformable solid and liquid-filled lenses with mechanical [295], electromechanical [296, 306], electro-wetting [303, 304], and thermal [305] tuning mechanisms have been demonstrated. Although these devices are more compact than regular multi-element varifocal lenses, they are still bulky (since they are regular refractive devices), and have low tuning speeds (ranging from a few Hz to a few tens of Hz). Liquid crystal lenses with tunable focus [297–299] have higher tuning speeds, but they suffer from polarization dependence and limited tuning range. Freeform optical elements (e.g., Alvarez lenses) that can tune the focal distance upon lateral displacement of the elements have also been demonstrated [257, 307]. These devices are generally based on mechanical movement of bulky elements and are therefore not very compact nor fast. Highly tunable diffractive and metasurface lenses based on stretchable substrates [36, 248, 291] have also been demonstrated, but they have

low speeds and require a radial stretching mechanism that might increase the total device size. Spatial light modulators (SLMs) and other types of diffractive elements that have pixels with controllable phase shifts have been used and proposed [308, 309] to achieve tunable beam steering and focusing. Liquid crystal based SLMs are polarization dependent and have limited speeds and NAs, and other proposals yet await an experimental demonstration of phase tuning over two dimensional arrays with high efficiency [308, 310].

The thin form factor of metasurfaces makes them suitable for development of ultra-thin conformal optical elements [125, 311], and their compatibility with conventional micro-fabrication techniques allows for monolithic fabrication of optical systems consisting of multiple metasurfaces on a single chip [120, 139]. These characteristics (i.e., the ability to precisely control the phase with subwavelength resolution and high gradients, thin and light form factor, and compatibility with micro-fabrication techniques) also make them very attractive for integration with the MEMS technology to develop metasurface-based micro-opto-electromechanical systems (MOEMS). To date, integration of metasurfaces and MEMS devices has been limited to moving uniform high-contrast grating mirrors to tune the resonance wavelength of Fabry-Pérot cavities [100, 312], or change the round trip propagation length of light to form SLMs [313].

In this section, we propose and demonstrate a metasurface doublet composed of a converging and a diverging metasurface lens with an electrically tunable focal distance. The large and opposite-sign optical powers of the two elements, as well as their very close proximity, make it possible to achieve large tuning of the optical power (~60 diopters, corresponding to about 4%) with small movements of one element (~1 micron). We have developed a fabrication process for making such metasurface doublets, and experimentally show metasurface lenses with over 60 μm tuning of the effective focal length (EFL) from 565 μm to 629 μm, corresponding to a ~180-diopter change in the optical power. Arrays of these devices can be fabricated on the same chip to allow for multiple lenses with different focal distances scanning different depths with frequencies potentially reaching several kHz. In addition, we show that such devices can be combined with the recently demonstrated monolithic metasurface optical systems design [139] to develop compact focus-scanning objectives with corrected monochromatic aberrations over a large FOV. It is worth noting that MOEMS devices with the ability to axially scan the focus have previously been demonstrated based on integration of refractive and Fresnel microlenses with axially

moving frames [300–302, 314]. However, in these devices the focal point is scanned by the same distance that the lens is moved, and the EFL (or equivalently the optical power) is not actually tuned. Nevertheless, the concepts and techniques used in such devices can be combined with the metasurface doublet demonstrated here to achieve enhanced functionalities (e.g., enable lateral scanning of focus).

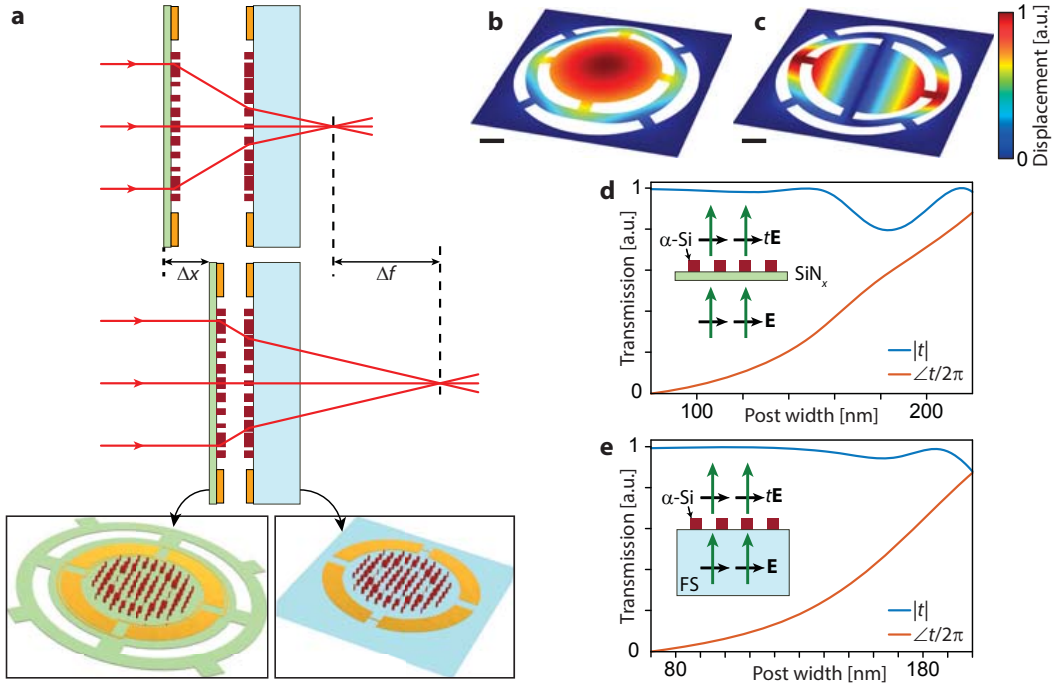

Figure 5.10: **Schematic illustration of the tunable doublet and design graphs.** **(a)** Schematic illustration of the proposed tunable lens, comprised of a stationary lens on a substrate, and a moving lens on a membrane. With the correct design, a small change in the distance between the two lenses (Δx ~1 μm) results in a large change in the focal distance (Δf ~35 μm). (Insets: schematics of the moving and stationary lenses showing the electrostatic actuation contacts.) **(b)** The first and **(c)** second mechanical resonances of the membrane at frequencies of ~2.6 kHz and ~5.6 kHz, respectively. The scale bars are 100 μm. **(d)** Simulated transmission amplitude and phase for a uniform array of α-Si nano-posts on a ~213-nm-thick SiN_x membrane versus the nano-post width. The nano-posts are 530 nm tall and are placed on the vertices of a square lattice with a lattice constant of 320 nm. **(e)** Simulated transmission amplitude and phase for a uniform array of α-Si nano-posts on a glass substrate versus the nano-post width. The nano-posts are 615 nm tall and are placed on the vertices of a square lattice with a lattice constant of 320 nm. FS: Fused silica.

Concept and design.

Figure **5.10a** shows a schematic of the tunable focus doublet. The system consists of a stationary metasurface on a glass substrate, and a moving metasurface on a SiN_x membrane. The membrane can be electrostatically actuated to change the distance between the two metasurfaces. The lenses are designed such that a small change in the distance between them, Δx ~1 μm, leads to a large tuning of the focal length (Δf ~36 μm change in the front focal length from 781 μm to 817 μm when the lens separation is changed from 10 μm to 9 μm, see Fig. **5.A8** for the phase profiles and their ray tracing simulations). The membrane and glass lenses are 300 μm in diameter, and have focal lengths of ~120 μm and ~-130 μm, respectively. The electrostatic actuation is achieved through contacts only to the glass substrate. The capacitor plates are shown in the inset of Fig. **5.10a**. The contacts are configured to make two series capacitors. Each capacitor has one plate on the glass substrate and another one on the membrane, resulting in an attractive force between the membrane and the glass substrate. Figures **5.10b** and **5.10c** show the first two mechanical resonance modes of the membrane at ~2.6 kHz and ~5.6 kHz, respectively. This limits the operation frequency of the device to ~4 kHz to avoid unwanted excitation of the second resonance.

The metasurfaces are based on high contrast dielectric transmitarrays [67, 76]. These devices consist of arrays of high index dielectric scatterers (nano-posts) with different shapes and sizes. With proper design, the nano-posts enable complete control of phase and polarization on a subwavelength scale [14, 132, 137]. When only phase control is required, the nano-posts should have a symmetric cross-section (i.e., square, circular, etc.). For fabrication considerations, we choose nano-posts with square-shaped cross-section on a square lattice. Since both the moving and stationary metasurface lenses have high NAs (NA~0.8), we used a recently developed technique for choosing the metasurface parameters (i.e., α-Si layer thickness, lattice constant, and minimum and maximum post side lengths) to maximize the efficiency of high NA lenses for both TE and TM polarizations [130]. The method is based on approximating the efficiency of a lens designed with certain metasurface parameters through efficiencies of periodic gratings designed with the same parameters. Using this method and considering the design wavelength of 915 nm, the α-Si layer thicknesses were chosen to be 530 nm and 615 nm for the moving and stationary lenses, respectively. The lattice constant was set to 320 nm in both cases. Figures **5.10d** and **5.10e** show simulated transmission amplitudes and phases for uniform arrays of nano-posts on the membrane and the glass substrate, respectively. Given a required phase profile,

one can find the best nano-post for each site on the metasurface using Figs. **5.10d** or **5.10e** [67].

Device fabrication.

A summary of the key fabrication steps for the moving and stationary lenses is schematically depicted in Figs. **5.11a**–**5.11f** (for more details see Appendix 5.3). The moving metasurface fabrication was started on a silicon wafer with a ~210-nm-thick low stress SiN_x. A 20-nm-thick SiO_2 layer followed by a 530-nm-thick α-Si layer was deposited on the SiN_x layer. The SiO_2 layer acts both as an adhesion promoter between the SiN_x and the α-Si layers, and as an etch-stop during the dry-etch process to form the metasurface. In the next step, patterns for backside holes were defined and transferred to an alumina layer. This layer was then used as a hard mask to partially etch through the silicon wafer (a ~50-μm-thick layer was left to maintain the mechanical strength of the sample during the next steps). Alignment marks were then etched through the α-Si layer for aligning the top and bottom sides. The metasurface lens was then patterned into the α-Si layer. Next, the metallic contacts were deposited and patterned. The top side of the device was covered with a protective polymer, and the remaining part of the wafer under the membrane was wet etched. Finally, the membrane was patterned and dry etched to release the metasurface. An optical image of the fabricated metasurface on a membrane is shown in Fig. **5.11b**. Due to the residual stress in the membranes, the beams are slightly bent such that the central part of the lens is about 6 to 8 μm above the surface of the wafer.

The fabrication steps of the stationary metasurface are schematically shown in Fig. **5.11c**. A 615-nm-thick layer of α-Si was deposited on a glass substrate. The metasurface pattern was generated and etched through the layer, followed by deposition and patterning of the contacts. An optical image of a completed metasurface on the glass substrate is shown in Fig. **5.11d**. Finally, a 20 μm spacer layer was spin coated and patterned on the glass substrate (to achieve a ~12 μm distance between the lenses), and the two chips were aligned and bonded with an ultraviolet (UV) curable epoxy [Fig. **5.11e**]. An optical image of the final device is shown in Fig. **5.11f**. Figures **5.11g** and **5.11h** show scanning electron micrographs of the fabricated metasurfaces.

Experimental doublet characterization results.

Figure **5.12** summarizes the focusing measurement results under application of a direct current (DC) voltage. For these measurements, the device was illuminated

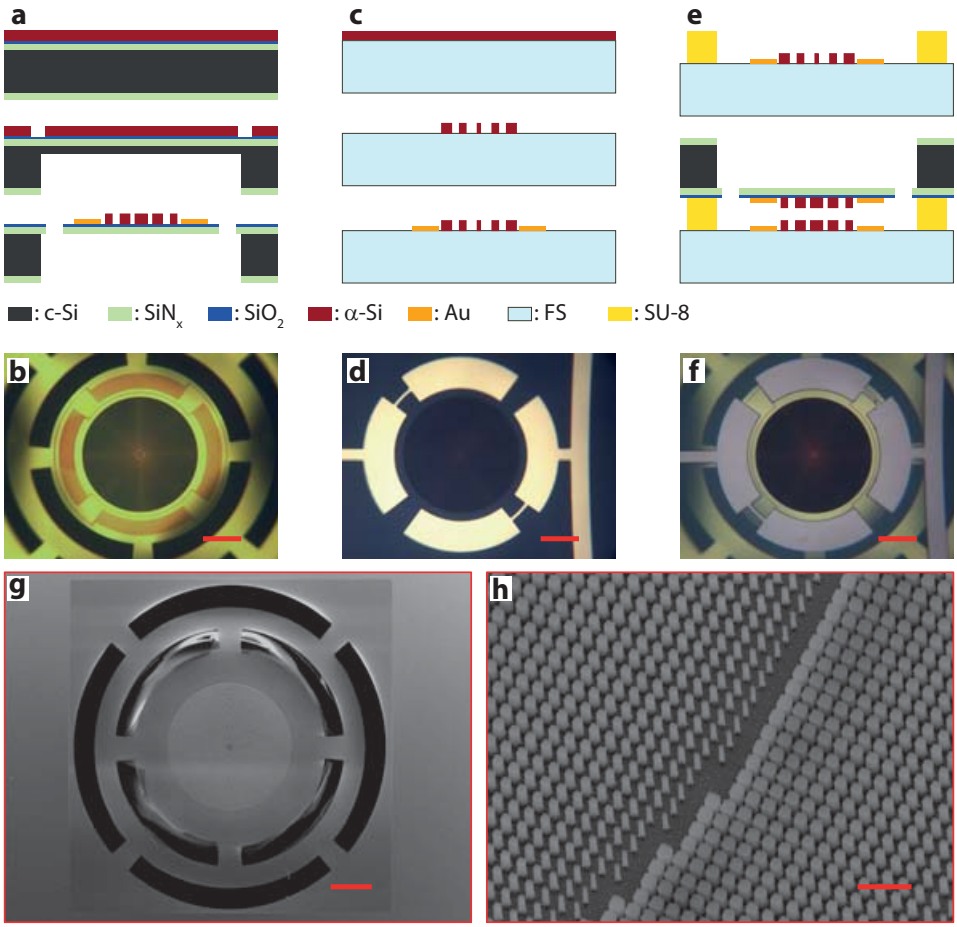

Figure 5.11: **Fabrication process summary. (a)** Simplified fabrication process of a lens on a membrane: a SiO_2 spacer layer and an α-Si layer are deposited on a silicon substrate with a pre-deposited SiN_x layer. The backside of the substrate is partially etched, and alignment marks are etched into the α-Si layer. The lens is patterned and etched into the α-Si layer, and gold contacts are evaporated on the membrane. The remaining substrate thickness is etched and the membrane is released. c-Si: crystalline silicon; FS: fused silica. **(b)** An optical microscope image of a fabricated lens on a membrane. **(c)** Simplified fabrication process of the lens on the glass substrate: an α-Si layer is deposited on a glass substrate and patterned to form the lens. Gold contacts are evaporated and patterned to from the contacts. **(d)** An optical microscope image of the fabricated lens on the glass substrate. **(e)** Schematic of the bonding process: an SU-8 spacer layer is patterned on the glass substrate, the two chips are aligned and bonded. **(f)** A microscope image of the final device. **(g)** Scanning electron micrograph of the lens on the membrane, and **(h)** nano-posts that form the lens. Scale bars are 100 μm in **b**, **d**, **f**, and **g**, and 1 μm in **h**.

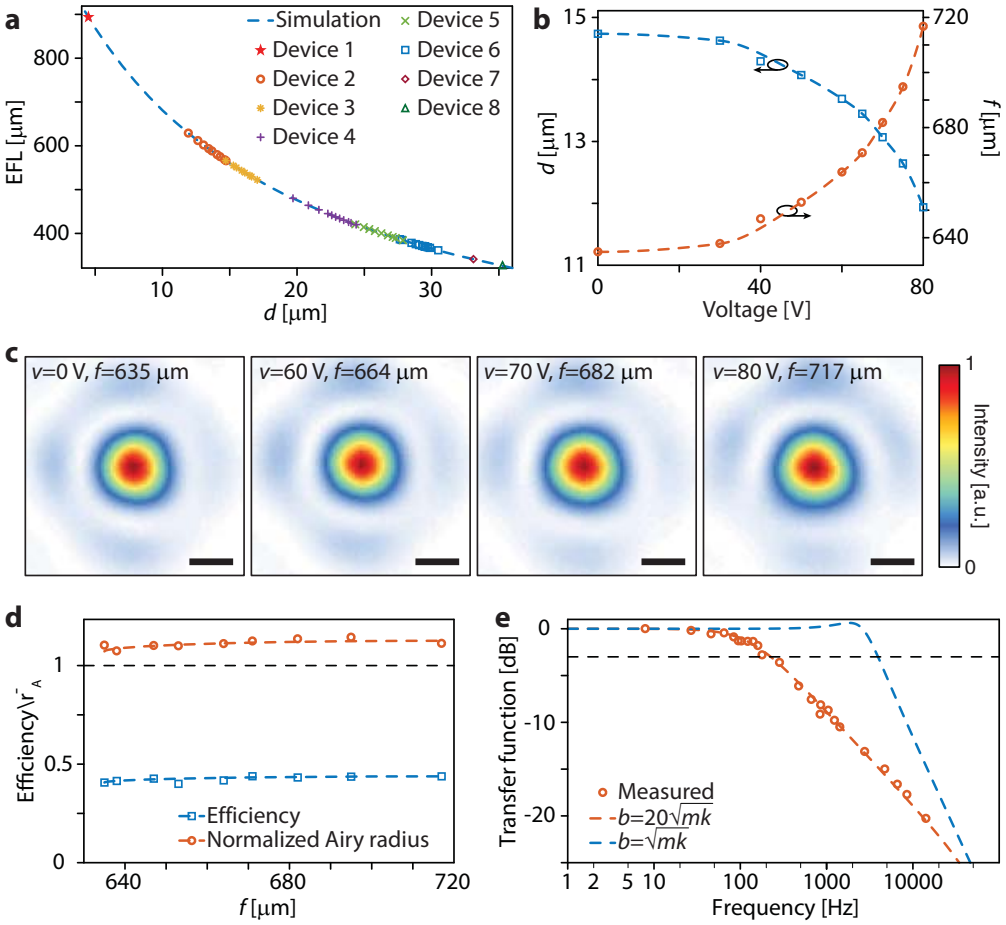

Figure 5.12: **Focusing measurement results of the tunable doublet. (a)** Simulated EFL versus the distance between lenses, along with measured EFL values for 8 devices under different applied voltages. Different devices have different initial lens separations, resulting in different focal distances under no applied voltage. **(b)** Measured front focal length versus the applied DC voltage for device 2 of panel **a**. The separation values between the moving and stationary lenses are also plotted. **(c)** Intensity distributions in the focal plane of the doublet lens at different actuation voltages. The scale bars are 2 μm. **(d)** Measured Airy radius (normalized to their corresponding diffraction-limited values), and measured absolute focusing efficiency of the tunable doublet. **(e)** Measured frequency response of the system, along with second order transfer functions with two values of the damping factor (b) equal to $20\sqrt{mk}$ and $\sqrt{mk}$.

with a collimated beam from a 915-nm diode laser, and the focal plane intensity patterns were imaged using a custom-built microscope (for details of the measurement setup, see Appendix 5.3 and Fig. **5.A9**). The simulated EFL is plotted against the distance between the two lenses in Fig. **5.12a**, along with the measured values for multiple devices with different initial separations between the membrane and the glass substrate. In all measurements, these separations were extracted by comparing the measured focal distances to their simulated values. We should note that devices 2 and 3 are on the same chip, and devices 4 to 8 are on another chip. This shows the potential of the proposed structure for integrating multiple devices on the same chip with the ability to scan different ranges of focal distances to simultaneously image a larger range of depths. Figure **5.12b** shows the measured front focal length (i.e., the physical distance between the focus and the stationary lens), and the extracted lens separation for device 2 versus the applied DC voltage, indicating that the optical power changes by more than 180 diopters when applying 80 V. The difference between the measured focal distances in a few measurements falls within the measurement error of ~5 μm. The possibility of changing the applied voltage very finely, makes it possible to tune the membrane separation and thus the optical power very finely, in the absence of external vibrations. Intensity distributions measured in the focal plane under application of different DC voltages are shown in Fig. **5.12c** for device 2. As seen in Figs. **5.12c** and **5.12d**, the measured Airy disk radii are smaller than 1.1 times their corresponding theoretical values. The observed aberrations are caused by the mechanical deformation of the moving lens resulting from the residual stress in the SiN_x layer. The metasurface lenses are designed for optimal performance when their separation changes from 12 to 6 μm. As a result of this change, the EFL should be tuned from 627 μm to 824 μm. The achieved initial distance between the metasurfaces is slightly different from the design value (~15 μm instead of ~12 μm) because the spacer layer was slightly thicker than intended. Besides, in order to avoid the pull-in instability (which would destroy the device), we stayed away from higher voltage values than 80 V in this sample. In principle, one should be able to decrease the lens separation in device 2 from 15 μm to about 10 μm, and thus increase the front focal distance from 635 μm to 781 μm (or change the EFL from 560 μm to 681 μm, tuning optical power by more than 300 diopters, or ~20%).

Figure **5.12d** shows the measured absolute focusing efficiency of the doublet (defined as the power passing through a ~20-μm-diameter aperture to the total power hitting the device). The absolute efficiency is between 40% and 45% for all applied voltage values. The high-NA (NA~0.8) singlets used here are expected to be ~75%

efficient [130]. Because the doublet uses two of such lenses, its efficiency is estimated to be ~55%. Taking into account the reflections at the three air-glass interfaces (a glass wafer is used to cap the backside of the membrane to fully isolate it from the environment airflow), we obtain a total efficiency of ~50% which agrees well with the measured efficiency values. We attribute the slightly lower measured efficiency to fabrication imperfections. It is foreseeable that the efficiency can be significantly improved with better optimization and design processes [131], use of anti-reflection coatings to reduce reflection losses, and optimizing the fabrication process.

The frequency response of the doublet is measured and plotted in Fig. **5.12e** (see Appendix 5.3 Fig. **5.A9** for details of frequency response measurement). The frequency response transfer function is defined as the membrane displacement at frequency f, normalized to its value under the same voltage applied in DC. The black dashed line shows the -3-dB line, showing a ~230 Hz bandwidth for the device. The red and blue dashed lines show second order system fits (i.e., $H(f) = \frac{1}{1-i(b/\sqrt{mk})(f/f_0)-(f/f_0)^2}$, where f_0 is the resonance frequency for the first mode, b is a damping factor, and m and k are the oscillator mass and spring constant, respectively), indicating that the fit follows the measurement well for $b = 20\sqrt{mk}$. This corresponds to a highly over damped system with a damping ratio ($b/2\sqrt{mk}$) of ~10. Under the atmosphere pressure the dominant loss mechanism is the air damping [315]. If the damping is reduced by about 20 times by reducing the air pressure inside the lens packaging (i.e., $b/2\sqrt{mk} \approx 0.5$), then the frequency response will follow the blue dashed line in Fig. **5.12e**, with a 3-dB bandwidth reaching 4 kHz. This would correspond to a quality factor of ~1 for the mechanical resonator, which should be feasible by reducing air damping. In addition, at such a low quality factor, oscillation and long settling times should not be an issue. Vacuum packaging could be done through bonding the backside glass substrate (the one with no metasurface) and the silicon chip carrying the membrane in a vacuum chamber with controllable pressure.

Imaging with electrical focusing.

The tunable doublet can be used for imaging with electrically controlled focusing. To demonstrate this, we formed an imaging setup using the doublet and a refractive lens. The setup is schematically shown in Fig. **5.13a**. A transmissive object was placed in front of the imaging system. A 1.8-mm diameter pinhole was placed in front of the aspheric lens to reduce the aperture and increase contrast. The system images the object to a plane ~130 μm outside the stationary lens substrate. Since

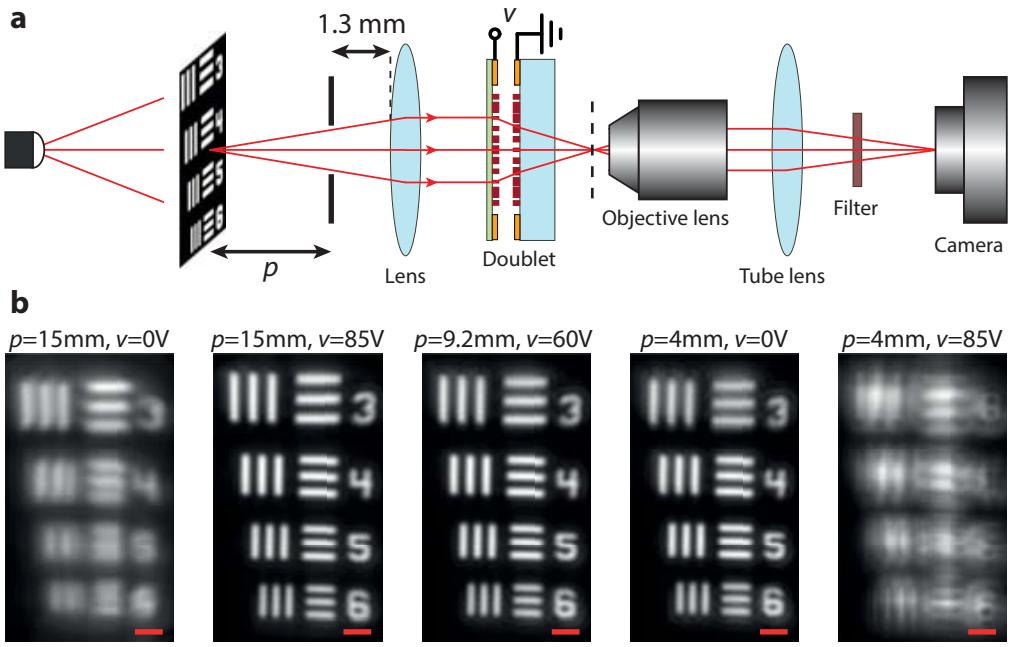

Figure 5.13: **Imaging with the tunable doublet.** **(a)** Schematic illustration of the imaging setup using a regular glass lens and the tunable doublet. The image formed by the doublet is magnified and re-imaged using a custom-built microscope with a ×55 magnification onto an image sensor. **(b)** Imaging results, showing the tuning of the imaging distance of the doublet and glass lens combination with applied voltage. By applying 85 V across the device, the imaging distance p increases from 4 mm to 15 mm. The scale bars are 10 μm.

this image is very small and close to the lens, we used a custom-built microscope (×55 magnification) to re-image it onto the camera. The results are summarized in Fig. 5.13**b**. When the object is p ~15 mm away and no voltage is applied, the image is out of focus. If the applied voltage is increased to 85 V in the same configuration, the image comes to focus. Changing the object distance to p ~9.2 mm, the voltage should also be changed to 60 V to keep the image in focus. At 0 V, the object should be moved to p ~4 mm to be in focus, and applying 85 V to the doublet will result in a completely out of focus image in this configuration. As observed here, by moving the membrane only about 4 μm, the overall system EFL changes from 44 mm to 122 mm, a ratio of about 1:2.8. This is an example of the importance of the large absolute optical power tunability of the metasurface doublet, especially when it is integrated into a system with a comparably small overall optical power. It also allows for changing the object distance from 4 mm to 15 mm by electrically controlled refocusing.

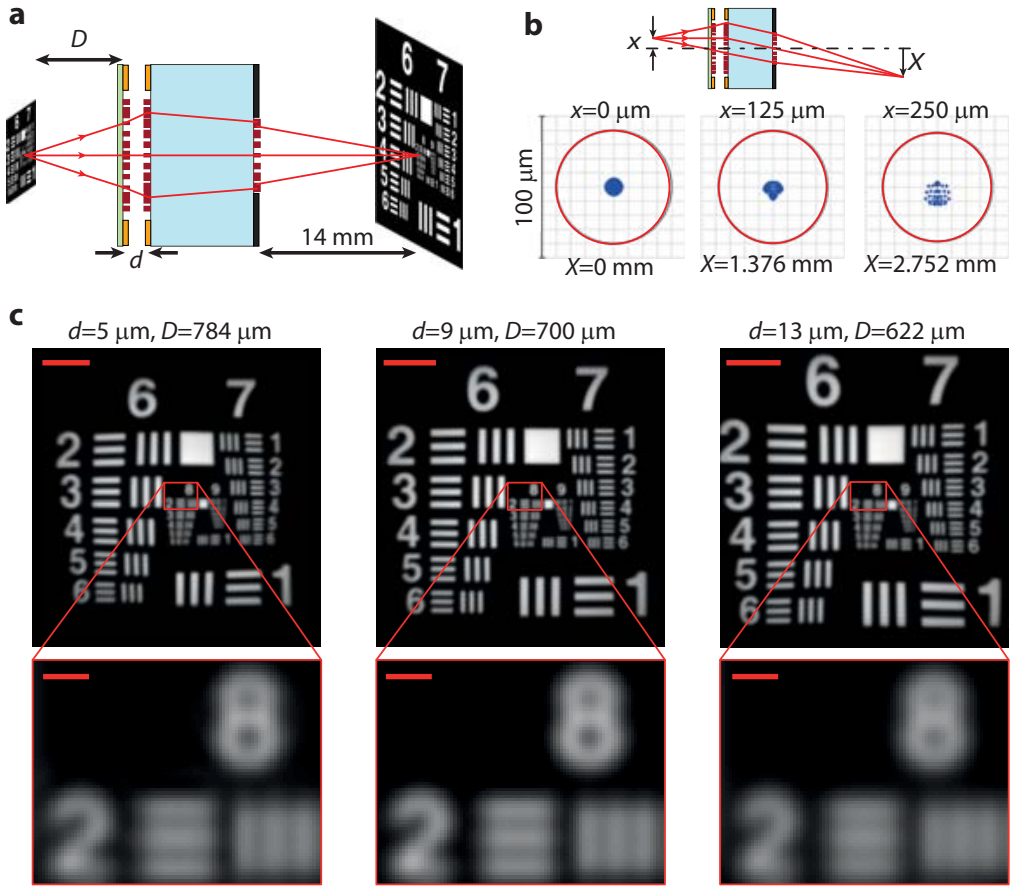

Figure 5.14: **Metasurface microscope with tunable focus.** **(a)** Schematic illustration of a metasurface triplet operating as a compact electrically tunable microscope. The metasurfaces have diameters of 540 μm, 560 μm, and 400 μm from the left to the right, respectively, and the glass substrate is 1 mm thick. Moving the membrane by about 8 μm moves the object plane more than 160 μm. **(b)** Ray optics simulation of spot diagrams of the microscope for the case of d =9 μm. The inset shows a schematic of the triplet, the locations of the point source in the object plane and the image plane. The phase profiles of the metasurfaces are designed to keep the focus almost diffraction-limited for a 500-μm-diameter FOV when d is changed from 5 to 13 μm. The system has a magnification close to 11 and an NA of 0.16 when d =9 μm. **(c)** Image simulation results using the triplet for different values of d and D. The scale bars are 50 μm in the zoomed-out images, and 5 μm in the zoomed-in areas.

Electrically tunable compact microscope.

To further demonstrate the capabilities of this platform, we use it to design a 1-mm-thick electrically tunable microscope. The structure is schematically shown in Fig. **5.14a**, and is a metasurface triplet composed of a tunable doublet (with an optical design different from the fabricated one), and an additional metasurface lens. The lenses, from left to right are 540 μm, 560 μm, and 400 μm in diameter. They have focal lengths of about -290 μm, 275 μm, and 1470 μm. The glass substrate is 1-mm thick, and the image plane is located 14 mm behind the third lens. The stop aperture is located at the plane of the right-most lens, and has the same diameter of 400 μm. By moving the membrane and changing the separation d from 13 μm to 5 μm, the object plane distance D changes from 622 μm to 784 μm. The triplet can be optimized to correct for monochromatic aberrations [139] to keep the focus close to the diffraction limit over a large FOV (see Fig. **5.A8** for phase profiles, and Table **5.A4** for the corresponding coefficients). Here, we have optimized the phase profiles to keep the focus almost diffraction-limited in a ~500 μm diameter FOV (corresponding to a ~40-degree FOV in the D=700 μm case). Spot diagrams of point sources at 0, 125, and 250 μm distances from the optical axis are shown in Fig. **5.14b**, demonstrating a diffraction-limited behavior. The spot diagrams are ray-optics simulation results from a point source at their corresponding distances from the optical axis. The red circles show the diffraction-limited Airy disks for different cases, with ~40-μm radii. Figure **5.14c** shows the image formation simulation results for the system at three different values of d (and D). The insets show that the system can resolve the ~3.5 μm line-space in an object. The EFL for the whole system is ~1160 μm (for d=9 μm case), which is significantly larger than the focal lengths of the membrane and first glass lenses, similar to the fabricated doublet. As a result, the object space NA is about 0.16, corresponding to a resolution of ~3.5 μm at the object plane. Considering the 14-mm distance between the image plane and the backside aperture, the image space NA is ~0.014 which results in an Airy radius of about 40 μm in the image plane. As the EFL of the system changes with tuning d, the total magnification of the system also changes from 11.3 (for d=5 μm) to 10.3 (for d=13 μm).

Discussion

The lenses demonstrated here have small sub-millimeter aperture sizes suitable for applications in ultra-compact optical systems. In principle, the lenses can have centimeter-scale apertures, as SiN_x membranes at these scales have already been

demonstrated [316, 317]. In addition, the electrostatic forces and the mechanical resonance frequencies can be engineered by appropriate choice of the electrostatic actuation plate areas, membrane thickness, and mechanical beam design.

The high optical power of the elements, and the small aperture of the doublet result in a relatively high sensitivity to the membrane bending, and to misalignment between the two lenses (see Fig. **5.A10** for modulation transfer function and Strehl ratio simulation results). We estimate the radius of curvature of the measured membranes to be ~20 mm, using mechanical simulations of the structure and the observed ~6-μm distance between the center of the lens and the surface of the wafer. This would result in a Strehl ratio slightly larger than 0.95. A Strehl ratio of 0.9 (as an acceptability criterion) corresponds to a radius of curvature of ~15 mm. If the membrane curvature is larger than this and known a priori, the lens design can be optimized to include the effects of the bending. In addition, to have a Strehl ratio better than 0.9, the misalignment between the two lenses should be better than 2 μm. Based on the symmetric measured focal spots, we estimate the misalignment in the doublets to be smaller than this limit. Considering the high alignment precision achievable with industrial aligners, achieving a 2-μm resolution is not a challenge.

Similar to other diffractive and metasurface optical devices, the lenses demonstrated here suffer from chromatic aberrations [23, 135, 233]. The exact "acceptable" operation bandwidth of the lens depends on the EFL, the NA, and a criterion for "acceptability". Using the criterion given in [139] that is based on the focal spot area increasing to twice its value at the center wavelength, and assuming an EFL of ~600 μm (corresponding to an NA of 0.24), the operation bandwidth is given by $\Delta\lambda = 2.27\lambda^2/(f\mathrm{NA}^2) \approx 50$ nm. To make multiwavelength tunable doublets, many of the recently demonstrated approaches for making multiwavelength metasurfaces can be directly applied [136, 137, 181, 227]. In addition, the recently introduced concept of phase-dispersion control [119, 261, 318] can be used to increase the operation bandwidth of the metasurface lenses by correcting the chromatic aberrations over a continuous bandwidth.

Here we introduced a category of MOEMS devices based on combining metasurface optics with the MEMS technology. To showcase the capabilities of the proposed platform, we experimentally demonstrated tunable lenses with over 180 diopters change in the optical power, and measured focusing efficiencies exceeding 40%. In principle, the optical power tunability could be increased to above 300 diopters for the presented design. We demonstrated how such tunable lenses can be used in

optical systems to provide high-speed electrical focusing and scanning of the imaging distance. The potentials of the introduced technology go well beyond what we have demonstrated here, and the devices can be designed to enable compact fast-scanning endoscopes, fiber-tip-mounted confocal microscopes, etc. In principle, metasurfaces can replace many of the refractive and diffractive micro-optical elements used in conventional MOEMS devices to make them more compact, increase their operation speed, and enhance their capabilities.

5.4 Folded metasurface spectrometer

An optical design space that can highly benefit from the recent developments in metasurfaces is the folded optics architecture where light is confined between reflective surfaces, and the wavefront is controlled at the reflective interfaces. In this section we introduce the concept of folded metasurface optics by demonstrating a compact spectrometer made from a 1-mm-thick glass slab with a volume of 7 cubic millimeters. The spectrometer has a resolution of ~1.2 nm, resolving more than 80 spectral points from 760 to 860 nm. The device is composed of three reflective dielectric metasurfaces, all fabricated in a single lithographic step on one side of a substrate, which simultaneously acts as the propagation space for light. The folded metasystem design can be applied to many optical systems, such as optical signal processors, interferometers, hyperspectral imagers and computational optical systems, significantly reducing their sizes and increasing their mechanical robustness and potential for integration.

Introduction

Optical spectrometry is a key technique in various areas of science and technology with a wide range of applications [319, 320]. This has resulted in a large demand for spectrometers and/or spectrum analyzers with different properties (e.g., operation bandwidth, resolution, size, etc.) required for different applications [321–323]. Conventional optical spectrometers are composed of a dispersive element, such as a prism or a diffraction gating, that deflects different wavelengths of light by different angles, followed by focusing elements that focus light incoming from different angles to different points (or lines). As schematically shown in Fig. **5.15a**, the intensity at different wavelengths can then be measured using an array of detectors. Diffraction gratings have typically larger dispersive powers than transparent materials, and therefore diffractive spectrometers generally have better resolutions [319]. The

combination of several free space optical elements (the grating, focusing mirrors, etc.) and the free space propagation volume result in bulky spectrometers. In recent years, there has been an increased interest in high-performance compact spectrometers that can be easily integrated into consumer electronics for various medical and technological applications such as medical diagnosis, material characterization, quality control, etc. [324, 325]. As a result, various schemes and structures have been investigated for realization of such spectrometers [325–334]. One class of miniaturized spectrometers integrate a series of band-pass filters with different center wavelengths on an array of photodetectors [102, 326]. Although these devices are compact and compatible with standard micro-fabrication techniques, they have resolutions limited by achievable filter quality factors, and low sensitivities caused by the filtering operation that rejects a large portion of the input power. Spectrometers based on planar on-chip integrated photonics provide another solution with high spectral resolution [325, 327–331]. However, the loss associated with on-chip coupling of the input light and the reduced throughput because of the single-mode operation [335] are still major challenges for widespread adoption in many applications.

Another type of compact spectrometers are conceptually similar to the conventional table-top spectrometers, however, they use micro-optical elements to reduce size and mass [332, 333]. Due to the inferior quality and limited control achievable by micro-optical elements as well as the shorter optical path lengths, these devices usually have lower spectral resolutions. Higher resolution has been achieved by using aberration-correcting planar gratings [334], however an external spherical mirror makes the device bulky.

A key feature of metasurfaces is their compatibility with micro and nano-fabrication techniques, which allows for integration of multiple metasurfaces for realizing complex optical metasystems [120, 139]. Such metasystems allow for significantly improving optical properties of metasurfaces through aberration correction (such as lenses with diffraction-limited operation over wide FOV [139]), or functionalities fundamentally unachievable with local single-layer metasurfaces such as retroreflection [120].

Concept and design

Taking a different approach to device integration, here we introduce folded optical metasystems where multiple metasurfaces are integrated on a single substrate that is

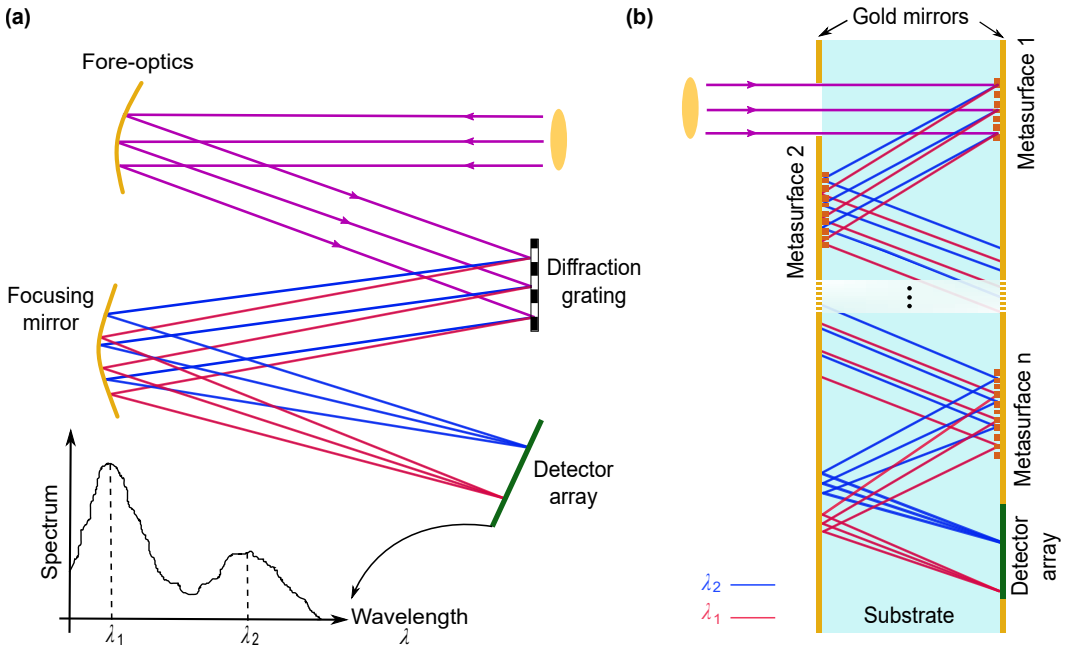

Figure 5.15: **Schematics of a conventional and a folded metasurface spectrometer. (a)** Schematic illustration of a typical diffractive spectrometer. The main components are comprised of the fore-optics section, diffraction grating, focusing lenses and detector array. **(b)** The proposed scheme for a folded compact spectrometer. All the dispersive and focusing optics can be implemented as reflective metasurfaces on the two sides of a single transparent substrate. Mirrors on both sides confine and direct light to propagate inside the substrate, and the detector can be directly the output aperture of the device. If required, transmissive metasurfaces can also be added to the input and output apertures to perform optical functions. Although the schematic here includes metasurfaces on both sides to show the general case, the actual devices demonstrated here are designed to have metasurfaces only on one side to simplify their fabrication.

also playing the role of propagation space for light [Fig. **5.15b**]. Using this platform, we experimentally demonstrate a compact folded optics device for spectroscopy with a 1-mm thickness (~7-mm^3 volume) that provides a ~1.2-nm resolution over a 100-nm bandwidth (more than 80 points over a ~12% bandwidth) in the near infrared. As schematically shown in Fig. **5.15b**, multiple reflective metasurfaces can be designed and fabricated on the same transparent substrate to disperse and focus light to different points on a plane parallel to the substrate. To the best of our knowledge, this is the first demonstration of an optical metasystem comprising more than two metasurfaces that implements a sophisticated optical functionality like spectrometry. Furthermore, the presented configuration allows for the integration of the detector array on top of the folded spectrometer, resulting in a compact

monolithic device. We should note here that it was recently demonstrated that an off-axis metasurface lens (i.e., a lens with an integrated blazed grating phase profile [336, 337]) can disperse and focus different wavelengths to different points. However, there are fundamental and practical limitations for such elements that significantly limits their application as a spectrometer (which is the reason why other types of diffractive optical elements, such as holographic optical elements and kinoforms, that can essentially perform the same function have not been used for this application before). Fundamentally, the chromatic dispersion [119, 135, 219, 232, 233] and angular response correlation of diffractive optical elements and metasurfaces [15, 338] limit the bandwidth and angular dispersion range where the device can provide tight aberration-free focusing. This in turn limits the achievable resolution and bandwidth of the device. Moreover, the chromatic dispersion results in a focal plane almost perpendicular to the metasurface, which will then require the photodetector array to be placed almost normal to the metasurface plane [336, 337, 339]. In addition to the distance for the propagation of dispersed light, this normal placement undermines the compactness of the device.

Figure **5.16a** shows the ray tracing simulations of the designed spectrometer. The device consists of three metasurfaces, all patterned on one side of a 1-mm-thick fused silica substrate. The first metasurface is a periodic blazed grating with a period of 1 μm that disperses different wavelengths of a collimated input light to different angles, centered around 33.9° at 810 nm. The second and third metasurfaces focus light coming from different angles (corresponding to various input wavelengths) to different points on the focal plane. We have recently demonstrated a metasurface doublet capable of correcting monochromatic aberrations to achieve near-diffraction-limited focusing over a wide FOV [139]. The second and third metasurfaces here essentially work similar to the mentioned doublet, with the difference of working off axis and being designed in a folded configuration, such that the focal plane for our desired bandwidth is parallel to the substrate. To simplify the device characterization, the focal plane was designed to be located ~200 μm outside the substrate. The asymmetric design of the focusing metasurfaces in an off-axis doublet configuration allows for the focal plane to be parallel to the substrate. This makes the integration of the spectrometer and the detector array much simpler, results in a more compact and mechanically robust device, and allows for direct integration into consumer electronic products like smartphones. The optimized phase profiles for the two surfaces are shown in Fig. **5.16a**, right (see Table **5.A5** for the analytical expression of the phases). Simulated spot diagrams of the spectrometer are plotted in Fig. **5.16b** for three

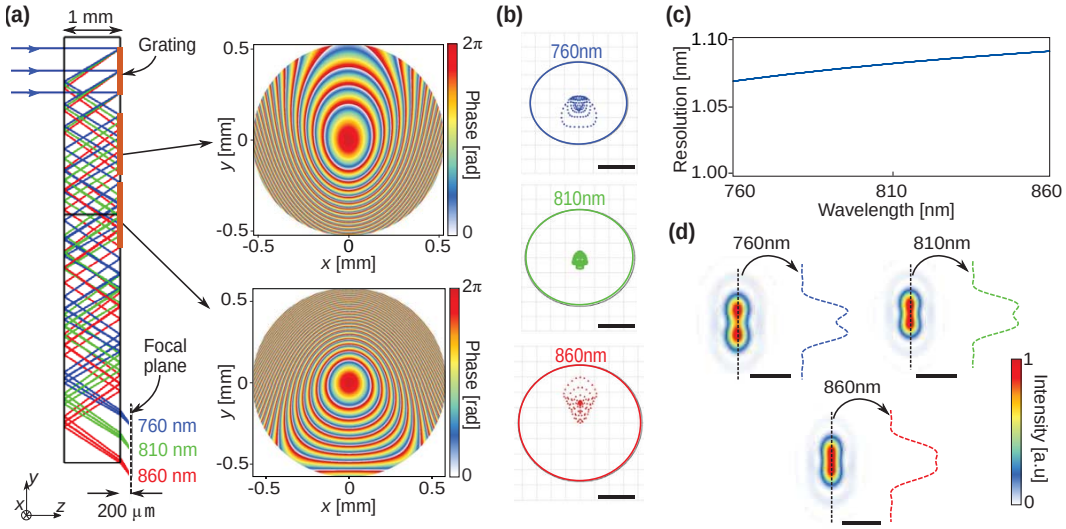

Figure 5.16: **Ray-optics design and simulation results of the folded spectrometer. (a)** Ray tracing simulation results of the folded spectrometer, shown at three wavelengths in the center and two ends of the band. The system consists of a blazed grating that disperses light to different angles, followed by two metasurfaces optimized to focus light for various angles (corresponding to different input wavelengths). The grating has a period of 1 μm, and the optimized phase profiles for the two metasurfaces are shown on the right. **(b)** Simulated spot diagrams for three wavelengths: center and the two ends of the band. The scale bars are 5 μm. **(c)** Spectral resolution of the spectrometer, which is calculated from simulated Airy disk radii and the lateral displacement of the focus with wavelength. **(d)** Simulated intensity distribution for two wavelengths separated by 1.1 nm around three different center wavelengths of 760 nm, 810 nm, and 860 nm. The intensity distributions show that wavelengths separated by 1.1 nm are theoretically resolvable. The scale bars are 20 μm.

wavelengths at the center and the two ends of the bandwidth showing negligible geometric aberrations. The spot diagrams are plotted only at three wavelengths, but the small effect of optical aberrations was confirmed for all wavelengths in the 760–860 nm bandwidth. As a result, the spectral resolution of the device can be calculated using the diffraction-limited Airy radius and the lateral displacement of the focus by changing the wavelength. The calculated resolution is plotted in Fig. **5.16c**, showing a theoretical value of better than 1.1 nm across the band. Point spread functions (PSFs) calculated for input beams containing two wavelengths 1.1 nm apart, and centered at 760 nm, 810 nm, and 860 nm are plotted in Fig. **5.16d**, showing two resolvable peaks.

To implement the reflective metasurfaces, we used a structure similar to the reflective

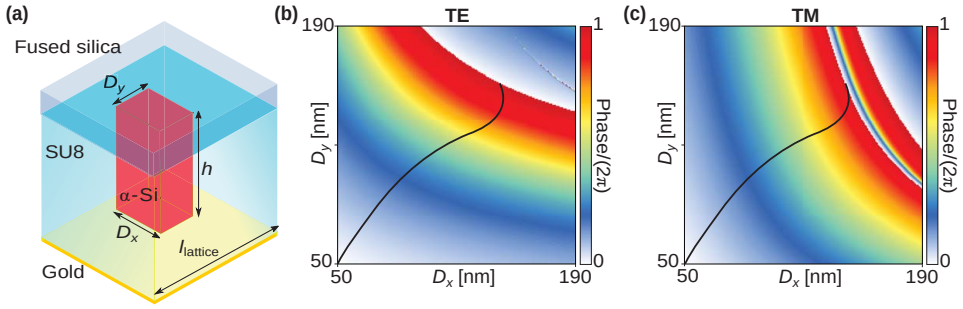

Figure 5.17: **Metasurface structure and design graphs.** **(a)** Schematics of the reflective rectangular meta-atom. The meta-atom consists of α-Si nano-posts on a fused silica substrate, capped by a layer of SU-8 polymer and backed by a gold mirror. The nano-post is 395 nm tall and the lattice constant is 250 nm for the blazed grating and 246 nm for the focusing metasurfaces. Schematics of the simulated structure and conditions are shown on the bottom. **(b)** and **(c)** Simulated reflection phase plotted for TE and TM polarizations. The black curve highlights the path through the D_x-D_y plane that results in equal phases for the two polarizations. Nano-posts on this path were used to design the two focusing metasurface elements to make them insensitive to the input polarization.

elements in [120]. Each of the meta-atoms, shown schematically in Fig. **5.17a**, consists of an α-Si nano-post with a rectangular cross section, capped by a ~2-μm-thick SU-8 layer and backed by a gold mirror. The post height and lattice constant were chosen to be 395 nm and 246 nm, respectively, to achieve full 2π phase coverage while minimizing variation of the reflection phase derivative across the band [Fig. **5.A11**]. Minimizing the phase derivative variation will mitigate the reduction of device efficiency over the bandwidth of interest [119] by decreasing the wavelength dependence of the phase profiles [Fig. **5.A12**]. In addition, since the two focusing metasurfaces are working under an oblique illumination (θ ~33.9°), the nano-posts were chosen to have a rectangular cross-section to minimize the difference in reflection amplitude and phase for the TE and TM polarizations (for the oblique incidence angle of 33.9° at 810 nm). Reflection coefficients are found through simulating a uniform array of nano-posts under oblique illumination (θ ~33.9°) with TE and TM polarized light [Fig. **5.17a**, right]. The simulated reflection phase as a function of the nano-posts side lengths are shown in Fig. **5.17b** and **5.17c** for TE and TM polarizations. The black triangles highlight the path through the D_x-D_y plane along which the reflection phase for the TE and TM polarizations is almost equal. In addition, as shown in Fig. **5.A12**, having almost the same reflection phases for the TE and TM polarizations holds true for the whole desired 760–860 nm bandwidth. The nanopost dimensions calculated from this path were used to implement the two

focusing metasurfaces

The blazed grating has a periodic phase profile (with a period of ~1 μm) that deflects normally incident light to a large angle inside the substrate. With a proper choice of the lattice constant (250 nm, in our case), its structure can also be periodic. This different structure and operation require a different design approach. The periodicity of the grating allows for its efficient full-wave simulation which can be used to optimize its operation over the bandwidth of interest. A starting point for the optimization was chosen using the recently developed high-NA lens design method [130], and the structure was then optimized using the particle swarm optimization algorithm to simultaneously maximize deflection efficiency at a few wavelengths in the band for both polarizations (see Appendix 5.5 and Fig. **5.A13** for details).

Device fabrication

The device was fabricated using conventional micro- and nano-fabrication techniques. First, a 395-nm-thick layer of α-Si was deposited on a 1-mm-thick fused silica substrate. All metasurfaces were then patterned using EBL in a single step, followed by a pattern inversion through the lift-off and dry etching processes. The metasurfaces were capped by a ~2 μm-thick SU-8 layer, and a 100-nm-thick gold layer was deposited as the reflector. A second reflective gold layer was deposited on the second side of the substrate. Both the input and output apertures (with diameters of ~790 μm and ~978 μm, respectively) were defined using photolithography and lift-off. An optical microscope image of the three metasurfaces, along with a scanning electron micrograph of a part of the fabricated device are shown in Fig. **5.18a**.

Experimental and characterization results

To experimentally characterize the spectrometer, a normally incident collimated beam from a tunable continuous wave laser was shinned on the input aperture of the device. A custom-built microscope was used to image the focal plane of the spectrometer, ~200 μm outside its output aperture (see Appendix 5.5 and Fig. **5.A15** for details of the measurement setup). The input wavelength was tuned from 760 to 860 nm in steps of 10 nm, and the resulting intensity distributions were imaged using the microscope. The resulting one-dimensional intensity profiles are plotted in Figs. **5.18b** and **5.18c** for TE and TM polarizations. The intensity profiles were measured over the whole 1.2-mm length of the y-direction in the focal plane (as shown in Fig. **5.18**, inset) at each wavelength. The background intensity is beyond visibility in the linear scale profiles plotted here for all wavelengths (see Figs. **5.A16** and

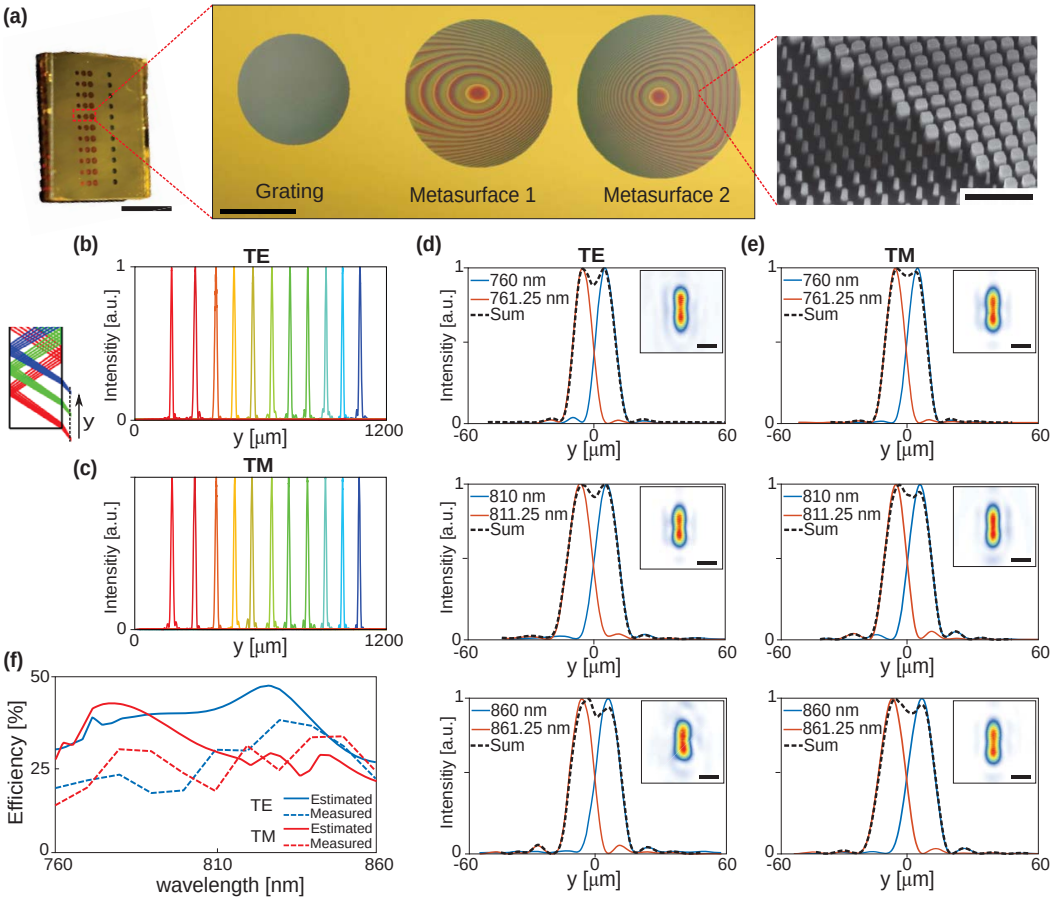

Figure 5.18: **Experimental characterization results. (a)** An optical microscope image of the fabricated device and metasurfaces before deposition of the second gold layer. Inset shows a scanning electron micrograph of a portion of one of the two focusing metasurfaces (scale bars from left to right: 10 mm, 500 μm, and 1 μm). **(b)** and **(c)** One dimensional focal spot profiles measured for several wavelengths in the bandwidth along the *y*-direction (as indicated in the inset) for TE and TM polarizations. The wavelengths start at 760 nm (blue curve) and increase at 10-nm steps up to 860 nm (red curve). **(d)** and **(e)** Measured intensity distributions for two input wavelengths that are 1.25 nm apart for TE and TM polarizations. The measurements were carried out at the center and and the two ends of the wavelength range for both polarizations. The insets show the corresponding 2-dimensional intensity profiles, demonstrating two resolvable peaks (scale bars: 10 μm). **(f)** Calculated and measured absolute focusing efficiencies of the spectrometer for TE and TM polarizations. Both polarizations have average measured efficiencies of ~25%.

5.A17 for two-dimensional and logarithmic-scale plots of the intensity distribution, respectively). Figures 5.18**d** and 5.18**e** show the measured intensity profiles for three sets of close wavelengths, separated by 1.25 nm. The insets show the corresponding two-dimensional intensity distribution profiles. For all three wavelengths, and for both polarizations the two peaks are resolvable. The experimentally obtained spectral resolution is plotted in Fig. 5.A18 versus the wavelength. The average resolution for both polarizations is ~1.2 nm, which is slightly worse than the theoretically predicted value (~1.1 nm). We attribute the difference mostly to practical imperfections such as the substrate having an actual thickness different from the design value and thickness variation. In addition the metasurface phases are slightly different from the designed profiles due to fabrication imperfections. The angular sensitivity/tolerance of the device was also measured with respect to polar and azimuthal angle deviations from 0 incidence angle, in the *x*-*z* and *y*-*z* planes, using the setup shown in Fig. 5.A19**c**. In the *y*-*z* plane the maximum tilt angle to maintain the same 1.25 nm resolution is ±0.15°, while in the *x*-*z* plane the device has a ±1° degree acceptance angle. The measurement results in Fig. 5.A19 match well with the predictions from ray-tracing simulations.

The measured and calculated focusing efficiencies are plotted in Fig. 5.18**f**. The focusing efficiency, defined as the power passing through a ~30 μm diameter pinhole around the focus divided by the total power hitting the input aperture, was measured using the setup shown in Fig. 5.A15. For both polarizations, the average measured efficiency is about 25%. As seen from the measured efficiency curves, the optimization of the blazed grating efficiency versus wavelength and the choice of the design parameters to minimize variations in the phase-dispersion for the doublet metasurface lens, have resulted in a smooth measured efficiency. An estimate for the expected efficiency (shown as simulated efficiency in Fig. 5.18**f**) is calculated by multiplying the deflection efficiency of the grating, the efficiency of seven reflections off the gold mirrors, the input and output aperture transmission efficiencies, and the average reflectivities of the uniform nano-post arrays (as an estimate for the two focusing metasurface efficiencies). It is worth noting that considering only the reflection losses at the interfaces (nine reflective ones, and two transmissive ones) reduces the efficiency to about 48%, showing a close to 50% efficiency for the three metasurfaces combined. We attribute the remaining difference between the measured and estimated values to fabrication imperfections (e.g., higher loss for the actual gold mirrors, and imperfect fabrication of the metasurfaces), the lower efficiency of metasurfaces compared to the average reflectivity of uniform arrays, and to the minor

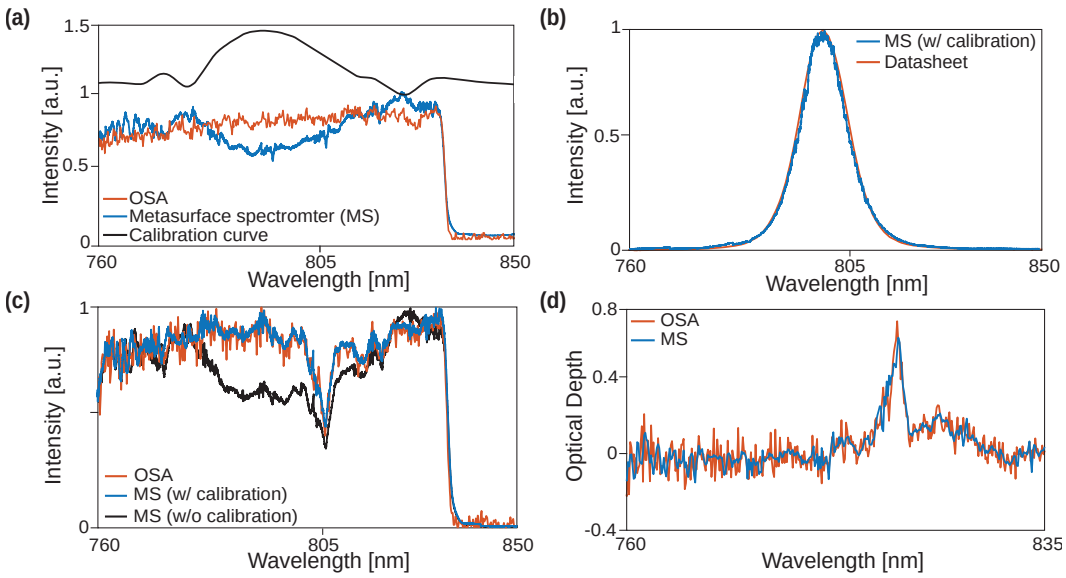

Figure 5.19: **Sample spectrum measurement results. (a)** Spectrum of a wideband source (a super-continuum laser with an 840-nm short-pass filter) measured by a commercial OSA and the MS. This measurement was used to extract the calibration curve. **(b)** Spectrum of a 10-nm band-pass filter centered at 800 nm measured by the MS, compared to the spectrum acquired from the filter datasheet. **(c)** Transmission spectrum of a Nd : YVO_4 crystal sample measured both with a commercial OSA and the MS. **(d)** The optical depth of the sample extracted from the spectrum measurements both with the OSA and the MS.

difference from the designed value of the metasurface phase profiles at wavelengths other than the center frequency.

Spectrum Measurement

To demonstrate that the metasurface spectrometer actually has the ability to measure dense optical spectra, we use it to measure the transmission spectra of two different samples. First, we measured the spectrum of a wideband source (a super-continuum laser source, filtered with an 840-nm short-pass filter), both with the metasurface spectrometer (MS) and a commercial optical spectrum analyzer (OSA). By dividing the spectra measured by the two devices, we extract the required calibration curve that accounts for the variation of the metasurface spectrometer as well as the non-uniformities in the responsivity of the optical setup used to image the focal plane (i.e., the objective lens and the camera, as well as the optical fiber used to couple the signal to the OSA). The measured spectra and the extracted calibration curve are plotted in Fig. **5.19a**. Next, we used this calibration curve to measure the transmission spectrum of a band-pass filter with a nominal 10-nm full width at half maximum bandwidth and

centered at 800 nm. The measured spectrum along with the transmission spectrum obtained from the filter datasheet are plotted in Fig. **5.19b**, showing a good agreement. Finally, we used the metasurface spectrometer to measure the optical depth of a Nd:YVO_4 crystal sample. The spectrum measured with the metasurface spectrometer (after calibration) is compared with the transmission spectrum of the same sample measured with the OSA in Fig. **5.19c**. Dividing the spectrum without and with the sample, we have extracted the optical depth of the sample which is plotted in Fig. **5.19d**. A good agreement is observed between the two measurement results. It is worth noting that the Nd:YVO_4 crystal sample was cut though the z-plane, resulting in an equal absorption spectrum for the two polarizations. Therefore, we can assume that all spectral measurements were done with the same state of input polarization. This justifies the use of only one calibration curve for all the measurements.

Discussion

The measured efficiency of the spectrometer demonstrated here is about 25%. This value can be significantly increased to about 70% by using mirrors with higher reflectivity (e.g., DBRs or high contrast grating mirrors [340, 341]), and anti-reflection coatings on the input and output apertures. In addition, more advanced optimization techniques [131] could be exploited to optimize the diffraction grating to achieve high efficiency and polarization insensitivity. Implementing these changes and optimizing the fabrication process, one can expect to achieve efficiencies exceeding 70% for the spectrometer.

The metasurface spectrometers are fabricated in a batch process, and therefore many of them can be fabricated on the same chip, even covering multiple operation bandwidths. This can drastically reduce the price of these devices, allowing for their integration into various types of systems for different applications. In addition, the demonstrated structure is compatible with many of the techniques developed for the design of multi-wavelength metasurfaces [135, 136], and therefore one might be able to combine different optical bandwidths into the same device (e.g., using a grating that deflects to the right at one bandwidth, and to the left at the other), resulting in compact devices with enhanced functionalities.

The optical throughput (etendue) is a fundamental property of any optical system, setting an upper limit on the ability of the system to accept light from spatially incoherent sources. It can be estimated as the product of the physical aperture size and the acceptance solid angle of the system. Furthermore, the total etendue

of a system is limited by the element with the lowest etendue. To calculate the throughput of the metasurface spectrometer, we have performed simulations and measurements to characterize its acceptance angle. According to the measurement results in Fig. **5.A19** the acceptance angle of the system is about 2 degrees in the horizontal direction, and 0.3 degrees in the vertical direction. Given this and the input aperture dimensions, the optical throughput of our device is calculated to be ~90 μm^2. For comparison, the etendue of optical systems operating around ~1 μm that utilize single-mode input channels (i.e., most optical spectrometers based on integrated optics platforms) is around ~1 $Sr\mu m^2$. Furthermore, the demonstrated spectrometer is optimized for maximum sensitivity and not throughput. To show that the achieved throughput here does not denote an upper limit for the etendue of a folded metasurface spectrometer with similar characteristics (i.e., resolution, bandwidth, etc.), we have designed a second device with a throughput of ~13000 $Sr\mu m^2$ (see Appendix 5.5 and Fig. **5.A20** for design details and simulation results). Table 5.1 provides a comparison of the optical throughput of several compact spectrometers from recent literature. According to Table 5.1, the spectrometers designed using the folded metasurface platform can collect 2 to 4 orders of magnitude more light compared to on-chip spectrometers that are based on single/few-mode input waveguides, resulting in a much higher sensitivity.

Table 5.1: **Comparison of different spectrometers in terms of throughput (etendue) and their dimensions**

Spectrometer	Etendue [$Sr\mu m^2$]	Size (dimensions)
[329]	<0.5	$50\mu m \times 100\mu m \times$ thickness
[342]	~ 0.8	$16mm \times 7mm \times 15\mu m$
This work	~ 90	$1mm \times 1mm \times 7mm$
[333]	8250	$20.1mm \times 12.5mm \times 10.1mm$
Fig. **5.A20**	~13000	$2mm \times 2.5mm \times 8mm$

The development of thin and compact optical elements and systems has been a key promise of optical metasurfaces. Although many optical devices have been developed in thin and compact form factors using metasurfaces, significantly reducing the volume of optical systems using metasurfaces has not been previously demonstrated due to the requirement of the free-space propagation in many systems (e.g., imaging systems, spectrometers, etc.). The folded metasystem configuration introduced here can significantly reduce the size of many of these optical systems using the substrate as the propagation space for light. Based on this configuration, we demonstrated a 1-mm-thick spectrometer with a 7-mm^3 volume, reduced by a factor of ten compared

to the same system implemented in an unfolded scheme (twenty times reduction, if the same system was designed in air). The spectrometer has a resolution of ~1.2 nm over a 100-nm bandwidth (>12%) in the near infrared. Using this design, multiple spectrometers can be fabricated on the same chip and in the same process, significantly reducing the costs and enabling integration of spectrometers covering multiple optical bands into consumer electronics. Moreover, by improving the angular response of the current device one can design a compact hyperspectral imager capable of simultaneous one-dimensional imaging and spectroscopy. In a broader sense, we expect that the proposed platform will also be used for on-chip interferometers, imaging systems, and other devices performing complex transformations of the field.

5.5 Planar metasurface retroreflector

In this section we show that cascaded metasurfaces, each performing a pre-defined mathematical transformation [343], provide a new optical design framework [139] that enables new functionalities not previously demonstrated with single metasurfaces. Specifically, we demonstrate that retroreflection can be achieved with two vertically stacked planar metasurfaces, the first performing a spatial Fourier transform and its inverse, and the second imparting a spatially varying momentum to the Fourier transform of the incident light. Using this concept, we fabricate and test a planar monolithic near-infrared retroreflector, made of two layers of silicon nano-posts, that reflects light along its incident direction with normal incidence efficiency of 78%, and a large half power FOV of 60°. The metasurface retroreflector demonstrates the potential of cascaded metasurfaces for implementing novel high performance components and enables low-power and low-weight passive optical transmitters [344–346].

The achievements in the field of metasurfaces open up a new paradigm in optical design, as we now can envision optical devices where light undergoes precise mathematical transformation as it propagates through multiple metasurface layers either planar of with arbitrary 2D shape. Compared to single-layer devices, multi-layer metasurfaces enable both increased performance [139] and new functionalities.

One functionality that has not previously been reported using single metasurfaces is retroreflection, defined as the ability to reflect light along its incident direction over a continuous range of incident angles. Optical retroreflectors are desirable in laser tracking [347] and for integration with planar modulators to realize modulating retroreflectors. A modulating retroreflector uses power from the incident

beam to transmit data, thus enabling passive transmitters with very low power consumption. Such passive transmitters have applications in optical free space communication [344–346], dynamic optical tags [348], optical sensor networks [349], and remote sensing [350]. Low weight and cost, and a planar shape (which is required for integration with modulators) are desirable features in these applications, but neither conventional retroreflector designs (i.e., corner cubes and cat's eye configurations) based on bulk optics nor novel designs [351, 352] have been able to offer them. Here we present retroreflection as a spatial linear filtering that can be implemented using cascaded metasurfaces, and experimentally demonstrate an efficient and low-weight planar metasurface retroreflector which can be mass-produced using cost-effective conventional semiconductor manufacturing techniques.

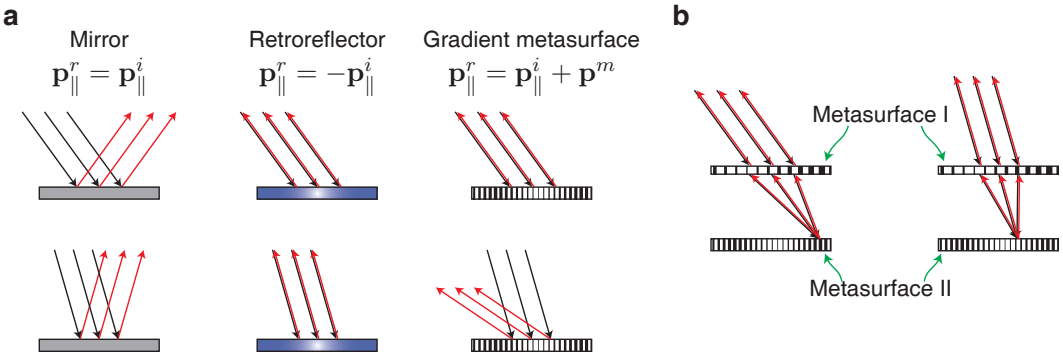

Figure 5.20: **Planar retroreflector concept. (a)** Schematic illustration of reflection by a mirror, a planar retroreflector, and a gradient metasurface. The mirror does not change the in-plane component of the momentum ($\mathbf{p}_{||}$) of incident light, while a retroreflector changes its sign, and the gradient metasurface adds a momentum ($\mathbf{p}^{m}$) to it. **(b)** Illustration of a planar retroreflector composed of two metasurfaces. Metasurface I performs a spatial Fourier transformation directing light with different incident angles to different spots on the metasurface II. The metasurface II operates as a gradient metasurface and adds a spatially varying momentum equal to twice that of the incident light but with the opposite sign.

Figure **5.20a** illustrates reflection form a mirror, a retroreflector, and a reflective gradient metasurface. All three of these components flip the direction of the normal component of the momentum of incident light. However, the mirror does not change the in-plane component of the momentum of incident light ($\mathbf{p}_{||}^{i}$), the retroreflector flips the direction of $\mathbf{p}_{||}^{i}$, and the gradient metasurface adds an in-plane momentum component ($\mathbf{p}^{m}$) to it. The in-plane momentum added by the gradient metasurface is proportional to the gradient of the local reflection phase [21], has negligible dependence on the incident angle [125], and might vary across the metasurface. The

gradient metasurface might be designed such that it reflects back light incident at a particular angle (i.e., $\mathbf{p}^m = -2\mathbf{p}_{||}^{i_0}$), but it will reflect light incident at any other angle to a direction different from the incident one (as shown in Fig. **5.20**). This issue can be resolved if optical waves with different incident angles are directed to different locations on the gradient metasurface, and the gradient metasurface is designed to impart a spatially varying momentum $\mathbf{p}^m(\mathbf{x}) = -2\mathbf{p}_{||}^{i}(\mathbf{x})$, where $\mathbf{p}_{||}^{i}(\mathbf{x})$ is the in-plane momentum of optical waves directed to the location $\mathbf{x}$ on the metasurface.

Directing optical waves with different incident angles to different locations is equivalent to taking the spatial Fourier transform of incident waves, and can be conducted using a transmissive gradient metasurface. This is schematically shown in Fig. **5.20b**, where metasurface I functions as a lens and focuses optical waves with different incident angles to different points on metasurface II. The combination of metasurfaces I and II operates as a retroreflector provided that the metasurface II imparts a spatially varying momentum given by $\mathbf{p}^m(\mathbf{x}) = -2\mathbf{p}_{||}^{i}(\mathbf{x})$. In the paraxial regime (i.e., incident angles within a few degrees from normal) the two metasurfaces can be considered as approximations of the two curved surfaces of a cat's eye retroreflector [121]. However, as we show here, the metasurface retroreflector can operate over a much larger range of incident angles by selecting aspheric phase profiles for the metasurfaces. As proof of principle, we considered two metasurfaces as shown in Fig. **5.20b**, and assumed they were patterned on two sides of a 500-μm-thick glass substrate. We optimized the phase profiles of the metasurfaces using the ray tracing technique by minimizing the wavefront error of the retroreflected light over ±50° incident angles. The retroreflector was designed for operation at the wavelength of 850 nm. The details of the optimization process and the optimized phase profiles are presented in Appendix 5.7 and in Figs. **5.A21** and **5.A22**, and Table **5.A8**.

We used the HCTA platform [67] to realize the metasurfaces. Metasurface I was implemented using the transmissive metasurface shown schematically in Fig. **5.21a**. The transmissive metasurface is composed of an array of α-Si nano-posts resting on a fused silica substrate, arranged on a hexagonal lattice with the lattice constant of 450 nm, and covered with a layer of SU-8 polymer. The array is non-diffractive in the substrate for incident angles up to ~47° (see Appendix 5.7). The transmittance and transmission phase of the nano-posts as a function of their diameters are shown in Fig. **5.21c**, showing that the phase of the transmitted light can be varied from 0 to 2π by changing the nano-post diameters while keeping the transmittance close to one.

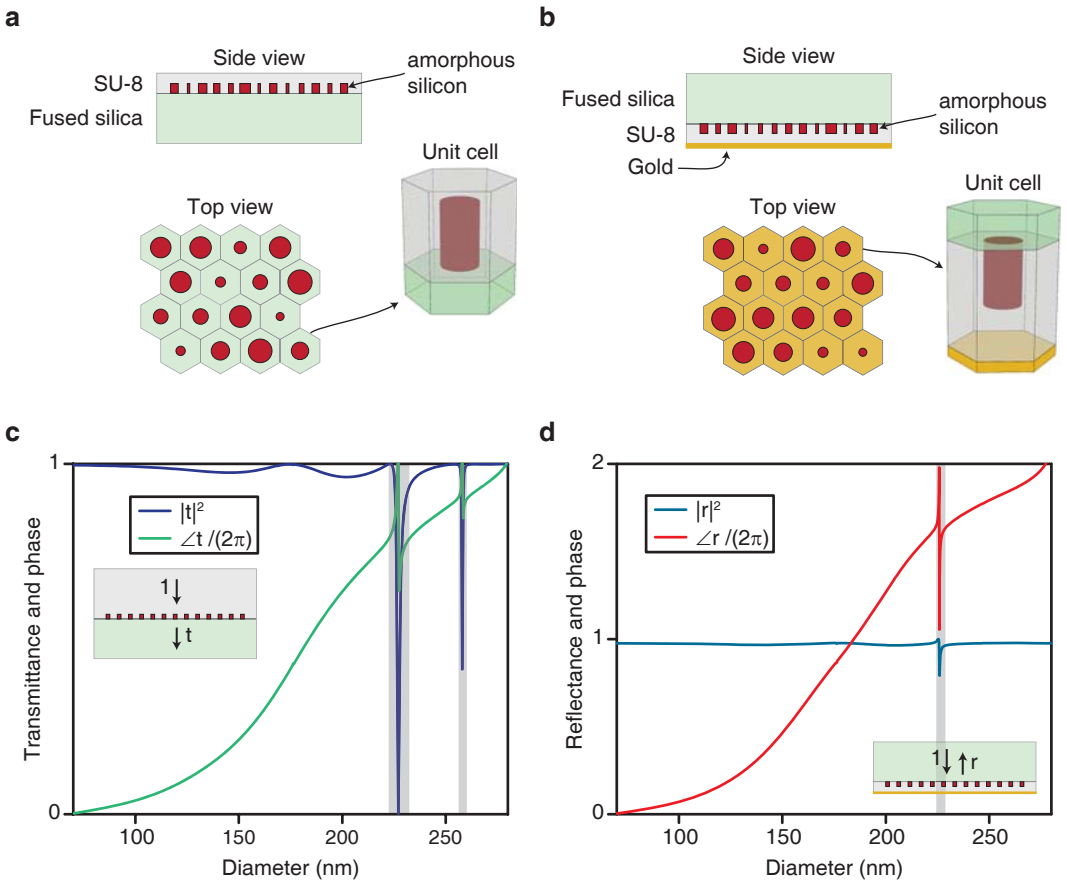

Figure 5.21: **Transmissive and reflective metasurfaces composing the retroreflector. (a)** Schematic illustration of the transmissive metasurface design used to implement metasurface I. The metasurface is composed of an array of α-Si nano-posts with different diameters that are arranged in a hexagonal lattice and covered with a layer of SU-8 polymer. **(b)** Similar to **a**, but for the reflective metasurface design used to realize metasurface II. The reflective metasurface is similar to the transmissive one except for an additional gold layer deposited over the SU-8 cladding. **(c)**, Simulated transmittance and transmission phase as a function of the nano-post diameter for the transmissive metasurface shown in **a**. **(d)** Simulated reflectance and reflection phase as a function of the nano-post diameter for the metasurface shown in **b**. The nano-post diameters corresponding to low transmittance (in **c**) or reflectance (in **d**), which are highlighted by grey rectangles, are excluded from the designs. The nano-posts are 600 nm tall, the lattice constant is 450 nm, and the simulation wavelength is 850 nm. See Appendix 5.7 for simulation details.

Intuitively, the nano-posts can be considered as short waveguides with circular cross section that support multiple resonances with relatively low quality factors [14, 67, 125]. These localized resonances lead to the high transmission of the metasurface for a wide range of nano-post diameters, and enable high fidelity implementation of metasurfaces with rapidly varying phase profiles. We note that each of these resonances has several significant terms in their multipole expansions. This is in contrast to short silicon posts (nano-disks) that typically only support two main resonances; one with a significant electric and the other with a significant magnetic dipole term. The large number of significant terms in the multipole expansion of longer nano-posts prevents a simple explanation of their operation using multipoles. Due to the high refractive index of α-Si, the nano-posts are weakly coupled, thus allowing the realization of any desired phase profile by spatially varying the nano-post diameters (as shown in Fig. **5.21a**) [67]. The metasurface II was implemented using the reflective metasurface design shown in Fig. **5.21b**. The reflective metasurface design is the same as the transmissive one shown in Fig. **5.21a** except for the addition of a reflective gold layer deposited on the SU-8 layer. Light incident from the substrate side passes through the nano-post layer, reflects from the gold layer, and passes through the nano-post layer again; therefore, it experiences twice the phase shift imparted by the nano-post layer. The reflectance and the reflection phase of the reflective metasurface as a function of the nano-post diameter are depicted in Fig. **5.21d**, showing that 4π phase shift and high reflectance are achieved by varying the nano-post diameter from 68 to 288 nm.

An array of retroreflectors was fabricated by patterning the metasurfaces I and II on opposite sides of a 500-μm-thick fused silica substrate. The schematic illustration of a single retroreflector is shown in Fig. **5.22a**. The diameters of the metasurface I and II are 500 μm and 600 μm, respectively. The metasurface I was first fabricated on one side of the substrate and was covered with a layer of SU-8. The SU-8 layer was then cured to form a rigid layer over the metasurface I and protect it during the fabrication of the metasurface II on the other side of the substrate (see Appendix 5.7 for fabrication details). An optical image of the fabricated array of retroreflectors is presented in Fig. **5.22b** that shows the two metasurface layers patterned on the two sides of the substrate. A scanning electron micrograph of the nano-posts composing the metasurfaces (taken before the SU-8 cladding step) is shown as an inset in Fig. **5.22b**.

The retroreflectance of the fabricated planar retroreflector for unpolarized light was

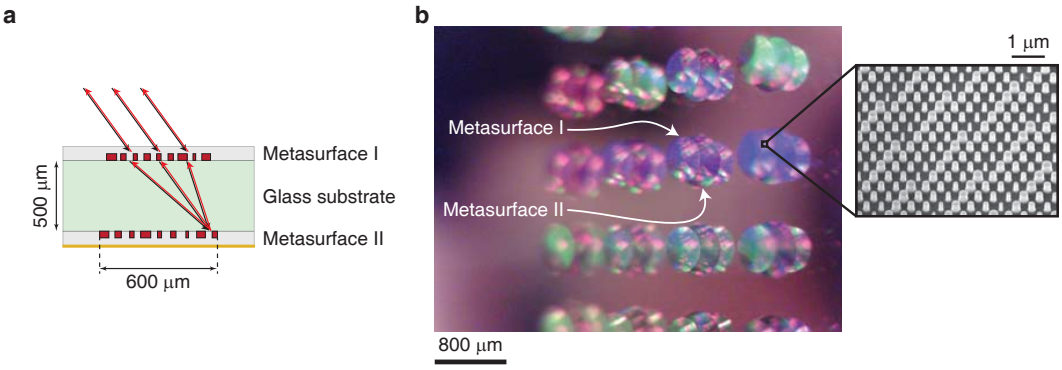

Figure 5.22: **Monolithic planar retroreflector made of two metasurfaces. (a)** Schematic drawing of the planar retroreflector. Two metasurfaces are patterned on opposite sides of a glass substrate. **(b)** Optical image of an array of retroreflectors. Each retroreflector is composed of metasurface I on the front side and metasurface II on the backside. The third metasurface seen in the photo behind metasurface II is the image of the metasurface I in the reflective gold coating of metasurface II. An SEM image of the nano-posts composing the metasurfaces is also shown. The image is taken before covering nano-posts with SU-8. See Appendix 5.7 for fabrication details.

characterized using the setup schematically shown in Fig. **5.23a**. The retroreflector was illuminated by unpolarized light emitted from an LED (center wavelength: 850 nm, FWHM bandwidth: ~40 nm), and the reflected light was imaged using a camera for different rotation angles of the retroreflector (θ). We note that the retroreflector is circularly symmetric and all the rotation axes are equivalent. The measured retroreflectance profiles for θ from 0° to 50° in 10° steps are shown in Fig. **5.23a** (for the profiles measured at smaller steps see Fig. **5.A23**). The reflectance profile at normal incidence ($\theta = 0°$) shows the retroreflector and also areas of the sample without the metasurfaces (i.e., reflection from the backside gold layer). At larger θ values, the two metasurfaces retroreflect while the light impinging on the areas without the metasurfaces is not reflected back along its incident direction and is not captured by the camera. The clear aperture of the retroreflector decreases as θ increases, which is partly due to the geometrical projection of the physical aperture (reduction proportional to $\cos(\theta)$) and partly due to the reduction of the overlap between the metasurface I and II (see Fig. **5.A21**).

The retroreflection efficiency, defined as the ratio of the power of the retroreflected beam to the power of the incident beam, was measured using the setup schematically shown in Fig. **5.23b** (see Appendix 5.7 for the measurement details). A polarized laser beam (center wavelength: 850 nm, FWHM bandwidth: ~0.9 nm) was retroreflected

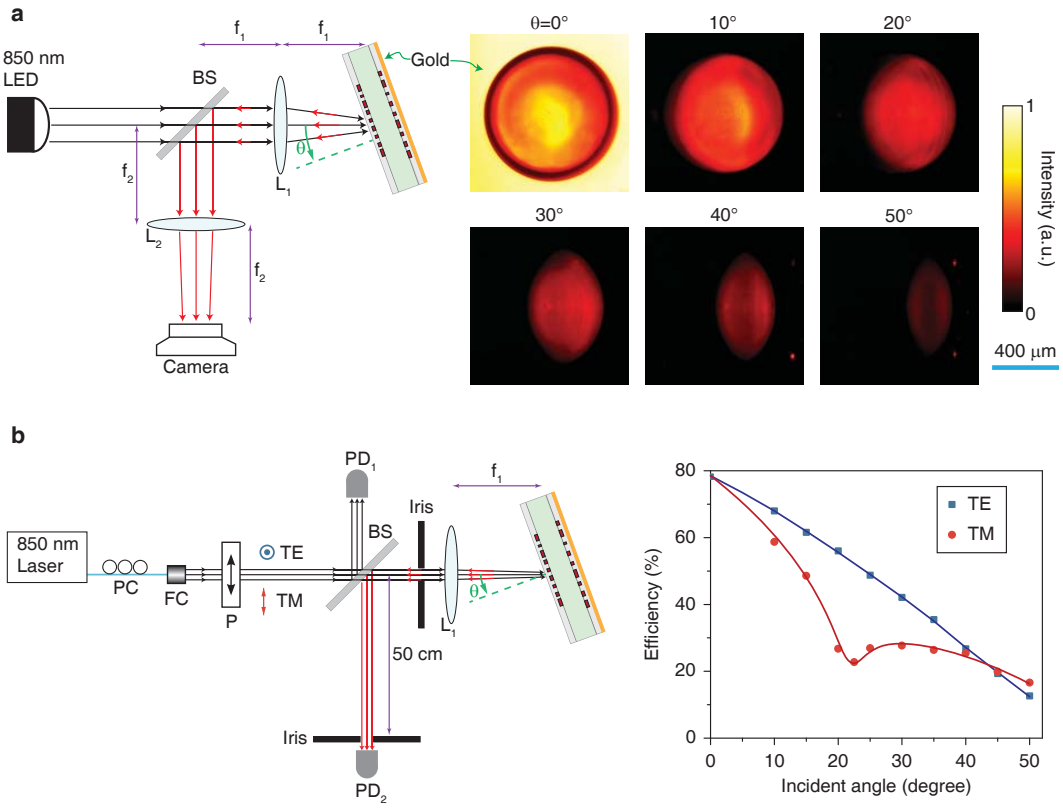

Figure 5.23: **Retroreflection profile and efficiency. (a)** Schematic of the measurement setup (left), and measured reflectance of the retroreflector as a function of the illumination incident angle (right). An LED was used as the illumination (center wavelength: 850 nm, FWHM bandwidth: ~40 nm), and the reflectance profile of the retroreflector was captured by the camera as the incident angle was varied by rotating the retroreflector. **(b)** Schematic of the measurement setup used for measuring retroreflection efficiency of the planar retroreflector (left), and measured efficiency as a function of incident angle (right). The efficiency values are measured for the TE and TM polarizations of the incident light. The measured data are shown by symbols and the solid lines are eye guides. See Appendix 5.7 for measurement details. BS: beamsplitter, L: lens, PC: polarization controller, FC: fiber collimator, P: polarizer, PD: photodetector. The focal lengths of lenses L_1 and L_2 are $f_1 = 5$ cm and $f_2 = 20$ cm, respectively.

by the device and the retroreflection efficiency was measured as a function of the incident angle for TE and TM polarizations. The absolute measured efficiency values are presented in Fig. **5.23b**. The retroreflection efficiency is approximately 78% close to normal incidence and decreases as the incident angle increases. The retroreflection efficiency for the TM polarization is lower than the TE polarization and shows a minimum for incident angles around 20°, a response similar to what has been previously observed for beam deflectors implemented using a similar nano-post metasurface platform [67]. Nano-posts with large diameters support a reflective resonant mode with a large axial electric field component (i.e., a dominant axial magnetic dipole) [125]. This mode has zero overlap with the in-plane components of the electric field of the incident wave; therefore, it is not excited at normal incidence or with TE-polarized incident waves. However, the electric field of TM-polarized waves has significant axial component and may efficiently excite this mode, leading to higher reflection and lower transmission of the TM-polarized waves. Therefore, we attribute the polarization dependence and the retroreflection efficiency reduction at larger angles to the incident angle dependence of the deflection efficiency of the nano-post metasurfaces [67, 125].

The dependence of the deflection efficiency on the deflection angle causes the non-uniformity of the retroreflection efficiency across the aperture of the device as observed in the normal incidence result shown in Fig. **5.23a**. As the simplified ray diagram depicted in Fig. **5.20b** (or the more detailed one shown in Fig. **5.A21**) shows, rays are deflected twice by metasurface I and once by metasurface II. Rays incident further away from the center of the device undergo larger deflection by both metasurfaces, and because the deflection efficiency of the metasurfaces decreases by increasing the deflection angle; the retroreflection efficiency of the device decreases as we move away from the center of the device.

To further confirm the wavefront preservation upon retroreflection by the device, we used the setup shown in Fig. **5.24a** and projected a demagnified image of a resolution target on to the retroreflector using the combination of lens L_3 and the objective lens. The light retroreflected by the device was then re-imaged by the combination of the objective lens and the lens L_2. The results showing the image reflected by the backside gold mirror, as well as the image reflected by the retroreflector for different incident angles up to 20° are shown in Fig. **5.24a**, confirming that the retroreflector preserves the quality of the images. The slight reduction in the quality of the retroreflected images compared to the reflected image (i.e., the image formed by the

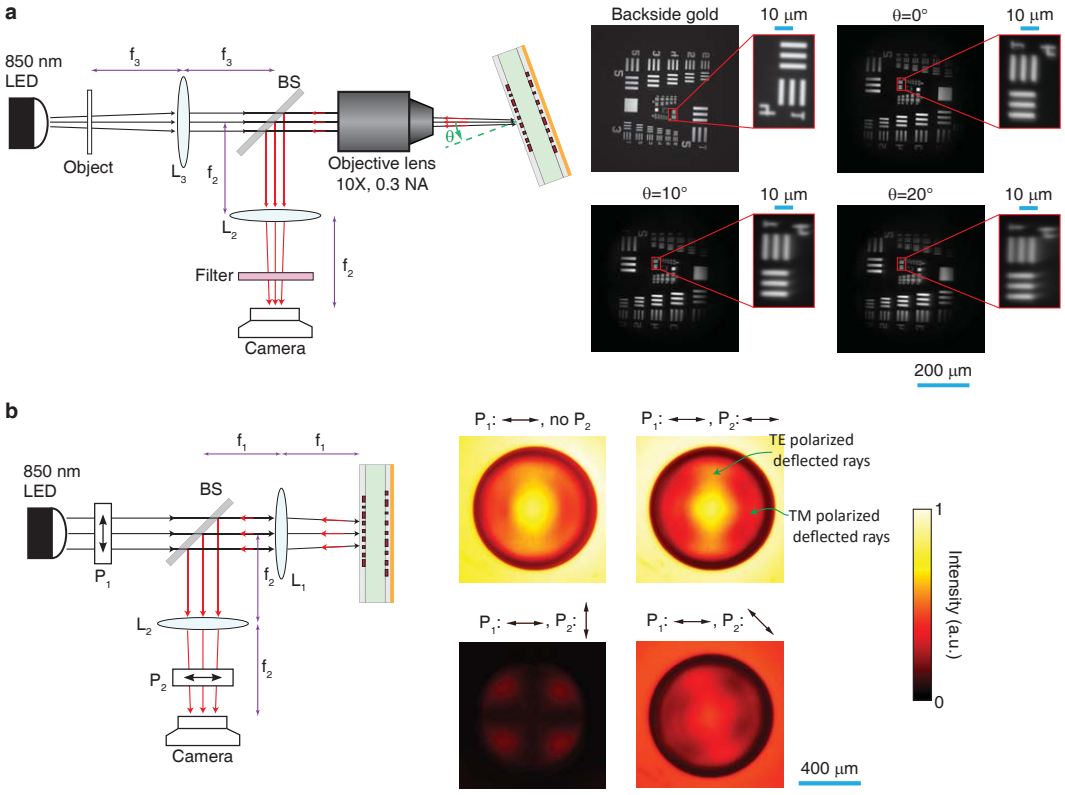

Figure 5.24: **Characterization of the wavefront and polarization modifications by the retroreflector. (a)** Illustration of the measurement setup (left), and measured images of the object in the backside gold mirror and the retroreflector as a function of the retroreflector rotation angle (right). The insets show expanded views of a small area on the images. A band-pass filter (center wavelength: 850 nm, FWHM bandwidth: ~10 nm) is placed in front of the camera to reduce the chromatic aberration introduced by the retroreflector. **(b)** Illustration of the setup used to characterize the polarization of the retroreflected light (left), and the images recorded by the camera for different orientations of the polarization axis of P_2. Areas of the retroreflector where horizontally polarized incident light is deflected with TE and TM polarization are labelled. BS: beamsplitter, L: lens, PC: polarization controller, FC: fiber collimator, P: polarizer, PD: photodetector. The focal lengths of lenses L_1, L_2, and L_3 are $f_1 = 5$ cm, $f_2 = 20$ cm, and $f_3 = 20$ cm, respectively.

backside gold layer) is mainly due to the chromatic aberration of the retroreflector, and the limited depth of focus of the objective lens which prevents the whole image to be in focus at large incident angles. Note that the retroreflected image is centrally reflected when compared with the reflected image. Similar images obtained for incident angles up to 40° using an objective lens with a longer depth of focus are presented in Fig. **5.A24**.

The polarization dependence of the deflection efficiency leads to slight modification of the polarization of optical waves upon retroreflection. If both metasurfaces I and II were functioning as ideal polarization independent phase masks, then the retroreflector would not change the polarization of the incident light. The nano-post metasurfaces are polarization insensitive upon normal incidence, but exhibit somewhat different deflection efficiencies for TE- and TM-polarized light when the incident rays have non-zero incident or deflection angles [67]. As a result, the polarization of rays that are incident on the device and are deflected with a combination of the TE and TM polarization might be slightly modified by the device. Using the setup shown in Fig. **5.24b**, we experimentally verified that the device does not modify the polarization of incident light that impinges on the central portion of the device and at locations where the light is purely deflected with TE or TM polarizations. The measurement results are also shown in Fig. **5.24b** and show that the polarization of a horizontally polarized incident light is not changed upon retroreflection by the device in the central part of the device and along the horizontal and vertical axes of the device where the deflected light is TM- and TE-polarized, respectively. However, along the ±45° axes, where the deflected light has both TE and TM components, the polarization of light is slightly modified upon retroreflection.

For a given substrate thickness, the maximum size of a single metasurface retroreflector is limited by the NA of the metasurfaces. High-NA metasurfaces deflect light by large angles and have lower efficiency than the metasurfaces with lower NAs. However, an arbitrarily large planar retroreflector can be realized by forming a 2D array of smaller metasurface retroreflectors presented here. The aperture of individual retroreflectors can be modified (e.g., to a square or a hexagon) to enable seamless tiling of the metasurface retroreflectors.

The metasurfaces and the planar retroreflector are designed for operation at a single wavelength (850 nm). As the wavelength of the incident light is detuned from the design wavelength, both the efficiency and the optical power of the metasurfaces change. The change of the efficiency (which is due to imperfect blazing at wavelengths

other than the design one) is moderate for the nano-post metasurfaces: the efficiency drops to ~90% of its peak value over 10% fractional bandwidth (i.e., ~8% drop in the retroreflector efficiency over 85 nm bandwidth) [67]. The chromatic change of the optical power of metasurfaces is caused by the wavelength dependence of the outline of the phase profiles of metasurfaces which in turn is caused by phase jumps at zone boundaries [23, 135]. The paraxial analysis of the planar metasurface retroreflector shows that the overall effect of the chromatic change of optical powers of both the metasurfaces is equivalent to placing a lens with the focal length of $f\lambda/\Delta\lambda$ in front of an achromatic retroreflector (f: focal length of the metasurface I, $\Delta\lambda$: wavelength deviation from the design wavelength λ) [353]. This chromatic lensing effect increases the divergence of the retroreflected light and decreases the backscattered light detected by a remote interrogator, thus limiting the retroreflector bandwidth. For example, for the retroreflector we presented here, 1 nm wavelength deviation from 850 nm would increase the divergence angle of a beam from 0.18° to 0.22° (assuming a beam with the waist radius of 350 μm whose 98% of power passes through the retroreflector aperture). The larger divergence angle of the retroreflected beam results in an estimated FWHM bandwidth of ~2.6 nm for the retroreflected power received at a remote location, which is large enough for applications employing laser sources such as free space optical communications and optical remote sensing. The bandwidth of the retroreflector can be increased by using dispersion engineered metasurfaces, and the retroreflector operation can be extended to multiple bands by using multi-wavelength metasurfaces [135, 227, 229].

The light weight and the planar form factor of the metasurface retroreflector enables its monolithic integration with planar optical modulators and detectors for implementation of low-power free space optical communication transceivers [344]. Furthermore, the metasurface retroreflector shows how cascading metasurfaces can provide novel functionalities in a planar form factor, thus paving the way for realizing novel and complex optical systems using metasurfaces.

Appendix 5.1: Doublet lens additional information and discussion

Simulation and design. The phase profiles of the two metasurfaces composing the doublet lenses were obtained through the ray tracing technique using a commercial optical design software (Zemax OpticStudio, Zemax LLC). The phase profiles were defined as even order polynomials of the radial coordinate ρ as

$$\phi(\rho) = \sum_{n=1}^{5} a_n \left(\frac{\rho}{R}\right)^{2n}, \tag{5.1}$$

where R is the radius of the metasurface, and the coefficients a_n were optimized for minimizing the focal spot size (root mean square spot size) at incident angles up to 30°. Two different metasurface doublet lenses were designed. The first doublet lens (metasurface doublet lens I) is optimized for focusing incident light in air, and was used in measurements shown in Figs. **5.3**, **5.4b**, and **5.4d**. The second doublet lens (metasurface doublet lens II) is optimized for focusing through the ~445-μm-thick cover glass of the CMOS image sensor, and was used in the implementation of the miniature camera as shown in Figs. **5.4f** and **5.4g**. The optimal values of the coefficients for the two doublet lenses are listed in Tables **5.A1** and **5.A2**, and the corresponding phase profiles are plotted in Fig. **5.A7**. The phase profile for the spherical-aberration-free metasurface singlet is given by $\phi(\rho) = -(2\pi/\lambda)\sqrt{\rho^2 + f^2}$, where f=717 μm is the focal length of the singlet (which is the same as the focal length of the doublet lens I).

The simulation results shown in Figs. **5.1b**, **5.1d**, **5.2b**, **5.2c**, and Fig. **5.A2** were computed assuming the metasurfaces operate as ideal phase masks (i.e., their phase profile is independent of the incident angle). Incident light was modelled as a plane wave and optical waves passed though the metasurfaces were propagated through the homogeneous regions (i.e., fused silica and air) using the PWE technique [219]. The simulated focal plane intensity results for wideband incident light, which are shown Fig. **5.5a**, were obtained by computing a weighted average of the optical intensity at several discrete wavelengths in the bandwidth of the incident light. The weights were chosen according to the power density of incident light (Fig. **5.5a**, bottom) assuming the diffraction efficiency of the metasurfaces is constant over the incident light's bandwidth. This assumption is justified because the efficiency of dielectric nano-post metasurfaces does not vary significantly over ~10% fractional bandwidth [67]. The simulated bandwidth-dependent modulation transfer function of the metasurface doublet lens shown in Fig. **5.5b** and Fig. **5.A6** were obtained by taking the Fourier transform of the simulated focal plane intensity distributions presented in Fig. **5.5a**.

Simulated transmission data of the periodic array of α-Si nano-posts presented in Fig. **5.2b** were obtained by using the RCWA technique using a freely available software package [217]. The simulations were performed at λ =850 nm. The α-Si nano-posts (with refractive index of 3.6 at 850 nm) are 600 nm tall, rest on a fused silica substrate (refractive index of 1.45), and are cladded with a layer of the SU-8 polymer (refractive index of 1.58 at 850 nm). The imaginary part of the refractive index of α-Si is smaller than 10^{-4} at 850 nm and was ignored in the simulations. The nano-posts are arranged in a hexagonal lattice with the lattice constant of a=450 nm. For normal incidence, the array is non-diffractive in both SU-8 and fused silica at wavelengths longer than $\lambda = n_{\mathrm{SU-8}}\sqrt{3}/2a$ =616 nm. The refractive indices of α-Si and SU-8 polymer were obtained through variable angle spectroscopic measurements.

The metasurface patterns were generated using their phase profiles $\phi(\rho)$ and the relation between the transmission and the diameter of the nano-posts shown in Fig. **5.2b**. The diameter of the nano-post at each lattice site (d) was chosen to minimize the transmission error defined as $E = |t(d) - \exp(i\phi)|$, which is the difference between the nano-post transmission $t(d)$ and the desired transmission $\exp(i\phi)$. The nano-posts diameters corresponding to low transmission, which are highlighted in Fig. **5.2b**, are automatically avoided in this selection process, as the low transmission amplitude results in a large transmission error.

Device fabrication. The metasurfaces forming the doublet lenses shown in Fig. **5.2c** were fabricated on both sides of a 1-mm-thick fused silica substrate. The substrate was cleaned using a piranha solution and an oxygen plasma. A 600-nm-thick layer of hydrogenated α-Si was deposited on each side of the substrate using the PECVD technique with a 5% mixture of silane in argon at 200° C. Next, the nano-post patterns for the correcting metasurfaces were defined on one side of the substrate as follows. First a ~300-nm-thick positive electron resist (ZEP-520A) was spin coated on the substrate and baked at 180° C for 5 min. Then a ~60-nm-thick layer of a water soluble conductive polymer (aquaSAVE, Mitsubishi Rayon) was spin coated on the resist to function as a charge dissipating layer during electron-beam patterning. The metasurface patterns and alignment marks were written on the resist using EBL. The conductive polymer was then dissolved in water and the resist was developed in a resist developer solution (ZED-N50, Zeon Chemicals). A 70-nm-thick layer of Al_2O_3 was deposited on the resist and was patterned by lifting-off the resist in a solvent (Remover PG, MicroChem). The patterned Al_2O_3 was then used as the hard

mask in dry etching of the underlying α-Si layer. The dry etching was performed in a mixture of SF_6 and C_4F_8 plasmas using an inductively coupled plasma reactive ion etching process. Next, the Al_2O_3 mask was dissolved in a 1:1 mixture of ammonium hydroxide and hydrogen peroxide heated to 80° C. Figure **5.2d** shows SEM images of the top and oblique view of the nano-posts at this step of the fabrication process. The metasurfaces were then cladded by the SU-8 polymer (SU-8 2002, MicroChem) which acts as a protective layer for the metasurfaces during the processing of the substrate's backside. A ~2-μm-thick layer of SU-8 was spin coated on the sample, baked at 90° C for 5 min, and reflowed at 200° C for 30 min to achieve a completely planarized surface. The SU-8 polymer was then UV exposed and cured by baking at 200° C for another 30 min. The complete planarization of the metasurfaces, and the void-free filling of the gaps between the nano-posts were verified by cleaving a test sample fabricated using a similar procedure and inspecting the cleaved cross section using a SEM.

The focusing metasurfaces were patterned on the backside of the substrate using a procedure similar to the one used for patterning the correcting metasurfaces. To align the top and bottom metasurface patterns, a second set of alignment marks was patterned on the backside of the substrate and aligned to the topside alignment marks using optical lithography. The focusing metasurface pattern was subsequently aligned to these alignment marks. The aperture and field stops were then patterned by photo-lithography, deposition of chrome/gold (10 nm/100 nm) layers, and photoresist lift-off. To reduce the reflection at the interface between SU-8 and air, a ~150-nm-thick layer of hydrogen silsesquioxane (XR-1541 from Dow Corning with refractive index of 1.4 at 850 nm) was spin coated on both sides of the substrate and baked at 180° C for 5 min.

Systematic fabrication errors due to non-optimal exposure dose in EBL, or over and under etching will generally increase or decrease the nano-post diameters almost by the same amount. To compensate for such errors, we fabricated a set of devices (as shown in Fig. **5.2c**) with all nano-post diameters biased by the same amount (in steps of 5 nm) from their design values. All the devices in the set showed similar focal spots, but with different focusing efficiencies. The focusing efficiency at normal incidence decreased by ~2.5% for every 5 nm error in the nano-post diameters.

Measurement procedure and data analysis. The measurement results shown in Figs. **5.3b**–**5.3e** were obtained using the experimental setup schematically shown in Fig. **5.3a**. An 850 nm semiconductor laser (Thorlabs L850P010, measured spectrum

shown in Fig. 5.A3) was coupled to a single mode fiber. The fiber passed through a manual polarization controller and was connected to a fiber collimation package (Thorlabs F220APC-780, $1/e^2$ beam diameter: ~2.3 mm). The collimated beam was passed through an LP (Thorlabs LPNIR050-MP) which sets the polarization of light incident on the doublet. The collimator and the LP were mounted on a rotation stage whose rotation axis coincides with the metasurface doublet lens. The focal plane of the doublet lens was imaged using an objective lens, a tube lens (Thorlabs AC254-200-B, focal length: 20 cm), and a camera (Photometrics CoolSNAP K4, pixel size: 7.4 μm). A 100× objective lens (Olympus UMPlanFl, NA=0.95) was used in the measurements shown in Figs. 5.3**b**–5.3**d**, and a 50× objective lens (Olympus LMPlanFl N, NA=0.5) with a larger FOV was used for obtaining the focal spot position data shown in Fig. 5.3**e**. A calibration sample with known feature sizes was used to accurately determine the magnification of the objective/tube lens combination for both of the objectives. The dark noise of the camera was subtracted from the measured intensity images shown in Figs. 5.3**b** and 5.3**c**.

The focusing efficiency presented in Fig. 5.3**d** is defined as the ratio of the optical power focused by the lens to the optical power incident on the lens aperture. The focusing efficiency for the normal incidence (zero incident angle) was measured by placing a 15-μm-diameter pinhole in the focal plane of the doublet lens and measuring the optical power passed through the pinhole and dividing it by the power of the incident optical beam. For this measurement, the $1/e^2$ diameter of the incident beam was reduced to ~500 μm by using a lens (Thorlabs LB1945-B, focal length: 20 cm) to ensure that more than 99% of the incident power passes through the aperture of the doublet lens (800 μm input aperture diameter). The incident and focused optical powers were measured using an optical power meter (Thorlabs PM100D with Thorlabs S122C power sensor). The pinhole was a 15-μm-diameter circular aperture formed by depositing ~100 nm chrome on a fused silica substrate and had a transmission of ~94% (i.e., 6% of the power was reflected by the two fused silica/air interfaces), and therefore the reported focusing efficiency values presented in Fig. 5.3**d** underestimate the actual values by a few percent.

The focusing efficiency values for non-zero incident angles were found using the focal spot intensity distributions captured by the camera and the directly measured focusing efficiency for normal incidence. First, the focused optical powers for different incident angles were obtained by integrating the focal plane intensity distributions within a 15-μm-diameter circle centered at the intensity maximum. The

intensity distributions were captured by the camera when the doublet was illuminated by a large diameter beam ($1/e^2$ beam diameter of ~2.3 mm) and the dark noise of the camera was subtracted from the recorded intensities before integration. Next, the focused optical powers for different incident angles were compared with the focused power at normal incidence and corrected for the smaller effective input aperture (i.e., a $\cos(\theta)$ factor). The measurement was performed for transverse electric (TE, with electric field parallel to the doublet lens's surface) and transverse magnetic (TM, with magnetic field parallel to the doublet lens's surface) polarizations of the incident beam.

The images presented in Figs. **5.4b** and **5.4c** were captured using the experimental setup schematically shown in Fig. **5.4a**. A pattern was printed on a letter-size paper (approximately 22 cm by 28 cm) and used as an object. The object was placed in front of the metasurface lens at a distance of ~25 cm from it. Three ruler marks were also printed as a part of the pattern at viewing angles of 0°, 15°, and 30°. The object was illuminated by an 850 nm LED (Thorlabs LED851L, measured spectrum shown in Fig. **5.A3**). The images formed by the metasurface lenses were magnified by approximately 10× using an objective lens (Olympus UMPlanFl, 10×, NA=0.3) and a tube lens (Thorlabs AC254-200-B, focal length: 20 cm). A bandpass filter (Thorlabs FL850-10, center wavelength: 850 nm, FWHM bandwidth: 10 nm) was placed between the objective lens and the tube lens. The placement of the filter between the objective and the tube lens did not introduce any discernible aberrations to the optical system. The magnified images were captured using a camera (Photometrics CoolSNAP K4) with pixel size of 7.4 μm. The images shown in Figs. **5.5c** and **5.5d** and Fig. **5.A4** were also captured using the same setup but with a different objective lenses (Olympus LMPlanFl, 20×, NA=0.4 for Figs. **5.5c** and **5.5d** and Olympus LMPlanFl N, 50×, NA=0.5 for Fig. **5.A4**).

The miniature camera schematically shown in Fig. **5.4f** is composed of the metasurface doublet lens II (with parameters listed in Table **5.A2**) and a low-cost color CMOS image sensor (OmniVision OV5640, pixel size: 1.4 μm) with a cover glass thickness of 445 ± 20 μm. An air gap of 220 μm was set between the metasurface doublet lens and the image sensor to facilitate the assembly of the camera. The metasurface doublet was mounted on a 3-axis translation stage during the measurements. To set the distance between the image sensor chip and the doublet, a far object was imaged and the distance was adjusted until the image was brought into focus.

The MTFs shown in Figs. **5.4d** and **5.4e** were computed by taking the Fourier

transform of the measured focal plane intensity distributions shown in Figs. **5.3b** and **5.3c**, respectively. The dark noise of the camera was first subtracted from the recorded intensity distributions. The diffraction limit curves shown in Figs. **5.4d** and **5.4e** is the simulated modulation transfer function of a diffraction-limited lens (i.e., Fourier transform of a the diffraction-limited Airy disk) with the same focal length (f=717 μm) and aperture diameter (D=800 μm) as the metasurface doublet and singlet lenses used in the measurements.

The image shown in Fig. **5.5e** was obtained using Wiener deconvolution [273], and by filtering the image shown in Fig. **5.5c** by the Wiener filter

$$\mathrm{H}(\nu) = \frac{\mathrm{MTF}(\nu)}{\mathrm{MTF}^2(\nu) + \mathrm{N}(\nu)/\mathrm{S}(\nu)}, \tag{5.2}$$

where ν is the spatial frequency, $\mathrm{MTF}(\nu)$ is the on-axis modulation transfer function of the metasurface doublet lens for illumination with 40 nm FWHM bandwidth (shown in Fig. **5.5b**), and $\mathrm{N}(\nu)$ and $\mathrm{S}(\nu)$ are the power spectral densities of the noise and the image, respectively. The noise was assumed to be white (i.e., constant power spectral density), and $\mathrm{S}(\nu)$ was assumed to be equal to the power spectral density of an image formed with a diffraction-limited imaging system withNA=0.4 (i.e., the NA of the objective lens used for magnification in the experimental setup). The signal to noise ratio was found as ~250 by estimating the camera's noise, and was used to set the constant value for $\mathrm{N}(\nu)$.

Imaging bandwidth of metasurface lenses. Here we discuss the relation between the NA, focal length, and bandwidth of a metasurface lens. We consider a metasurface lens with the focal length of f which is designed for operation at the wavelength λ, and is placed at the distance f from an image sensor. The metasurface lens focuses light with the wavelength of $\lambda + \Delta\lambda$ to the distance of $f - \Delta f$ from the metasurface lens. Because of the phase jumps at the zone boundaries of the metasurface lens, the fractional change in the focal length is equal to the fractional change in the wavelength [135], that is

$$\frac{\Delta f}{f} = \frac{\Delta\lambda}{\lambda}. \tag{5.3}$$

As $\Delta\lambda$ increases the focal plane of the lens moves further away from the image sensor and the size of the spot recorded by the image sensor increases. As a quantitative measure, we define the bandwidth of the metasurface lens as the wavelength change $\Delta\lambda$ that increases the diameter of the recorded spot by a factor of $\sqrt{2}$ compared to its value at λ. With this definition, the distance between the image sensor and the focal

plane at the wavelength of $\lambda + \Delta\lambda$ is equal to the Rayleigh range z_0 of the focused light (i.e., $\Delta f = z_0$). The Rayleigh range is given by

$$z_0 = \frac{\pi w_0^2}{\lambda}, \tag{5.4}$$

where w_0 is the $1/e^2$ focal spot radius and is inversely proportional to the NA of the metasurface lens

$$w_0 = \frac{\lambda}{2\sqrt{\ln(2)}\mathrm{NA}}. \tag{5.5}$$

Therefore, the fractional bandwidth of the metasurface lens is given by

$$\frac{\Delta\lambda}{\lambda} = \frac{\pi w_0^2}{\lambda f} = \frac{\pi}{4\ln(2)} \frac{\lambda}{f\mathrm{NA}^2}, \tag{5.6}$$

and is proportional to $\lambda/(f\mathrm{NA}^2)$.

Appendix 5.2: Doublet lens supporting figures and tables

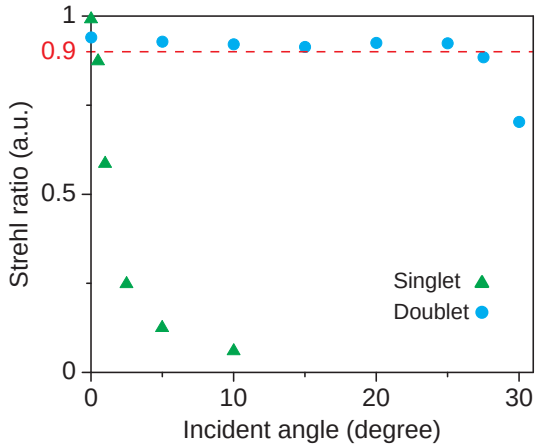

Figure 5.A1: **Strehl ratio of the singlet and doublet metasurface lenses**. Strehl ratio is the ratio of the volume under the 2D MTF of a lens to the volume under the 2D MTF of a diffraction-limited lens with the same NA. The red dashed line shows the Strehl ratio value of 0.9 which we have used as a threshold for referring to the focal spot as being "nearly diffraction-limited".

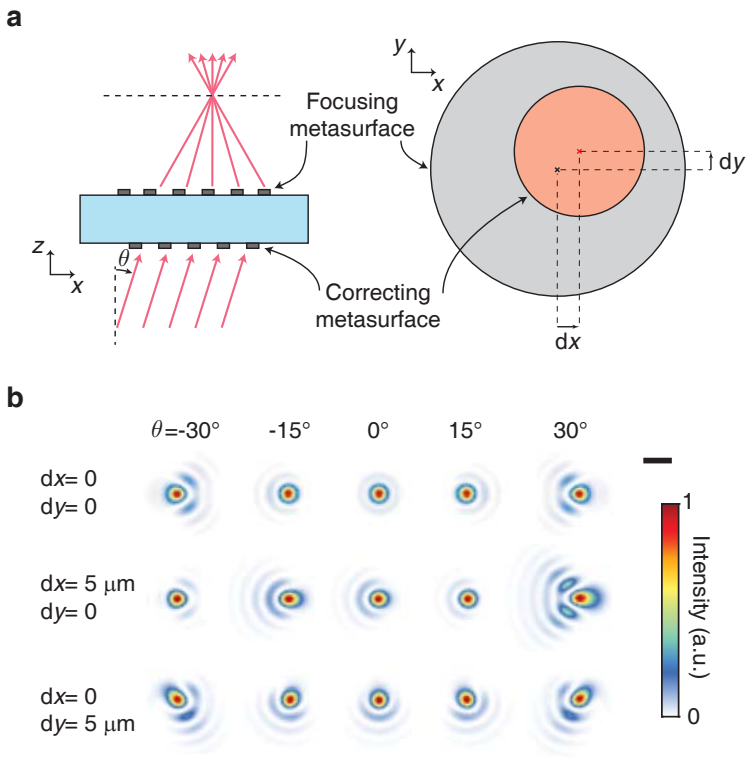

Figure 5.A2: **Effect of misalignment between the two metasurfaces**. **(a)** Schematic illustration of the side and the top views of the metasurface doublet lens. The misalignments along *x* and *y* directions (*dx* and *dy*) are shown in the top view illustration. **(b)** Simulated focal plane intensity of the metasurface doublet lens for different misalignments between the metasurfaces and at several different incident angles θ. The aperture and field stops are assumed to be aligned with the metasurfaces on their corresponding sides. Scale bar: 2 μm.

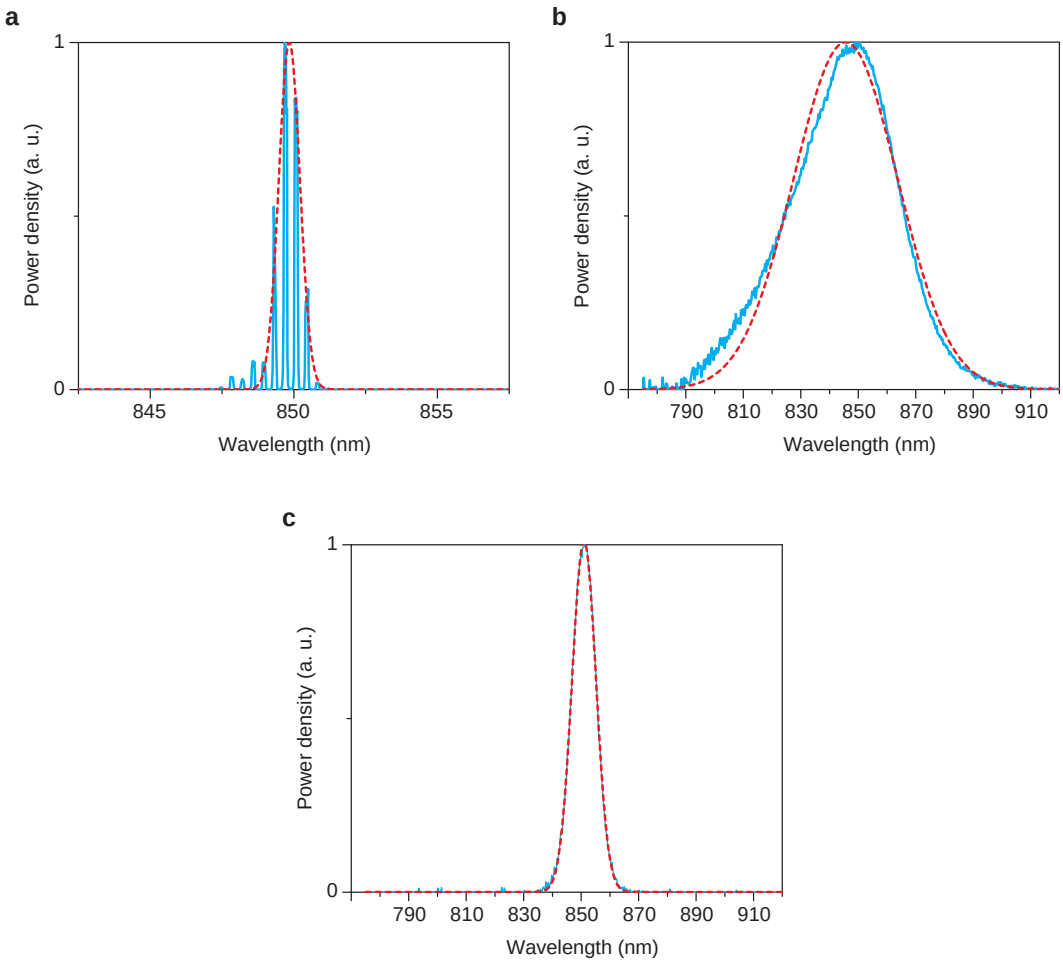

Figure 5.A3: **Measured spectra of the sources used to characterize the metasurface lenses and the miniature camera**. **(a)** Measured spectrum of the laser used in the measurement of incident angle dependent focusing of the metasurface doublet and singlet lenses [Fig. **5.3a**]. Different peaks observed in the spectrum correspond to different Fabry-Pérot modes of the laser cavity. **(b)** Measured spectrum of the LED used to capture the image shown in Fig. **5.5c**. **(c)** Measured spectrum of the filtered LED used as illumination for the images shown in Figs. **5.4b**, **5.4c**, **5.4g**, and **5.5d**. The solid blue curves show the measured spectra and the dashed red curves represent the best Gaussian function fits. The FWHM bandwidth values for the Gaussian fits are equal to 0.9 nm, 42.7 nm, and 9.8 nm for the spectra shown in **a**, **b**, and **c**, respectively.

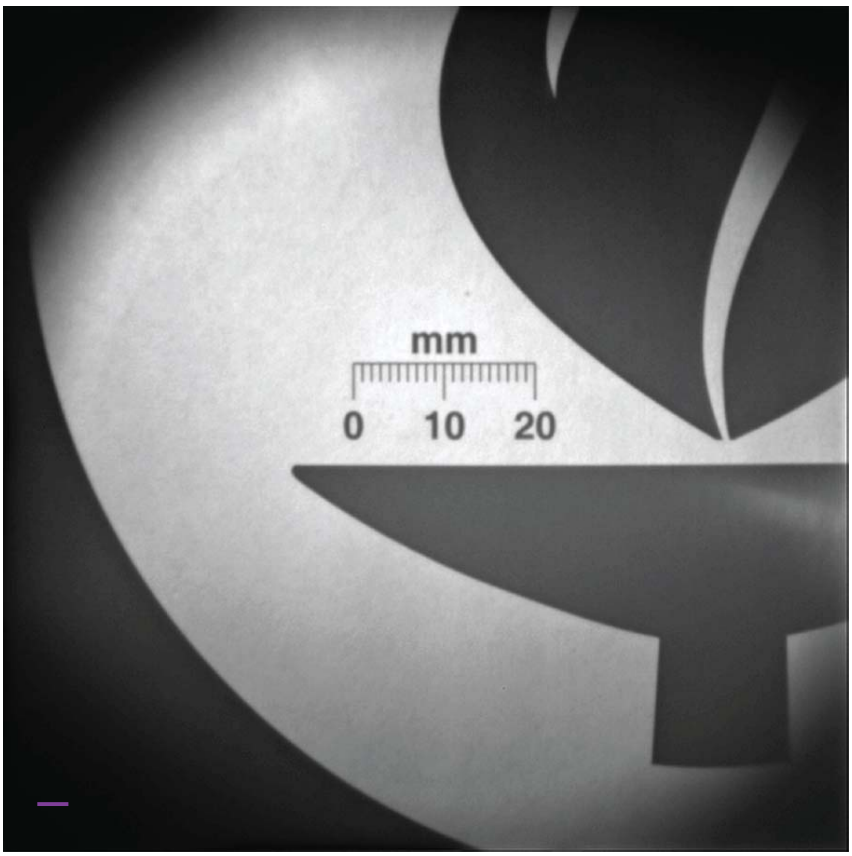

Figure 5.A4: **Image captured by the metasurface doublet lens.** Image taken using the setup shown in Fig. **5.4a**, but with an objective lens with higher magnification and NA (50×, NA = 0.5). See Appendix 5.1 for the measurement details. The vignetting observed at the corners of the image is due to the limited FOV of the objective lens used to magnify the image. Scale bar: 10 μm.

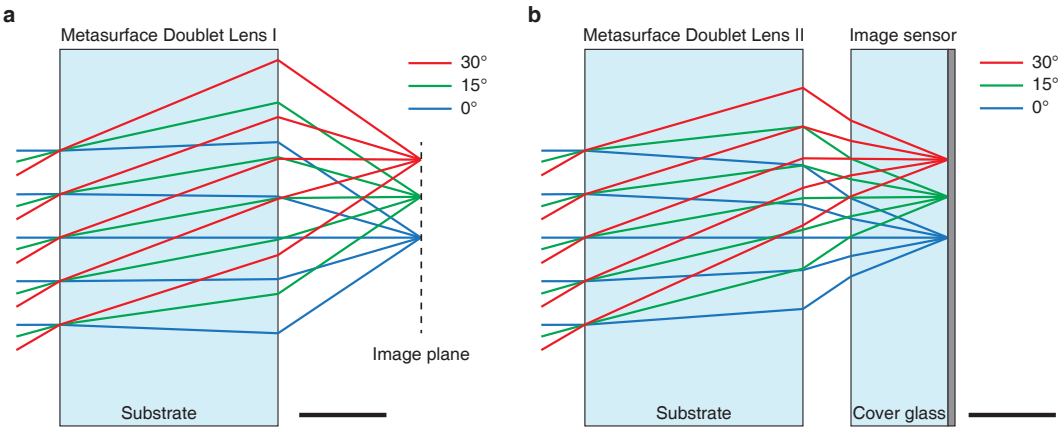

Figure 5.A5: **Image-space telecentricity of the metasurface doublet lenses. (a)** Ray diagram for the metasurface doublet lens I (designed for focusing in air), and **(b)** the metasurface doublet lens II (designed for focusing through the cover glass). The correcting and focusing metasurfaces (not shown) are assumed to be patterned on the left and right sides of the substrates, respectively. The chief rays are nearly normal to the image planes (i.e., the lenses are telecentric in the image space), and the angular distributions of the focused rays are independent of the incident angle. Scale bars: 400 μm.

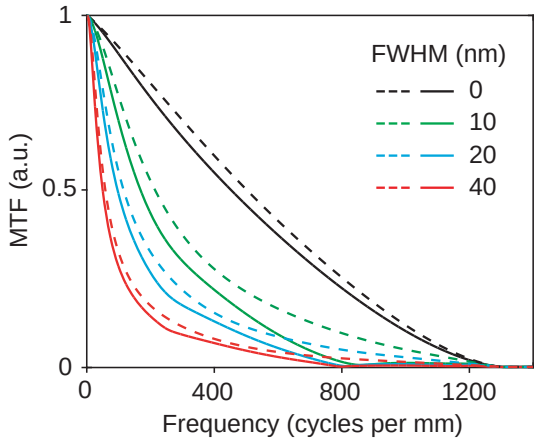

Figure 5.A6: **Simulated MTFs for the metasurface doublet lens at the incident angle of 15°**. The solid and dashed lines show the modulation transfer function in the tangential plane (along *x* in Fig. **5.5a**) and sagittal plane (along *y* in Fig. **5.5a**), respectively.

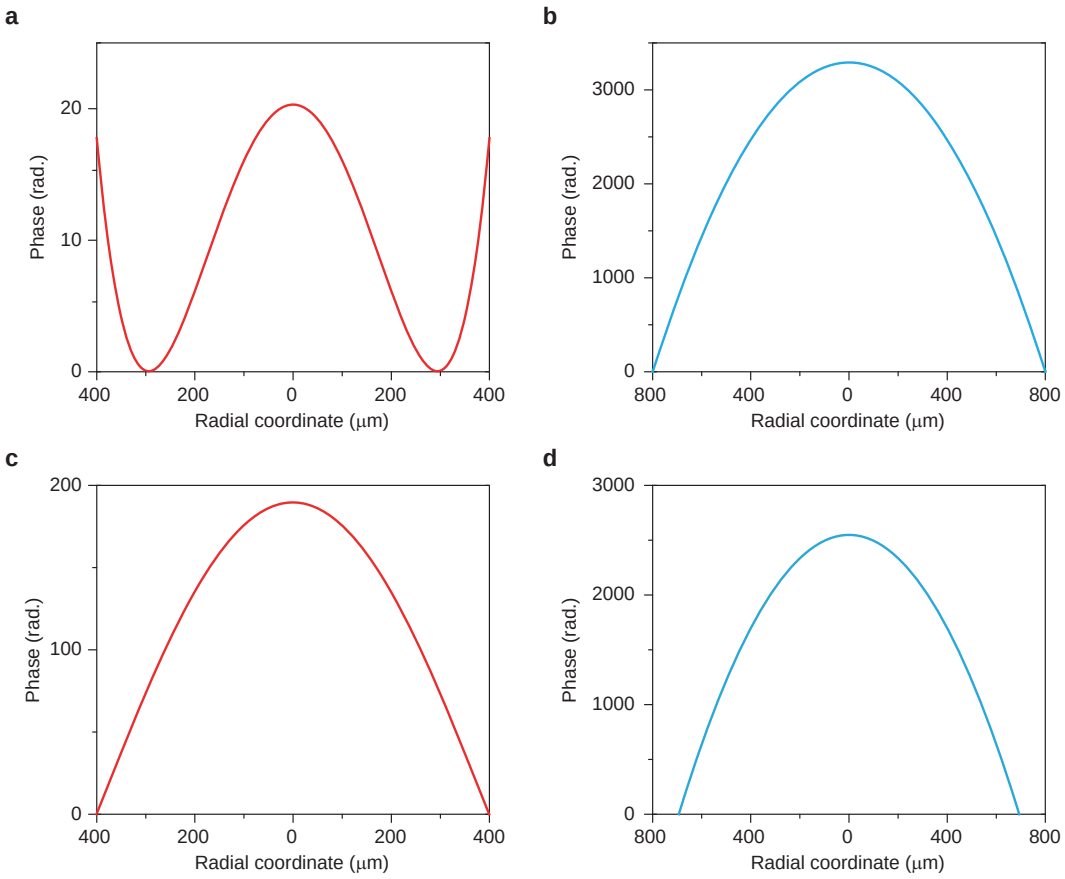

Figure 5.A7: **Phase profiles of the metasurfaces composing the doublet lenses.** **(a)** Phase profile of the correcting and **(b)** focusing metasurfaces of the doublet lens I (designed for focusing in air). **(c)** and **(d)** Similar plots as **a** and **b** but for the metasurface doublet lens II which is designed for focusing through the cover glass of a CMOS image sensor (as shown in Figs. **5.4f** and **5.4g**).

Table 5.A1: Phase profile parameters for the metasurface doublet lens I

Metasurface	Correcting Metasurface	Focusing Metasurface
R (μm)	400	800
a_1	-71.86	-3285.68
a_2	57.90	-31.88
a_3	9.62	33.77
a_4	1.30	-8.41
a_5	0.66	1.51

Table 5.A2: Phase profile parameters for the metasurface doublet lens II

Metasurface	Correcting Metasurface	Focusing Metasurface
R (μm)	400	700
a_1	-225.92	-2559.04
a_2	31.29	11.57
a_3	3.84	0.83
a_4	0.49	-3.58
a_5	0.34	1.94

Appendix 5.3: Additional information for the MEMS-tunable doublet

Simulation. The optimized phase profiles (for both the fabricated doublet and the triplet shown in Fig. 5.14) were obtained using Zemax OpticStudio. The phase profiles are defined as even-order polynomials of the radial coordinate r according to $\phi(r) = \sum_{2n} a_{2n}(r/R_0)^{2n}$, where R_0 is a normalization radius and a_{2n} are the coefficients (see Fig. 5.A8 and Tables 5.A3 and 5.A4 for the phase profiles and the optimized coefficients). This was done through simultaneously minimizing the root mean square radius of the focal spot for several configurations (i.e., different lens separations, and, in the case of the triplet, the lateral source position). The image formation simulations (for Fig. 5.14) were done using the extended scene simulations of Zemax OpticStudio and took into account the aberrations and limitations resulting from diffraction.

Mechanical simulation of the MEMS structure was performed in COMSOL Multiphysics to find the resonances of the structure. The metallic contacts and the α-Si metasurface were treated as additional masses on the membrane. The Young modulus of SiN_x was assumed to be 250 GPa and its Poisson ratio was set to be 0.23. The following densities were used for different materials: 3100 kgm^{-3} for SiN_x, 2320 kg/m^{-3} for α-Si, and 19300 kg/m^{-3} for gold. To account for the fact that

the whole metasurface volume is not filled with α-Si, an average fill factor of 0.5 was used.

Transmission amplitudes and phases of the metasurface structures on both fused silica and silicon nitride were computed through rigorous coupled-wave analysis [217]. The transmission values were calculated by illuminating a uniform array of nano-posts with a normally incident plane wave at 915 nm wavelength and finding the amplitude and phase of the transmitted zeroth-order wave right above the nano-posts. The subwavelength lattice ensures that this single number is adequate to describe the optical behavior of a uniform array. The following refractive indices were used in the simulations: 3.5596 for α-Si, 2.1 for SiN_x, 1.4515 for fused silica. The lattice constant was 320 nm in both cases, and the α-Si thickness was 530 nm for the moving, and 615 nm for the stationary lens.

Device fabrication. Fabrication of the stationary lenses was started by depositing a 615-nm-thick layer of α-Si on a 500-µm-thick fused silica substrate through a PECVD process. The metasurface pattern was written on a ~300-nm-thick layer of ZEP520A positive electron resist with a Vistec EBPG5000+ electron beam lithography system. After development of the resist, a 70-nm-thick Al_2O_3 layer was evaporated on the sample that was used as a hard mask. The pattern was then transformed to the α-Si layer via a dry etch process. The metallic contacts' pattern was defined using photolithography on AZ 5214 E photoresist which was used as a negative resist. A ~10-nm-thick layer of Cr, followed by a ~100-nm-thick Au layer was evaporated onto the sample, and a lift-off process transferred the photoresist pattern to the metal layer. Finally, a ~20-µm-thick layer of SU-8 2015 was spin coated on the sample and patterned to function as a spacer.

The moving lens fabrication started with a silicon wafer with ~450-nm-thick low-stress low-pressure chemical vapor SiN_x deposited on both sides. The device side was etched down to about 213 nm with a dry etch process. A ~20-nm-thick SiO_2 layer, followed by a ~530-nm-thick α-Si layer was deposited on the sample with a PECVD process. Through hole patterns were defined on the backside of the sample using the AZ 5214 E photoresist, and a lift-off process was performed to transfer the pattern to a ~200-nm-thick Al_2O_3 layer that was used as a hard mask. The holes were partially etched through the wafer with a Bosch process (leaving a ~50-µm-thick silicon layer to provide mechanical support for the membrane in the following steps). Alignment marks (for aligning the lenses to the backside holes) were patterned and etched into the α-Si layer using a backside-aligned photolithography process. A

process similar to the one used for the stationary lenses was performed to fabricate the metasurfaces and the metallic contacts. The top-side (with the metasurfaces and contacts) was then covered with a protective polymer coating (ProTEK PSB, Brewer Science) layer, and the remaining ~50-μm-thick silicon layer was etched in a 3:1 water-diluted potassium hydroxide solution at 80°C. The membrane pattern was defined on the sample using photolithography with AZ nLOf 2020 photoresist, and was etched through the SiN_x membrane to release the membrane. The photoresist was then removed in an oxygen plasma. A fused silica piece was bonded to the backside of the membrane sample using a UV-curable epoxy (NOA 89, Norland Products) to isolate the membranes from ambient airflow. At the end, the moving and stationary samples were aligned and bonded using an MA6/BA6 aligner (Suss MicroTec). A UV-curable epoxy was used to bond the two samples. Using this technique, an alignment precision of a few microns is feasible.

Measurement procedure. The doublet characterization setup is schematically shown in Fig. **5.A9**. A collimated beam from a fiber coupled 915-nm diode laser connected to a fiber collimation package (F240FC-B, Thorlabs) was used to illuminate the doublet from the membrane side. A custom-built microscope consisting of a ×50 objective (LCPlanFL N, NA=0.7, Olympus) and a tube lens with a 20-cm focal length was used to image the focal plane of the doublet to a charge-coupled device camera (CoolSNAP K4, Photometrics). An air coplanar probe (ACP40 GSG 500, Cascade Microtech) was used to apply a voltage to the doublet. For measuring the frequency response, square pulses with different base frequencies were applied to the probe (CFG250 function generator, Tektronix). The change in the optical power passing through a 50-μm pinhole in the image plane (equivalent to a ~1-μm pinhole in the focal plane) was then measured with a fast detector (PDA36A, Thorlabs) connected to an oscilloscope. The frequency response was then extracted through Fourier transforming the input voltage and the resulting change in the output power (see below for more details).

The efficiency was calculated through measuring the power passing through a ~1-mm iris in the image plane (corresponding to a ~20-μm pinhole in the focal plane) and dividing it by the total power before the doublet. To make sure that the total beam power was incident on the doublet, the beam was partially focused by a lens with a 10-cm focal length. The distance between the lens and the doublet was adjusted such that the beam had a ~100-μm FWHM at the place of the doublet (i.e., one third of the doublet diameter). This way, more than 99% of the power is expected to hit the

doublet area.

The imaging experiments in Fig. 5.13 were also performed using a similar setup. For imaging, a 910-nm LED (LED910E, Thorlabs) was used as an illumination. To reduce the effects of chromatic dispersion, a bandpass filter (FB910-10, 910-nm center wavelength, 10-nm FWHM) was placed in front of the camera. A negative 1951 USAF Resolution target (R1DS1N, Thorlabs) was used as an imaging object. A 4-f system consisting the doublet and a glass lens with focal length of 8 mm (ACL12708U-B, Thorlabs) was used to form images of the resolution target at different distances. To reduce the aperture size and increase contrast, a 1.8-mm-diameter aperture (AP1.5, Thorlabs) was placed at a ~1.3-mm distance in front of the refractive lens. The distance between the backside of the refractive lens and the doublet was ~4.5 mm. The resulting image was magnified and re-imaged onto the camera with the same microscope used for the focal spot characterization.

Frequency response measurements. The frequency response of the doublet is defined as the ratio of the membrane movement upon application of an alternating voltage at frequency f, to the membrane movement upon application of the same DC voltage. To measure this response we used the setup schematically shown in Fig. 5.A9**a** (including the mirror, a 50-μm pinhole, and a power detector). Square shaped pulse trains at different frequencies were applied to the contacts [Figs. 5.A9**b**–5.A9**d**]. Modulation of the optical power passing through the pinhole is also measured with the power detector connected to an oscilloscope [Figs. 5.A9**e**–5.A9**g**]. To maximize the modulation of the optical power passing through the pinhole, the objective was adjusted to image a plane a few microns away from the focal spot of the doublet. The optical power was measured in four different intervals (plotted in the figures with different colors), and their average was used as the output to reduce noise. The input voltage and output powers were then Fourier transformed, resulting in the spectra shown in Figs. 5.A9**h**–5.A9**j**. The transfer function for each input frequency band (i.e., for each of the Figs. 5.A9**b**–5.A9**d** inputs) can be calculated via dividing the output and input spectra at the harmonic frequencies [Figs. 5.A9**k**–5.A9**m**]. We chose the base harmonic frequencies (i.e., 10 Hz, 100 Hz, and 1 kHz) so that there is an overlap in the bandwidths where the transfer function is calculated for each input. Using this overlap, we can cascade the transfer functions to find the frequency response plotted in Fig. 5.12**e**. We should note that there are inherent approximations in the method used here for finding the frequency response. First, the membrane displacement is a nonlinear function of the applied voltage. Second, the change in

the focal distance with the membrane movement is weakly nonlinear. Third, the optical power passing through the pinhole is a nonlinear function of the focal distance change. Assuming that all changes are small compared to their respective rest values, we can linearize all these functions, and find the transfer functions. Nevertheless, traces of the nonlinearities could be seen in the excitation of output harmonics that are not present in the input [Figs. **5.A9h**–**5.A9j**]. The fact that these new harmonics have small amplitudes compared to the linearly excited ones, and the good agreement between the resulting frequency response and the over-damped fit indicate that the linearization approximation is valid.

Appendix 5.4: Supporting figures and tables for the MEMS-tunable doublet

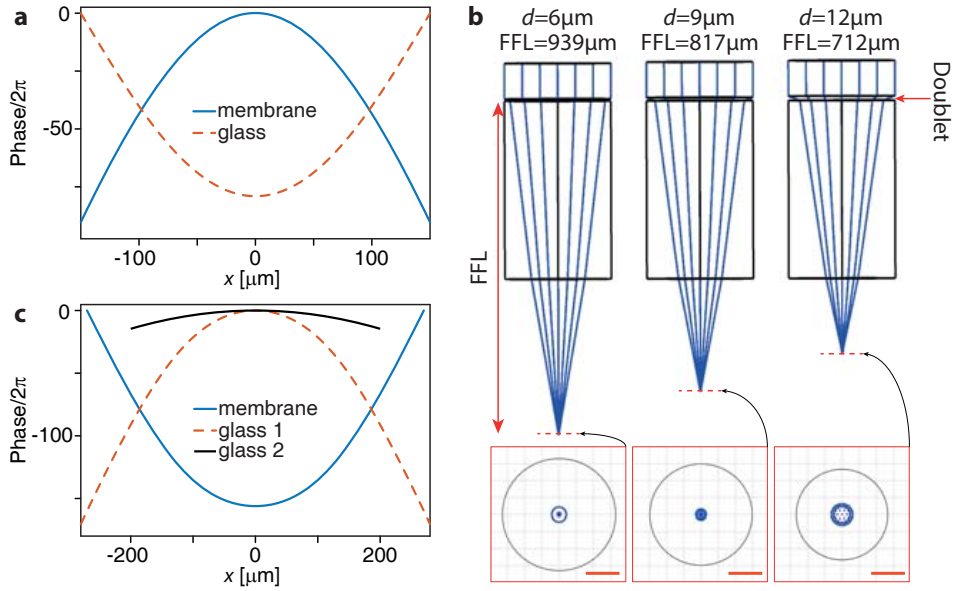

Figure 5.A8: **Phase profiles and ray optics simulations.** **(a)** Optimized phase profiles for the fabricated doublet metasurfaces. **(b)** Ray optics simulation results for the doublet in three different configurations. The scale bars are 2 μm. FFL: Front focal length. **(c)** Phase profiles for the three elements of the microscope shown in Fig. **5.14**.

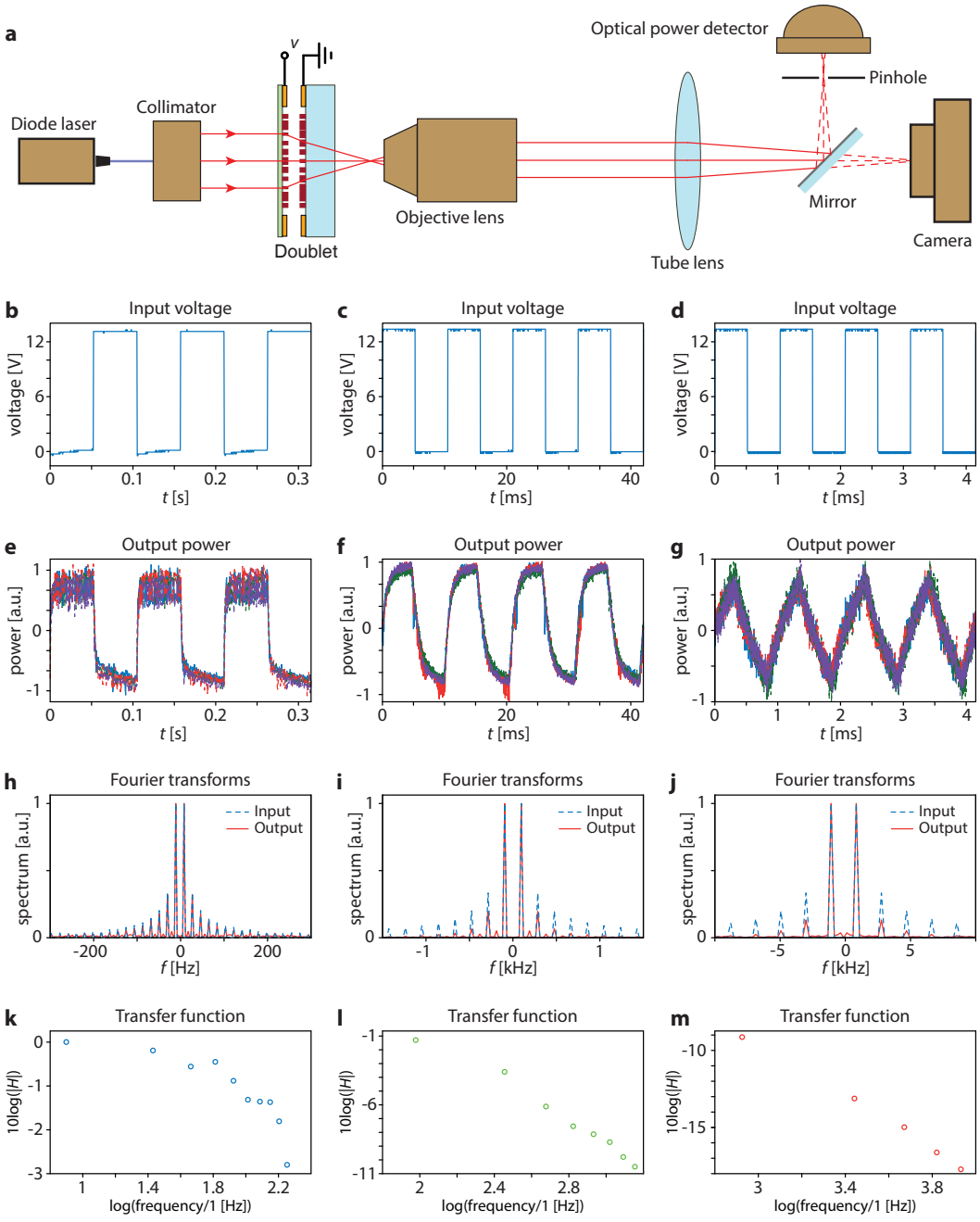

Figure 5.A9: **Measurement setup and raw frequency measurement results. (a)** Measurement setup used to characterize the doublet. The mirror, pinhole and optical power detector are used for measurement of frequency response and efficiency. **(b)–(d)** Input voltage waveforms for different base frequencies. **(e)–(g)** Measured output powers for corresponding input voltages **b–d**. **(h)–(j)** Fourier transforms of the mean measured output voltages. **(k)–(m)** The calculated pieces of the transfer function over different frequency bands. See Appendix 5.3 for details of the measurement procedure.

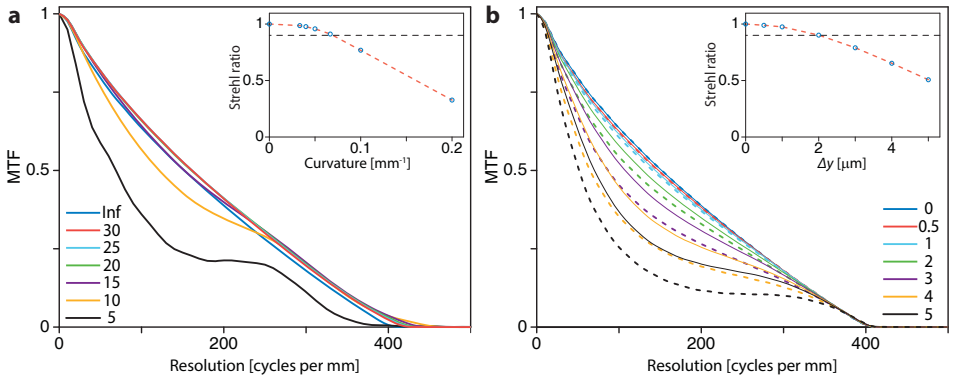

Figure 5.A10: **Aberrations resulting from membrane bending and lens misalignment. (a)** On-axis MTF of the doublet plotted for various radii of curvature (the numbers are in millimeters). Inset: the calculated Strehl ratio plotted versus curvature (i.e., one over radius). The red dashed line is an eye-guide, and the black dashed line corresponds to a Strehl ratio of 0.9. **(b)** On-axis MTF of the doublet plotted for various transverse displacements between the lenses (the numbers are in micrometers). For each color, the solid line is the sagittal plane, and the dashed line is the tangential plane. Inset: the calculated Strehl ratio plotted versus displacement. The red dashed line is an eye-guide, and the black dashed line corresponds to a Strehl ratio of 0.9.

Table 5.A3: **Optimized phase profile coefficients for the fabricated doublet.**

Element	Moving lens	Stationary lens
R_0 [μm]	150	150
a_2	-6.479×10^{2}	5.835×10^{2}
a_4	5.430×10^{1}	-4.717×10^{1}
a_6	8.997×10^{1}	-1.317×10^{2}
a_8	-1.532×10^{2}	2.324×10^{2}
a_{10}	1.557×10^{2}	-2.201×10^{2}
a_{12}	-8.498×10^{1}	7.967×10^{1}
a_{14}	1.871×10^{1}	3.145×10^{0}

Appendix 5.5: Additional information and discussion for the metasurface spectrometer

Simulation and design. Ray tracing simulations of the spectrometer were performed using Zemax OpticStudio. In the simulations, metasurfaces were assumed to be phase-only diffractive surfaces. The grating was modeled as a blazed grating with a linear phase along the direction of dispersion (y), and independent of the other direction (x). The phase was chosen to correspond to a period of 1 μm, resulting in deflection angles of 31.6° and 36.35° at 760 nm and 860 nm, respectively. The

Table 5.A4: **Optimized phase profile coefficients for the triplet microscope.**

Element	Moving lens	Stationary lens 1	Stationary lens 2
R_0 [μm]	270	280	200
a_2	8.657×10^{2}	-9.800×10^{2}	-9.354×10^{1}
a_4	7.828×10^{2}	-7.474×10^{2}	1.675×10^{0}
a_6	-1.240×10^{3}	1.280×10^{3}	5.765×10^{-1}
a_8	7.004×10^{2}	-8.157×10^{2}	-6.854×10^{-1}
a_{10}	-1.281×10^{2}	1.921×10^{2}	0.2783×10^{-1}

angles were chosen such that the focused light could be captured by an objective with a NA of 0.95, while maximizing the dispersive power. The second and third surfaces were modeled as a summation of Cartesian coordinate polynomials (Binary 1), $\Sigma_{n,m}a_{m,n}x^m y^n$, and cylindrical coordinate radially symmetric polynomials (Binary 2) $\Sigma_i b_{2i}\rho^{2i}$. The coefficients were optimized to reduce geometric aberrations by minimizing the root mean square geometric spot radii for several input wavelengths covering the bandwidth. The optimized coefficients are given in Table **5.A5**. As shown in to Fig. **5.16b**, all focal spots are optimized and are within the airy disks. This indicates that the designed spectrometer has small geometrical aberrations. The diffraction-limited resolution curve obtained is shown in Fig. **5.16**c. The simulations and optimizations were first performed in an unfolded configuration for simplicity. There were several constraints in finding the sizes for input and output apertures. Two opposing factors existed in determination of the 790-μm input aperture diameter. On one hand, a larger input aperture results in a higher throughput and more captured light as well as a higher NA and potentially better resolution. On the other hand, the aperture size for the folded platform cannot be arbitrarily large because different metasurfaces should not overlap. Thus, the 790-μm aperture diameter was chosen in the ray-tracing simulations as the largest size for which metasurface overlap can be avoided and diffraction-limited focusing can be achieved. The output aperture spatially filters the out of band wavelengths while passing through the bandwidth of interest. Therefore, its size was chosen as the smallest possible aperture that allows for all wavelengths of interest to pass through. Using the ray-tracing simulations, this optimum size was found to be 978 μm.

The RCWA technique [217] was used to obtain reflection phases of the nano-posts. For each specific set of dimensions, a uniform array of the α-Si nano-posts was illuminated with a plane wave at the wavelength of 810 nm under an illumination angle of 33.9° and the reflected amplitudes and phases were extracted for each

polarization. To choose the height of the nano-posts, we performed these simulations for nano-posts with square cross-sections and different heights and side lengths [Fig. **5.A11**]. The height was then chosen to minimize the variation of the derivative of the phase with respect to wavelength for different side lengths, while providing a full 2π phase coverage and high reflectivity. Considering the results of Fig. **5.A11b** and Fig. **5.A11d**, we chose the thickness to be 395 nm. Although this height is slightly less than $\lambda/2$, it is large enough to provide a full 2π phase coverage as the device operates in reflection mode. The lattice constant was chosen to be 246 nm in order to satisfy the sub-wavelength condition and avoid higher order diffractions, which require $l_c < \lambda/n(1 + \sin(\theta_{\max}))$, where l_c is the lattice constant, n is the refractive index of the substrate, and $\theta_{\max}$ is the maximum deflection angle [36]. We chose $\sin(\theta_{\max}) = 1/n$, since light traveling at larger angles will undergo total internal reflection at the output aperture. To make the two focusing metasurfaces polarization-insensitive, reflection phase and amplitudes were obtained for nano-posts with rectangular cross section under oblique illumination with both TE and TM polarizations [Fig. **5.17**]. The design curves were then generated by determining a path in the D_x-D_y plane along which TE and TM reflection phases are almost equal.

For designing the blazed diffraction grating, we chose to use the same α-Si thickness of 395 nm (for ease of fabrication). The lattice constant was set to be 250 nm, such that a grating period contains four nano-posts, and the structure becomes fully periodic. This allows for using periodic boundary conditions in the full-wave simulations of the structure, reducing the simulation domain size significantly. The initial values of the post widths were chosen using a recently developed high-NA metasurface design approach [130]. The simulation results for nano-post-width vs reflection-phase and the initial post widths are plotted in Fig. **5.A13a**. These values were then fed to a particle swarm optimization algorithm (using an RCWA forward solver) as a starting point. The algorithm optimizes the deflection efficiency of the grating for both polarizations at 11 wavelengths spanning the bandwidth of interest. The optimization parameters are the side lengths of the rectangular nano-posts, while their thickness and spacing is fixed. Deflection efficiencies of the initial and optimized gratings are plotted in Fig. **5.A13b**. The corresponding nano-post widths for both gratings are given in Table **5.A6**.

Sample fabrication A summary of the key steps of the fabrication process is shown in Fig. **5.A14**. A 395-nm-thick layer of α-Si was deposited on one side of a 1-mm-thick fused silica substrate through a PECVD process at 200°C. The metasurface pattern

was then generated in a ~300-nm-thick layer of ZEP-520A positive electron resist (spun for 1 minute at 5000 rpm) using an EBPG5200 EBL system. After development of the resist in a developer (ZED-N50, Zeon Chemicals), a ~70-nm-thick Al_2O_3 layer was evaporated on the sample in an electron beam evaporator. After lift-off, this layer was used as a hard mask for dry etching the α-Si layer in a mixture of SF_6 and C_4F_8 plasma. The alumina layer was then removed in a 1:1 solution of H_2O_2 and NH_4OH. A ~2-μm-thick layer of SU-8 2002 polymer was spin-coated, hard-baked, and cured on the sample to protect the metasurfaces. The output aperture (which is on the same side as the metasurfaces) was defined using photolithography (AZ-5214E positive resist, MicroChemicals) and lift-off. A ~100-nm-thick gold layer was deposited as the reflective surface. To protect the gold reflector, a second layer of SU-8 2002 was used. To define the input aperture, a ~2-μm-thick layer of SU-8 2002 polymer was spin-coated and cured on the second side of the wafer to improve adhesion with gold. The input aperture was then defined in a process similar to the output aperture.

Device characterization procedure The measurement setups used to characterize the spectrometer are schematically shown in Fig. **5.A15**. Light from a tunable Ti-sapphire laser (SolsTiS, M-Squared) was coupled to a single mode optical fiber and collimated using a fiber collimator (F240FC-B, Thorlabs). A fiber polarization controller and a free space polarizer (LPVIS100-MP2, Thorlabs) were used to control the input light polarization, and different neutral density filters were used to control the light intensity. The beam illuminated the input aperture of the spectrometer at normal incidence. The focal plane of the spectrometer, located ~200 μm away from the output aperture, was then imaged using a custom built microscope (objective: 100× UMPlanFl, NA=0.95, Olympus; tube lens: AC254-200-C-ML, Thorlabs; camera: CoolSNAP K4, Photometrics). Since the FOV is ~136 μm (limited by the ~15-mm image sensor, and the ~111× magnification), while the total length over which the wavelengths are dispersed in the focal plane exceeds 1 mm, the objective is scanned along the dispersion direction to cover the whole focal plane at each wavelength (11 images captured for each wavelength). These images were then combined to form the full intensity distribution at each wavelength. The measurements were performed at 11 wavelengths (760 nm to 860 nm, 10-nm steps) to form the results shown in Figs. **5.18b**, **5.18c** , Fig. **5.A16**, and Fig. **5.A17**. The measurements were also performed at a second set of wavelengths (761.25 nm, 811.25 nm, and 861.25 nm). These results are summarized in Fig. **5.18d** and Fig. **5.18e** for TE and TM polarizations. The resolution [Fig. **5.A18**] was estimated by finding the FWHM at each wavelength in addition to the displacement rate of the focus center along the

y direction by changing the wavelength.

The setup was slightly changed for measuring the focusing efficiencies. The input beam was partially focused by a lens (f =10 cm) such that all the beam power passed through the input aperture (with a ~400 μm FWHM). In addition, the camera was replaced by a photodetector and a pinhole with a diameter of 3.5 mm in front of it to measure the focused power. The pinhole, corresponding to a ~31-μm area in the focal plane, allows only for the in-focus light to contribute to the efficiency. The efficiency is then calculated at each wavelength by dividing these measured powers by the total power tightly focused by a 10-cm focal length lens that was imaged onto the power meter using the same microscope (i.e., by removing the spectrometer and the pinhole).

The experimental setup for capturing the sample spectra is almost identical to Fig. **5.A15b**, with the only difference of the polarizer being replaced by the sample of interest, and an 840-nm short-pass filter inserted before the sample. The light source was also replaced by a supercontinuum laser (Fianium Whitelase Micro, NKT Photonics).

Angular response measurement. To measure the angular response of the device we used the setup shown in Fig. **5.A19c**, equipped with a rotating stage with 0.1° precision in the x-z plane and 0.002° in the y-z plane. The collimator (connected to the fiber coming from the source) was mounted on this rotating stage, where the folded spectrometer was exactly located at its center. The incident angles were adjusted accordingly for 0°, ±0.3°, ±0.6°, ±1° angles. As can be observed in Fig. **5.A19a**, the focal spots did not change much in size as the angle is varied between -1° to +1° in x-direction. For measuring the tilt angle in the y-z plane, the distance from the collimator to the device was measured to be 280 mm. In order to impose ±0.15° tilt in the y direction, the mounted collimator level is raised or lowered by 0.73 mm, and its tilt was adjusted accordingly such that the beam hits the center of the input aperture. As shown in Fig. **5.A19b**, such a tilt in input incident angle does not degrade the spectral resolution of 1.25 nm.

Design of the spectrometer with high throughput. To further demonstrate the capabilities of the platform, we have designed a second spectrometer with significantly increased throughput. In order to achieve higher throughput, a larger input aperture is required, so the slab thickness was increased to 2 mm to give more freedom on the non-overlapping condition for the metasurfaces. The design, as shown in Fig. **5.A20**, has a 2.5 mm input aperture. To further improve the throughput, the acceptance

angle of the device was increased. To achieve this goal, we took an approach similar to the fabricated spectrometer with the difference of adding extra phase terms to the input diffraction grating. This helps with orienting the focuses on the image plane for different incident angles, as well as relaxing the condition for focusing in the x-direction. This in turn allows for increasing the input incident angle to $\pm 15^{\circ}$ degrees. The phase profile coefficients for metasurfaces 1 to 3 in Fig. **5.A20** are given in Table **5.A7**. In the final design, the power is distributed in an area close to 200 μm wide in the x-direction in the focal plane, instead of a diffraction-limited focus. According to the intensity profiles shown in Fig. **5.A20b**, the device can distinguish between wavelengths spaced by 0.5 nm both at the center wavelength of 810n m, and also at the side wavelengths of 760 nm and 860 nm. Based on the angular response of the device in the x-z and y-z planes, and also the input aperture size of the device, an etendue of around ~13000 Srμm^2 is estimated.

Appendix 5.6: Additional figures and tables for the metasurface spectrometer

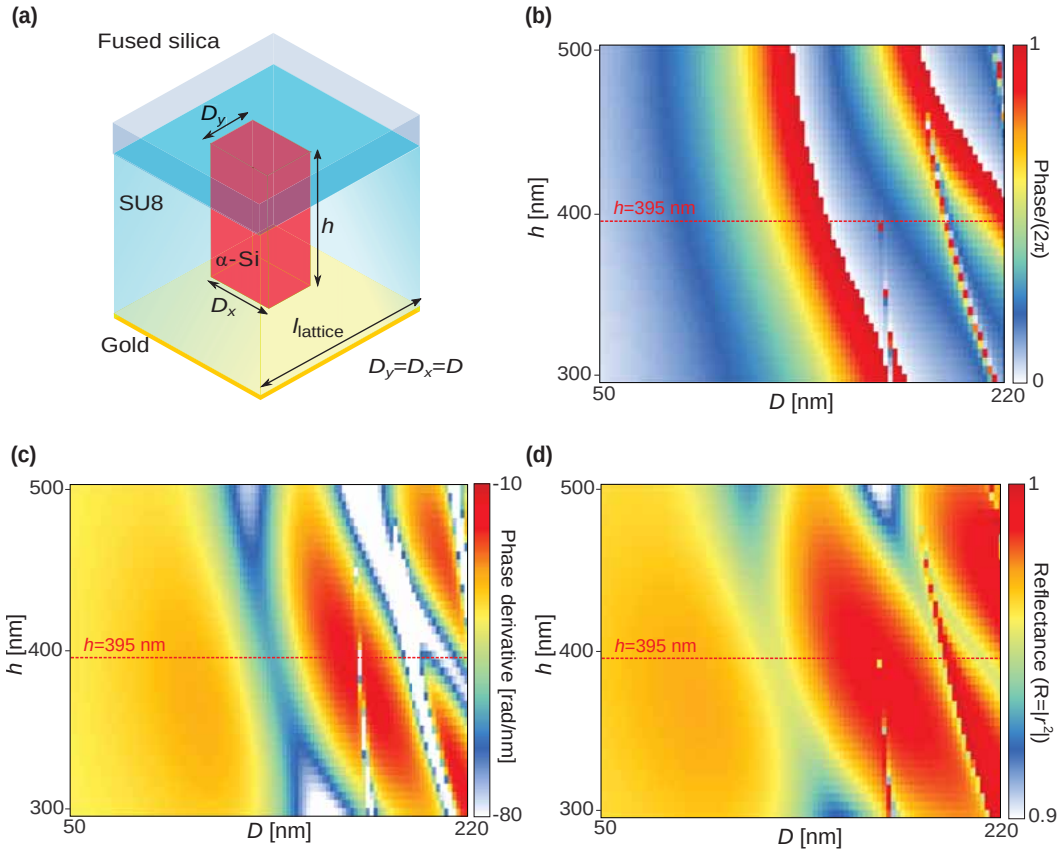

Figure 5.A11: **Single-post periodic lattice simulations. (a)** Schematic of a rectangular post on top of a fused silica substrate, showing the post dimensions. The nano-posts are capped by a 2-μm-thick layer of SU-8, and backed by a reflective gold layer. **(b)** Simulated reflection phase under TE illumination with 33.9° incident angle. **(c)** Derivative of the phase with respect to the wavelength calculated and plotted versus the height (h) and width of the post ($D_x = D_y = D$). The nano-post height that provides full 2π phase coverage with high reflectance while minimizing variation of the phase derivative is found to be $h = 395$ nm (the red line). **(d)** Reflectance as a function of post-width and height.

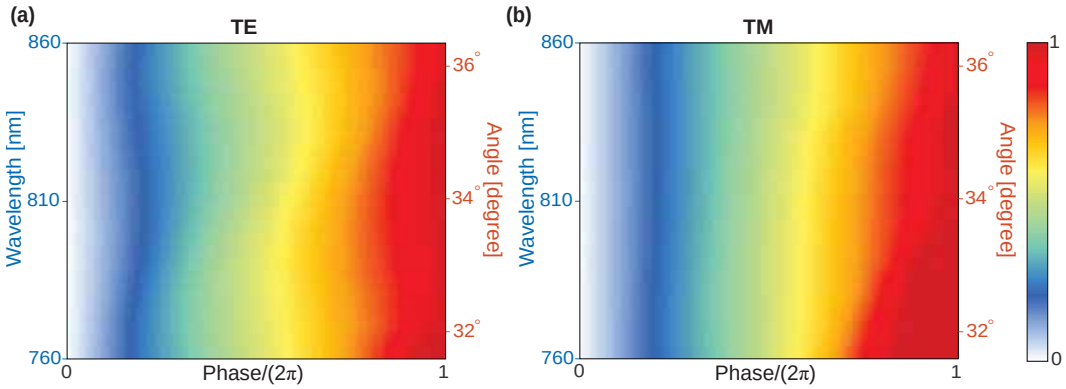

Figure 5.A12: **Reflection phase variation versus wavelength.** **(a)** Reflection phase for TE-polarized light from a uniform array of meta-atoms corresponding to the black curves in Fig. 5.17 versus wavelength. As depicted by the vertical axis on the right, the simulation for each wavelength is performed under an incident angle corresponding to the deflection angle of the input blazed grating at that wavelength. **(b)** Same as **a** for TM polarization.

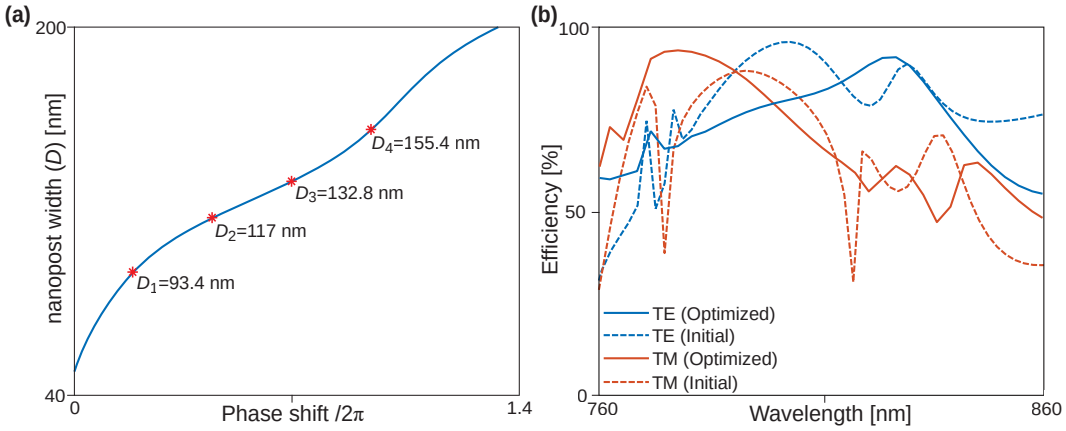

Figure 5.A13: **Grating design curves and deflection efficiencies.** **(a)** Post width versus reflection phase for 395-nm-tall posts on a square lattice with a 250-nm lattice constant. The red stars correspond to the nano-post sizes found from this graph that have the highest deflection efficiency over the bandwidth. **(b)** TE and TM polarization deflection efficiency curves versus wavelengths for the initial (i.e., the red stars in **a**) and optimized nano-post dimensions given in Table 5.A6.

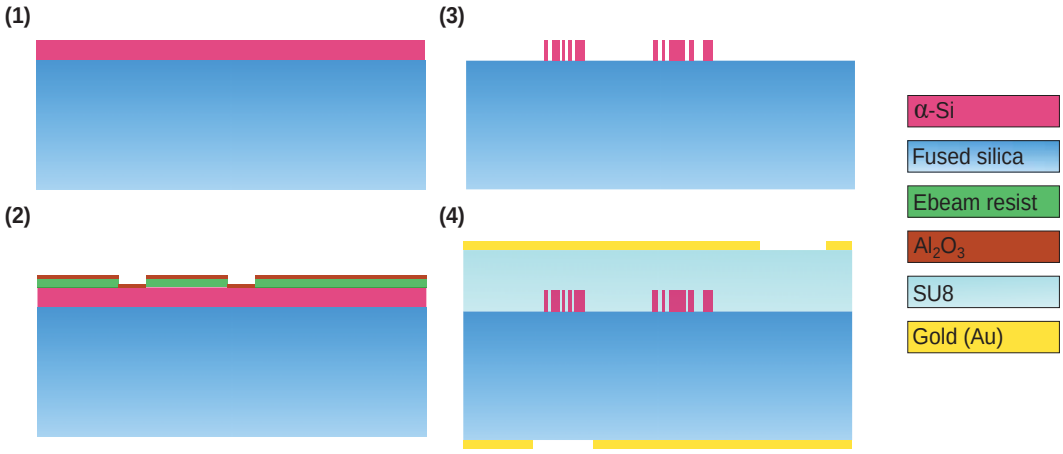

Figure 5.A14: **The key fabrication steps.** A 395-nm-thick layer of α-Si is deposited on a 1-mm-thick fused silica substrate using PECVD. The metasurface pattern is generated with electron beam lithography, negated and transferred to the α-Si layer via lift-off and dry-etching processes. Both sides are covered with and SU-8 layer, and the input and output apertures are defined through photolithography and lift-off.

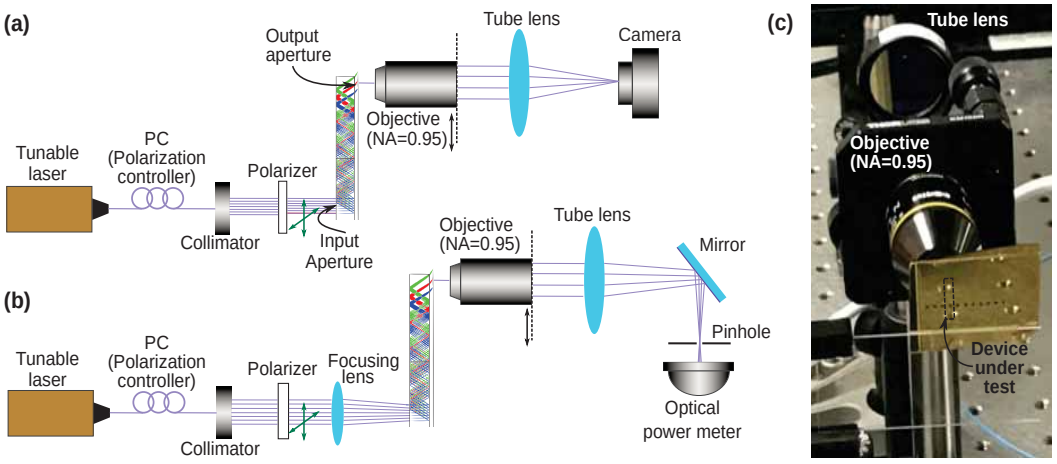

Figure 5.A15: **Measurement setups. (a)** Schematics of the measurement setup used for device characterization. **(b)** Schematics of the setup used to measure the focusing efficiencies. **(c)** An optical image of a part of the actual measurement setup showing the device, the objective lens, and the tube lens.

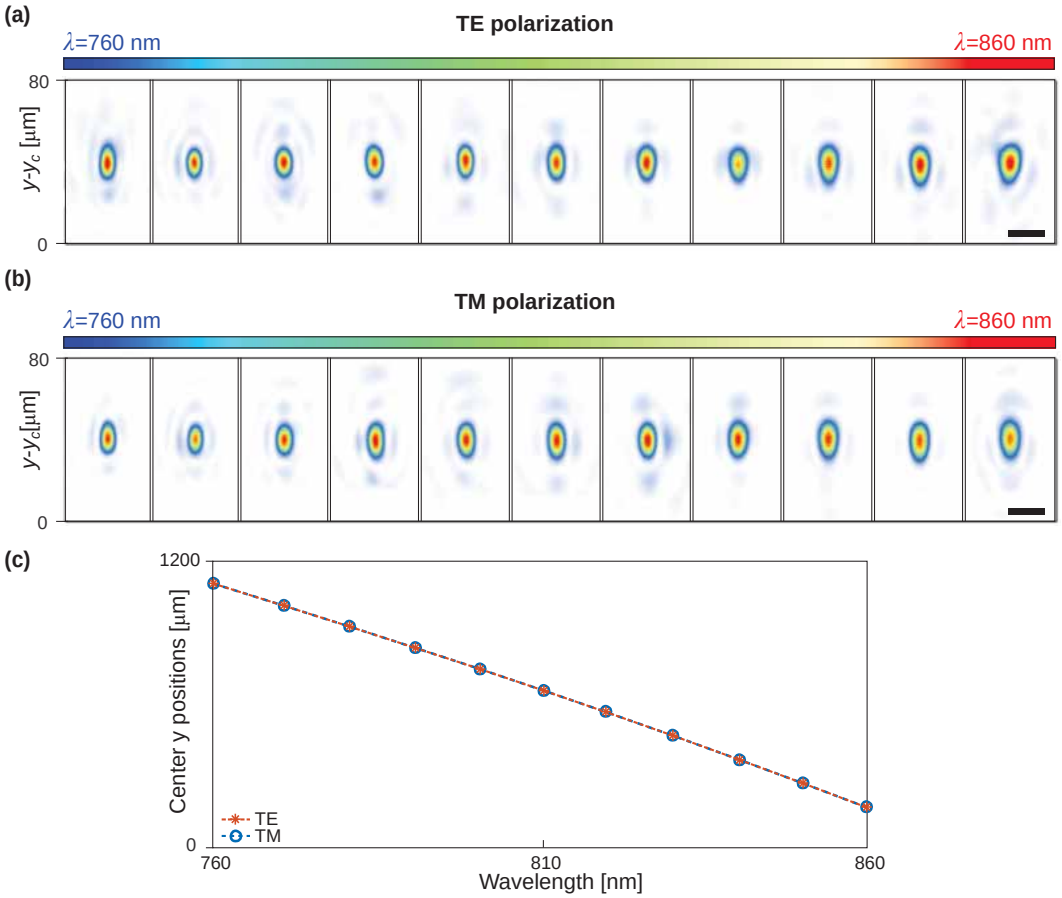

Figure 5.A16: **Focal plane intensity profiles.** **(a)** Two-dimensional intensity profiles measured at several wavelengths (y_c is the center position of each profile) under illumination with TE-polarized light, and **(b)** TM-polarized light. **(c)** The position of the center of the focal spot along the dispersion direction, y, versus wavelength. The symbols represent the measured data, and the solid line is an eye guide. The scale bars are 20 μm.

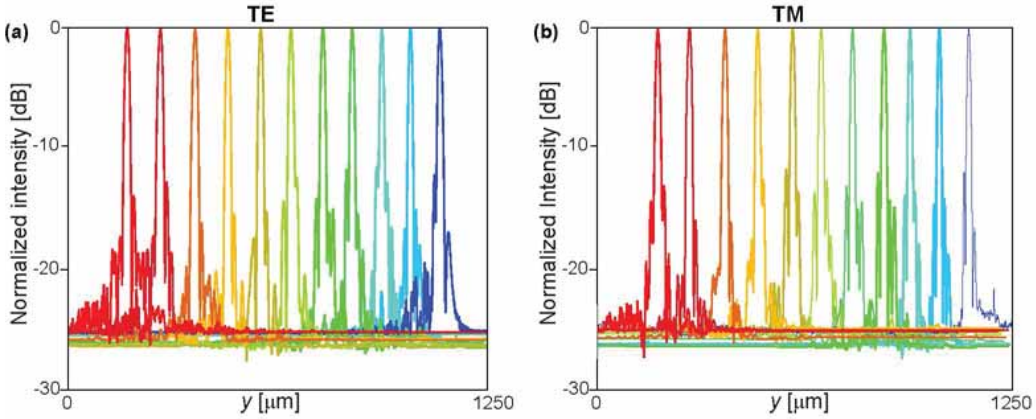

Figure 5.A17: **Intensity distribution profiles on logarithmic scales.** **(a)** Same information as Fig. **5.18b** and **5.18c** of the main text, plotted on logarithmic scale for TE polarization, and **(b)**) for TM polarization.

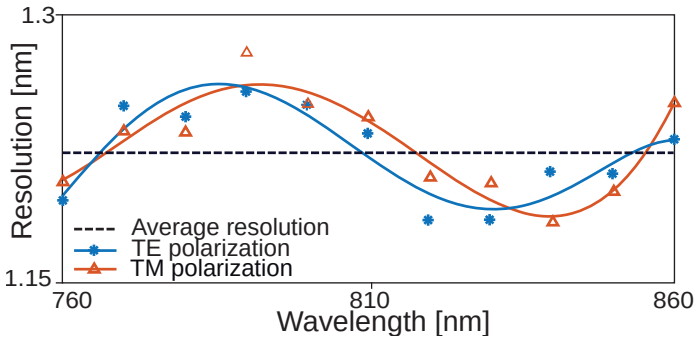

Figure 5.A18: **Measured spectral resolution versus wavelength.** Spectral resolution estimated using the measured focal spot FWHM and the displacement rate of the focal spot with changing the wavelength. The average resolution is 1.22 nm for both polarizations. The symbols show the measured date and the solid lines are eye guides.

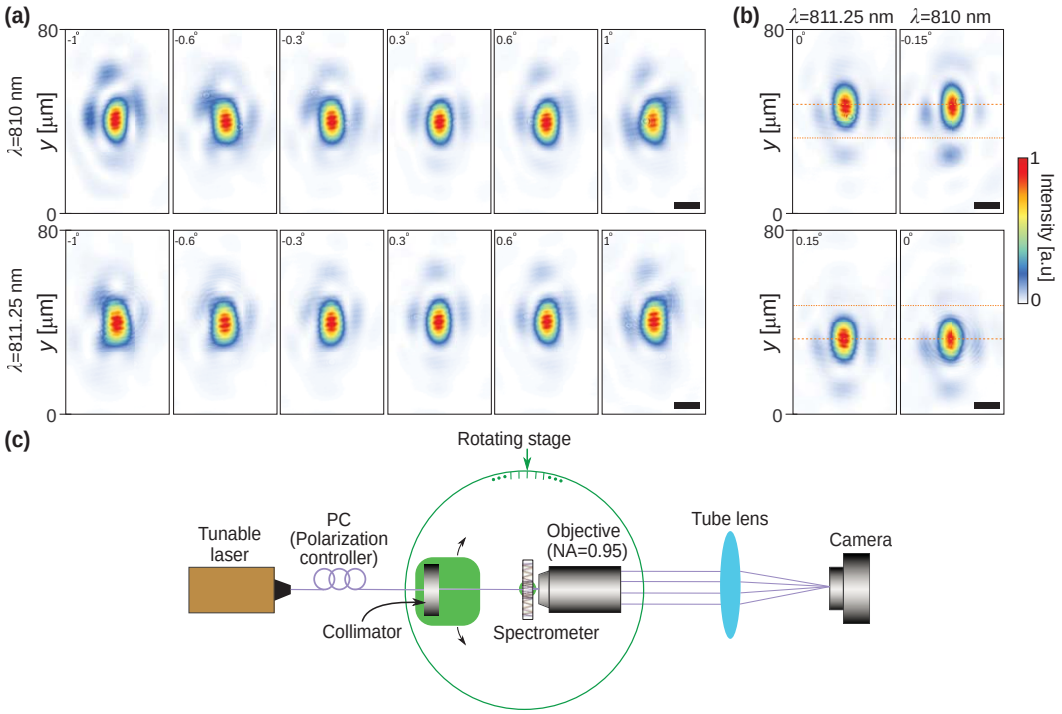

Figure 5.A19: **Measured angular response of the device for polar angle variation with respect to 0 angle in *x-z* and *y-z* planes. (a)** Angular response of the device for different tilted incident angles between -1° to +1° in the *x-z* plane. **(b)** Angular response of the device for ±0.15° tilted incident angles in the *y-z* plane. **(c)** experimental setup used for measuring the angular response. The scale bars are 10 μm.

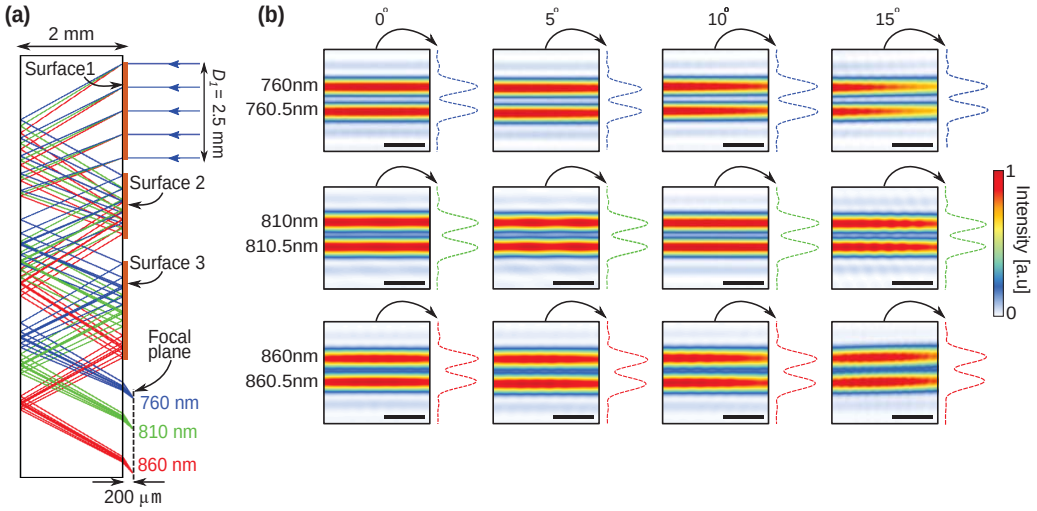

Figure 5.A20: **Ray-optics design and simulation results of an extended-throughput folded spectrometer.** **(a)** Ray tracing simulation results of the extended-throughput folded spectrometer, shown at three wavelengths in the center and two ends of the band. The system consists of three metasurfaces optimized to separate different wavelengths of the light and focus them on the focal plane. **(b)** Simulated intensity distribution for two wavelengths separated by 0.5 nm around three different center wavelengths of 760 nm, 810 nm, and 860 nm for 4 different incident angles of 0°, 5°, 10° and 15°. The intensity distributions show that wavelengths separated by 0.5 nm are theoretically resolvable for all aforementioned incident angles. The scale bars are 15 μm.

Table 5.A5: Phase profile coefficients in terms of $[rad/mm^{m+n}]$ for metasurfaces 1 and 2

Metasurface	I (R=525.0 μm)	II (R=582.5 μm)
$a_{x^2y^0}$	−4.02	−3.91
$a_{x^0y^2}$	−2.08	−3.70
$a_{x^2y^1}$	0.47	−0.68
$a_{x^0y^3}$	0.20	−0.24
$a_{x^4y^0}$	-5.68×10^{-4}	6.26×10^{-3}
$a_{x^2y^2}$	7.55×10^{-3}	0.021
$a_{x^0y^4}$	2.36×10^{-3}	6.34×10^{-3}
a_{ρ^6}	1.93×10^{-4}	-2.48×10^{-4}
a_{ρ^8}	-3.22×10^{-6}	4.82×10^{-6}
$a_{\rho^{10}}$	-5.886×10^{-9}	-2.974×10^{-9}

Table 5.A6: Optimized grating post sizes [nm] (D_x, D_y)

Optimization	Diffraction efficinecy	Particle swarm optimization
D_{x1}	93.4	68
D_{y1}	93.4	134
D_{x2}	117	115.2
D_{y2}	117	119.6
D_{x3}	132.8	147.4
D_{y3}	132.8	151.2
D_{x4}	155.4	137.8
W_{y4}	155.4	178.8

Appendix 5.7: Additional methods and discussion for the retroreflector

Simulation and design. The simulation results presented in Figs. **5.21c** and **5.21d** were obtained by finding the transmission and reflection coefficients of the corresponding periodic metasurfaces using the RCWA technique [217]. The α-Si nano-posts were 600 nm tall and the lattice constant was 450 nm. A 70-nm-thick Al_2O_3 disk was added on top of the nano-posts forming the reflective metasurface. The disk was used to model the Al_2O_3 hard mask which was used to etch the nano-posts and became an integral part of the reflective metasurface. The thickness of the SU-8 layer for the reflective metasurface was assumed to be 2 μm, although the relative reflection coefficient of the metasurface was found to have negligible dependence on the thickness of the SU-8 layer. The simulations were performed at $\lambda = 850$ nm by assuming the following refractive indices:

Table 5.A7: Phase profile coefficients of the increased throughput design (Fig. 5.A20) in terms of $[rad/mm^{m+n}]$

Metasurface	I (R=2.5 mm)	II (R=1.5 mm)	III (R=2.15 mm)
$a_{x^2y^0}$	-0.44	-3.13	-2.45
$a_{x^0y^2}$	-2.98	1.91	-2.69
$a_{x^2y^1}$	0.015	0.027	-0.067
$a_{x^0y^3}$	0.035	-0.04	-0.06
$a_{x^4y^0}$	-1.5×10^{-5}	-8.2×10^{-4}	3.56×10^{-4}
$a_{x^2y^2}$	-6.16×10^{-5}	-0.72×10^{-4}	-1.73×10^{-5}
$a_{x^0y^4}$	-3.1×10^{-4}	3.8×10^{-3}	-9.14×10^{-4}
a_{ρ^6}	1.42×10^{-7}	1.12×10^{-5}	6.71×10^{-7}
a_{ρ^8}	-2.26×10^{-10}	-5.26×10^{-8}	-1.72×10^{-9}
$a_{\rho^{10}}$	-5.886×10^{-13}	7.58×10^{-11}	1.62×10^{-12}

$n_{\alpha\mathrm{Si}} = 3.596$, $n_{\mathrm{SiO_2}} = 1.4525$, $n_{\mathrm{Au}} = 0.129 + 5.42i$, $n_{\mathrm{Al_2O_3}} = 1.76$, $n_{\mathrm{SU-8}} = 1.582$. The measured refractive index and extinction coefficient of α-Si are shown in Fig. 5.A25, showing that the material has negligible loss at 850 nm. Note that the array of nano-posts arranged on a hexagonal lattice is non-diffractive (i.e., only has the zeroth diffraction order propagating) in the substrate for incident angle θ if $2\pi/(\lambda/n_{\mathrm{SiO_2}}) < 2\pi/(\sqrt{3}/2a) - 2\pi/\lambda\sin(\theta)$ or $\theta < \sin^{-1}\left(\lambda/(\sqrt{3}/2a) - n_{\mathrm{SiO_2}}\right) \approx 47°$.

The optimum phase profiles of the two metasurfaces composing the retroreflector were obtained by minimizing the average RMS wavefront error of the retroreflected beam. The RMS wavefront error was averaged over different incident angles (0° to 50°, 10° step). The wavefront errors were found through the ray tracing technique using a commercial optical design software (Zemax OpticStudio, Zemax LLC). The phase profiles (ϕ) of the metasurfaces were defined as even order polynomials of the radial coordinate ρ as

$$\phi(\rho) = \sum_{n=1}^{7} a_n \left(\frac{\rho}{R}\right)^{2n}, \tag{5.7}$$

where R is the radius of the metasurface. The ray diagram and the RMS wavefront error for the optimized design are shown in Figs. 5.20**a** and 5.20**b**, respectively. The corresponding optimum phase profiles of the metasurfaces are shown in Fig. 5.A22, and the optimum values of a_n for both metasurfaces are listed in Table 5.A8. The dominant terms in the phase profiles of both metasurfaces are the quadratic terms. This is consistent with the operation of the metasurface I as a Fourier transform lens (Fourier transform lenses have quadratic phase profiles in the paraxial regime), and the function of metasurface II as a concave mirror in the paraxial regime.

The metasurface nano-post pattern was obtained using these optimum phase profiles and the transmission and reflection results shown in Figs. **5.21c** and **5.21d** through the procedure discussed previously in detail [67]. Due to the weak coupling among nano-posts, the transmission and reflection coefficients shown in Figs. **5.21c** and **5.21d** can be regarded as approximations for the local transmission and reflection coefficients for metasurfaces with spatially varying nano-post diameters. Because both metasurfaces I and II are considered as phase masks in the ray tracing simulation, their desired spatially-varying complex transmission and reflection profiles are in the form of $\exp(i\phi(\rho))$ where $\phi(\rho)$ is given by Eq. 5.7 with coefficients a_n listed in the Table **5.A8** for both metasurfaces. Using these complex transmission and reflection profiles, and the assumption of the locality of the transmission and reflection by the metasurfaces, we realized the metasurfaces by forming an empty hexagonal lattice and sampling the desired complex transmission (for metasurface I) and reflection (for metasurface II) coefficients of the metasurfaces at the lattice sites. Then, at each lattice site, a nano-post is placed with the diameter that most closely approximates (using the data shown in Figs. **5.21c** and **5.21d**) the sampled complex valued transmission or reflection coefficients of the metasurfaces at that lattice site. The diameters of the nano-posts for the metasurfaces I and II were obtained using this procedure.

Device fabrication. The metasurfaces were fabricated on two sides of a 500-μm-thick fused silica substrate. Two 600-nm-thick layers of α-Si were deposited on both sides of the substrate using PECVD. A ~300-nm-thick layer of an electron beam resist (ZEP-520A, Zeon chemicals) was spin coated on one side of the substrate and the nano-post pattern for the metasurface I was written on it by EBL. A ~60-nm-thick layer of a charge dissipating polymer (aquaSave, Mitsubishi Rayon) was spin coated on the resist prior to EBL to prevent pattern distortion due to electrostatic charging. After the lithography step, the charge dissipating layer was removed and the resist was developed in a developer (ZED-N50, Zeon chemicals). A ~70-nm-thick layer of Al_2O_3 was deposited on the resist and patterned by lifting off the resist in a solvent. The Al_2O_3 pattern was transferred to the underlying α-Si layer by dry etching in a mixture of C_4F_8 and SF_6 gases. Then, the Al_2O_3 layer was removed in a mixture of ammonia and hydrogen peroxide at 80° C. To protect the nano-posts from mechanical damage during the processing of the other side of the sample, a ~2-μm-thick layer of SU-8 polymer (SU-8 2002, MicroChem Corp.) was spin coated over the nano-posts, reflown, and cured, thus yielding a rigid planarized layer that encapsulates and protects the nano-posts.

Metasurface II was fabricated on the other side of the substrate using the same processing steps used for fabrication of metasurface I, except for skipping the Al_2O_3 removal step. The Al_2O_3 mask was not removed from the top of the metasurface II nano-posts, because the solution conventionally used for its removal (i.e., mixture of ammonia and hydrogen peroxide at 80° C) attacks the SU-8 cladding layer of metasurface I. The Al_2O_3 layer was assumed as an integral part of metasurface II and its effect was considered in the simulations presented in Fig. **5.21d**. After the SU-8 planarization step, a 100-nm-thick layer of gold was deposited directly on the SU-8 cladding layer of metasurface II using electron beam evaporation. Finally, to reduce the reflection from the SU-8/air interface above the metasurface I, a ~150-nm-thick layer of hydrogen silsesquioxane (XR-1541 from Dow Corning with refractive index of 1.4 at 850 nm) was added over the SU-8 layer by spin coating followed by baking at 180° C, thus forming a quarter-wavelength anti-reflection coating.

Measurement procedure. The planar retroreflector was characterized using setups schematically shown in Figs. **5.23** and **5.24**. The retroreflector was mounted on a three axis translation stage that was mounted on a rotation stage. The retroreflector was aligned such that the rotation axis was co-planar with metasurface I and passed through its center. The setup shown in Fig. **5.23a** was used to obtain the reflectance images shown in Fig. **5.23a**. Light from an 850-nm LED (Thorlabs LED851L, measured spectrum shown in Fig. **5.A25a**) passed through a non-polarizing beam splitter (BS005, Thorlabs) and then the lens L_1 (AC254-050-B-ML, focal length: 5 cm, Thorlabs) before impinging on and illuminating the retroreflector. The LED was located ~50 cm away from the retroreflector, thus the portion of its light reaching the lens aperture had relatively small angular spread (full-angle beam divergence of ~3 degrees). The reflected light was imaged by the lenses L_1 and L_2 (AC254-200-B-ML, focal length: 20 cm, Thorlabs) which function as objective and tube lenses, respectively, and form a microscope. The reflectance images were recorded for different rotation angles of the retroreflector using a CMOS camera (EO-1312M-GL, Edmund Optics). The dark noise of the camera was obtained by turning off the LED and was subtracted from the recorded intensities.

The retroreflection efficiency was measured using the setup schematically shown in Fig. **5.23b**. The emission from an 850-nm laser diode (Thorlabs L850P010, measured spectrum shown in Fig. **5.A25b**) was coupled to a single mode optical fiber, passed through a polarization controller, and a fiber collimation package (F220APC-780, Thorlabs), thus resulting in a collimated beam with an estimated $1/e^2$ diameter of

~1.5 mm. The beam was passed through a polarizer (LPNIR050-MP, Thorlabs), a non-polarizing beam splitter (BS005, Thorlabs), and was focused on the sample using the lens L_1 (Thorlabs AC254-050-B-ML, focal length: 5 cm). The power of the portion of light reflected by the beam splitter was monitored by an optical power meter PD_1 (Thorlabs PM100D with Thorlabs S122C power sensor) and was used to correct for any potential fluctuations of the laser output power. The focused beam has an estimated $1/e^2$ diameter of ~34 μm on the sample. The reflected light was collimated by passing through the lens L_1, and was directed by the beam splitter to the power meter PD_2 (Thorlabs PM100D with Thorlabs S122C power sensor). Two irises (with opening aperture diameter of ~2.5 mm) were placed in the reflected beam path to ensure only the retroreflected portion of the reflected light is detected by PD_2. The measurements were performed for two different polarizations of incident beam: TE and TM with electric and magnetic fields parallel to the retroreflector plane, respectively.

To obtain absolute values for the reflectance and the retroreflection efficiency, we measured reflectance of 93.1% for a portion of the sample without the metasurfaces (i.e., a portion that only has backside gold reflector) by using a laser beam incident on it at ~ 5° from the normal, and directly measuring the power of the incident and reflected beams. The reflectance value found this way was used to quantify the reflectance of the area of the sample labelled as "Gold" in the $\theta = 0°$ image shown in Fig. **5.23a**. It was also used as the reference for calibration of the measured retroreflection efficiency values in the setup shown in Fig. **5.23b**. The reflected power from an area of the sample without metasurfaces was measured in this setup at normal incidence and the measured retroreflected powers were referenced to it.

Appendix 5.8: Additional figures and tables for the retroreflector

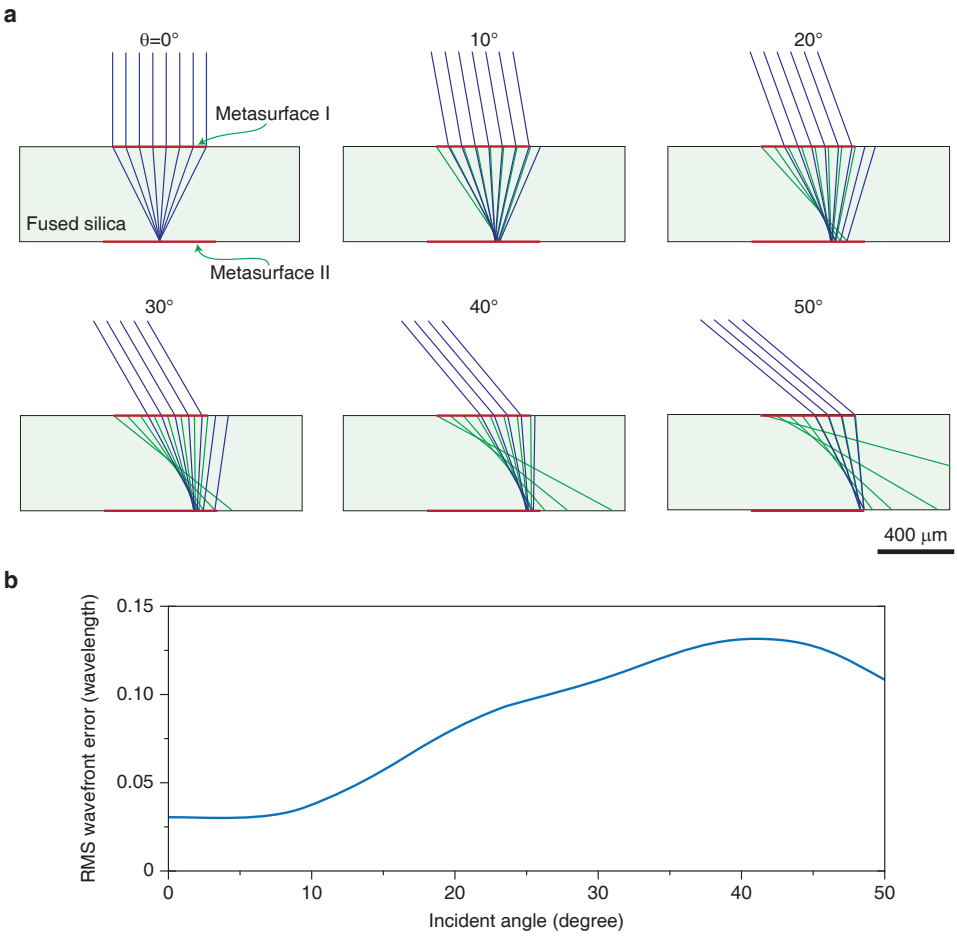

Figure 5.A21: **Simulation results of the planar retroreflector. (a)** Ray diagram for different incident angles. The incident rays (green) are not shown outside the substrate so that the reflected rays (dark blue) are seen more clearly. **(b)** RMS wavefront error of the retroreflected light as a function of the incident angle.

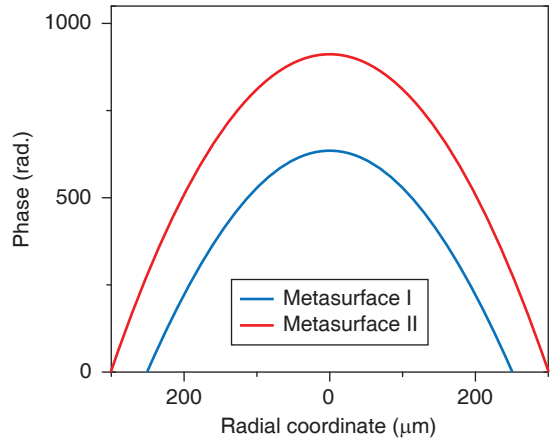

Figure 5.A22: **Phase profiles of the metasurfaces composing the planar retroreflector.** Optimized phase profiles of the metasurfaces that minimize the average RMS wavefront error (see Fig. **5.A21**).

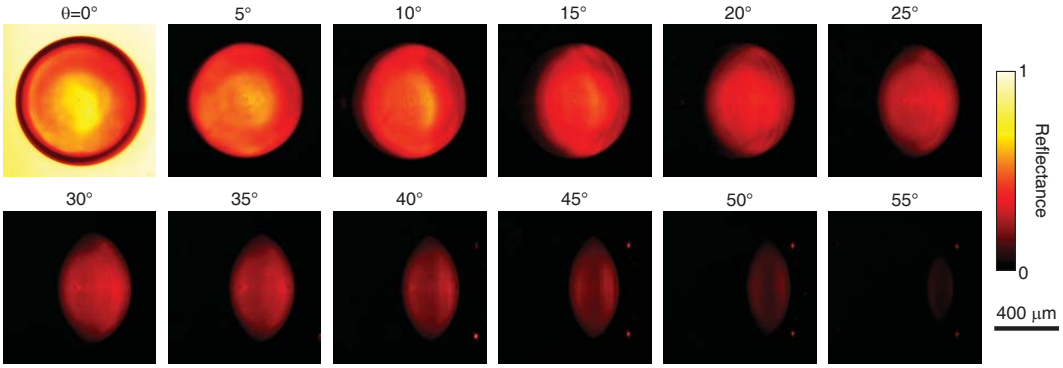

Figure 5.A23: **Extended reflectance measurement results.** The results are the same as the ones shown in Fig. **5.23a**, but are presented here in 5° steps.

Table 5.A8: **Phase profile parameters for the metasurfaces composing the retroreflector**

Metasurface	Metasurface I	Metasurface II
R (μm)	250	300
a_1	-669.15	-903.33
a_2	33.67	-9.03
a_3	0.32	6.47
a_4	6.61	-2.85
a_5	-3.77	0.67
a_6	1.11	-0.08
a_7	-0.12	0.00

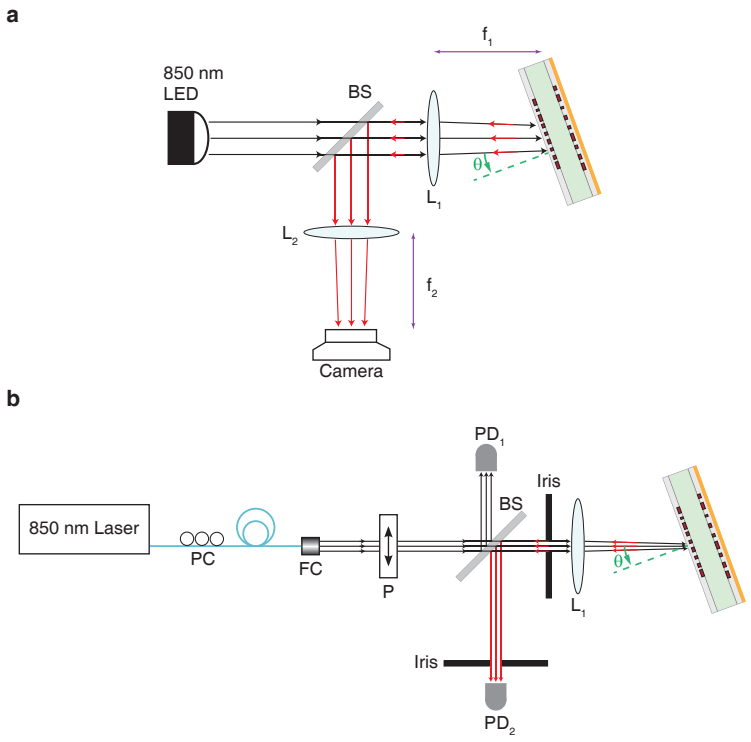

Figure 5.A24: **Measurement setups. (a)** Detailed schematic illustration of the experimental setup used in the reflectance measurement and **(b)** experimental setup used to measure the retroreflection efficiency. BS: beam splitter, L: lens, PC: polarization controller, FC: fiber collimator, P: polarizer, PD: photodetector. The focal lengths of lenses L_1 and L_2 are $f_1 = 5$ cm and $f_2 = 20$ cm, respectively.

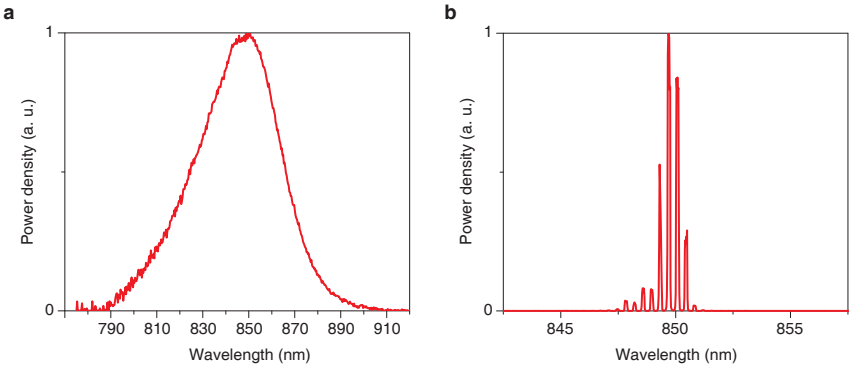

Figure 5.A25: **Spectra of sources used for the retroreflector characterization. (a)** Measured spectrum of the LED used in the measurement shown in Fig. **5.23a**. **(b)** Measured spectrum of the laser used in retroreflection efficiency measurement [Fig. **5.23b**]. The FWHM bandwidth values for the best Gaussian fits to the spectra shown in **a** and **b** are 42.7 nm and 0.9 nm, respectively.

Chapter 6

CONCLUSION AND OUTLOOK

HCAs outperform the other metasurface platforms in wavefront manipulation, as they provide high efficiencies and novel functionalities such as control over the polarization, spectral, and angular degrees of freedom that are not available using other platforms. The development and study of optical metasurfaces have been a rapidly growing field of research in the past few years, because of their capabilities to mimic the functionality of conventional diffractive optical elements with higher efficiencies and resolutions, and more importantly for their advantages in providing new functionalities not achievable with conventional diffractive optics. Their subwavelength thickness, planar form factor, compatibility with conventional micro/nano-fabrication techniques, potentially low-cost batch fabrication, ability to replace a system of multiple bulky conventional elements with a miniature element, new capabilities to control different degrees of freedom of light, and prospects for a paradigm change in how optical systems are designed make them very promising for the realization of the next generation of compact high-performance optical systems.

Despite all the advancements made in the past few years, several challenges still remain unresolved both from fundamental and practical points of view. An important theoretical issue is the number of available degrees of freedom that exist in a single surface or a specific volume. This would determine the number of functionalities that can be encoded in such a device with negligible performance degradation. The importance of this issue becomes more clear as one considers the great interest in realizing multi-functional metasurfaces. Despite several such devices including multi-wavelength metasurfaces [135, 137, 228], multi-angle metasurfaces [15, 354], and metasurfaces with independent polarization and phase control [14, 133], the number of available degrees of freedom in such a device, and how exactly they can be utilized is still mostly unknown. Although optimization techniques have been used to improve the performance of multi-functional devices [131, 256, 355], they still do not determine the possible number of functionalities. Another area which requires significant advancements is the modeling and design of non-periodic metasurfaces. Currently, almost all of the design methods are based on results of simulation of periodic lattices of the meta-atoms. Although this approach works

well for slowly varying metasurfaces with small deflection angles, its underlying assumptions (namely locality, angle independence, and weak coupling of meta-atoms) cease to be valid for devices with large deflection angles. Therefore, more precise design methods that take all of these into account, and at the same time can be applied to large non-periodic structures are of great interest. In addition to enabling high-efficiency high-NA devices, such methods could also allow for the design and analysis of novel metasurfaces that are not bound by the assumption of locality. Finally, despite several attempts at realizing achromatic and dispersion-engineered metasurfaces, the operation bandwidths, sizes, and numerical apertures of devices that are possible with the existing platforms are very limited. The dependence of all of these limitations on the possible controllable quality factors that the platform provides makes the problem even more challenging. As a result, there is still a long way to the realization of achromatic and dispersion-engineered metasurfaces with practical sizes (i.e., aperture sizes of a few millimeters) and moderate to high numerical apertures.

In addition to fundamental challenges, there are also several unresolved practical issues hindering the realization of high-volume low-cost metasurface devices for real-life applications. One issue worth addressing is the absence of a low-loss high-index material for visible light. Although there have been several realization of dielectric metasurfaces in the visible [124, 210, 260, 279], their efficiency is still not as high as infrared metasurfaces where materials with low loss and high refractive index like silicon can be used. This is especially true for the cases of polarization independent metasurfaces, and devices with independent control of phase and polarization. In addition, for several applications, it is essential that the metasurface is capped by a low-index material (for instance for mechanical robustness, fabrication requirements, or realization of flexible and conformal metasurfaces). In such scenarios, the refractive index of currently available low-loss materials in the visible is not high enough to provide low-coupling between nanoposts and full phase coverage.

To have a significant industrial impact, the manufacturing processes of metasurfaces should be compatible with the existing low-cost large-scale foundry technology. Although this might already be possible for devices working in near and mid-IR (above 1.5 μm wavelength), it is challenging for devices that work below 1 μm, which are fabricated almost exclusively with EBL. In principle, large-scale fabrication techniques like DUV lithography, roll-to-roll nano-imprint, and soft lithography

could address this challenge; however, there still exist practical barriers that should be overcome before this becomes a reality.

Another category of highly desirable devices is the tunable metasurfaces. Despite several demonstrations of wavefront tuning using metasurfaces, none of them can still compete with the commercially available liquid crystal based SLMs. High-efficiency, ultra-fast, high-resolution wavefront tuning is of great need, and there is a lot of room for optimizing high-performance metadevices for beam steering applications, spatial light modulators, and dynamic holographic displays.

With the future advancements of metasurfaces in mind, we envision them at least as a complementary platform, if not a paradigm changing one, in optical element and system design for various applications.

BIBLIOGRAPHY

[1] S. M. Kamali*, E. Arbabi*, A. Arbabi, and A. Faraon, "A review of dielectric optical metasurfaces for wavefront control", Nanophotonics **7**, 1041–1068 (2018) DOI: 10.1515/nanoph-2017-0129, (cited on pp. 1, 23).

[2] C. L. Holloway, E. F. Kuester, J. A. Gordon, J. O'Hara, J. Booth, and D. R. Smith, "An overview of the theory and applications of metasurfaces: the two-dimensional equivalents of metamaterials", IEEE Antennas Propag. Mag. **54**, 10–35 (2012) (cited on p. 1).

[3] A. V. Kildishev, A. Boltasseva, and V. M. Shalaev, "Planar photonics with metasurfaces", Science **339**, 1232009 (2013) (cited on pp. 1, 4, 125).

[4] N. Yu, and F. Capasso, "Flat optics with designer metasurfaces", Nat. Mater. **13**, 139–150 (2014) (cited on pp. 1, 125).

[5] N. M. Estakhri, and A. Alu, "Recent progress in gradient metasurfaces", J. Opt. Soc. Am. B **33**, A21–A30 (2016) (cited on p. 1).

[6] S. Jahani, and Z. Jacob, "All-dielectric metamaterials", Nat. Nanotechnol. **11**, 23–36 (2016) (cited on pp. 1, 125).

[7] P. Lalanne, and P. Chavel, "Metalenses at visible wavelengths: past, present, perspectives", Laser Photon. Rev. **11**, 1600295 (2017) (cited on pp. 1, 23).

[8] I. Staude, and J. Schilling, "Metamaterial-inspired silicon nanophotonics", Nat. Photon. **11**, 274–284 (2017) (cited on p. 1).

[9] P. Genevet, F. Capasso, F. Aieta, M. Khorasaninejad, and R. Devlin, "Recent advances in planar optics: from plasmonic to dielectric metasurfaces", Optica **4**, 139–152 (2017) (cited on p. 1).

[10] H.-H. Hsiao, C. H. Chu, and D. P. Tsai, "Fundamentals and applications of metasurfaces", Small Methods **1**, 1600064 (2017) (cited on p. 1).

[11] P. Qiao, W. Yang, and C. J. Chang-Hasnain, "Recent advances in high-contrast metastructures, metasurfaces, and photonic crystals", Adv. Opt. Photonics **10**, 180–245 (2018) (cited on pp. 1, 23).

[12] W. Zi Jing, W. Yuan, O. Kevin, R. Junsuk, Y. Xiaobo, Z. Shuang, F. Nicholas, Y. Ta-Jen, and Z. Xiang, "Optical and acoustic metamaterials: superlens, negative refractive index and invisibility cloak", J. Opt. **19**, 084007 (2017) (cited on p. 1).

[13] S. Kruk, and Y. Kivshar, "Functional meta-optics and nanophotonics governed by Mie resonances", ACS Photonics **4**, 2638–2649 (2017) (cited on p. 1).

[14] A. Arbabi, Y. Horie, M. Bagheri, and A. Faraon, "Dielectric metasurfaces for complete control of phase and polarization with subwavelength spatial resolution and high transmission", Nat. Nanotechnol. **10**, 937–943 (2015) (cited on pp. 1, 4, 5, 9, 12–16, 21, 23, 24, 43, 47, 58–60, 66, 68, 125, 126, 150, 176, 222).

[15] S. M. Kamali, E. Arbabi, A. Arbabi, Y. Horie, M. Faraji-Dana, and A. Faraon, "Angle-multiplexed metasurfaces: encoding independent wavefronts in a single metasurface under different illumination angles", Phys. Rev. X **7**, 041056 (2017) DOI: 10.1103/PhysRevX.7.041056 (cited on pp. 1, 9, 66, 163, 222).

[16] J. Huang, and J. A. Encinar, *Reflectarray antennas* (John Wiley & Sons, Inc., 2007) (cited on p. 2).

[17] D. M. Pozar, and T. A. Metzler, "Analysis of a reflectarray antenna using microstrip patches of variable size", Electron. Lett. **29**, 657–658 (1993) (cited on p. 2).

[18] N. Yu, P. Genevet, M. A. Kats, F. Aieta, J.-P. Tetienne, F. Capasso, and Z. Gaburro, "Light propagation with phase discontinuities: generalized laws of reflection and refraction", Science **334**, 333–337 (2011) (cited on pp. 2, 3).

[19] C. S. Malagisi, "Microstrip disc element reflect array", in Eascon '78; electronics and aerospace systems convention (1978), pp. 186–192 (cited on p. 2).

[20] J. Huang, and R. J. Pogorzelski, "A ka-band microstrip reflectarray with elements having variable rotation angles", IEEE Trans. Antennas Propag. **46**, 650–656 (1998) (cited on p. 2).

[21] R. C. Fairchild, and J. R. Fienup, "Computer-originated aspheric holographic optical elements", Opt. Eng. **21**, 211133–211140 (1982) (cited on pp. 2, 173).

[22] L. B. Lesem, P. M. Hirsch, and J. A. Jordan, "The kinoform: a new wavefront reconstruction device", IBM J. Res. Dev. **13**, 150–155 (1969) (cited on p. 2).

[23] D. C. O'Shea, T. J. Suleski, A. D. Kathman, and D. W. Prather, *Diffractive optics: design, fabrication, and test* (SPIE Press, 2004) (cited on pp. 2, 64, 67, 85, 86, 159, 182).

[24] W. Stork, N. Streibl, H. Haidner, and P. Kipfer, "Artificial distributed-index media fabricated by zero-order gratings", Opt. Lett. **16**, 1921–1923 (1991) (cited on p. 2).

[25] M. W. Farn, "Binary gratings with increased efficiency", Appl. Opt. **31**, 4453–4458 (1992) (cited on p. 2).

[26] G. J. Swanson, *Binary optics technology: theoretical limits on the diffraction efficiency of multilevel diffractive optical elements*, tech. rep. (DTIC Document, 1991) (cited on p. 2).

[27] G. J. Swanson, *Binary optics technology: the theory and design of multi-level diffractive optical elements*, tech. rep. (DTIC Document, 1989) (cited on pp. 2, 38, 39, 41, 145).

[28] W. T. Welford, "Aplanatic hologram lenses on spherical surfaces", Opt. Commun. **9**, 268–269 (1973) (cited on pp. 3, 125).

[29] D. A. Buralli, and G. M. Morris, "Design of diffractive singlets for monochromatic imaging", Appl. Opt. **30**, 2151–2158 (1991) (cited on p. 3).

[30] D. A. Buralli, and G. M. Morris, "Design of a wide field diffractive landscape lens", Appl. Opt. **28**, 3950–3959 (1989) (cited on pp. 3, 126, 131, 141).

[31] "Https://www.rpcphotonics.com/", (access date: 12/11/2017) (cited on p. 3).

[32] D. Fattal, J. Li, Z. Peng, M. Fiorentino, and R. G. Beausoleil, "Flat dielectric grating reflectors with focusing abilities", Nat. Photon. **4**, 466–470 (2010) (cited on pp. 3, 5, 125).

[33] D. Lin, P. Fan, E. Hasman, and M. L. Brongersma, "Dielectric gradient metasurface optical elements", Science **345**, 298–302 (2014) (cited on pp. 3, 4, 23, 125, 141).

[34] C. Pfeiffer, and A. Grbic, "Metamaterial Huygens' surfaces: tailoring wave fronts with reflectionless sheets", Phys. Rev. Lett. **110**, 197401 (2013) (cited on pp. 3, 4, 48).

[35] Y. F. Yu, A. Y. Zhu, R. Paniagua-Dominguez, Y. H. Fu, B. Luk'yanchuk, and A. I. Kuznetsov, "High-transmission dielectric metasurface with 2π phase control at visible wavelengths", Laser Photon. Rev. **9**, 412–418 (2015) (cited on pp. 3, 4, 6).

[36] S. M. Kamali, E. Arbabi, A. Arbabi, Y. Horie, and A. Faraon, "Highly tunable elastic dielectric metasurface lenses", Laser Photon. Rev. **10**, 1062–1062 (2016) DOI: 10.1002/lpor.201600144 (cited on pp. 3, 5, 9, 18, 66, 72, 141, 146, 147, 203).

[37] F. Lu, F. G. Sedgwick, V. Karagodsky, C. Chase, and C. J. Chang-Hasnain, "Planar high-numerical-aperture low-loss focusing reflectors and lenses using subwavelength high contrast gratings", Opt. Express **18**, 12606–12614 (2010) (cited on pp. 3, 5).

[38] D. Fattal, J. Li, Z. Peng, M. Fiorentino, and R. G. Beausoleil, "A silicon lens for integrated free-space optics", in Advanced photonics, OSA Technical Digest (CD) (2011), ITuD2 (cited on pp. 3–6, 8).

[39] Y. Zhao, and A. Alu, "Manipulating light polarization with ultrathin plasmonic metasurfaces", Phys. Rev. B **84**, 205428 (2011) (cited on p. 3).

[40] Y. Zhao, N. Engheta, and A. Alu, "Homogenization of plasmonic metasurfaces modeled as transmission-line loads", Metamaterials **5**, 90–96 (2011) (cited on p. 3).

[41] F. Aieta, P. Genevet, M. A. Kats, N. Yu, R. Blanchard, Z. Gaburro, and F. Capasso, "Aberration-free ultrathin flat lenses and axicons at telecom wavelengths based on plasmonic metasurfaces", Nano Lett. **12**, 4932–4936 (2012) (cited on pp. 3, 4, 125, 141).

[42] L. Huang, X. Chen, H. Muhlenbernd, G. Li, B. Bai, Q. Tan, G. Jin, T. Zentgraf, and S. Zhang, "Dispersionless phase discontinuities for controlling light propagation", Nano Lett. **12**, 5750–5755 (2012) (cited on p. 3).

[43] A. Di Falco, Y. Zhao, and A. Alu, "Optical metasurfaces with robust angular response on flexible substrates", Appl. Phys. Lett. **99**, 163110 (2011) (cited on p. 4).

[44] N. Yu, F. Aieta, P. Genevet, M. A. Kats, Z. Gaburro, and F. Capasso, "A broadband, background-free quarter-wave plate based on plasmonic metasurfaces", Nano Lett. **12**, 6328–6333 (2012) (cited on p. 4).

[45] G. Li, M. Kang, S. Chen, S. Zhang, E. Y.-B. Pun, K. W. Cheah, and J. Li, "Spin-enabled plasmonic metasurfaces for manipulating orbital angular momentum of light", Nano Lett. **13**, 4148–4151 (2013) (cited on p. 4).

[46] X. Ni, A. V. Kildishev, and V. M. Shalaev, "Metasurface holograms for visible light", Nat. Commun. **4**, 2807 (2013) (cited on p. 4).

[47] A. Pors, and S. I. Bozhevolnyi, "Plasmonic metasurfaces for efficient phase control in reflection", Opt. Express **21**, 27438–27451 (2013) (cited on p. 4).

[48] A. Pors, M. G. Nielsen, R. L. Eriksen, and S. I. Bozhevolnyi, "Broadband focusing flat mirrors based on plasmonic gradient metasurfaces", Nano Lett. **13**, 829–834 (2013) (cited on p. 4).

[49] S. Datthanasombat, A. Prata, L. R. Arnaro, J. A. Harrell, S. Spitz, and J. Perret, "Layered lens antennas", in Antenn. propag. soc. symp. Vol. 2 (2001), pp. 777–780 (cited on p. 4).

[50] F. Monticone, N. M. Estakhri, and A. Alu, "Full control of nanoscale optical transmission with a composite metascreen", Phys. Rev. Lett. **110**, 203903 (2013) (cited on p. 4).

[51] A. Arbabi, and A. Faraon, "Fundamental limits of ultrathin metasurfaces", Sci. Rep. **7**, 43722 (2017) (cited on pp. 4, 38).

[52] E. Hasman, V. Kleiner, G. Biener, and A. Niv, "Polarization dependent focusing lens by use of quantized Pancharatnam-Berry phase diffractive optics", Appl. Phys. Lett. **82**, 328–330 (2003) (cited on p. 4).

[53] A. Epstein, and G. V. Eleftheriades, "Floquet-Bloch analysis of refracting Huygens metasurfaces", Phys. Rev. B **90**, 235127 (2014) (cited on p. 4).

[54] A. Epstein, and G. V. Eleftheriades, "Passive lossless Huygens metasurfaces for conversion of arbitrary source field to directive radiation", IEEE Trans. Antennas Propag. **62**, 5680–5695 (2014) (cited on p. 4).

[55] M. Kim, A. M. H. Wong, and G. V. Eleftheriades, "Optical Huygens' metasurfaces with independent control of the magnitude and phase of the local reflection coefficients", Phys. Rev. X **4**, 041042 (2014) (cited on p. 4).

[56] S. L. Jia, X. Wan, X. J. Fu, Y. J. Zhao, and T. J. Cui, "Low-reflection beam refractions by ultrathin Huygens' metasurface", AIP Adv. **5**, 067102 (2015) (cited on p. 4).

[57] A. Epstein, J. P. S. Wong, and G. V. Eleftheriades, "Cavity-excited Huygens' metasurface antennas for near-unity aperture illumination efficiency from arbitrarily large apertures", Nat. Commun. **7**, 10360 (2016) (cited on pp. 4, 48).

[58] A. Epstein, and G. V. Eleftheriades, "Huygens' metasurfaces via the equivalence principle: design and applications", J. Opt. Soc. Am. B **33**, A31–A50 (2016) (cited on p. 4).

[59] I. Staude, A. E. Miroshnichenko, M. Decker, N. T. Fofang, S. Liu, E. Gonzales, J. Dominguez, T. S. Luk, D. N. Neshev, and I. e. a. Brener, "Tailoring directional scattering through magnetic and electric resonances in subwavelength silicon nanodisks", ACS Nano **7**, 7824–7832 (2013) (cited on pp. 4, 6).

[60] S. Campione, L. I. Basilio, L. K. Warne, and M. B. Sinclair, "Tailoring dielectric resonator geometries for directional scattering and Huygens' metasurfaces", Opt. Express **23**, 2293–2307 (2015) (cited on p. 4).

[61] M. Decker, I. Staude, M. Falkner, J. Dominguez, D. N. Neshev, I. Brener, T. Pertsch, and Y. S. Kivshar, "High-efficiency dielectric Huygens' surfaces", Adv. Opt. Mater. **3**, 813–820 (2015) (cited on pp. 4, 6).

[62] V. Asadchy, M. Albooyeh, and S. Tretyakov, "Optical metamirror: all-dielectric frequency-selective mirror with fully controllable reflection phase", J. Opt. Soc. Am. B **33**, A16–A20 (2016) (cited on p. 4).

[63] W. Zhao, H. Jiang, B. Liu, J. Song, Y. Jiang, C. Tang, and J. Li, "Dielectric Huygens' metasurface for high-efficiency hologram operating in transmission mode", Sci. Rep. **6**, 30613 (2016) (cited on p. 4).

[64] A. Forouzmand, and H. Mosallaei, "All-dielectric c-shaped nanoantennas for light manipulation: tailoring both magnetic and electric resonances to the desire", Adv. Opt. Mater. **5**, 1700147 (2017) (cited on p. 4).

[65] A. Arbabi, M. Bagheri, A. J. Ball, Y. Horie, D. Fattal, and A. Faraon, "Controlling the phase front of optical fiber beams using high contrast metastructures", in Conference on lasers and electro-optics (cleo) (2014), STu3M.4 (cited on pp. 4–6, 8, 125).

[66] S. Vo, D. Fattal, W. V. Sorin, P. Zhen, T. Tho, M. Fiorentino, and R. G. Beausoleil, "Sub-wavelength grating lenses with a twist", IEEE Photon. Technol. Lett. **26**, 1375–1378 (2014) (cited on pp. 4–8, 125, 141).

[67] A. Arbabi, Y. Horie, A. J. Ball, M. Bagheri, and A. Faraon, "Subwavelength-thick lenses with high numerical apertures and large efficiency based on high-contrast transmitarrays", Nat. Commun. **6**, 7069 (2015) (cited on pp. 4–8, 12, 18, 41, 43, 47, 49, 59, 63, 73, 96, 98, 125, 126, 129, 141, 150, 151, 174, 176, 179, 181–183, 216).

[68] A. Arbabi, R. M. Briggs, Y. Horie, M. Bagheri, and A. Faraon, "Efficient dielectric metasurface collimating lenses for mid-infrared quantum cascade lasers", Opt. Express **23**, 33310–33317 (2015) (cited on pp. 4, 31, 125).

[69] A. Zhan, S. Colburn, R. Trivedi, T. K. Fryett, C. M. Dodson, and A. Majumdar, "Low-contrast dielectric metasurface optics", ACS Photonics **3**, 209–214 (2016) (cited on pp. 4, 8, 136).

[70] S. Kruk, B. Hopkins, I. I. Kravchenko, A. Miroshnichenko, D. N. Neshev, and Y. S. Kivshar, "Invited article: broadband highly efficient dielectric metadevices for polarization control", APL Photonics **1**, 030801 (2016) (cited on pp. 4, 5, 8, 23).

[71] M. Khorasaninejad, W. T. Chen, R. C. Devlin, J. Oh, A. Y. Zhu, and F. Capasso, "Metalenses at visible wavelengths: diffraction-limited focusing and subwavelength resolution imaging", Science **352**, 1190–1194 (2016) (cited on pp. 4, 5, 12, 66).

[72] R. Paniagua-Dominguez, Y. F. Yu, E. Khaidarov, S. Choi, V. Leong, R. Bakker, X. Liang, Y. H. Fu, V. Valuckas, L. A. Krivitsky, and A. I. Kuznetsov, "A metalens with near-unity numerical aperture", Nano Lett. **18**, 2124–2132 (2018) (cited on pp. 4, 5, 8, 12).

[73] B. H. Chen, P. C. Wu, V.-C. Su, Y.-C. Lai, C. H. Chu, I. C. Lee, J.-W. Chen, Y. H. Chen, Y.-C. Lan, and C.-H. e. a. Kuan, "GaN metalens for pixel-level full-color routing at visible light", Nano Lett. **17**, 6345–6352 (2017) (cited on p. 4).

[74] B. Wang, F. Dong, Q.-T. Li, D. Yang, C. Sun, J. Chen, Z. Song, L. Xu, W. Chu, and Y.-F. e. a. Xiao, "Visible-frequency dielectric metasurfaces for multiwavelength achromatic and highly dispersive holograms", Nano Lett. **16**, 5235–5240 (2016) (cited on pp. 4, 86).

[75] S. Astilean, P. Lalanne, P. Chavel, E. Cambril, and H. Launois, "High-efficiency subwavelength diffractive element patterned in a high-refractive-index material for 633 nm", Opt. Lett. **23**, 552–554 (1998) (cited on pp. 4, 12).

[76] P. Lalanne, S. Astilean, P. Chavel, E. Cambril, and H. Launois, "Blazed binary subwavelength gratings with efficiencies larger than those of conventional echelette gratings", Opt. Lett. **23**, 1081–1083 (1998) (cited on pp. 4–6, 12, 136, 141, 150).

[77] P. Lalanne, "Waveguiding in blazed-binary diffractive elements", J. Opt. Soc. Am. A **16**, 2517–2520 (1999) (cited on pp. 4, 6, 41, 49, 59, 94).

[78] P. Lalanne, S. Astilean, P. Chavel, E. Cambril, and H. Launois, "Design and fabrication of blazed binary diffractive elements with sampling periods smaller than the structural cutoff", J. Opt. Soc. Am. A **16**, 1143–1156 (1999) (cited on pp. 4–6, 8, 136).

[79] H. Mosallaei, and K. Sarabandi, "A one-layer ultra-thin meta-surface absorber", in Antenn. propag. soc. symp. Vol. 1B (2005), pp. 615–618 (cited on p. 5).

[80] I. Martinez, A. H. Panaretos, D. H. Werner, G. Oliveri, and A. Massa, "Ultra-thin reconfigurable electromagnetic metasurface absorbers", in 7th european conference on antennas and propagation (eucap) (2013), pp. 1843–1847 (cited on p. 5).

[81] Y. Yao, R. Shankar, M. A. Kats, Y. Song, J. Kong, M. Loncar, and F. Capasso, "Electrically tunable metasurface perfect absorbers for ultrathin mid-infrared optical modulators", Nano Lett. **14**, 6526–6532 (2014) (cited on p. 5).

[82] J. Y. Jung, J. Lee, D. G. Choi, J. H. Choi, J. H. Jeong, E. S. Lee, and D. P. Neikirk, "Wavelength-selective infrared metasurface absorber for multispectral thermal detection", IEEE Photon. Jour. **7**, 1–10 (2015) (cited on p. 5).

[83] Z. Yang, B. O. Zhu, and Y. Feng, "Free space electromagnetic wave modulation using tunable metasurface absorber", in Asia-pacific microwave conference (apmc), Vol. 1 (2015), pp. 1–3 (cited on p. 5).

[84] Y. Ra'di, V. S. Asadchy, S. U. Kosulnikov, M. M. Omelyanovich, D. Morits, A. V. Osipov, C. R. Simovski, and S. A. Tretyakov, "Full light absorption in single arrays of spherical nanoparticles", ACS Photonics **2**, 653–660 (2015) (cited on p. 5).

[85] A. K. Azad, W. J. M. Kort-Kamp, M. Sykora, N. R. Weisse-Bernstein, T. S. Luk, A. J. Taylor, D. A. R. Dalvit, and H.-T. Chen, "Metasurface broadband solar absorber", Sci. Rep. **6**, 20347 (2016) (cited on p. 5).

[86] W. Guo, Y. Liu, and T. Han, "Ultra-broadband infrared metasurface absorber", Opt. Express **24**, 20586–20592 (2016) (cited on p. 5).

[87] S. J. Kim, J. Park, M. Esfandyarpour, E. F. Pecora, P. G. Kik, and M. L. Brongersma, "Superabsorbing, artificial metal films constructed from semiconductor nanoantennas", Nano Lett. **16**, 3801–3808 (2016) (cited on p. 5).

[88] Z. Luo, J. Long, X. Chen, and D. Sievenpiper, "Electrically tunable metasurface absorber based on dissipating behavior of embedded varactors", Appl. Phys. Lett. **109**, 071107 (2016) (cited on p. 5).

[89] C. Wan, Y. Ho, S. Nunez-Sanchez, L. Chen, M. Lopez-Garcia, J. Pugh, B. Zhu, P. Selvaraj, T. Mallick, and S. e. a. Senthilarasu, "A selective metasurface absorber with an amorphous carbon interlayer for solar thermal applications", Nano Energy **26**, 392–397 (2016) (cited on p. 5).

[90] J.-Y. Jung, K. Song, J.-H. Choi, J. Lee, D.-G. Choi, J.-H. Jeong, and D. P. Neikirk, "Infrared broadband metasurface absorber for reducing the thermal mass of a microbolometer", Sci. Rep. **7**, 430 (2017) (cited on p. 5).

[91] A. Li, S. Kim, Y. Luo, Y. Li, J. Long, and D. F. Sievenpiper, "High-power transistor-based tunable and switchable metasurface absorber", IEEE Trans. Microw. Theory Tech. **65**, 2810–2818 (2017) (cited on p. 5).

[92] Z. Sun, J. Zhao, B. Zhu, T. Jiang, and Y. Feng, "Selective wave-transmitting electromagnetic absorber through composite metasurface", AIP Adv. **7**, 115017 (2017) (cited on p. 5).

[93] B. Tang, Z. Li, E. Palacios, Z. Liu, S. Butun, and K. Aydin, "Chiral-selective plasmonic metasurface absorbers operating at visible frequencies", IEEE Photon. Technol. Lett. **29**, 295–298 (2017) (cited on p. 5).

[94] R. Magnusson, and S. Wang, "Optical guided-mode resonance filter", US Patent, 5, 216, 680 (1993) (cited on p. 5).

[95] D. Shin, S. Tibuleac, T. A. Maldonado, and R. Magnusson, "Thin-film optical filters with diffractive elements and waveguides", Opt. Eng. **37**, 2634–2646 (1998) (cited on p. 5).

[96] M. Shokooh-Saremi, and R. Magnusson, "Particle swarm optimization and its application to the design of diffraction grating filters", Opt. Lett. **32**, 894–896 (2007) (cited on p. 5).

[97] J. D. Ortiz, J. D. Baena, R. Marques, and F. Medina, "A band-pass/stop filter made of SRRs and C-SRRs", in Ieee international symposium on antennas and propagation (apsursi) (2011), pp. 2669–2672 (cited on p. 5).

[98] T. Ellenbogen, K. Seo, and K. B. Crozier, "Chromatic plasmonic polarizers for active visible color filtering and polarimetry", Nano Lett. **12**, 1026–1031 (2012) (cited on pp. 5, 13).

[99] J. D. Ortiz, J. D. Baena, V. Losada, F. Medina, R. Marques, and J. L. A. Quijano, "Self-complementary metasurface for designing narrow band pass/stop filters", IEEE Microw. Wirel. Compon. Lett. **23**, 291–293 (2013) (cited on p. 5).

[100] Y. Wang, D. Stellinga, A. B. Klemm, C. P. Reardon, and T. F. Krauss, "Tunable optical filters based on silicon nitride high contrast gratings", IEEE J. Sel. Top. Quantum Electron. **21**, 108–113 (2015) (cited on pp. 5, 148).

[101] Y. Horie, A. Arbabi, S. Han, and A. Faraon, "High resolution on-chip optical filter array based on double subwavelength grating reflectors", Opt. Express **23**, 29848–29854 (2015) (cited on p. 5).

[102] Y. Horie, A. Arbabi, E. Arbabi, S. M. Kamali, and A. Faraon, "Wide bandwidth and high resolution planar filter array based on DBR-metasurface-DBR structures", Opt. Express **24**, 11677–11682 (2016) DOI: 10.1364/OE.24.011677 (cited on pp. 5, 161).

[103] Y. Horie, S. Han, J.-Y. Lee, J. Kim, Y. Kim, A. Arbabi, C. Shin, L. Shi, E. Arbabi, S. M. Kamali, H.-S. Lee, S. Hwang, and A. Faraon, "Visible wavelength color filters using dielectric subwavelength gratings for backside-illuminated CMOS image sensor technologies", Nano Lett. **17**, 3159–3164 (2017) DOI: 10.1021/acs.nanolett.7b00636 (cited on p. 5).

[104] W. Yue, S. Gao, S.-S. Lee, E.-S. Kim, and D.-Y. Choi, "Subtractive color filters based on a silicon-aluminum hybrid-nanodisk metasurface enabling enhanced color purity", Sci. Rep. **6**, 29756 (2016) (cited on p. 5).

[105] K. Yamada, K. J. Lee, Y. H. Ko, J. Inoue, K. Kintaka, S. Ura, and R. Magnusson, "Flat-top narrowband filters enabled by guided-mode resonance in two-level waveguides", Opt. Lett. **42**, 4127–4130 (2017) (cited on p. 5).

[106] M. F. Limonov, M. V. Rybin, A. N. Poddubny, and Y. S. Kivshar, "Fano resonances in photonics", Nat. Photon. **11**, 543–554 (2017) (cited on p. 5).

[107] J. Lee, M. Tymchenko, C. Argyropoulos, P.-Y. Chen, F. Lu, F. Demmerle, G. Boehm, M.-C. Amann, A. Alu, and M. A. Belkin, "Giant nonlinear response from plasmonic metasurfaces coupled to intersubband transitions", Nature **511**, 65–69 (2014) (cited on p. 5).

[108] M. Tymchenko, J. S. Gomez-Diaz, J. Lee, N. Nookala, M. A. Belkin, and A. Alu, "Gradient nonlinear Pancharatnam-Berry metasurfaces", Phys. Rev. Lett. **115**, 207403 (2015) (cited on pp. 5, 48).

[109] O. Wolf, S. Campione, A. Benz, A. P. Ravikumar, S. Liu, T. S. Luk, E. A. Kadlec, E. A. Shaner, J. F. Klem, and M. B. e. a. Sinclair, "Phased-array sources based on nonlinear metamaterial nanocavities", Nat. Commun. **6**, 7667 (2015) (cited on pp. 5, 48).

[110] R. Camacho-Morales, M. Rahmani, S. Kruk, L. Wang, L. Xu, D. A. Smirnova, A. S. Solntsev, A. Miroshnichenko, H. H. Tan, and F. e. a. Karouta, "Nonlinear generation of vector beams from AlGaAs nanoantennas", Nano Lett. **16**, 7191–7197 (2016) (cited on p. 5).

[111] N. Nookala, J. Lee, M. Tymchenko, J. Sebastian Gomez-Diaz, F. Demmerle, G. Boehm, K. Lai, G. Shvets, M.-C. Amann, and A. e. a. Alu, "Ultrathin gradient nonlinear metasurface with a giant nonlinear response", Optica **3**, 283–288 (2016) (cited on pp. 5, 48).

[112] S. Jafar-Zanjani, J. Cheng, V. Liberman, J. B. Chou, and H. Mosallaei, "Large enhancement of third-order nonlinear effects with a resonant all-dielectric metasurface", AIP Adv. **6**, 115213 (2016) (cited on p. 5).

[113] S. Liu, M. B. Sinclair, S. Saravi, G. A. Keeler, Y. Yang, J. Reno, G. M. Peake, F. Setzpfandt, I. Staude, and T. e. a. Pertsch, "Resonantly enhanced second-harmonic generation using III-V semiconductor all-dielectric metasurfaces", Nano Lett. **16**, 5426–5432 (2016) (cited on p. 5).

[114] S. V. Makarov, M. I. Petrov, U. Zywietz, V. Milichko, D. Zuev, N. Lopanitsyna, A. Kuksin, I. Mukhin, G. Zograf, and E. e. a. Ubyivovk, "Efficient second-harmonic generation in nanocrystalline silicon nanoparticles", Nano Lett. **17**, 3047–3053 (2017) (cited on p. 5).

[115] A. E. Miroshnichenko, A. B. Evlyukhin, Y. F. Yu, R. M. Bakker, A. Chipouline, A. I. Kuznetsov, B. Luk'yanchuk, B. N. Chichkov, and Y. S. Kivshar, "Nonradiating anapole modes in dielectric nanoparticles", Nat. Commun. **6**, 8069 (2015) (cited on p. 5).

[116] P. C. Wu, C. Y. Liao, V. Savinov, T. L. Chung, W. T. Chen, Y.-W. Huang, P. R. Wu, Y.-H. Chen, A.-Q. Liu, and N. I. e. a. Zheludev, "Optical anapole metamaterial", ACS Nano **12**, 1920–1927 (2018) (cited on p. 5).

[117] A. B. Klemm, D. Stellinga, E. R. Martins, L. Lewis, G. Huyet, L. O'Faolain, and T. F. Krauss, "Experimental high numerical aperture focusing with high contrast gratings", Opt. Lett. **38**, 3410–3413 (2013) (cited on p. 5).

[118] Y. Yang, W. Wang, P. Moitra, I. I. Kravchenko, D. P. Briggs, and J. Valentine, "Dielectric meta-reflectarray for broadband linear polarization conversion and optical vortex generation", Nano Lett. **14**, 1394–1399 (2014) (cited on pp. 5, 6, 23).

[119] E. Arbabi, A. Arbabi, S. M. Kamali, Y. Horie, and A. Faraon, "Controlling the sign of chromatic dispersion in diffractive optics with dielectric metasurfaces", Optica **4**, 625–632 (2017) DOI: 10.1364/OPTICA.4.000625, (cited on pp. 5, 9, 21, 67, 69, 85, 145, 159, 163, 165).

[120] A. Arbabi, E. Arbabi, Y. Horie, S. M. Kamali, and A. Faraon, "Planar metasurface retroreflector", Nat. Photon. **11**, 415–420 (2017) DOI: 10.1038/nphoton.2017.96, (cited on pp. 5, 9, 13, 124, 148, 161, 165).

[121] A. Arbabi, Y. Horie, and A. Faraon, "Planar retroreflector", in Conference on lasers and electro-optics (cleo) (2014), pp. 1–2 (cited on pp. 6, 174).

[122] C. Hong, S. Colburn, and A. Majumdar, "Flat metaform near-eye visor", Appl. Opt. **56**, 8822–8827 (2017) (cited on p. 6).

[123] P. R. West, J. L. Stewart, A. V. Kildishev, V. M. Shalaev, V. V. Shkunov, F. Strohkendl, Y. A. Zakharenkov, R. K. Dodds, and R. Byren, "All-dielectric subwavelength metasurface focusing lens", Opt. Express **22**, 26212–26221 (2014) (cited on pp. 6, 7).

[124] M. Khorasaninejad, A. Y. Zhu, C. Roques-Carmes, W. T. Chen, J. Oh, I. Mishra, R. C. Devlin, and F. Capasso, "Polarization-insensitive metalenses at visible wavelengths", Nano Lett. **16**, 7229–7234 (2016) (cited on pp. 6–8, 223).

[125] S. M. Kamali, A. Arbabi, E. Arbabi, Y. Horie, and A. Faraon, "Decoupling optical function and geometrical form using conformal flexible dielectric metasurfaces", Nat. Commun. **7**, 11618 (2016) DOI: doi.org/10.1038/ncomms11618 (cited on pp. 7–9, 23, 41, 43, 49, 59, 66, 94, 96, 125, 126, 129, 146, 148, 173, 176, 179).

[126] K. E. Chong, I. Staude, A. James, J. Dominguez, S. Liu, S. Campione, G. S. Subramania, T. S. Luk, M. Decker, and D. N. e. a. Neshev, "Polarization-independent silicon metadevices for efficient optical wavefront control", Nano Lett. **15**, 5369–5374 (2015) (cited on p. 6).

[127] M. I. Shalaev, J. Sun, A. Tsukernik, A. Pandey, K. Nikolskiy, and N. M. Litchinitser, "High-efficiency all-dielectric metasurfaces for ultracompact beam manipulation in transmission mode", Nano Lett. **15**, 6261–6266 (2015) (cited on p. 6).

[128] Z. Zhou, J. Li, R. Su, B. Yao, H. Fang, K. Li, L. Zhou, J. Liu, D. Stellinga, and C. P. e. a. Reardon, "Efficient silicon metasurfaces for visible light", ACS Photonics **4**, 544–551 (2017) (cited on p. 8).

[129] S. J. Byrnes, A. Lenef, F. Aieta, and F. Capasso, "Designing large, high-efficiency, high-numerical-aperture, transmissive meta-lenses for visible light", Opt. Express **24**, 5110–5124 (2016) (cited on p. 8).

[130] A. Arbabi, E. Arbabi, S. M. Kamali, Y. Horie, S. Han, and A. Faraon, "Increasing efficiency of high-NA metasurface lenses", in Spie photon. west, Vol. 10113 (2017), 101130K–1 (cited on pp. 8, 18, 150, 155, 166, 203).

[131] D. Sell, J. Yang, S. Doshay, R. Yang, and J. A. Fan, "Large-angle, multifunctional metagratings based on freeform multimode geometries", Nano Lett. **17**, 3752–3757 (2017) (cited on pp. 8, 21, 155, 170, 222).

[132] M. P. Backlund, A. Arbabi, P. N. Petrov, E. Arbabi, S. Saurabh, A. Faraon, and W. E. Moerner, "Removing orientation-induced localization biases in single-molecule microscopy using a broadband metasurface mask", Nat. Photon. **10**, 459–462 (2016) DOI: 10.1038/nphoton.2016.93 (cited on pp. 9, 23, 31, 58, 150).

[133] E. Arbabi, S. M. Kamali, A. Arbabi, and A. Faraon, "Full-stokes imaging polarimetry using dielectric metasurfaces", ACS Photonics **5**, 3132–3140 (2018) DOI: 10.1021/acsphotonics.8b00362, (cited on pp. 9, 11, 23, 222).

[134] E. Arbabi, S. M. Kamali, A. Arbabi, and A. Faraon, "Vectorial holograms with a dielectric metasurface: ultimate polarization pattern generation", Submitted, (cited on pp. 9, 11).

[135] E. Arbabi, A. Arbabi, S. M. Kamali, Y. Horie, and A. Faraon, "Multiwavelength polarization-insensitive lenses based on dielectric metasurfaces with meta-molecules", Optica **3**, 628–633 (2016) DOI: 10.1364/OPTICA.3.

000628, (cited on pp. 9, 38, 55–57, 59, 64, 66, 72, 86, 103, 134, 145, 159, 163, 170, 182, 188, 222).

[136] E. Arbabi, A. Arbabi, S. M. Kamali, Y. Horie, and A. Faraon, "Multiwavelength metasurfaces through spatial multiplexing", Sci. Rep. **6**, 32803 (2016) DOI: 10.1038/srep32803, (cited on pp. 9, 21, 38, 72, 86, 134, 159, 170).

[137] E. Arbabi, A. Arbabi, S. M. Kamali, Y. Horie, and A. Faraon, "High efficiency double-wavelength dielectric metasurface lenses with dichroic birefringent meta-atoms", Opt. Express **24**, 18468–18477 (2016) DOI: 10.1364/OE.24.018468, (cited on pp. 9, 38, 68, 71, 81, 86, 134, 150, 159, 222).

[138] S. M. Kamali, E. Arbabi, A. Arbabi, Y. Horie, and A. Faraon, "Metasurfaces with controlled angular phase dispersion", in Spie photon. west (2017), 101130Q (cited on p. 9).

[139] A. Arbabi, E. Arbabi, S. M. Kamali, Y. Horie, S. Han, and A. Faraon, "Miniature optical planar camera based on a wide-angle metasurface doublet corrected for monochromatic aberrations", Nat. Commun. **7**, 13682 (2016) DOI: 10.1038/ncomms13682, (cited on pp. 9, 13, 21, 57, 64, 66, 72, 124, 141, 148, 158, 159, 161, 163, 172).

[140] E. Arbabi, A. Arbabi, S. M. Kamali, Y. Horie, M. Faraji-Dana, and A. Faraon, "Mems-tunable dielectric metasurface lens", Nat. Commun. **9**, 812 (2018) DOI: 10.1038/s41467-018-03155-6, (cited on pp. 9, 13, 66, 72, 124, 146).

[141] M. Faraji-Dana*, E. Arbabi*, A. Arbabi, S. M. Kamali, H. Kwon, and A. Faraon, "Compact folded metasurface spectrometer", Nat. Commun. **9**, 4196 (2018) DOI: 10.1038/s41467-018-06495-5, (cited on pp. 9, 124, 145, 146).

[142] M. Faraji-Dana, E. Arbabi, H. Kwon, S. M. Kamali, A. Arbabi, J. G. Bartholomew, and A. Faraon, "Miniaturized metasurface hyperspectral-imager", Submitted (cited on p. 9).

[143] C.-I. Chang, *Hyperspectral imaging: techniques for spectral detection and classification*, Vol. 1 (Springer Science & Business Media, 2003) (cited on p. 11).

[144] D.-W. Sun, *Hyperspectral imaging for food quality analysis and control* (Elsevier, 2010) (cited on p. 11).

[145] J. S. Tyo, D. L. Goldstein, D. B. Chenault, and J. A. Shaw, "Review of passive imaging polarimetry for remote sensing applications", Appl. Opt. **45**, 5453–5469 (2006) (cited on pp. 11–13).

[146] N. M. Garcia, I. de Erausquin, C. Edmiston, and V. Gruev, "Surface normal reconstruction using circularly polarized light", Opt. Express **23**, 14391–14406 (2015) (cited on p. 11).

[147] D. L. Coffeen, “Polarization and scattering characteristics in the atmospheres of earth, venus, and jupiter”, J. Opt. Soc. Am. **69**, 1051–1064 (1979) (cited on p. 11).

[148] R. Walraven, “Polarization imagery”, in Spie opt. eng. Vol. 20 (1981), p. 200114 (cited on p. 11).

[149] W. G. Egan, W. R. Johnson, and V. S. Whitehead, “Terrestrial polarization imagery obtained from the space shuttle:characterization and interpretation”, Appl. Opt. **30**, 435–442 (1991) (cited on p. 11).

[150] Y. Liu, T. York, W. Akers, G. Sudlow, V. Gruev, and S. Achilefu, “Complementary fluorescence-polarization microscopy using division-of-focal-plane polarization imaging sensor”, J. Biomed. Opt. **17**, 116001 (2012) (cited on p. 11).

[151] N. W. Roberts, M. J. How, M. L. Porter, S. E. Temple, R. L. Caldwell, S. B. Powell, V. Gruev, N. J. Marshall, and T. W. Cronin, “Animal polarization imaging and implications for optical processing”, Proceed. IEEE **102**, 1427–1434 (2014) (cited on p. 11).

[152] T. Charanya, T. York, S. Bloch, G. Sudlow, K. Liang, M. Garcia, W. J. Akers, D. Rubin, V. Gruev, and S. Achilefu, “Trimodal color-fluorescence-polarization endoscopy aided by a tumor selective molecular probe accurately detects flat lesions in colitis-associated cancer”, J. Biomed. Opt. **19**, 14 (2014) (cited on p. 11).

[153] M. Garcia, C. Edmiston, R. Marinov, A. Vail, and V. Gruev, “Bio-inspired color-polarization imager for real-time in situ imaging”, Optica **4**, 1263–1271 (2017) (cited on pp. 11, 12).

[154] J. Johnson, “Infrared polarization signature feasibility tests”, US Army Mobility Equipment Research and Development Center **TR-EO-74-1 (AD COO1-133)** (1974) (cited on p. 11).

[155] S. A. Chin-Bing, “Infrared polarization signature analysis”, Defense Technical Information Center **Rep. ADC008418** (1976) (cited on p. 11).

[156] J. E. Solomon, “Polarization imaging”, Appl. Opt. **20**, 1537–1544 (1981) (cited on p. 11).

[157] J. L. Pezzaniti, and R. A. Chipman, “Mueller matrix imaging polarimetry”, in Opt. eng. Vol. 34 (1995), p. 11 (cited on p. 11).

[158] G. P. Nordin, J. T. Meier, P. C. Deguzman, and M. W. Jones, “Micropolarizer array for infrared imaging polarimetry”, J. Opt. Soc. Am. A **16**, 1168–1174 (1999) (cited on pp. 11, 12).

[159] J. Guo, and D. Brady, “Fabrication of thin-film micropolarizer arrays for visible imaging polarimetry”, Appl. Opt. **39**, 1486–1492 (2000) (cited on pp. 11, 12).

[160] V. Gruev, J. V. d. Spiegel, and N. Engheta, "Image sensor with focal plane extraction of polarimetric information", in 2006 ieee international symposium on circuits and systems (2006), pp. 214–216 (cited on p. 11).

[161] D. Rust, "Integrated dual imaging detector", US Patent, 5, 438, 414 (1995) (cited on p. 12).

[162] A. G. Andreou, and Z. K. Kalayjian, "Polarization imaging: principles and integrated polarimeters", IEEE Sens. Jour. **2**, 566–576 (2002) (cited on p. 12).

[163] V. Gruev, A. Ortu, N. Lazarus, J. V. d. Spiegel, and N. Engheta, "Fabrication of a dual-tier thin film micropolarization array", Opt. Exp. **15**, 4994–5007 (2007) (cited on p. 12).

[164] V. Gruev, R. Perkins, and T. York, "Ccd polarization imaging sensor with aluminum nanowire optical filters", Opt. Express **18**, 19087–19094 (2010) (cited on p. 12).

[165] P. C. Deguzman, and G. P. Nordin, "Stacked subwavelength gratings as circular polarization filters", Appl. Opt. **40**, 5731–5737 (2001) (cited on p. 12).

[166] G. Myhre, W.-L. Hsu, A. Peinado, C. LaCasse, N. Brock, R. A. Chipman, and S. Pau, "Liquid crystal polymer full-Stokes division of focal plane polarimeter", Opt. Express **20**, 27393–27409 (2012) (cited on p. 12).

[167] W.-L. Hsu, G. Myhre, K. Balakrishnan, N. Brock, M. Ibn-Elhaj, and S. Pau, "Full-stokes imaging polarimeter using an array of elliptical polarizer", Opt. Express **22**, 3063–3074 (2014) (cited on p. 12).

[168] W.-L. Hsu, J. Davis, K. Balakrishnan, M. Ibn-Elhaj, S. Kroto, N. Brock, and S. Pau, "Polarization microscope using a near infrared full-stokes imaging polarimeter", Opt. Express **23**, 4357–4368 (2015) (cited on p. 12).

[169] B. Groever, W. T. Chen, and F. Capasso, "Meta-lens doublet in the visible region", Nano Lett. **17**, 4902–4907 (2017) (cited on pp. 13, 72).

[170] D. Wen, F. Yue, S. Kumar, Y. Ma, M. Chen, X. Ren, P. E. Kremer, B. D. Gerardot, M. R. Taghizadeh, and G. S. e. a. Buller, "Metasurface for characterization of the polarization state of light", Opt. Express **23**, 10272–10281 (2015) (cited on p. 13).

[171] M. Khorasaninejad, W. Zhu, and K. B. Crozier, "Efficient polarization beam splitter pixels based on a dielectric metasurface", Optica **2**, 376–382 (2015) (cited on p. 13).

[172] A. Pors, M. G. Nielsen, and S. I. Bozhevolnyi, "Plasmonic metagratings for simultaneous determination of stokes parameters", Optica **2**, 716–723 (2015) (cited on p. 13).

[173] W. T. Chen, P. Torok, M. R. Foreman, C. Y. Liao, W. Y. Tsai, P. R. Wu, and D. P. Tsai, "Integrated plasmonic metasurfaces for spectropolarimetry", Nanotechnology **27**, 224002 (2016) (cited on p. 13).

[174] J. P. Balthasar Mueller, K. Leosson, and F. Capasso, "Ultracompact metasurface in-line polarimeter", Optica **3**, 42–47 (2016) (cited on p. 13).

[175] F. Ding, A. Pors, Y. Chen, V. A. Zenin, and S. I. Bozhevolnyi, "Beam-size-invariant spectropolarimeters using gap-plasmon metasurfaces", ACS Photonics **4**, 943–949 (2017) (cited on p. 13).

[176] E. Maguid, I. Yulevich, M. Yannai, V. Kleiner, M. L. Brongersma, and E. Hasman, "Multifunctional interleaved geometric-phase dielectric metasurfaces", Light: Sci. Appl. **6**, e17027 (2017) (cited on p. 13).

[177] S. Wei, Z. Yang, and M. Zhao, "Design of ultracompact polarimeters based on dielectric metasurfaces", Opt. Lett. **42**, 1580–1583 (2017) (cited on p. 13).

[178] S. Huard, *Polarization of light*, Vol. 1 (Wiley-VCH, 1997) (cited on p. 13).

[179] R. C. Jones, "A new calculus for the treatment of optical systems. i. description and discussion of the calculus", J. Opt. Soc. Am. **31**, 488–493 (1941) (cited on p. 15).

[180] B. Bayer, "Color imaging array", US Patent, 3, 971, 065 (1976) (cited on pp. 21, 48).

[181] D. Lin, A. L. Holsteen, E. Maguid, G. Wetzstein, P. G. Kik, E. Hasman, and M. L. Brongersma, "Photonic multitasking interleaved Si nanoantenna phased array", Nano Lett. **16**, 7671–7676 (2016) (cited on pp. 21, 72, 86, 159).

[182] J. Hu, C.-H. Liu, X. Ren, L. J. Lauhon, and T. W. Odom, "Plasmonic lattice lenses for multiwavelength achromatic focusing", ACS Nano **10**, 10275–10282 (2016) (cited on p. 21).

[183] X. Zhu, Z. Ge, T. X. Wu, and S.-T. Wu, "Transflective liquid crystal displays", J. Display Technol. **1**, 15 (2005) (cited on p. 23).

[184] D.-K. Yang, *Fundamentals of liquid crystal devices* (John Wiley & Sons, 2014) (cited on p. 23).

[185] Q. Zhan, "Trapping metallic rayleigh particles with radial polarization", Opt. Express **12**, 3377–3382 (2004) (cited on p. 23).

[186] Y. Kozawa, and S. Sato, "Optical trapping of micrometer-sized dielectric particles by cylindrical vector beams", Opt. Express **18**, 10828–10833 (2010) (cited on p. 23).

[187] M. Meier, V. Romano, and T. Feurer, "Material processing with pulsed radially and azimuthally polarized laser radiation", Appl. Phys. A **86**, 329–334 (2007) (cited on p. 23).

[188] R. Weber, A. Michalowski, M. Abdou-Ahmed, V. Onuseit, V. Rominger, M. Kraus, and T. Graf, "Effects of radial and tangential polarization in laser material processing", Physics Procedia **12**, 21–30 (2011) (cited on p. 23).

[189] G. S. Duesberg, I. Loa, M. Burghard, K. Syassen, and S. Roth, "Polarized raman spectroscopy on isolated single-wall carbon nanotubes", Phys. Rev. Lett. **85**, 5436–5439 (2000) (cited on p. 23).

[190] J. M. Benevides, S. A. Overman, and G. J. Thomas Jr, "Raman, polarized raman and ultraviolet resonance raman spectroscopy of nucleic acids and their complexes", J. Raman Spectrosc. **36**, 279–299 (2005) (cited on p. 23).

[191] O. Bryngdahl, "Polarizing holography", J. Opt. Soc. Am. **57**, 545–546 (1967) (cited on p. 23).

[192] M. Nakajima, H. Komatsu, Y. Mitsuhashi, and T. Morikawa, "Computer generated polarization holograms: phase recording by polarization effect in photodichroic materials", Appl. Opt. **15**, 1030–1033 (1976) (cited on p. 23).

[193] L. Nikolova, and T. Todorov, "Diffraction efficiency and selectivity of polarization holographic recording", Optica Acta **31**, 579–588 (1984) (cited on p. 23).

[194] T. Todorov, L. Nikolova, and N. Tomova, "Polarization holography. 2: polarization holographic gratings in photoanisotropic materials with and without intrinsic birefringence", Appl. Opt. **23**, 4588–4591 (1984) (cited on p. 23).

[195] C. Oh, and M. J. Escuti, "Achromatic diffraction from polarization gratings with high efficiency", Opt. Lett. **33**, 2287–2289 (2008) (cited on p. 23).

[196] J. Kim, Y. Li, M. N. Miskiewicz, C. Oh, M. W. Kudenov, and M. J. Escuti, "Fabrication of ideal geometric-phase holograms with arbitrary wavefronts", Optica **2**, 958–964 (2015) (cited on p. 23).

[197] A. Jamali, D. Bryant, Y. Zhang, A. Grunnet-Jepsen, A. Bhowmik, and P. J. Bos, "Design of a large aperture tunable refractive fresnel liquid crystal lens", Appl. Opt. **57**, B10–B19 (2018) (cited on pp. 23, 146).

[198] M. Fratz, P. Fischer, and D. M. Giel, "Full phase and amplitude control in computer-generated holography", Optics Letters **34**, 3659–3661 (2009) (cited on p. 23).

[199] M. Fratz, D. M. Giel, and P. Fischer, "Digital polarization holograms with defined magnitude and orientation of each pixel's birefringence", Opt. Lett. **34**, 1270–1272 (2009) (cited on p. 23).

[200] P. Lalanne, J. Hazart, P. Chavel, E. Cambril, and H. Launois, "A transmission polarizing beam splitter grating", J. Opt. A Pure Appl. Opt. **1**, 215 (1999) (cited on p. 23).

[201] Z. Bomzon, V. Kleiner, and E. Hasman, "Pancharatnam-Berry phase in space-variant polarization-state manipulations with subwavelength gratings", Opt. Lett. **26**, 1424–1426 (2001) (cited on p. 23).

[202] G. Biener, A. Niv, V. Kleiner, and E. Hasman, "Formation of helical beams by use of Pancharatnam-Berry phase optical elements", Opt. Lett. **27**, 1875–1877 (2002) (cited on p. 23).

[203] W. Yu, T. Konishi, T. Hamamoto, H. Toyota, T. Yotsuya, and Y. Ichioka, "Polarization-multiplexed diffractive optical elements fabricated by subwavelength structures", Appl. Opt. **41**, 96–100 (2002) (cited on p. 23).

[204] U. Levy, C.-H. Tsai, L. Pang, and Y. Fainman, "Engineering space-variant inhomogeneous media for polarization control", Opt. Lett. **29**, 1718–1720 (2004) (cited on p. 23).

[205] I. Kim, G. Yoon, J. Jang, P. Genevet, K. T. Nam, and J. Rho, "Outfitting next generation displays with optical metasurfaces", ACS Photonics **5**, 3876–3895 (2018) (cited on p. 23).

[206] V.-C. Su, C. H. Chu, G. Sun, and D. P. Tsai, "Advances in optical metasurfaces: fabrication and applications [invited]", Opt. Express **26**, 13148–13182 (2018) (cited on p. 23).

[207] Q. He, S. Sun, S. Xiao, and L. Zhou, "High-efficiency metasurfaces: principles, realizations, and applications", Adv. Opt. Mater. **6**, 1800415 (2018) (cited on p. 23).

[208] X. Zang, F. Dong, F. Yue, C. Zhang, L. Xu, Z. Song, M. Chen, P.-Y. Chen, G. S. Buller, and Y. e. a. Zhu, "Polarization encoded color image embedded in a dielectric metasurface", Adv. Mater. **30**, 1707499 (2018) (cited on p. 23).

[209] J. P. Balthasar Mueller, N. A. Rubin, R. C. Devlin, B. Groever, and F. Capasso, "Metasurface polarization optics: independent phase control of arbitrary orthogonal states of polarization", Phys. Rev. Lett. **118**, 113901 (2017) (cited on p. 23).

[210] N. K. Emani, E. Khaidarov, R. Paniagua-Dominguez, Y. H. Fu, V. Valuckas, S. Lu, X. Zhang, S. T. Tan, H. V. Demir, and A. I. Kuznetsov, "High-efficiency and low-loss gallium nitride dielectric metasurfaces for nanophotonics at visible wavelengths", Appl. Phys. Lett. **111**, 221101 (2017) (cited on pp. 23, 66, 223).

[211] S. Kruk, F. Ferreira, N. Mac Suibhne, C. Tsekrekos, I. Kravchenko, A. Ellis, D. Neshev, S. Turitsyn, and Y. Kivshar, "Transparent dielectric metasurfaces for spatial mode multiplexing", Laser Photon. Rev. **12**, 1800031 (2018) (cited on p. 23).

[212] E. Arbabi, J. Li, R. J. Hutchins, S. M. Kamali, A. Arbabi, Y. Horie, P. Van Dorpe, V. Gradinaru, D. A. Wagenaar, and A. Faraon, "Two-photon microscopy with a double-wavelength metasurface objective lens", Nano Lett. **18**, 4943–4948 (2018) DOI: 10.1021/acs.nanolett.8b01737, (cited on pp. 23, 31, 38, 141).

[213] H. Kwon, E. Arbabi, S. M. Kamali, M. Faraji-Dana, and A. Faraon, "Computational complex optical field imaging using a designed metasurface diffuser", Optica **5**, 924–931 (2018) DOI: 10.1364/OPTICA.5.000924 (cited on p. 23).

[214] Z.-L. Deng, J. Deng, X. Zhuang, S. Wang, K. Li, Y. Wang, Y. Chi, X. Ye, J. Xu, and G. P. e. a. Wang, "Diatomic metasurface for vectorial holography", Nano Lett. **18**, 2885–2892 (2018) (cited on p. 24).

[215] R. Zhao, B. Sain, Q. Wei, C. Tang, X. Li, T. Weiss, L. Huang, Y. Wang, and T. Zentgraf, "Multichannel vectorial holographic display and encryption", Light Sci. Appl. **7**, 95 (2018) (cited on p. 24).

[216] N. A. Rubin, A. Zaidi, M. Juhl, R. P. Li, J. P. B. Mueller, R. C. Devlin, K. Leósson, and F. Capasso, "Polarization state generation and measurement with a single metasurface", Optics Express **26**, 21455–21478 (2018) (cited on p. 31).

[217] V. Liu, and S. Fan, "S4 : a free electromagnetic solver for layered periodic structures", Comput. Phys. Commun. **183**, 2233–2244 (2012) (cited on pp. 31, 33, 50, 59, 73, 77, 101, 184, 196, 202, 214).

[218] M. Young, "Zone plates and their aberrations", J. Opt. Soc. Am. **62**, 972–976 (1972) (cited on p. 38).

[219] M. Born, and E. Wolf, *Principles of optics: electromagnetic theory of propagation, interference and diffraction of light*, 7th (Cambridge University Press, Cambridge, 1999) (cited on pp. 38, 41, 59, 64, 67, 85, 86, 88, 103, 163, 183).

[220] B. Saleh, and M. Teich, *Fundamentals of photonics* (Wiley, 2013) (cited on pp. 38, 41).

[221] J. N. Latta, "Analysis of multiple hologram optical elements with low dispersion and low aberrations", Appl. Opt. **11**, 1686–1696 (1972) (cited on p. 38).

[222] S. J. Bennett, "Achromatic combinations of hologram optical elements", Appl. Opt. **15**, 542–545 (1976) (cited on p. 38).

[223] W. Sweatt, "Achromatic triplet using holographic optical elements", Appl. Opt. **16**, 1390–1391 (1977) (cited on p. 38).

[224] I. Weingärtner, and K. J. Rosenbruch, "Chromatic correction of two- and three-element holographic imaging systems", Optica Acta **29**, 519–529 (1982) (cited on p. 38).

[225] D. A. Buralli, and J. R. Rogers, "Some fundamental limitations of achromatic holographic systems", J. Opt. Soc. Am. A **6**, 1863–1868 (1989) (cited on p. 38).

[226] Y. Wang, W. Yun, and C. Jacobsen, "Achromatic Fresnel optics for wideband extreme-ultraviolet and X-ray imaging", Nature **424**, 50–53 (2003) (cited on p. 38).

[227] F. Aieta, M. A. Kats, P. Genevet, and F. Capasso, "Multiwavelength achromatic metasurfaces by dispersive phase compensation", Science **347**, 1342–1345 (2015) (cited on pp. 38, 86, 103, 134, 159, 182).

[228] M. Khorasaninejad, F. Aieta, P. Kanhaiya, M. A. Kats, P. Genevet, D. Rousso, and F. Capasso, "Achromatic metasurface lens at telecommunication wavelengths", Nano Lett. **15**, 5358–5362 (2015) (cited on pp. 38, 86, 222).

[229] O. Eisenbach, O. Avayu, R. Ditcovski, and T. Ellenbogen, "Metasurfaces based dual wavelength diffractive lenses", Opt. Express **23**, 3928–3936 (2015) (cited on pp. 38, 86, 182).

[230] Z. Zhao, M. Pu, H. Gao, J. Jin, X. Li, X. Ma, Y. Wang, P. Gao, and X. Luo, "Multispectral optical metasurfaces enabled by achromatic phase transition", Sci. Rep. **5**, 15781 (2015) (cited on p. 38).

[231] J. Cheng, and H. Mosallaei, "Truly achromatic optical metasurfaces: a filter circuit theory-based design", J. Opt. Soc. Am. B **32**, 2115–2121 (2015) (cited on p. 38).

[232] K. Miyamoto, "The phase fresnel lens", J. Opt. Soc. Am. **51**, 17–20 (1961) (cited on pp. 41, 67, 145, 163).

[233] D. Faklis, and G. M. Morris, "Spectral properties of multiorder diffractive lenses", Appl. Opt. **34**, 2462–2468 (1995) (cited on pp. 41, 86, 103, 145, 159, 163).

[234] A. F. Oskooi, D. Roundy, M. Ibanescu, P. Bermel, J. D. Joannopoulos, and S. G. Johnson, "Meep: a flexible free-software package for electromagnetic simulations by the FDTD method", Comput. Phys. Commun. **181**, 687–702 (2010) (cited on pp. 45, 53, 73, 102).

[235] W. Zhao, B. Liu, H. Jiang, J. Song, Y. Pei, and Y. Jiang, "Full-color hologram using spatial multiplexing of dielectric metasurface", Opt. Lett. **41**, 147–150 (2016) (cited on pp. 48, 86).

[236] E. Maguid, I. Yulevich, D. Veksler, V. Kleiner, M. L. Brongersma, and E. Hasman, "Photonic spin-controlled multifunctional shared-aperture antenna array", Science **352**, 1202–1206 (2016) (cited on p. 48).

[237] D. B. Murphy, and M. W. Davidson, *Fundamentals of light microscopy and electronic imaging*, 2nd edn (Wiley-Blackwell, 2012) (cited on p. 64).

[238] W. Denk, J. H. Strickler, and W. W. Webb, "Two-photon laser scanning fluorescence microscopy", Science **248**, 73–76 (1990) (cited on p. 66).

[239] K. Konig, "Multiphoton microscopy in life sciences", Jour. Microsc. **200**, 83–104 (2000) (cited on p. 66).

[240] W. R. Zipfel, R. M. Williams, and W. W. Webb, "Nonlinear magic: multiphoton microscopy in the biosciences", Nat. Biotechnol. **21**, 1369–1377 (2003) (cited on p. 66).

[241] F. Helmchen, and W. Denk, "Deep tissue two-photon microscopy", Nat. Methods **2**, 932–940 (2005) (cited on p. 66).

[242] F. Helmchen, M. S. Fee, D. W. Tank, and W. Denk, "A miniature head-mounted two-photon microscope: high-resolution brain imaging in freely moving animals", Neuron **31**, 903–912 (2001) (cited on pp. 66, 72).

[243] K. Konig, A. Ehlers, I. Riemann, S. Schenkl, R. Buckle, and M. Kaatz, "Clinical two-photon microendoscopy", Microsc. Res. Tech. **70**, 398–402 (2007) (cited on pp. 66, 72).

[244] C. J. Engelbrecht, R. S. Johnston, E. J. Seibel, and F. Helmchen, "Ultra-compact fiber-optic two-photon microscope for functional fluorescence imaging in vivo", Opt. Express **16**, 5556–5564 (2008) (cited on pp. 66, 72).

[245] C. L. Hoy, N. J. Durr, P. Chen, W. Piyawattanametha, H. Ra, O. Solgaard, and A. Ben-Yakar, "Miniaturized probe for femtosecond laser microsurgery and two-photon imaging", Opt. Express **16**, 9996–10005 (2008) (cited on pp. 66, 72).

[246] W. Piyawattanametha, E. D. Cocker, L. D. Burns, R. P. J. Barretto, J. C. Jung, H. Ra, O. Solgaard, and M. J. Schnitzer, "In vivo brain imaging using a portable 2.9 g two-photon microscope based on a microelectromechanical systems scanning mirror", Opt. Lett. **34**, 2309–2311 (2009) (cited on pp. 66, 72).

[247] W. Zong, R. Wu, M. Li, Y. Hu, Y. Li, J. Li, H. Rong, H. Wu, Y. Xu, and Y. e. a. Lu, "Fast high-resolution miniature two-photon microscopy for brain imaging in freely behaving mice", Nat. Methods **14**, 713–719 (2017) (cited on pp. 66, 72).

[248] A. She, S. Zhang, S. Shian, D. R. Clarke, and F. Capasso, "Adaptive metalenses with simultaneous electrical control of focal length, astigmatism, and shift", Sci. Adv. **4**, eaap9957 (2018) (cited on pp. 66, 72, 147).

[249] E. Maguid, M. Yannai, A. Faerman, I. Yulevich, V. Kleiner, and E. Hasman, "Disorder-induced optical transition from spin Hall to random Rashba effect", Science **358**, 1411–1415 (2017) (cited on p. 66).

[250] J. Li, N. Verellen, D. Vercruysse, T. Bearda, L. Lagae, and P. Van Dorpe, "All-dielectric antenna wavelength router with bidirectional scattering of visible light", Nano Lett. **16**, 4396–4403 (2016) (cited on p. 66).

[251] M. Rahmani, L. Xu, A. E. Miroshnichenko, A. Komar, R. Camacho-Morales, H. Chen, Y. Zárate, S. Kruk, G. Zhang, and D. N. e. a. Neshev, "Reversible thermal tuning of all-dielectric metasurfaces", Adv. Funct. Mater. **27**, 1700580 (2017) (cited on p. 66).

[252] X. Yin, T. Steinle, L. Huang, T. Taubner, M. Wuttig, T. Zentgraf, and H. Giessen, "Beam switching and bifocal zoom lensing using active plasmonic metasurfaces", Light: Sci. Appl. **6**, e17016 (2017) (cited on p. 66).

[253] C. Schlickriede, N. Waterman, B. Reineke, P. Georgi, G. Li, S. Zhang, and T. Zentgraf, "Imaging through nonlinear metalens using second harmonic generation", Adv. Mater. **30**, 1703843 (2018) (cited on p. 66).

[254] S. Colburn, A. Zhan, and A. Majumdar, "Metasurface optics for full-color computational imaging", Sci. Adv. **4**, eaar2114 (2018) (cited on p. 66).

[255] S. Wang, P. C. Wu, V.-C. Su, Y.-C. Lai, M.-K. Chen, H. Y. Kuo, B. H. Chen, Y. H. Chen, T.-T. Huang, and J.-H. e. a. Wang, "A broadband achromatic metalens in the visible", Nat. Nanotechnol. **13**, 227–232 (2018) (cited on pp. 69, 145).

[256] D. Sell, J. Yang, S. Doshay, and J. A. Fan, "Periodic dielectric metasurfaces with high-efficiency, multiwavelength functionalities", Adv. Opt. Mater. **5**, 1700645 (2017) (cited on pp. 72, 222).

[257] A. Zhan, S. Colburn, C. M. Dodson, and A. Majumdar, "Metasurface freeform nanophotonics", Sci. Rep. **7**, 1673 (2017) (cited on pp. 72, 147).

[258] B. Wang, F. Dong, D. Yang, Z. Song, L. Xu, W. Chu, Q. Gong, and Y. Li, "Polarization-controlled color-tunable holograms with dielectric metasurfaces", Optica **4**, 1368–1371 (2017) (cited on p. 72).

[259] C. Sauvan, P. Lalanne, and M.-S. L. Lee, "Broadband blazing with artificial dielectrics", Opt. Lett. **29**, 1593–1595 (2004) (cited on p. 86).

[260] Z.-L. Deng, S. Zhang, and G. P. Wang, "Wide-angled off-axis achromatic metasurfaces for visible light", Opt. Express **24**, 23118–23128 (2016) (cited on pp. 86, 223).

[261] E. Arbabi, A. Arbabi, S. M. Kamali, Y. Horie, and A. Faraon, "Dispersionless metasurfaces using dispersive meta-atoms", in Conference on lasers and electro-optics (cleo) (2016), FM2D.4 (cited on pp. 88, 159).

[262] P. A. Morton, and J. B. Khurgin, "Microwave photonic delay line with separate tuning of the optical carrier", IEEE Photon. Technol. Lett. **21**, 1686–1688 (2009) (cited on p. 91).

[263] R. Harrington, *Time-harmonic electromagnetic fields* (Wiley, 2001) (cited on p. 108).

[264] S. M. Kamali*, E. Arbabi*, and A. Faraon, "Metasurface-based compact light engine for ar headsets", in Spie photon. west (2019), p. 11040, DOI: 10.1117/12.2523720, (cited on p. 124).

[265] N. Meinzer, W. L. Barnes, and I. R. Hooper, "Plasmonic meta-atoms and metasurfaces", Nat. Photon. **8**, 889–898 (2014) (cited on p. 125).

[266] L. Zhang, S. Mei, K. Huang, and C.-W. Qiu, "Advances in full control of electromagnetic waves with metasurfaces", Adv. Opt. Mater. **4**, 818–833 (2016) (cited on p. 125).

[267] G. Zheng, H. Mühlenbernd, M. Kenney, G. Li, T. Zentgraf, and S. Zhang, "Metasurface holograms reaching 80% efficiency", Nat. Nanotechnol. **10**, 308–312 (2015) (cited on p. 125).

[268] E. R. Fossum, "CMOS image sensors: electronic camera-on-a-chip", IEEE Trans. Electron Devices **44**, 1689–1698 (1997) (cited on p. 125).

[269] N. Bokor, and N. Davidson, "Aberration-free imaging with an aplanatic curved diffractive element", Appl. Opt. **40**, 5825–5829 (2001) (cited on p. 125).

[270] F. Aieta, P. Genevet, M. A. Kats, and F. Capasso, "Aberrations of flat lenses and aplanatic metasurfaces", Opt. Express **21**, 31530–31539 (2013) (cited on p. 125).

[271] M. Reiss, "Notes on the $\cos^4$ law of illumination", J. Opt. Soc. Am. **38**, 980–986 (1948) (cited on p. 131).

[272] W. J. Smith, *Principles of optics: electromagnetic theory of propagation, interference and diffraction of light*, 4th (McGraw Hill, New York, 2008) (cited on p. 133).

[273] N. Wiener, *Extrapolation, interpolation, and smoothing of stationary time series with engineering applications* (MIT Press, Cambridge, MA, 1949) (cited on pp. 134, 188).

[274] H. Han, M. Kriman, and M. Boomgarden, "Wafer level camera technology from wafer level packaging to wafer level integration", in 11th international conference on electronic packaging technology - high density packaging (icept-hdp) (2010), pp. 121–124 (cited on p. 134).

[275] F. Wippermann, M. Muller, M. Wany, and S. Voltz, "Miniaturized camera system for an endoscopic capsule for examination of the colonic mucosa", in Spie optical engineering and applications, Vol. 9192 (2014), pp. 91920–6 (cited on p. 134).

[276] T. Gissibl, S. Thiele, A. Herkommer, and H. Giessen, "Two-photon direct laser writing of ultracompact multi-lens objectives", Nat. Photon **10**, 554–5601 (2016) (cited on p. 134).

[277] T. Xu, Y. K. Wu, X. G. Luo, and L. J. Guo, "Plasmonic nanoresonators for high-resolution colour filtering and spectral imaging", Nat. Commun. **1**, 59 (2010) (cited on p. 134).

[278] C. C. Fesenmaier, Y. Huo, and P. B. Catrysse, "Optical confinement methods for continued scaling of CMOS image sensor pixels", Opt. Express **16**, 20457–20470 (2008) (cited on p. 134).

[279] Y. Ren, L. Li, Z. Wang, S. M. Kamali, E. Arbabi, A. Arbabi, Z. Zhao, G. Xie, Y. Cao, N. Ahmed, Y. Yan, C. Liu, A. J. Willner, S. Ashrafi, M. Tur, A. Faraon, and A. E. Willner, "Orbital angular momentum-based space division multiplexing for high-capacity underwater optical communications", Sci. Rep. **6**, 33306 (2016) DOI: doi.org/10.1038/srep33306 (cited on pp. 136, 223).

[280] B. C. Kress, and P. Meyrueis, *Applied digital optics: from micro-optics to nanophotonics* (John Wiley & Sons, Ltd, 2009) (cited on pp. 137, 145).

[281] B. Kress, and T. Starner, "A review of head-mounted displays HMD technologies and applications for consumer electronics", in Spie defense, security, and sensing, Vol. 8720 (2013), p. 13 (cited on p. 137).

[282] X. Hu, and J. Carollo, "Head mounted display device with multiple segment display and optics", US Patent App., 14/923, 144 (2017) (cited on p. 137).

[283] A. Travis, J. S. Kollin, and A. Georgiou, "Virtual image display with curved light path", US Patent, 9, 759, 919 (2017) (cited on p. 137).

[284] A. Maimone, A. Georgiou, and J. S. Kollin, "Holographic near-eye displays for virtual and augmented reality", ACM Trans. Graph. **36**, 1–16 (2017) (cited on p. 137).

[285] D. Lin, M. Melli, E. Poliakov, P. S. Hilaire, S. Dhuey, C. Peroz, S. Cabrini, M. Brongersma, and M. Klug, "Optical metasurfaces for high angle steering at visible wavelengths", Sci. Rep. **7**, 2286 (2017) (cited on p. 138).

[286] Z. Shi, W. T. Chen, and F. Capasso, "Wide field-of-view waveguide displays enabled by polarization-dependent metagratings", in Spie photonics europe, Vol. 10676 (2018), p. 6 (cited on p. 138).

[287] "http://www.eenewseurope.com/news/leti-solves-stacking-issue-micro-led-displays", (access date: 01/22/2019) (cited on p. 143).

[288] "Https://www.ledinside.com/news/2018/3/jbd_devises_new_micro_led_technology_to_make_ultra_compact_micro_led_microdisplays", (access date: 01/22/2019) (cited on p. 143).

[289] L. Wang, S. Kruk, H. Tang, T. Li, I. Kravchenko, D. N. Neshev, and Y. S. Kivshar, "Grayscale transparent metasurface holograms", Optica **3**, 1504–1505 (2016) (cited on p. 145).

[290] W. T. Chen, A. Y. Zhu, V. Sanjeev, M. Khorasaninejad, Z. Shi, E. Lee, and F. Capasso, "A broadband achromatic metalens for focusing and imaging in the visible", Nat. Nanotechnol. **13**, 220–226 (2018) (cited on p. 145).

[291] H.-S. Ee, and R. Agarwal, "Tunable metasurface and flat optical zoom lens on a stretchable substrate", Nano Lett. **16**, 2818–2823 (2016) (cited on pp. 146, 147).

[292] J. Burch, and A. Di Falco, "Surface topology specific metasurface holograms", ACS Photonics **5**, 1762–1766 (2018) (cited on p. 146).

[293] C. Peroz, V. Chauveau, E. Barthel, and E. Sondergard, "Nanoimprint lithography on silica sol–gels: a simple route to sequential patterning", Adv. Mater. **21**, 555–558 (2009) (cited on p. 146).

[294] C. Pina-Hernandez, V. Lacatena, G. Calafiore, S. Dhuey, K. Kravtsov, A. Goltsov, D. Olynick, V. Yankov, S. Cabrini, and C. Peroz, "A route for fabricating printable photonic devices with sub-10 nm resolution", Nanotechnology **24**, 065301 (2013) (cited on p. 146).

[295] K.-H. Jeong, G. L. Liu, N. Chronis, and L. P. Lee, "Tunable microdoublet lens array", Opt. Express **12**, 2494–2500 (2004) (cited on p. 147).

[296] S. W. Lee, and S. S. Lee, "Focal tunable liquid lens integrated with an electromagnetic actuator", Appl. Phys. Lett. **90**, 121129 (2007) (cited on p. 147).

[297] S. Sato, "Liquid-crystal lens-cells with variable focal length", Jpn. J. Appl. Phys. **18**, 1679–1684 (1979) (cited on p. 147).

[298] H. Ren, Y.-H. Fan, S. Gauza, and S.-T. Wu, "Tunable-focus flat liquid crystal spherical lens", Appl. Phys. Lett. **84**, 4789–4791 (2004) (cited on p. 147).

[299] O. Pishnyak, S. Sato, and O. D. Lavrentovich, "Electrically tunable lens based on a dual-frequency nematic liquid crystal", Appl. Opt. **45**, 4576–4582 (2006) (cited on p. 147).

[300] S. Kwon, and L. P. Lee, "Stacked two dimensional micro-lens scanner for micro confocal imaging array", in Technical digest. mems 2002 ieee international conference. fifteenth ieee international conference on micro electro mechanical systems (cat. no.02ch37266) (2002), pp. 483–486 (cited on pp. 147, 149).

[301] S. Kwon, V. Milanovic, and L. P. Lee, "Large-displacement vertical microlens scanner with low driving voltage", IEEE Photon. Technol. Lett. **14**, 1572–1574 (2002) (cited on pp. 147, 149).

[302] M. Baranski, S. Bargiel, N. Passilly, C. Gorecki, C. Jia, J. Frömel, and M. Wiemer, "Micro-optical design of a three-dimensional microlens scanner for vertically integrated micro-opto-electro-mechanical systems", Appl. Opt. **54**, 6924–6934 (2015) (cited on pp. 147, 149).

[303] F. Krogmann, W. Monch, and H. Zappe, "A MEMS-based variable micro-lens system", J. Opt. A Pure Appl. Opt. **8**, S330–S336 (2006) (cited on p. 147).

[304] L. Li, D. Wang, C. Liu, and Q.-H. Wang, "Zoom microscope objective using electrowetting lenses", Opt. Express **24**, 2931–2940 (2016) (cited on p. 147).

[305] S.-Y. Lee, H.-W. Tung, W.-C. Chen, and W. Fang, "Thermal actuated solid tunable lens", IEEE Photon. Technol. Lett. **18**, 2191–2193 (2006) (cited on p. 147).

[306] S. Shian, R. M. Diebold, and D. R. Clarke, "Tunable lenses using transparent dielectric elastomer actuators", Opt. Express **21**, 8669–8676 (2013) (cited on p. 147).

[307] Y. Zou, W. Zhang, F. S. Chau, and G. Zhou, "Miniature adjustable-focus endoscope with a solid electrically tunable lens", Opt. Express **23**, 20582–20592 (2015) (cited on p. 147).

[308] M. C. Sherrott, P. W. C. Hon, K. T. Fountaine, J. C. Garcia, S. M. Ponti, V. W. Brar, L. A. Sweatlock, and H. A. Atwater, "Experimental demonstration of $> 230^\circ$ phase modulation in gate-tunable graphene-gold reconfigurable mid-infrared metasurfaces", Nano Lett. **17**, 3027–3034 (2017) (cited on pp. 147, 148).

[309] S. Colburn, A. Zhan, and A. Majumdar, "Tunable metasurfaces via subwavelength phase shifters with uniform amplitude", Sci. Rep. **7**, 40174 (2017) (cited on pp. 147, 148).

[310] Y. Horie, A. Arbabi, E. Arbabi, S. M. Kamali, and A. Faraon, "High-speed, phase-dominant spatial light modulation with silicon-based active resonant antennas", ACS Photonics **5**, 1711–1717 (2018) DOI: 10.1021/acsphotonics.7b01073 (cited on p. 148).

[311] J. Cheng, S. Jafar-Zanjani, and H. Mosallaei, "All-dielectric ultrathin conformal metasurfaces: lensing and cloaking applications at 532 nm wavelength", Sci. Rep. **6**, 38440 (2016) (cited on p. 148).

[312] M. C. Y. Huang, Y. Zhou, and C. J. Chang-Hasnain, "A nanoelectromechanical tunable laser", Nat. Photon. **2**, 180–184 (2008) (cited on p. 148).

[313] B.-W. Yoo, M. Megens, T. Sun, W. Yang, C. J. Chang-Hasnain, D. A. Horsley, and M. C. Wu, "A 32×32 optical phased array using polysilicon subwavelength high-contrast-grating mirrors", Opt. Express **22**, 19029–19039 (2014) (cited on p. 148).

[314] L. Fan, M. C. Wu, K. D. Choquette, and M. H. Crawford, "Self-assembled microactuated XYZ stages for optical scanning and alignment", in International conference on solid state sensors and actuators, Vol. 1 (1997), pp. 319–322 (cited on p. 149).

[315] V. Kaajakari, *Practical MEMS* (Small Gear Pub., 2009) (cited on p. 155).

[316] E. Serra, M. Bawaj, A. Borrielli, G. D. Giuseppe, S. Forte, N. Kralj, N. Malossi, L. Marconi, F. Marin, and F. e. a. Marino, "Microfabrication of large-area circular high-stress silicon nitride membranes for optomechanical applications", AIP Adv. **6**, 065004 (2016) (cited on p. 159).

[317] J. P. Moura, R. A. Norte, J. Guo, C. Schafermeier, and S. Groblacher, "Centimeter-scale suspended photonic crystal mirrors", Opt. Express **26**, 1895–1909 (2018) (cited on p. 159).

[318] S. Wang, P. C. Wu, V.-C. Su, Y.-C. Lai, C. Hung Chu, J.-W. Chen, S.-H. Lu, J. Chen, B. Xu, and C.-H. e. a. Kuan, "Broadband achromatic optical metasurface devices", Nat. Commun. **8**, 187 (2017) (cited on p. 159).

[319] N. V. Tkachenko, *Optical spectroscopy: methods and instrumentations* (Elsevier, Amsterdam, 2006) (cited on p. 160).

[320] J. M. Hollas, *Modern spectroscopy*, 4th (John Wiley & Sons, West Sussex, 2004) (cited on p. 160).

[321] D. Nevejans, E. Neefs, E. Van Ransbeeck, S. Berkenbosch, R. Clairquin, L. De Vos, W. Moelans, S. Glorieux, A. Baeke, O. Korablev, I. Vinogradov, Y. Kalinnikov, B. Bach, J.-P. Dubois, and E. Villard, "Compact high-resolution spaceborne echelle grating spectrometer with acousto-optical tunable filter based order sorting for the infrared domain from 2.2 to 4.3 μm", Appl. Opt. **45**, 5191–5206 (2006) (cited on p. 160).

[322] C. E. Thomas, "Optical spectrum analysis of large space bandwidth signals", Appl. Opt. **5**, 1782–1790 (1966) (cited on p. 160).

[323] J. Azana, and M. A. a. Muriel, "Real-time optical spectrum analysis based on the time-space duality in chirped fiber gratings", IEEE J. Quantum Electron. **36**, 517–526 (2000) (cited on p. 160).

[324] M. Ferrari, and V. Quaresima, "A brief review on the history of human functional near-infrared spectroscopy (FNIRS) development and fields of application", Neuroimage **63**, 921–935 (2012) (cited on p. 161).

[325] B. Momeni, E. S. Hosseini, M. Askari, M. Soltani, and A. Adibi, "Integrated photonic crystal spectrometers for sensing applications", Opt. Commun. **282**, 3168–3171 (2009) (cited on p. 161).

[326] S.-W. Wang, C. Xia, X. Chen, W. Lu, M. Li, H. Wang, W. Zheng, and T. Zhang, "Concept of a high-resolution miniature spectrometer using an integrated filter array", Opt. Lett. **32**, 632–634 (2007) (cited on p. 161).

[327] N. K. Pervez, W. Cheng, Z. Jia, M. P. Cox, H. M. Edrees, and I. Kymissis, "Photonic crystal spectrometer", Opt. Express **18**, 8277–8285 (2010) (cited on p. 161).

[328] Z. Xia, A. A. Eftekhar, M. Soltani, B. Momeni, Q. Li, M. Chamanzar, S. Yegnanarayanan, and A. Adibi, "High resolution on-chip spectroscopy based on miniaturized microdonut resonators", Opt. Express **19**, 12356–12364 (2011) (cited on p. 161).

[329] B. Redding, S. F. Liew, R. Sarma, and H. Cao, "Compact spectrometer based on a disordered photonic chip", Nat. Photon. **7**, 746–751 (2013) (cited on pp. 161, 171).

[330] A. Nitkowski, L. Chen, and M. Lipson, "Cavity-enhanced on-chip absorption spectroscopy using microring resonators", Opt. Express **16**, 11930–11936 (2008) (cited on p. 161).

[331] X. Gan, N. Pervez, I. Kymissis, F. Hatami, and D. Englund, "A high-resolution spectrometer based on a compact planar two dimensional photonic crystal cavity array", Appl. Phys. Lett. **100**, 231104 (2012) (cited on p. 161).

[332] R. Bockstaele, B. Luyssaert, and K. Naessens, "Compact catadioptric spectrometer", US Patent, 7, 864, 317 (2011) (cited on p. 161).

[333] K. Shibayama, T. Suzuki, and M. Ito, "Spectroscope", US Patent, 8, 477, 306 (2013) (cited on pp. 161, 171).

[334] S. Grabarnik, A. Emadi, H. Wu, G. De Graaf, and R. F. Wolffenbuttel, "High-resolution microspectrometer with an aberration-correcting planar grating", Appl. Opt. **47**, 6442–6447 (2008) (cited on p. 161).

[335] M. Madi, F. Ceyssens, I. Shorubalko, H. P. Herzig, B. Guldimann, and P. Giaccari, "Lippmann waveguide spectrometer with enhanced throughput and bandwidth for space and commercial applications", Opt. Express **26**, 2682–2707 (2018) (cited on p. 161).

[336] M. Khorasaninejad, W. T. Chen, J. Oh, and F. Capasso, "Super-dispersive off-axis meta-lenses for compact high resolution spectroscopy", Nano Lett. **16**, 3732–3737 (2016) (cited on p. 163).

[337] A. Y. Zhu, W. T. Chen, M. Khorasaninejad, J. Oh, A. Zaidi, I. Mishra, R. C. Devlin, and F. Capasso, "Ultra-compact visible chiral spectrometer with meta-lenses", APL Photonics **2**, 036103 (2017) (cited on p. 163).

[338] M. Jang, Y. Horie, A. Shibukawa, J. Brake, Y. Liu, S. M. Kamali, A. Arbabi, H. Ruan, A. Faraon, and C. Yang, "Wavefront shaping with disorder-engineered metasurfaces", Nat. Photon. **12**, 84–90 (2018) (cited on p. 163).

[339] C. Zhang, G. Cheng, P. Edwards, M.-D. Zhou, S. Zheng, and Z. Liu, "G-fresnel smartphone spectrometer", Lab Chip **16**, 246–250 (2016) (cited on p. 163).

[340] D. A. Bekele, G. C. Park, R. Malureanu, and I.-S. Chung, "Polarization-independent wideband high-index-contrast grating mirror", IEEE Photon. Technol. Lett. **27**, 1733–1736 (2015) (cited on p. 170).

[341] C. J. Chang-Hasnain, and W. Yang, "High-contrast gratings for integrated optoelectronics", Adv. Opt. Photon. **4**, 379–440 (2012) (cited on p. 170).

[342] P. Gatkine, S. Veilleux, Y. Hu, J. Bland-Hawthorn, and M. Dagenais, "Arrayed waveguide grating spectrometers for astronomical applications: new results", Opt. Express **25**, 17918–17935 (2017) (cited on p. 171).

[343] A. Silva, F. Monticone, G. Castaldi, V. Galdi, A. Alu, and N. Engheta, "Performing mathematical operations with metamaterials", Science **343**, 160–163 (2014) (cited on p. 172).

[344] G. C. Gilbreath, "Large-aperture multiple quantum well modulating retroreflector for free-space optical data transfer on unmanned aerial vehicles", Opt. Eng. **40**, 1348–1356 (2001) (cited on pp. 172, 173, 182).

[345] W. S. Rabinovich, R. Mahon, P. G. Goetz, E. Waluschka, D. S. Katzer, S. C. Binari, and G. C. Gilbreath, "A cat's eye multiple quantum-well modulating retro-reflector", IEEE Photon. Technol. Lett. **15**, 461–463 (2003) (cited on pp. 172, 173).

[346] L. X. Zhou, J. M. Kahn, and K. S. J. Pister, "Corner-cube retroreflectors based on structure-assisted assembly for free-space optical communication", J. Microelectromech. Syst. **12**, 233–242 (2003) (cited on pp. 172, 173).

[347] T. Takatsuji, M. Goto, S. Osawa, R. M. Yin, and T. Kurosawa, "Whole-viewing-angle cat's-eye retroreflector as a target of laser trackers", Meas. Sci. Technol. **10**, 87–90 (1999) (cited on p. 172).

[348] S. P. Griggs, M. B. Mark, and B. J. Feldman, "Dynamic optical tags", in Battlespace digitization and network-centric systems iv, Vol. 5441 (2004), pp. 151–160 (cited on p. 173).

[349] B. A. Warneke, M. D. Scott, B. S. Leibowitz, L. Zhou, C. L. Bellew, J. A. Chediak, J. M. Kahn, B. E. Boser, and K. S. Pister, "An autonomous 16 mm^3 solar-powered node for distributed wireless sensor networks", in Ieee sensors, Vol. 2 (2002), pp. 1510–1515 (cited on p. 173).

[350] K. Ozawa, N. Koga, N. Sugimoto, Y. Saito, A. Nomura, T. Aoki, T. Itabe, and H. Kunimori, "Laser transmitter/receiver system for earth-satellite-earth long-path absorption measurements of atmospheric trace species using the retroreflector in space", Opt. Eng. **36**, 3235–3241 (1997) (cited on p. 173).

[351] Y. G. Ma, C. K. Ong, T. Tyc, and U. Leonhardt, "An omnidirectional retroreflector based on the transmutation of dielectric singularities", Nat. Mater. **8**, 639–642 (2009) (cited on p. 173).

[352] J. A. Vitaz, A. M. Buerkle, and K. Sarabandi, "Tracking of metallic objects using a retro-reflective array at 26 GHz", IEEE Trans. Antennas Propag. **58**, 3539–3544 (2010) (cited on p. 173).

[353] J. J. Snyder, "Paraxial ray analysis of a cat's-eye retroreflector", Appl. Opt. **14**, 1825–1828 (1975) (cited on p. 182).

[354] J. Cheng, S. Inampudi, and H. Mosallaei, “Optimization-based dielectric metasurfaces for angle-selective multifunctional beam deflection”, Sci. Rep. **7**, 12228 (2017) (cited on p. 222).

[355] Z. Lin, B. Groever, F. Capasso, A. W. Rodriguez, and M. Loncar, “Topology optimized multi-layered meta-optics”, Phys. Rev. Appl. **9**, 044030 (2018) (cited on p. 222).